UNIVERSITY OF SOUTHAMPTON

A STUDY OF SEMICONDUCTOR-BASED ATOMIC OXYGEN SENSORS FOR GROUND AND SATELLITE APPLICATIONS

by

James John Osborne

Thesis submitted for Doctor of Philosophy

ASTRONAUTICS

SCHOOL OF ENGINEERING SCIENCES

FACULTY OF ENGINEERING AND APPLIED SCIENCE

November 1999

UNIVERSITY OF SOUTHAMPTON

ABSTRACT

FACULTY OF ENGINEERING AND APPLIED SCIENCE

SCHOOL OF ENGINEERING SCIENCES (ASTRONAUTICS)

Doctor of Philosophy

A STUDY OF SEMICONDUCTOR-BASED ATOMIC OXYGEN SENSORS FOR GROUND AND SATELLITE APPLICATIONS

by James John Osborne

Near-Earth space is known to be a hazardous environment. For example, operation of satellites in the thermosphere is endangered by atomic oxygen impingement. Oxidative reactions of atomic oxygen erode, or otherwise deteriorate, many of the materials used to fabricate satellites, especially polymers and silver. As a result of these deleterious effects there is a requirement to perform in situ measurements of orbital oxygen atom densities. Review of the literature, coupled with a new quantitative, graphical comparison of the available AO measurement techniques reveals that sensors previously used for these evaluations suffer from several disadvantages, such as large mass and power budgets, and/or limited lifetime of operation. Thus, for these reasons, not one of the methods appears appropriate for regular inclusion on long duration microsatellite missions.

A novel technique has been investigated to create a suitable atomic oxygen detector. The method is based upon the same principles as the increasingly popular semiconductor gas sensor. In this study the semiconductor used is thin film, n-type, zinc oxide, deposited onto an alumina substrate equipped with a heater on the reverse side. Two different designs of sensor have been conceived; the difference between the two models is the method of making electrical contact to the oxide film, which is formed either by thin gold films, or by more robust thick gold interdigitated array.

Laboratory-based experiments have exposed several sensors to hyperthermal atomic oxygen. Upon exposure to this species, the conductance of the semiconductor is observed to decrease. It is found that the sensor response, which is measured by its rate of conductance decrease, is proportional to the magnitude of the flux engendering that change. Moreover, it is discovered that heating the sensor refreshes it, so that the sensor may be employed for further flux measurements - the technique is reusable, unlike many other oxygen atom sensors. Regeneration of the sensor is a complex process; a permanent decrease of conductivity is observed, with no recovery to the pre-exposure value. However, it is found that repeated flux measurements may still be made with the device.

The sensors have also been utilized to determine the axial flux variation in a ground-based atomic oxygen source. The results of this study agree closely with those of another measurement, using a second technique, and with gas dynamic predictions. This research represents the only employment of thin film zinc oxide sensors for the measurement of hyperthermal oxygen atom fluxes.

For the first time, a lightweight and low power experiment has been built to demonstrate the application of the devices in Earth orbit on the STRV-1c microsatellite. The design and interface of the experiment is described in detail. Launch of the vehicle is anticipated in spring 2000. Due to the mass and power properties of the unit it is suitable for application to other microsatellite missions.

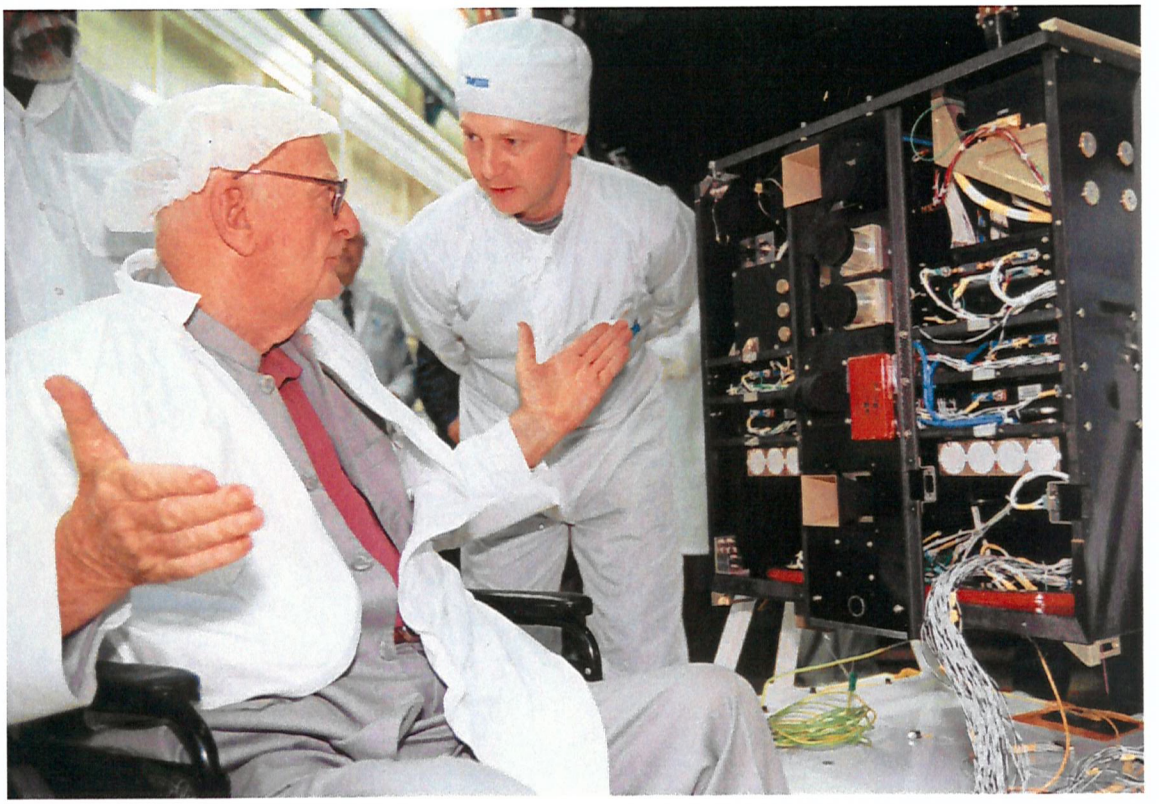

Frontispiece - Arthur C. Clarke (seated) visiting DERA Space Department. The vehicle beside Clarke is STRV-1c, which was under going assembly integration and testing at the time. The red rectangular box on the closing panel towards Clarke is the AOE-2 'remove before flight' cover. Photograph copyright and courtesy DERA Space Department, 1999.

CONTENTS

LIST OF FIGURES

LIST OF TABLES

ACKNOWLEDGEMENTS

'It is difficult to say that something is impossible, since yesterday's dream is today's hope and tomorrow's reality.' ***R. H. Goddard.***

Probably the oldest form of currency, I feel, is that of the 'favour'. During the course of my work I have inevitably built up a substantial 'debt' to many people - all of whom I will try to mention here. No doubt I shall miss a few, to them, many thanks.

Firstly, I would like to thank my supervisors **Graham Roberts** and **Alan Chambers** for their financial support. **Graham** must receive acknowledgement for teaching me to write proper, and always insisting that, I; punctuate sentences - correctly. Whilst, **Alan** showed me that delegation is always best.

The support of **Marc van Eesbeek**, **Jeremy Matcham** and the others at **ESTEC** was invaluable, especially the use of ATOX. Many thanks to **Angela Cant** at DERA who answered my silly questions without laughing (too much), and **DERA Space** for providing the launch opportunity. I am indebted to **Pete Dargie** and **John Atkinson** of the Thick Film Unit for their advice regarding the thick film sensor design. Many thanks to **Ken Lawson** at Cranfield University for all of the sensor depositions and free lunches.

Several people have been involved with the technical facet of the AOE-2 project. Without the assistance of **Robert Stansbridge** and **Anthony Wood** in the design of the electronics, the AOE-2 project would have been impossible. I am also grateful to **Simon Klitz** and **Colin Bielby** who manufactured many of my mechanical components, and **Adam Healey** for the XRD scans.

There are many other people that have made my research more fun. The office 'gang': **Ben**, **Franz**, **Hugh, Jon**, **Ismat** and **Izzy**. Also, everyone that has been there so that I did not have to be inebriated on my own: **they (might be able to) remember who they are**. Special recognition must also be given to **Nick Wood** for being the closest thing I had to a mentor, sorry the system treated you so badly, and **Adrian Tighe** for showing me that perseverance is indeed beneficial.

'Life cannot wait until the sciences may have explained the universe scientifically. We cannot put off living until we are ready. The most salient characteristic of life is its coerciveness: it is always urgent, "here and now" without any possible postponement. Life is fired at us point-blank.' ***José Ortega y Gasset.***

However, most of all, I would like to thank my close friends and family for their continued endurance of my excitements and woes. My **Mother** and **Father** for their unending (and unerring) support, but especially my **Father** for his scientific input. **Andrew**, my brother, offered much computer advice - the best 24/7 available. Above all though, **Emily** - to whom this thesis is dedicated - deserves extra special mention for proof-reading this document (good editorial experience?) and for all those chats that have dragged me back from the edge of insanity on more than one occasion. I owe you all so much.

Lastly, thanks to **Shepherd Neame** for brewing the best beer I have ever tasted - it truly is the stuff of life. *Nunc est bibendum.*

'God created solids, but surfaces are the work of the Devil.' **Wolfgang Pauli.**

ACRONYMS

AC	Alternating Current
ACOMEX	Advanced COmposite Materials EXperiment
ADC	Analogue to Digital Converter
AO	Atomic Oxygen
AOE	Atomic Oxygen Experiment (a series of University of Southampton spaceflight experiments)
ATOX	ATomic OXygen test rig (located at ESTEC)
BREMSAT	University of BREMen SATellite
CDU	Command Distribution Unit
CNES	Centre National D'Etudes Spatiales
CPU	Central Processing Unit
C-QCM	Carbon-coated QCM
CT	CermeT
CW	Continuous Wave
DAU	Data Acquisition Unit
DC	Direct Current
DERA	Defence Evaluation and Research Agency
DMM	Digital MultiMeter
DRA	Defence Research Agency (now part of DERA)
DSN	Deep Space Network
EM	Engineering Model
EMI	ElectroMagnetic Interference
ESA	European Space Agency
ESTEC	European Space research and Technology Centre
EU	Electronics Unit (part of AOE-2)
EUTEF	EUropean Technology Exposure Facility
EUV	Extreme UltraViolet
FM	Flight Model
FWHM	Full-Width, Half Maximum
GSFC	Goddard Space Flight Center
GTO	Geostationary Transfer Orbit
hcp	hexagonal close-packed
HILAT	[not known at the time of writing], a satellite
IPA	IsoPropyl Alcohol
IR	InfraRed

ISIS	[not known at the time of writing], a satellite
LDEF	Long Duration Exposure Facility
LED	Light Emitting Diode
LEO	Low Earth Orbit
MACOR	machinable glass ceramic
MEDET	Materials Exposure and Degradation Experiment on EuTEF
MOS	Metal Oxide Semiconductor
MSIS	Mass Spectrometer and Incoherent Scatter
MULTIPHOT	MULTI-PHOTometer payload
NASA	National Aeronautics and Space Administration
NO	Nitrogen Oxide
OBC	On-Board Computer
OBDHS	On-Board Data Handling Subsystem
OGO	Orbiting Geophysics Observatory
ONERA	Office National d'Etudes et de Recherches Aérospatiales
PCB	Printed Circuit Board
PCDS	Power Conditioning and Distribution System
PEEK	PolyEtherEtherKetone
PID	Proportional-Integral-Derivative controller
PMMA	PolyMethylMethAcrylate (Perspex)
PSA	Pressure Sensitive Adhesive
PTFE	PolyTetraFluoroEthylene
QCM	Quartz Crystal Microbalance
RF	Radio Frequency
RFCS	Radio Frequency Communication Subsystem
RMS	(1) Root Mean Square (2) Remote Manipulator System
RT	ResinaTe
SAA	South Atlantic Anomaly
SAW	Surface Acoustic Wave device
SCL	Space Charge Layer
SEM	Scanning Electron Microscope (or Microscopy)
SEU	Single Event Upset
STRV	Space Technology Research Vehicle
STS	Space Transportation System (the Space Shuttle)
SU	Sensor Unit (part of AOE-2)

TEA	Transversely Excited Atmospheric (CO_2 laser)
TG	Thin Gold
UT	Universal Time
UV	UltraViolet
VUV	Vacuum UltraViolet
www	world wide web
XRD	X-Ray Diffraction
ZnO	zinc oxide

SYMBOLS

α	fraction of ionized adatoms	[-]
γ	scattering coefficient	[-]
ε	dielectric constant	[-]
ε_d	donor level/energy	[eV]
ε_F	Fermi level/energy	[eV]
ε_j	energy of state j	[eV]
ε_o	permittivity of free space (8.85×10^{-12})	[$F.m^{-1}$]
η	recombination coefficient	[-]
θ	incident radiation angle or peak position	[degrees, ^{o} or radians]
κ	number of electrons trapped per ion	[-]
λ	wavelength of radiation	[nm or Å]
μ	charge carrier mobility	[$cm.s^{-1}.(V.cm)^{-1}$]
ν	frequency	[s^{-1}]
ρ	density	[$g.cm^{-3}$]
ρ	resistivity	[(Ω.m)]
σ	conductivity	[$(\Omega.m)^{-1}$]
τ	mean residency time	[s]
ψ	wave function	[-]
a	crystal lattice parameter	[Å]
a_∞	maximum possible adsorbed atom density	[$atoms.cm^{-2}$]
a(t)	adsorbed atom density at time (t)	[$atoms.cm^{-2}$]
a^*	ratio of crystal atom surface density to maximum possible adsorbed atom density	[-]
a_s	adsorbed atom density at saturation	[$atoms.cm^{-2}$]
A	sensor area, exposed area or cross-sectional area	[m^2]
A	constant	[-]
b	breadth of film	[m]
B(2θ)	full width, half maximum	[radians]
B	constant	[-]
c	crystal lattice parameter	[Å]

C	surface density of crystal atoms	[atoms.cm^{-2}]
d	thickness of film	[μm or m]
d_{hkl}	interplanar spacing	[Å]
D	diffusion coefficient	[cm^2.s^{-1}]
D^0	frequency factor	[cm^2.s^{-1}]
D	constant	[-]
e	electron charge (1.602 x 10^{-19})	[C]
E	energy of electron in potential V	[J or eV]
E_g	band gap energy	[eV]
f	fluence (time-integrated flux)	[atoms.cm^{-2}]
f_{sat}	saturation fluence	[atoms.cm^{-2}]
F	flux	[atoms.cm^{-2}.s^{-1}]
g	conductance	[mhos]
g_b	bulk conductance	[mhos]
g_{Film}	film conductance	[mhos]
g_s	surface conductance	[mhos]
g_{Tot}	total conductance	[mhos]
h	Planck's constant (6.626 x 10^{-34})	[J.s]
H	heat of recombination	[J.atom^{-1}]
i	surface density of ions	[ions.cm^{-2}]
I	current	[A]
j	imaginary number ($\sqrt{-1}$)	[-]
$\underline{k}$	wave-vector (Chapter 4 only)	[-]
k	Boltzmann's constant (1.380 x 10^{-23})	[J.K^{-1}]
L	crystal dimension, length	[Å or m]
l	distance between electrodes	[m]
M & m	mass	[g or kg]

n	carrier density	$[m^{-3}]$
n_b	bulk carrier density	$[m^{-3}]$
n_e	extrinsic charge carrier density	$[m^{-3}]$
n_i	intrinsic charge carrier density	$[m^{-3}]$
n_j	occupation probability of state j	[-]
n_s	surface charge carrier density	$[m^{-2}]$
N_a	acceptor/surface state density	$[m^{-3}]$
N_b	number of charge carriers in bulk	[-]
N_c	effective density of states	$[m^{-3}]$
N_d	donor density	$[m^{-3}]$
N_s	number of surface charge carriers	[-]
o	order of reflection	[-]
P	Power	[W]
p_p	partial pressure	[Pa]
Q	activation energy	[eV]
R	resistance of sensor	[Ω]
R_0	base resistance	[Ω]
S	number of sensors in mass m	[-]
t	time	[min or s]
t_{sat}	time to sensor saturation	[s]
T	absolute temperature	[K]
u	integer	[-]
V	voltage, potential	[V]
V_s	surface potential	[V]
V	film volume	$[m^3]$
x	diffusion depth, distance	[m]
Y_{vol}	volume erosion yield	$[cm^3.atom^{-1}]$

CHAPTER 1

INTRODUCTION

Inquisitiveness is an innate trait of the human species. The quest for greater knowledge, the search for new materials, and the desire to conquer the unknown has driven mankind into the exploration of new territories and regions. Frequently, the environmental conditions encountered in the new surroundings have been far harsher than those to which the explorers have been previously accustomed. High pressures in the depths of the oceans, low temperatures in the polar regions and reduced air density on the peaks of the tallest mountains have all challenged the stamina and ingenuity of man. Surely though, there can be few more extreme examples of the unfamiliar environment than that which exists outside the bounds of the breatheable atmosphere. That is, in space.

1.1 THE NEAR-EARTH SPACE ENVIRONMENT

Vehicles and astronauts sent to work far above the surface of the Earth are subject to an environment containing many deleterious components (*James et al., 1994; Silverman, 1995; Bedingfield et al., 1996*). Each constituent of near-Earth space may act in isolation, or synergistically with others. In this manner, the performance of nearly every spacecraft system, whether electrical, mechanical, structural or biological may be degraded. Many of these hazards are shielded by the atmosphere and, thus, are not encountered during the daily lives of the inhabitants of the Earth. This remoteness makes comprehension of the effects somewhat more difficult than they might be otherwise. In order to set the scene for the following work, it is the aim of this section to introduce the major environmental factors that act on spacecraft systems in Earth orbit.

Unsurprisingly, the most dominant influence on the near-Earth space environment is the star around which the planet is in orbit. The sun discharges large quantities of energy and matter into the solar system (*Domingo, 1993*). Energy is emitted in the form of infrared (IR), visible, ultraviolet (UV) and X-ray electromagnetic radiation, whilst the matter - called the solar wind - primarily consists of electrons and protons. The magnitude of these emissions varies over an eleven-year cycle, the next maximum of which is due in 2002. Throughout the whole of the solar cycle, but particularly at times of solar maximum, extra amounts of matter and energy are explosively ejected by solar-flare events. The resulting pulse of energy and charged particles can hinder the operation of satellite and ground-based systems alike (*Bedingfield et al., 1996*).

Solar ejected protons and electrons travelling close to the Earth's magnetic field lines may become trapped to form radiation belts - the Van Allen belts (*Stark and Gabriel, 1997*). If a satellite should be in an orbit through one or more of the belts, the impinging high energy particles add to the ionizing radiation environment that it experiences (*Bedingfield et al., 1996*). Such radiation may cause single event upsets (SEUs) and latch-ups of microelectronic circuits. Low Earth orbiting (LEO) satellites frequently reside below these belts and, thus, are shielded from particulate radiation by the magnetic field. However, asymmetry in this field reduces the altitude of the trapped particles above the South Atlantic Ocean, in a region called the South Atlantic Anomaly (SAA). So, even orbits that are normally below the van Allen belts may experience radiation from this source, if they should fly through the SAA. Intergalactic cosmic rays (*Matthews, 1993*), essentially nuclei of heavy atoms, also contribute to the radiation environment but the flux of these particles is approximately constant, unlike that of the solar driven radiation belts, or solar flare particles.

Solar insolation of the upper atmosphere, particularly by vacuum and extreme ultraviolet (VUV and EUV), is responsible for the formation of plasma in the ionosphere (*Danilov and Istomin, 1970*). Vehicles moving in this environment may become charged due to non-equal fluxes of electrons and ions. Subsequently, if significant surface areas of a satellite are not conductive, widely different surface potentials may occur, followed by rapid, and often destructive, electrical discharges (*Nanevicz and Adamo, 1980*). Electrically-biased and electromagnetic interference (EMI) sensitive instruments may be affected, and surface materials may be permanently damaged.

The thermal environment experienced by orbiting vehicles is influenced by two sources in addition to direct solar irradiation (*Gilmore, 1994*): reflected solar radiation (albedo) and Earth-emitted radiation (Earth shine). Therefore, thermal inputs to orbiting vehicles vary not only with the seasons, but also with the ground-track of the vehicle. Moon and Earth generated eclipses further complicate the definition of the thermal environment. The hot-cold cycling that results when a vehicle transits from solar illumination to shadow (and *vice versa*) can cause thermal fatigue of materials and components. Many spacecraft systems, but especially those requiring stable or low temperatures, are greatly influenced by the thermal balance of the vehicle.

Comet remnants and debris caused by human activity in space pose impact threats to orbiting equipment (*Kessler, 1992; McDonnell, 1993*). Due to the large relative impact velocities, which are exacerbated if the orbits are anti-rotational, the impact of even small particles (of a few millionths of a microgram) can cause significant damage (*Laurance and Brownlee, 1986*). Small particles are responsible for the degradation of thermal and optical properties of surfaces (*Gulino,*

1988a; 1988b), whilst larger impacts have the propensity to destroy vehicles (*Bedingfield et al., 1996*). Contrary to expectations, the hazard posed by large debris is not as significant as that from smaller particles. Ground-based radar can track items greater than ~ 10 cm in size, allowing moveable vehicles to be guided around any potential impact threat. No such procedure can be used for the smaller objects. Micrometeoroid and debris impacts generate yet more particles and, so, it is expected that the number of particles will increase for the foreseeable future.

Lastly, there is the neutral thermosphere, a region of the upper Earth atmosphere between 90 - 600 kilometres altitude. The vertical density distributions of gases in this region are governed by free-molecular flow, so that the species tend to stratify according to their molecular masses (*James et al., 1994*). Solar irradiation has a significant impact on the overall density of the atmosphere at these altitudes, and so density varies not only with time of day, but also with the seasons and the stage of the solar cycle. Although the density of the atmosphere is low compared to sea level values, drag forces can still have a great influence on satellite and other object orbital trajectories (*Stark and Gabriel, 1997*). Unless the drag is countered by a propulsion system, the altitude of the vehicle will decrease and it will, eventually, re-enter the atmosphere proper. The species with the largest density in the neutral thermosphere is atomic oxygen (AO). Atomic oxygen causes several phenomena but, as will become clear in following chapters, the major concern is that AO is erosive to many spacecraft materials. Thus, there is a need to quantify the AO fluxes experienced by satellites - for this, a sensor is required.

1.2 WHAT IS A SENSOR?

Throughout this study frequent reference will be made to the words sensor and detector. In this text these words are treated as synonyms, but one must ask what is a sensor, and what is its function?

The Oxford English Dictionary definition of the word sensor is 'a device that reacts to a certain stimulus' (*Pollard, 1994*). Thus, a sensor can provide a measurement of the magnitude of an action, or of a quantity. Commonly, the output of a sensor is an electrical charge, voltage or current.

Figure 1.1 presents a schematic representation of such a sensor. In this model, a sensor is any device that converts an effect in one of the five signal domains (thermal, mechanical, radiant, magnetic and chemical) into a response in the electrical domain.

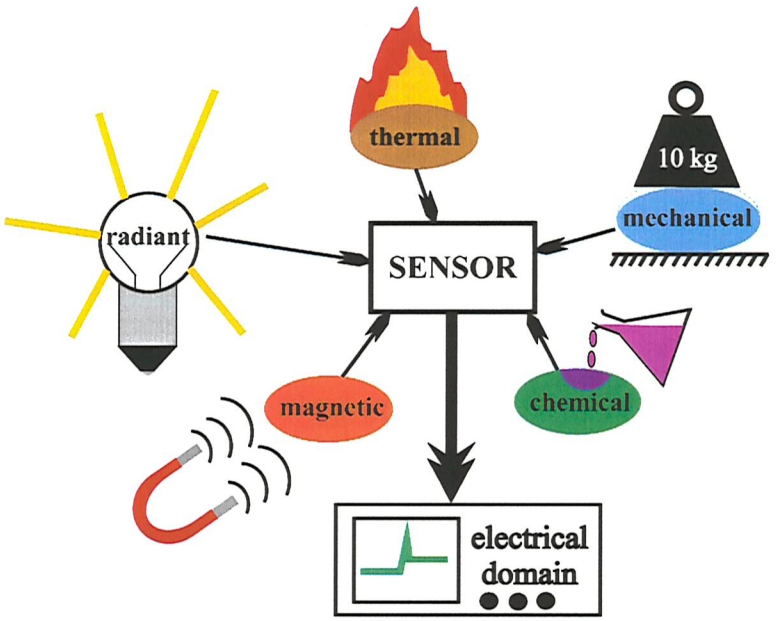

Figure 1.1 - Graphical representation of a sensor (after *White, 1998*)

1.3 AIMS OF PROJECT

The aims of this research project are:

- To design and fabricate a sensor able to measure hyperthermal atomic oxygen fluxes both in ground-based simulation sources and in orbit alike.
- To develop theoretical models describing sensor operation.
- To characterize the aforementioned sensor in a ground-based simulation source, in order to gain a scientific understanding of its response to atomic oxygen.
- To determine key sensor properties such as: calibration coefficients; operation methodology and the influences of certain other (not atomic oxygen) environments.
- To build a proto-flight space-based experiment suitable for launch on a specific microsatellite - meeting the available budgets and interface requirements of the satellite manufacturer - thereby enabling a demonstration of the performance of the sensor in continuous orbit; a scientific first.

1.4 THESIS LAYOUT

The following chapter of this work (2) discusses the formation of thermospheric AO, its effects on spacecraft materials, and the ground-based equipment used to simulate the LEO AO environment. It is the intention of this second chapter to highlight further the need for ground and space-based AO sensors. Chapter 3 reviews a number of techniques that have been employed for AO measurements. An inter-comparison of rocket and space-rated equipment demonstrates that

none of the devices used by the international community to date can be considered 'ideal'. Semiconductor physics, the topic of Chapter 4, is discussed at length to introduce the concepts necessary to enable a complete description of semiconductor gas sensor operation, which is the subject of Chapter 5. The following chapters then cover the design of the sensors used in this research (6); the investigations of the sensor material (7); the laboratory experiments performed (8); the results of these experiments (9 and 10); and, in Chapter 11, the design of the space flight equipment. Finally, conclusions from the research are drawn and suggestions for further work made.

CHAPTER 2

THERMOSPHERIC ATOMIC OXYGEN

It is the intention of this chapter to describe the effects of thermospheric atomic oxygen on the materials from which spacecraft are manufactured. Initially, the processes responsible for the creation and destruction of AO in the thermosphere are introduced. The following section concentrates on the erosive effects of AO on one of the most commonly used spacecraft materials - hydrocarbon-based polymers. Then, a short review of the literature concerning spaceflight experiments is used to highlight the problems and implications of such erosion. In this manner it is shown that there is a necessity to perform *in situ* measurements of AO densities and fluxes. Lastly, laboratory simulation sources that have been used to simulate space-based AO exposures are discussed and reviewed.

2.1 ATOMIC OXYGEN FORMATION AND THERMOSPHERIC MODELS

Within the thermosphere, neutral, ground state, atomic oxygen is formed through the photodissociation of molecular oxygen by solar ultraviolet radiation (*Banks et al., 1988*). At an altitude of around 80 to 100 km, AO undergoes a marked transition from being a minor, to a major constituent of the thermosphere (*Gumbel, 1997*). At still higher altitudes, in a range of approximately 180 - 700 km, AO becomes the most prevalent species (*Hedin et al., 1977*). Figure 2.1 shows the typical compositional variation of the major atmospheric constituents over the altitude range 100 - 800 km. Satellites circling the Earth at these altitudes are said to travel in Low Earth Orbits (LEO).

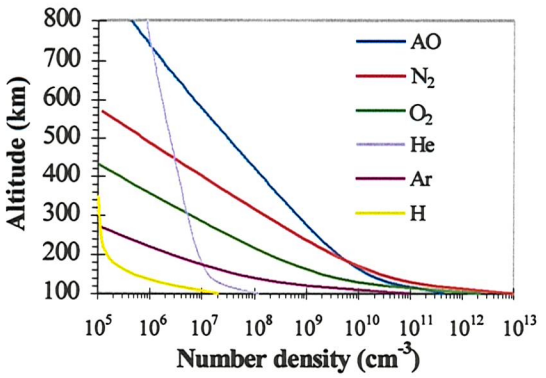

Figure 2.1 - Typical thermospheric composition (data from *Hedin, www resources*)

The thermosphere is a dynamic, rather than a stationary system. During periods of solar illumination, AO is continually formed by photolysis. At the same time, AO density is reduced by three-body recombination reactions (*Danilov and Istomin, 1970; Gumbel, 1997*). The

necessity of three-body reactions to remove AO is the reason for its dominance as an atmospheric constituent at the higher altitudes. Mean free paths vary with height from about 0.1 km at 180 km, to greater than 200 km at an altitude of 650 km. Thus, the probability of suitable collisions falls dramatically with increasing elevation (*Allen and Yung, 1981*). Hence, not only does the relative concentration of AO increase with height, but also the lifetime of the atoms before their recombination to molecular oxygen (*Reddy, 1995; Gumbel, 1997*).

Formation of atomic oxygen by solar UV ($\lambda < 243$ nm) leads to a correlation between level of solar illumination, especially at VUV and EUV wavelengths, and the rate of AO production in the thermosphere (*Leger et al., 1984*). Therefore, it is unsurprising that AO number density is influenced by the intensity variations associated with the solar cycle. Variation of AO number density with solar activity is demonstrated in Figure 2.2, which shows curves for solar minimum, maximum and mean irradiation levels‡. Clearly, the effect of solar activity is most significant at the higher altitudes, where AO density may alter by as much as two orders of magnitude between solar minimum and maximum. Near the bottom of the thermosphere, in comparison, the density varies by much less than one order of magnitude.

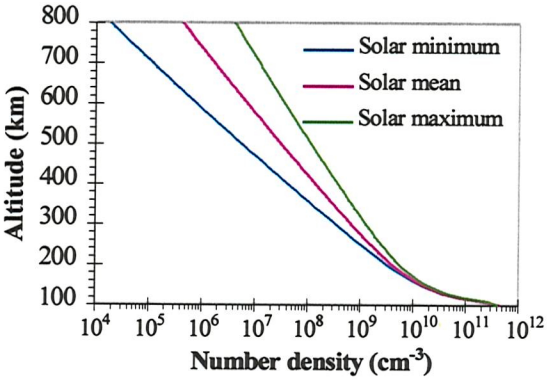

Figure 2.2 - Effect of solar activity on AO density (data from *Hedin, www resources*)

In fact, the AO number density at a given altitude depends not only on the stage of the solar cycle, but also on the geomagnetic conditions. The literature also contains observations of diurnal, seasonal and latitudinal variations of AO concentration (*Mauersberger et al., 1976; Hedin et al., 1977; Hedin, 1988*).

When compared to atmospheric sea-level values (typically 10^{19} cm^{-3}), thermospheric densities appear low. However, the high orbital velocities of artificial bodies in LEO, approximately

‡ Data for equatorial orbits generated using the MSISE-90 thermospheric model with the parameters of cycle 22. Minimum: 12:00 UT 01/06/86; Mean: 12:00 UT 01/06/88; Maximum: 12:00 UT 01/06/91.

8 km.s^{-1}, mean that large fluxes of AO impinge on velocity vector (ram) facing surfaces. If they have a portion of their orbit path in the thermosphere, vehicles in other orbits will also experience AO bombardment. For example, elliptical orbits like geostationary transfer orbits (GTO) often have their closest approach to the Earth - or perigee - at altitudes between 300 to 600 km. Such orbits have larger perigee velocities than those in LEO, perhaps as high as 10 km.s^{-1}. Consequently, even satellites that reside in the thermosphere for short periods can experience significant fluxes and fluences of atomic oxygen.

Typically, thermospheric temperatures are around 1,000 K (*Arnold and Peplinski, 1986*). Hence, the thermal impact energies of oxygen atoms upon stationary surfaces are low, at somewhat less than 0.2 eV. In comparison, the orbital velocity of satellites leads to greater collision energies - from around 5 eV in LEO, to 8 eV in GTO. Thus, ram-facing or, in the case of spin-stabilized satellites, periodic ram-facing surfaces are subject to large fluxes of chemically reactive, high energy oxygen atoms.

Many thermospheric models have been created to predict the composition of the atmosphere at a given epoch and/or location. A popular example is the MSIS (Mass Spectrometer and Incoherent Scatter) group (*Hedin, www resources*). A review of many of the thermospheric models developed to 1988, the links between them, and the measurements from which they are derived, is given by Hedin (*Hedin, 1988*).

Often, the estimates of AO flux and fluence (time-integrated flux) from such models are the only means by which the AO exposures of spaceflight experiments can be determined. Reliance on thermospheric models seems somewhat foolhardy; the models may be in error by 25 percent (*Visentine and Leger, 1986*), or more (*Bourde et al., 1994; Renard, 1994*). These errors are often ascribed to measurement errors associated with the input data, and the inability to account for all of the drivers of AO density (*Hedin, 1988*). Therefore, without exception, all thermospheric models require absolute, *in situ*, composition measurements to improve the accuracy of their predictions. To realize this need suitable atomic oxygen sensors must be developed. The next chapter reviews spaceflight equipment that has been used for this task.

2.2 ATOMIC OXYGEN EFFECTS

2.2.1 Atomic oxygen induced glow

From the previous discussion, it is evident that satellites in LEO move through a residual atmosphere that predominately consists of oxygen atoms. Several interactions may occur when AO collides with the surfaces of a spacecraft. For example, it may simply reflect, either in its

original, uncharged state or as an ion. Both outcomes leave the surface material unharmed. Otherwise, impinging AO may chemically react with nitrogen atoms, nitrogen molecules, nitrogen oxide molecules, or other oxygen atoms and molecules on or around the spacecraft surface, or in the wake of the vehicle. Again, the surface material is unaffected by these processes. Reactions of this type frequently form vibrationally excited species, which later relax to the ground state by photon emission. Such radiative emissions have become known as 'Shuttle Glow', because its presence was first confirmed by optical photography on the STS-3 Space Shuttle mission (*Banks et al., 1983*). However, it had been observed previously, for example by the Atmosphere Explorer Programme satellites (*Torr et al., 1977; Yee and Abreu, 1982*).

Shuttle Glow has component emissions in the IR, visible and UV wavelengths and can interfere with the operation of many optical devices, but especially those operating in these spectral bands (*Garrett et al., 1988; Green, 1988*). It appears that glow producing reactions fall into two groups: those that are surface mediated and those of the gas-phase (*Ahmadjian and Jennings, 1995; Greer et al., 1995*). Frequently, it is found that the glow from vehicles - such as the Space Shuttle - is enhanced by thruster firings, gas releases and fluid dumps (*Green, 1988*), presumably because events like these contribute to the density of potential reactants in the vicinity of the vehicle.

2.2.2 Atomic oxygen erosion

It is also possible for atomic oxygen to become adsorbed onto the surface with which it has collided. This can only occur if the kinetic energy of the atoms perpendicular to the surface is dissipated in the underlying material (*Baird, 1998*). Table 2.1 shows that the impact energy of thermospheric oxygen atoms is of a similar order of magnitude to the bond energies commonly found in polymeric materials (*Reddy et al., 1992*). Therefore, it is unsurprising that AO undergoes chemical reactions with many polymeric materials. That is not to say that only polymeric materials are affected by atomic oxygen impingement, indeed, adsorbed oxygen atoms are also found to oxidize metals such as silver and osmium.

Bond	Energy (eV)
C-C	3.58
C-H	4.24
C-O	3.70
C-N	3.16
C=C	6.24
C=O	8.27
AO energy	LEO ~ 5 GTO ~ 8

Table 2.1 - Common polymeric bond strengths

The most common manifestation of such oxidative reactions is surface erosion. If the oxides of the surface material are volatile, then the sample exhibits a mass loss. On the other hand, if the oxides are stable, the material will experience a mass increase. In general, although not true of all, polymeric materials experience mass loss under the action of AO impingement, whilst metals experience mass increases.

The standard way of presenting the susceptibility of materials to AO attack is the *volume erosion yield*, Y_{vol}, which can be calculated using Equation (2.1):

$$Y_{vol} = \frac{|\Delta m|}{\rho f A} \tag{2.1}$$

Where:

Δm = mass change of sample (g)

ρ = density of the sample ($g.cm^{-3}$)

f = AO fluence ($atoms.cm^{-2}$)

$\therefore f = \int F dt$, F = AO flux ($atoms.cm^{-2}.s^{-1}$)

A = exposed area (cm^2)

A high value of erosion yield (which has units $cm^3.atom^{-1}$) indicates that a material is prone to AO attack, whilst a low value shows that a material is more resistant. Some typical erosion yield figures, calculated from space-based experiments, are presented in Table 2.2 (*Reddy, 1995; Packirisamy et al., 1995*).

Material	Erosion yield ($\times 10^{-24}$ $cm^3.atom^{-1}$)
carbon	0.23 to 9.0
FEP	0.05 to 0.47
graphite-epoxy	0.2 to 2.9
polyimide	1.5 to 3.7
PTFE	0.03 to 0.5
silver	10.5

Table 2.2 - The erosion yields of some common materials

It is evident from the information in the table above that there is quite a range of erosion yield figures for each material examined. This spread is caused by the number of different orbital conditions - for example temperature, AO fluence and UV exposure - to which the materials have been exposed and, in some cases, the form of material used: carbon and carbon-based composites

especially so. Frequently, the AO fluence used to calculate the erosion yield of materials is the largest source of scatter in the resulting values; this is especially true if the fluence has been derived solely from a thermospheric model (see previous section).

2.2.3 Erosion of polymeric materials

In general, a large proportion of spacecraft surfaces exposed to the ambient LEO environment are manufactured from materials classed as polymers. It has already been demonstrated that the AO impact energy is often higher than the chemical bond strengths found in these materials, and that this leads to oxidation of the molecules. In fact, there are six key AO/polymer reactions - abstraction, addition, elimination, insertion, replacement and bond dissociation (*Banks, 1988; Reddy, 1995*).

The process of *abstraction* - the removal of an atom from the polymer chain by a colliding oxygen atom - is shown in the generalized scheme below. When compared to the number of atoms contained in a typical polymer chain, the amount of material removed by this process is small. However, the loss of single atoms from the hydrocarbon may increase the probability that other bonds will be attacked in subsequent AO collisions, thus it remains an important erosion mechanism.

abstraction

If an atom of oxygen becomes permanently added to a polymer, an *addition* reaction is said to have taken place. This reaction is frequently observed with alkene type molecules; the product is vibrationally excited.

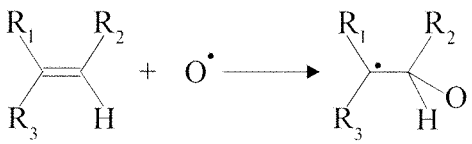

addition

However, because the product is unstable, addition is often followed by *elimination* of another atom; in this case, two reactions are at work in the erosion of the material.

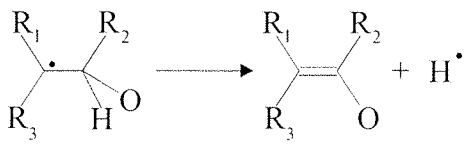

elimination

It is also found that AO may become part of the polymer molecule, by '*inserting*' itself between two other atoms, for example between a carbon atom and a hydrogen atom. See diagram below.

This third reaction scheme does not directly lead to material erosion, because oxygen atoms become included within the polymer chain:

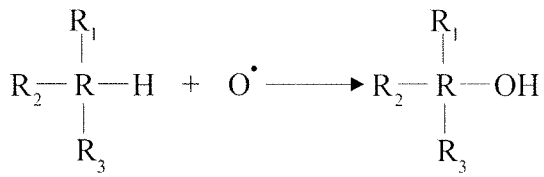

insertion

Reacting oxygen atoms can also *replace* side groups present on the 'back-bone' of the polymer molecule, breaking a bond that once existed within the polymer chain. In this manner, alkoxy or alkyl radicals are formed. The two reactions of this variety shown below clearly demonstrate that in this mechanism, the carbon chain is split into two smaller units.

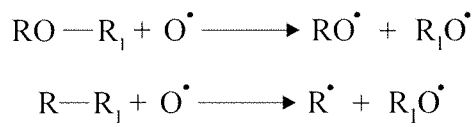

replacement

Lastly, bond *dissociation* occurs when the bond between two polymer sub-groups is split to form two small radicals, but unlike the previous situations, the oxygen atom remains free to enter into further reactions. Bond dissociation may be represented by the mechanism outlined below.

dissociation

The last three reactions show that AO impingement can fragment polymer chains into smaller molecules. Under the vacuum conditions of space, these lower mass molecules and fragments may be more volatile than the original substance. Hence, they may desorb from the surface, to form a 'cloud' around the vehicle. On the other hand, the first three reactions indicate how single atoms are removed from the polymer molecules. It is these losses of atoms and molecular fragments that are solely responsible for the erosion of polymer samples.

The volatile polymer fragments so produced may, subsequently, condense onto other - colder - spacecraft surfaces, such as optics, detectors and solar arrays. Thus, the products generated during AO erosion are a potential source of deleterious contamination (*Haruvy, 1990*). Layers formed in this way alter the optical transmission and thermal radiative properties of the surfaces on which they reside, affecting the efficiency of radiators, solar arrays and such like.

Once adsorbed onto a surface, the condensate may be polymerized, hence fixed, by the action of UV. As a result, the rate of contaminant removal (by thermal desorption and/or further AO attack) is reduced, or even prevented (*Haruvy, 1990; Matcham 1998a*). This source of induced

contamination can be hard to evaluate or predict on the ground, because many seemingly vacuum-hard, non-contaminating materials become contaminant sources under the synergistic influence of AO and UV. Moreover, AO-induced contamination adds to that of traditional out- and off-gassing products, and so may exacerbate an already marginal situation.

In order to monitor AO erosion, some way of predicting or measuring the AO environment is required. Thermospheric models can be used but, as shown in the last section, they can be in significant error. It would therefore seem that the best way of following AO erosion would be to have a sensor capable of directly measuring the AO fluxes experienced on orbit.

2.2.4 Spaceflight experiences

The literature shows that, prior to the first few Space Shuttle flights, the effects of environmental erosion on returned spacecraft materials (*Blair et al., 1971; Smith, 1972; Lehn and Hurley, 1974*) was masked by contamination caused by debris, thruster firings and outgassing products (*Leger, 1982; 1983*). Therefore, the LEO environment was considered relatively benign, especially for missions of short duration (*Leger et al., 1984*).

Conclusive proof of the action of an erosive medium on spacecraft materials was gained after the return of 'clean' material samples, used in the early Space Shuttle flights STS-1 to 3. Affected materials included polymer films used in thermal control blankets and the polymer components of paints (*Leger, 1982*). Of the polymers, a polyimide called Kapton†, exhibited particularly substantial surface erosion, mass loss and change in surface morphology. These alterations affected the optical and thermal radiative properties for which Kapton was originally employed (*Leger, 1983*). Sputtering of the films was discounted as the cause of the erosion, because the kinetic energy of even 'massive' nitrogen molecules in the LEO atmosphere was below the 10 eV threshold necessary to induce material removal (*Peters et al., 1983*). So, it seemed that chemical reaction between the exposed materials and incident AO must be responsible for the observed changes.

Atomic oxygen erosion rapidly became the accepted cause of the degradation of many materials, which was manifested as surface recession and mass loss of organic materials (*Leger, 1983*), carbon and osmium (*Peters et al., 1983*). Silver - which is often used for electrical inter-connections in solar arrays - exhibited a mass increase due to the formation of a stable oxide layer (*Peters et al., 1983*). It was found that some materials, such as aluminium and silicones

† Kapton is a registered trademark of E.I. du Pont de Nemours & Co. Ltd.

formed protective oxide layers in the initial stages of AO attack, whilst others such as quartz (SiO_2) and gold were inherently stable (*Reddy, 1995*).

To investigate further the effects of AO erosion, material exposure experiments were conducted on the two following STS flights, 4 and 5 (*Leger, 1983*) and later on STS-8 (*Leger et al., 1984; Visentine et al., 1985, Slemp et al., 1985*). The STS-8 flight exposed more than 300 individual samples including coatings, polymer films, and polymeric and metal matrix composites to the LEO AO environment.

Fresh interest in the long-term effects of AO was aroused by the proposal, and subsequent design, of the International Space Station (*Leger et al., 1985*). This, in part, led to the flight of the Long Duration Exposure Facility (LDEF), which was used to investigate the effects of all aspects of the space environment on new, candidate materials. Of the new materials, particular interest seems to have been paid to polymeric composites, proposed for lightweight yet stiff structures (*Zimcik et al., 1985; Zimcik and Maag, 1988*). Due to the inhomogeneous structure of these materials, the affect of AO erosion was found to be somewhat more complicated than the homogenous materials investigated previously. For example, it is often observed that the polymer matrix will erode faster than the reinforcing fibres or *vice versa*, changing the once smooth surface to a 'corduroy'-like eroded structure.

Since the early in-orbit experiments, many more have been flown. These later experiments have become more sophisticated than the simple experiments flown in the early 1980s (*Visentine and Leger, 1986; Linton et al., 1993*). A key feature of many of these later flights was to use mass spectrometry (or other techniques) to measure the ambient AO levels, rather than using thermospheric models. Hence, the experienced AO fluences could be determined to a far greater accuracy than before. Mass spectrometers have also been used to monitor the products of the AO/polymer reactions, to enable better interpretation of the erosion mechanisms (*Koontz et al., 1995a; 1995b*). Additionally, some experiments were flown to monitor material erosion rates *in situ*, rather than relying on expensive retrieval of the host vehicle (*Koontz et al., 1991a; Harris, 1996*).

With these discoveries, it became clear that the erosion caused by AO was significant for both long and short duration missions (*Zimcik and Maag, 1988*). Atomic oxygen can significantly alter the optical properties of materials, especially if there are synergistic effects with other elements of the space environment, e.g. debris and micrometeoroid impacts (*Gulino, 1988a; Gulino 1988b*), or solar VUV (*Koontz et al., 1990; Rousslang et al., 1992; Alet, 1997*). Optical property

changes can alter the thermal balance of a spacecraft or sub-system and, hence, can impact the operation of spacecraft instruments (*Peters et al., 1986; de Groh and Banks, 1994; Alet, 1997*).

Additionally, atomic oxygen attack has the propensity to cause loss of power generating capacity from solar arrays. The silver interconnects used on solar panels (*Koontz et al., 1991a; Reddy, 1995*); the flexible polymers used to support the cells (*Leger et al., 1985; Banks et al., 1990; Packirisamy et al., 1995*); the antireflection coatings used on the cover glasses (*Rancourt et al., 1991; Trumble, 1992*) and other optical materials (*Koontz et al., 1991a*) have all been shown to be eroded to differing extents by AO. For very long duration missions and long-lifetime platforms, such as the 30 year expected lifetime of the International Space Station, it might even be possible for there to be a loss of structural integrity if susceptible materials are used without adequate protection (*Leger et al., 1985*).

Thus, experience has shown that AO impingement erodes many commonly used spacecraft materials - erosion that can cause changes in surface morphology, optical, thermal radiative and even mechanical properties. These changes can influence the operation of satellite systems, and so AO erosion is of great interest to the space community. Extensive reviews of the effects of AO and the results from many *in situ* spacecraft experiments are given by Reddy (*Reddy, 1995*) and Harris (*Harris, 1996*). In the same reference Harris also reviews literature concerning laboratory experiment data.

2.3 GROUND-BASED SIMULATION OF THE ATOMIC OXYGEN ENVIRONMENT

2.3.1 Atomic oxygen sources

Spaceflight experiments are expensive to conduct and, because of the many different environmental components to which materials may be simultaneously exposed (see Section 1.1), analysis of the results gained is complicated. Indeed, the exact cause of the observed effects may never be ascertained. These issues have been the main drivers for the development of ground-based AO sources. The aim of each source is the same; to conduct controlled materials exposure tests that adequately simulate LEO, yet at reduced cost relative to space-based experiments. To be used as a simulator of the LEO AO environment, a source of oxygen atoms must have the following characteristics (*Wood et al., 1994; Reddy, 1995*):

- Production of ground-state oxygen atoms O^1 ($^3P_2$).
- Beam energy of 5 eV, or higher to simulate GTOs for example.
- Flux on target material matching that in LEO, or higher for accelerated testing.
- Sufficient beam exposure times to allow representative fluences.

- Minimal beam contaminants.
- Large AO beam area to allow simultaneous exposure of several samples.
- *In situ* measurements of critical parameters should be possible.
- Thermal cycling and temperature control of samples should be possible.

Many AO sources have been developed, each of which achieve some of the ideal qualities presented in the above list (*Packirisamy et al., 1995*). None of the sources, as yet, possess all of these characteristics. Banks *et al.*, Caledonia, and Kudryavtsev *et al.* provide good reviews of many different sources (*Banks et al., 1988; Caledonia, 1988; Kudryavtsev et al., 1994*). Table 2.3 summarises the information found in several papers to date and, with regard to ground-based space simulation, covers all of the important types of AO sources. It is evident from the energy and flux figures presented in the table that as AO energy is increased, the maximum AO flux that can be generated decreases.

NB. Several other AO sources exist, such as effusion furnaces, shock wave devices and metal oxide target sputterers, yet to the knowledge of the author, these have not been used to simulate the LEO space environment. The interested reader is referred to the papers by Caledonia and Kudryavtsev (*ibid.*) for further information.

2.3.2 Some problems of ground-based testing

It is often desirable to perform accelerated testing of materials, for example, in the situation where a component is to be used for longer duration than can be reasonably simulated in the laboratory using equivalent LEO fluxes. Thus, the material must be exposed to AO flux levels far higher than those experienced in orbit, so that the necessary simulation time is reduced. However, it has been postulated that there might be an upper flux intensity, which limits the acceleration that can be applied to a given AO exposure test (*Kudryavtsev et al., 1994*). The limit is imposed by the possibility of flux-induced changes of the predominant erosion mechanisms, which may invalidate the simulation methodology. In particular, pulsed AO sources may suffer from this problem, even though the time-averaged fluxes may be of a similar order to that experienced in space. Frequently, such equipment generates a burst of AO, the flux of which may be several orders of magnitude higher than the continuous flux in LEO (*Caledonia et al., 1987*).

Hence, ground-based material testing is an inherently difficult task. To date, no one source fully simulates the LEO environment, whilst many expose the material under test to unwanted additional, complicating influences (e.g. VUV radiation). Therefore, it is not surprising that the results generated in these experiments are source dependent, and often do not compare well with

space-based measurements (*Packirisamy et al., 1995*). However, it may be possible to extrapolate ground-based test results to actual space-based erosion rates, at least for some materials (*Stevens, 1990; Cross et al., 1991*). It is difficult to determine the accuracy of such methods; the technique advocated by Stevens seems to be accurate to within a few percent, but only for Kapton.

An additional problem experienced during ground-based testing is the lack of a 'standard', real-time AO sensor. Consequently, many researchers have adopted an arbitrary standard fluence monitor. Yet, as will be shown in the following chapter, the resolution of this technique is limited in time, whilst its accuracy is affected by water adsorption from the atmosphere. Clearly, what is needed is a sensor that can be used to measure AO fluxes *in situ* during experiments.

2.4 SUMMARY

This chapter has discussed, at length, the effects of thermospheric AO on spacecraft materials. It has been demonstrated that AO impingement upon surfaces causes several phenomena, including Shuttle Glow. Most importantly, however, AO-induced oxidation was shown to occur at the surface of many materials. The reactions of AO with polymers were reviewed in detail. Such reactions lead to the erosion of materials, and can induce changes of the thermal, mechanical, electrical and optical properties of the substance. Thus, AO erosion may engender changes in the generating ability of solar arrays, thermal balance of satellite systems and even the strength of structures.

The uses and shortcomings of thermospheric models for establishing the doses of AO experienced by space-based experiments were highlighted. It was shown that improved accuracy might be attained only by the inclusion of more measurements of thermospheric AO number densities in the input data, to characterize better the variation of AO density with altitude and time. In order to achieve this, adequate space-rated AO sensors must be developed

A review of ground-based AO sources that have been used to simulate the LEO environment was conducted, and the problems associated with material erosion experiments described. Apart from discrepancies in the simulations due to incorrect AO energy, AO flux, or the presence of other, complicating species, the lack of a suitable sensor was highlighted as a key problem.

Hence, the literature reviews conducted in this chapter have shown that there are two requirements for AO detectors. Chapter 3 reviews several different AO sensors that have been used for this task.

Source type	Description	Pulsed	Flux ($atoms.cm^{-2}.s^{-1}$)	AO energy (eV)	Advantages	Disadvantages	Reference
RF discharge	Plasma asher	N	~ 10^{19}	0.04 - 0.06	Simple	VUV flux, low beam energy, charged species	Koontz *et al.*, 1991b
	Microwave discharge	N	~ 10^{15}	0.14	Simple, beam flux at correct value	Low beam energy, inert carrier gas	Arnold *et al.*, 1987
	Microwave discharge, SURFATRON	N	~ 10^{16}	2.2	Simple, high beam flux	Inert carrier gas, low beam energy	Tennyson, 1991
	Magnetically confined microwave discharge	N	~ 10^{16}	5 - 10	Low pressure, low VUV flux, no inert carrier gas	Large spread of atom energy	Cuthbertson *et al.*, 1990
	Multiple reflection of atoms from an electron cyclotron resonance source	N	~ 10^{14}	10 - 15	Low pressure, low beam contamination, low VUV irradiation	Large spread of atom energy	Goeckner *et al.*, 1997
Optical discharge	1) CW laser-induced breakdown	N	~ 10^{17}	1 - 5	High beam flux	High beam temperature, VUV flux	Cross and Blais, 1988
	2) Pulsed laser-induced breakdown	Y	~ 10^{16} ~ 10^{13} - 10^{15}	~ 5 5 - 8	High beam flux	Pulsed, VUV flux	Caledonia *et al.*, 1987; Osborne, 1998a
Electron stimulated desorption	Oxygen diffusion through silver film, desorption of oxygen atoms stimulated by electron bombardment	N	~ 10^{12}	~ 5	High beam purity	Low beam flux, large thermal input to test materials, radiation content	Hofland and Weaver, 1994
Ion beam	Oxygen ion acceleration	N	~ 10^{13} - 10^{14}	10 - 1000	Controllable energy	Charged species, low beam flux	Martin, 1988 Matlis *et al.*, 1993 Vered *et al.*, 1994
Gas dynamic	DC arc heaters	N	~ 10^{14}	~ 1	Simple and cheap to operate	Low beam energy, inert carrier gas, low AO flux	Stark and Kinnersley, 1988 Kinnersley, 1988
	DC arc heaters	N	~ 10^{15}	~ 1	Simple and cheap to operate	Low beam energy, inert carrier gas, small exposure area	Arnold and Peplinski, 1985

Table 2.3 - A comparison of several AO sources

CHAPTER 3

ATOMIC OXYGEN MEASUREMENT TECHNIQUES

The need for satellite-based atomic oxygen sensors was demonstrated in the preceding chapter. However, many of the sensing techniques in use today were developed before oxygen atom erosion of spacecraft materials was of concern. Instead, the emphasis was upon studying chemical reactions associated with combustion, and those reactions occurring naturally in the upper atmosphere. This chapter is devoted to the review of the wide range of *in situ* techniques that have been used to measure thermospheric AO densities on rocket and satellite missions. There is a clear, two-part division of the methods; the division is based upon the measurand used. The first group consists of those devices that use some form of optical property, either of AO itself, or of a surface affected by AO action. Non-optical methods for the determination of AO densities, fluxes or fluences constitute the second group.

3.1 INTRODUCTION

Sounding rocket and satellite equipment used to measure thermospheric AO densities experience demanding conditions during launch and, if they attain sufficient velocity and altitude, whilst in orbit. These environments impose particular requirements on the instruments, so not every laboratory facility may be adapted for use in space-rated or rocket-rated systems. Kaufman conducted an early review of laboratory techniques applicable to the measurement of oxygen atom densities (*Kaufman, 1961*). However, none of the methods reviewed by Kaufman have been used for LEO research, although two of them have been used in sounding rocket studies.

It is intended that this review should present the reader with a summary and description of the different AO measurement techniques that have been used to date, rather than a complete list of every flight and utilization thereof. A comprehensive review of sounding rocket AO measurements in the lower thermosphere, performed between 1962 and 1993, can be found in the doctoral thesis of Gumbel (*Gumbel, 1997*). Unfortunately, there appears to exist no equivalently complete review of equipment used in Earth orbit in the open literature, whilst the Ph.D. thesis of Harris (*1996*) describes only a few of the available methods.

3.2 OPTICAL METHODS OF AO SENSING

3.2.1 Chemiluminescence methods

Nitrogen oxide (NO) molecules combine with oxygen atoms according to Reaction 3.1.a (*Kaufman, 1961*). The products of the reaction are excited nitrogen dioxide molecules (NO_2^*),

which produce a greenish-yellow chemiluminescent photon when they relax to the ground state (Reaction 3.1.b). Clearly, the number of NO_2^* molecules formed is proportional to the number density of AO in the region of the NO/AO reaction. Hence, the intensity of the resultant glow - the number of emitted photons - is also proportional to AO number density.

$$O + NO \rightarrow NO_2^* \quad (3.1.a)$$

$$NO_2^* \rightarrow NO_2 + h\nu \quad (3.1.b)$$

Reaction 3.1 is the basis of the oldest recognized procedure for measuring AO number densities. Nitrogen oxide is injected into the atmosphere of interest and the luminosity of the resulting glow measured by photographic film or photomultiplier tube. The test is highly specific and is not affected by the presence of other species, because the wavelength of the AO/NO emission is characteristic and distinctive (*Kaufman, 1961*). This technique is frequently referred to as the *afterglow* method.

The wavelength structure of the glow appears to be complex. It is reported that the emission is, in fact, a continuum extending from 370 to 900 nm, perhaps with a peak at about 650 nm (*Heath, 1959; Kaufman, 1961*). It is interesting to note that the AO/NO emission is one of the components of Shuttle Glow (*Garrett et al., 1988*).

The afterglow method has been employed to measure atomic oxygen densities in the upper atmosphere (*Golomb et al., 1965*). In this study, a rocket carried a tank of nitric oxide to 90 km, whereupon a stream of nitric oxide was ejected into the surrounding atmosphere. The rocket flight was conducted at night and the release of NO produced a bright headglow, observable from the ground. The gas ejection was timed so that the solid rocket motor of the vehicle had burned out before the NO discharge began. Photographs of the NO release; knowledge of the vehicle aerodynamics; a model of the NO/atmosphere mixing processes and reaction rate coefficients were used to calculate the altitudinal variation of AO concentration. The upper altitude in this study was 150 km.

This first experiment was simple in principle, but the quantitative determination of AO density from the photographic records proved to be complicated, and a source of substantial uncertainty. Golomb and Good (*Golomb and Good, 1972*) subsequently adapted the technique, replacing the ground-based cameras with rocket-mounted, forward-looking photometers to measure directly the headglow intensity.

No satellite-based applications of this technique have been reported in the literature. There is evidence, however, that such a method might work at orbital altitudes. The Critical Ionization Velocity Experiment - flown on STS-39 - released small amounts of gases, including NO, into space. Immediately after the NO release, optical instruments and the crew of the orbiter observed a bright glow described by Reactions 3.1 (*Ahmadjian and Jennings, 1995*).

It therefore seems possible that the release of NO from a satellite in LEO, and observation of the resultant glow, could serve as a method to measure the surrounding AO density. If this technique was applied to LEO the equipment might be bulky, due to the requirement of a tank of NO and a valve to enable controlled ejection of the gas into the surrounding atmosphere. That is, unless the NO tank and delivery equipment could replace an existing satellite subsystem, such as the cold-gas thrusters frequently used on small satellites. A photometer, fitted with a band-pass filter, would also be needed to measure the glow intensity.

The altitude limit of this technique would appear to be influenced by the probability of NO reaction with AO, which is a function of AO density, and by the sensitivity of the photon counter used. Also, the number of measurements that can be performed is limited by the amount of NO carried by the vehicle.

3.2.2 Airglow studies

The term 'airglow' is used to describe the process of photon emission resulting from the various natural reactions of AO with itself, or with other constituents of the thermosphere. The intensity of the emissions is dependent upon the densities of the reacting species, therefore, glow luminosity can be used as a direct measure of reactant concentration. A number of airglow studies, using several different AO reactions, have been employed to quantify the AO density in the thermosphere. As in the afterglow method, the photons emitted from the various airglow reactions are characteristic of the product(s) of the reacting species, so the reactions can be monitored independently.

Donahue *et al.* and Offermann and Drescher both report studies that employed the $O(^1S) \rightarrow O(^1D)$ green airglow emission at a wavelength of 557.7 nm (*Donahue et al., 1973; Offermann and Drescher, 1973*). Within the thermosphere, excited AO - $O(^1S)$ - is produced in the three-body recombination of AO to molecular oxygen (Section 2.1 and Reaction 3.2). Both research groups monitored the same emission, yet two different approaches were applied to the measurement of AO density.

$$O + O + O \rightarrow O_2 + O^*(^1S) \qquad (3.2.a)$$

$$O^*(^1S) \rightarrow O(^1D) + h\nu \qquad (3.2.b)$$

Offermann and Drescher mounted their equipment - a photometer with a band-pass filter - on board a sounding rocket, and used it to observe the ambient night-time thermosphere in the ascent and descent trajectories of the rocket flight (*Offermann and Drescher, 1973*). The signal from the photometer was converted to a volume photon emission rate and, with knowledge of the rate coefficients of the three-body reaction, subsequently into the AO density. Readings were performed to 130 km altitude.

In contrast, the photometer employed by Donahue *et al.* was mounted on the orbiting geophysical observatory satellite, OGO-6 (*Donahue et al., 1973*). It was equipped with a moveable mirror to scan a swath of atmosphere. A mathematical analysis was used to reduce the photomultiplier signal to an AO density profile between 80 and 120 km. Other satellite-mounted photometers have been applied in a similar fashion, although moveable mirrors are not always included (*Hays et al., 1973; Cogger and Murphree, 1980; Yee and Abreu, 1987*).

An example of another emission that has been exploited for the determination of thermospheric AO densities are the measurements of Good, who employed the IR emissions associated with reaction of ozone and atomic hydrogen to produce excited hydroxyl, see Reaction 3.3 (*Good, 1976*). Unlike the previous study, the photon producing step (relaxation of excited hydroxyl - 3.3.c) does not involve a product formed as a result of direct reaction with AO but, instead, with ozone. However, because the ozone is formed by the reaction of atomic and molecular oxygen with nitrogen, the final emission can still be used as an indicator of AO density.

$$O + O_2 + N_2 \rightarrow O_3 + N_2 \qquad (3.3.a)$$

$$H + O_3 \rightarrow OH^* + O_2 \qquad (3.3.b)$$

$$OH^* \rightarrow OH + h\nu \qquad (3.3.c)$$

The equipment used by Good was similar to that of Offermann and Drescher, in that the photometer was mounted on a rocket and was equipped with band-pass filters (centres at 1.34 μm and 1.64 μm). Despite these filters, the technique was limited to altitudes below 90 km: above this level the photometer signal became saturated by the 557.7 nm green line emission, discussed previously.

Several other airglow emissions have been used in this manner, for example the infra-red emissions of $O_2(^1\Delta_g)$ at 1.279 μm and the red line emission of AO at 630.0 nm (*Philbrick et al., 1973a; Shepherd et al., 1973*). In addition, atomic oxygen number densities have been

determined from UV AO emissions at 130.4 and 135.6 nm (*Bailey, 1998*). Offermann and Drescher present a tabular summary of photometer airglow studies conducted between 1955 and 1972 (*Offermann and Drescher, 1973*).

It would seem that uncertainties in the reaction rate coefficients are the largest source of uncertainty in the airglow method, no matter what reaction system is used. Also, it is rather unfortunate that some of the emissions are not visible during the day, limiting the usefulness of the technique. However, the airglow technique would seem to have one significant advantage over the chemiluminescent afterglow method - the absence of a limited reactant supply. Since airglow reactions are continuously (and naturally) taking place in the thermosphere, with no necessary release of an 'artificial' species, the technique can be considered to be totally reusable. After all, it is unlikely that the general chemistry of the thermosphere will change dramatically during the mission lifetime of a satellite, although, there may be diurnal and seasonal variations. Hence, during the periods of observation it may be necessary to assume steady-state photochemical equilibrium (*Philbrick, 1973a*).

3.2.3 The resonance fluorescence approach

The resonance fluorescence method employs a collimated beam of VUV light at 130 nm to probe the atmosphere. Oxygen atoms in the VUV beam resonantly absorb and then scatter the photons, some of which are collected at a detector. The number of back-scattered photons is dependent on the AO density in the illuminated volume, so the magnitude of the detector signal is used as the measurand in this method.

Equipment for performing these measurements consists of a lamp to produce the VUV illumination; a collimator to ensure that the illumination is confined to a known path and, usually, a photomultiplier to observe the illuminated volume. A schematic of a typical resonance fluorescence device can be found in Figure 3.1. R. A. Young designed the first resonance lamps for these measurements - a radio frequency discharge in an inert gas seeded with oxygen produces the emission of the required wavelength (*Young, 1961*). The lamps actually emit the OI oxygen triplet, with lines at 130.217, 130.486 and 130.603 nm (*Gumbel, 1997*).

This technique has been applied over a wide range of altitudes from inside the stratosphere upwards. Anderson mounted his equipment in a nacelle that was dropped from a balloon at 40 km altitude. Readings were taken until a height of 24 km was reached in the descent (*Anderson, 1975*). Dickinson *et al.* (*1974; 1976; 1980*) and many other experimenters (*Howlett et al., 1980; Sharp, 1980; Thomas and Young, 1981; Kita et al., 1996*) have launched their equipment on sounding rockets into the lower thermosphere.

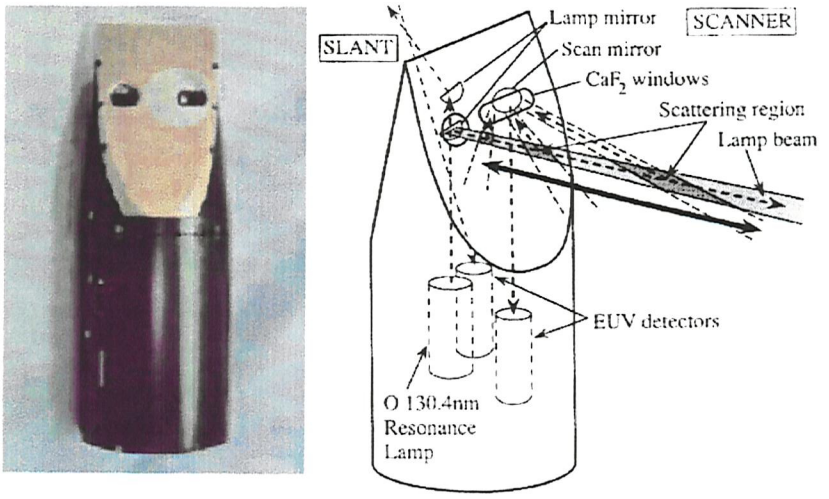

Figure 3.1 - Rocket mounted fluorescence equipment (after *Kita et al., 1996*)

Gumbel reports that the resonance fluorescence method is sensitive and highly specific (*Gumbel, 1997*). Several improvements have been made to the simple method outlined above. Solar-blind photomultiplier tubes may be employed, in combination with filters, to eliminate the background illumination of solar Lyman-α and auroral UV emissions. Otherwise, background intensity correction measurements are made by modulating the lamp intensity in an on-off mode, and recording the photomultiplier voltage when the lamp is off.

Uncertainties in the method result from the adverse aerodynamic influence of the host vehicle on the measurement volume, lamp calibration errors, outgassing contamination and Doppler shift of the lamp emission. Some of the problems of Doppler shift and aerodynamic influence of the vehicle on the measurement volume can be reduced by careful design of the vehicle and by using mirrors to scan the lamp beam, see for example Figure 3.1. Like the airglow method, this AO measurement technique would appear to be totally reusable since it is not limited by a finite supply of reactant, although the intensity of lamp UV output may decrease with usage.

3.2.4 Resonance absorption and solar occultation

The resonance fluorescence method described in the previous section is frequently complemented with resonance absorption measurements. In this method, a portion of the VUV resonance lamp emission is reflected around a series of mirrors deployed so that the beam passes through the atmosphere. The intensity of the returned beam is measured by a photomultiplier and compared to that originally emanating from the lamp. In this way, the amount of absorption is determined. Since it is assumed that only AO absorbs the lamp emission, conversion of the photomultiplier signal to AO density follows from a mathematical analysis. Rocket- (*Dickinson et al., 1980;*

Gumbel, 1997) and satellite-based (*Donahue et al., 1977*) measurements have been performed with this technique.

3.2.5 Solar occultation

A closely related technique to the previous one is that of solar occultation. This method relies upon the fact that certain emissions of the sun - mainly UV, VUV and EUV - are absorbed by atomic oxygen. Therefore, if an instrument observes the sun through the atmospheric limb, the reduced intensity of the wavelengths concerned, relative to the actual emission, can be used to calculate the AO density in the optical path. A mathematical analysis can then be used to determine the altitudinal variation of AO density. For example, the Laboratory for Atmospheric and Space Physics (LASP) group at Colorado University used a rocket-mounted EUV grating spectrograph, without a telescope, to observe the solar intensity in the wavelength range 30 - 100 nm (*Bailey, 1998*).

3.2.6 Reflection and transmission studies

Atomic oxygen fluences can also be determined by measuring the changing optical properties of solid substances that are reactive with AO. Three approaches exercising this principle have been found in the literature.

The first method involves measuring the AO-induced reflectance changes of an optically thin (< 25 nm), metal film deposited on the end of an optical fibre (*Butler and Ricco, 1988; 1989*). As the film is oxidized by AO, the reflectance at the fibre/film interface alters with time. Therefore, the change of reflectance may be used as an indicator of accumulated AO exposure. Reflectance changes of the film are measured by passing the radiation from a light emitting diode (LED) along the fibre and comparing the intensity of the back-reflection to that of the LED output. Once the reacting film on the face of the optical fibre becomes fully consumed, no further measurements of AO flux may be made. Thus, this technique is limited to a finite number of measurements. There are no reports of adaptation of this technique for LEO or sounding rocket research in the literature, but a lightweight, low power experiment has been designed for operation on the Martian surface, as part of the ill-fated Mars '96 mission (*Grunthaner et al., 1995*).

A technique, which utilizes the change in transmission of a material subjected to AO erosion, has been proposed as a microsatellite-based sensor (*Hersom, 1997*). In this second method, the material is polymethylmethacrylate (PMMA or Perspex®) in the form of a multi-mode optical fibre. Atomic oxygen erosion of the fibre alters its transmission, which is measured - like the previous reflectance changes - by shining the light from an LED along the fibre and comparing

the intensities of the light before and after transmission (*Li, 1995*). Again, this technique has not actually been flown on a mission, but shows promise due to its inherent simplicity, even though it suffers the same type of measurement limit as the previous optical fibre method.

Zimcik *et al.* briefly report the use of a carbon-based fluence monitor that was included in the ACOMEX (Advance COmposite Materials EXperiment) package located on the remote manipulator system (RMS) of STS-41G (*Zimcik et al., 1985; Zimcik and Maag, 1988*). The monitor consisted of a glass plate over which three parallel bands of gold of different thicknesses were deposited. These gold layers were then over-coated with carbon so that the total thickness of gold and carbon was the same for each band.

The package was exposed to AO, whence the carbon was eroded (Section 2.2.2). Orbiter crew members observed the monitor at regular intervals using the naked eye and cameras. As each gold band became visible, a known thickness of carbon had been eroded and the total AO fluence to that point could be calculated. Again, because this technique relies upon AO erosion of a material, it is limited to a finite number of measurements. It would seem that the time resolution of this device is limited because only the end point of the erosion could be used to gauge the amount of material removed. In comparison, the two optical fibre methods are able to monitor erosion throughout its course, hence, the time-dependent accumulation of AO fluence may be established. Moreover, due to the visual interpretation of the extent of erosion, the definition of the end point in this last optical method would seem to be rather subjective.

3.3 NON-OPTICAL AO MEASUREMENT TECHNIQUES

3.3.1 The witness sample

The witness sample is surely the simplest method of measuring AO fluences. This technique relies on the fact that, if a material is susceptible to AO attack, it will experience a mass change as a result of reaction with oxygen atoms (Chapter 2). Atomic oxygen fluence is calculated, using Equation 2.1, from the change of sample mass over the duration of the experiment, and the known erosion yield of the material. More often than not, the mass loss of the sample is corrected by an amount measured from a piece of the material exposed to the same conditions of temperature and vacuum, but shielded from AO action. In this way, mass losses associated with out- and off-gassing are taken into account.

Kapton polyimide has become the standard witness sample material because it has a long heredity in space, with many measurements of its erosion yield. This technique has been used in laboratory and space-based experiments alike, but no report of its application to sounding rockets

has been found. Presumably, this is due to the low accumulated AO fluences in the short flight times, and the potential for significant sample contamination.

Unfortunately, the simplicity of this method is also the source of many of its problems. The key disadvantage for space-based applications is that the exposed witness sample requires retrieval, so that its mass can be measured. This necessity significantly reduces the usefulness of the technique, and limits the number of missions on which it can be used, since most satellites are never recaptured or returned to the Earth's surface. In addition, during retrieval the samples may become contaminated, which alters the recorded mass change, thereby invalidating the results. By this technique, only the total AO fluence can be estimated - the method has poor time-resolution, like the ACOMEX monitor.

Although the AO erosion yield of Kapton is accepted as 3.0×10^{-24} $cm^3.atom^{-1}$ at ~ 5 eV impact energy, there is no guarantee that this is the correct value. Many of the measurements of this yield have been performed in the synergistic space environment, with the AO fluence calculated from thermospheric models. Errors in the erosion yield subsequently feed directly into errors in measured AO fluence. Determination of the mass loss of Kapton is also problematic. Sufficient Kapton must be eroded so that errors of mass measurement are reduced to a small fraction of the total mass loss - this effectively dictates a minimum necessary AO exposure (*Matcham, 1998a*). Also, the mass of the witness sample is greatly affected by the humidity of the air surrounding the samples. This requires the humidity in and around the mass balance to be controlled, and for the samples to be conditioned at this humidity for some time before any mass measurement (*Matcham, 1998b*).

Erosion of Kapton by AO appears to be an energy dependent process (*Banks et al., 1988; Cross et al., 1991*), see also Figure 3.2. Therefore, the energy of exposure should be taken into consideration. For LEO-based research, the energy of AO exposure - on ram facing surfaces - is always approximately 5.0 eV, so there is no significant variation in the energy of the reacting atoms. In contrast, ground-based simulation sources produce a wide range of energies. Hence, comparison of results from different laboratory facilities needs careful consideration, and the results may require modification to correct for differences in exposure energy. For these reasons, many comparisons may be difficult to achieve or, otherwise, may be invalid.

Of more concern is that new research performed by the author (*Osborne, 1998b*) seems to confirm that the erosion of Kapton is temperature sensitive (*Leger et al., 1988; Pippin et al., 1989*) - a fact that many researchers fail to address in their investigations. Temperature variations are frequently observed on orbit and in AO sources. If the witness sample method is to be used

for AO measurement, the exposure temperatures must be known and any temperature oscillations must be taken into account. Thus, although the witness sample method is cheap, simple and lightweight, there are significant problems that reduce its usefulness.

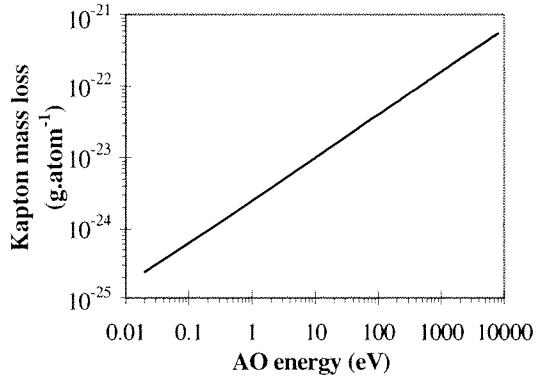

Figure 3.2 - The energy dependency of Kapton AO erosion (after *Stevens, 1990*)

3.3.2 Mass spectrometers

There are four parts to any mass spectrometer designed to measure the masses of neutral atoms and molecules. In this regard, laboratory and space-rated equipment are similar (*Harris, 1989*):

1) Ion source - in this stage the incoming species are ionized by electron bombardment.
2) Mass analyser - the ions from part 1 are drawn into the analyser electrostatically and are separated according to their mass/charge ratio.
3) Ion detector - the ions selected by part 2 are collected and generate a small current proportional to the charge of the ions.
4) Signal amplifier - the signal current is amplified.

The output from a mass spectrometer is a number of counts versus mass plot, hence the term mass spectrum. Essentially, there are two varieties of mass spectrometers, the magnetic deflection type and the quadrupole type. The distinction between the two is in the design and operation of the mass analyser stage.

In the magnetic deflection type, a magnetic field in the mass analyser enables selection of ions with the desired mass/charge ratio. Upon entering the magnetic field, the ions travel in circular paths - heavier, slower ions are deflected less than lighter, faster ones. The accelerating voltage, which is applied to draw the ions from the ion source, is varied to select those of the required mass-charge ratio. Figure 3.3 (below) schematically demonstrates the operation of this type of spectrometer. It should be noted that, for spacecraft applications, the presence of a permanent

magnetic field might interfere with other items of equipment on the rocket or satellite, for example magnetotorquers and magnetometers.

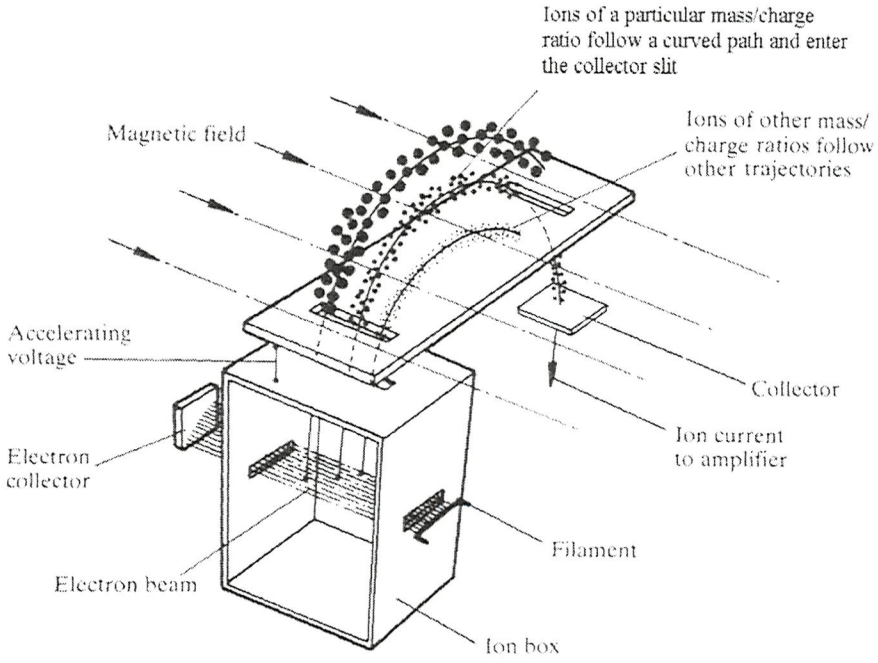

Figure 3.3 - The magnetic deflection mass spectrometer (after *Harris, 1989*)

Operation of the quadrupole mass spectrometer (shown in Figure 3.4 below) is somewhat different. In this device there is no magnetic field; instead, the ions are selected by passing them through a region of RF AC and DC electric fields. At any given electric field frequency, only ions of certain mass will undergo stable oscillations and reach the ion detector at the far end of the device. All other ions have unstable paths, so they impact on the rods that form the quadrant electrode to which the oscillating electric field is applied.

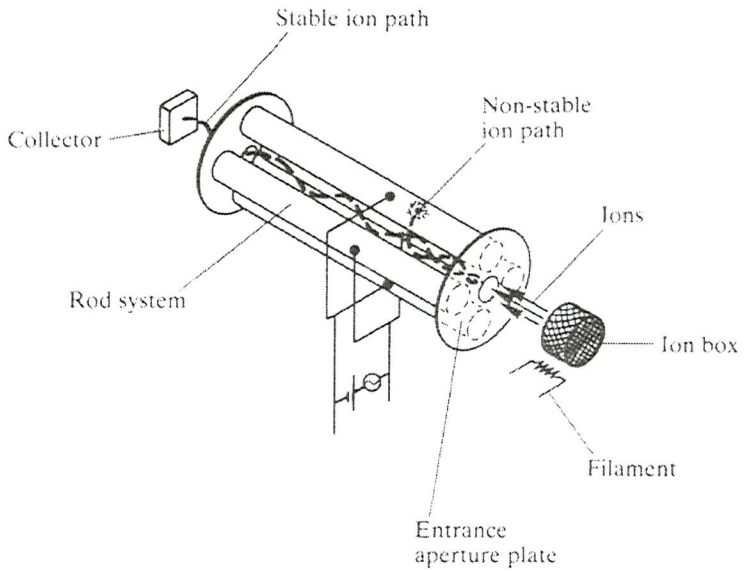

Figure 3.4 - The quadrupole mass spectrometer (after *Harris, 1989*)

The absence of the magnetic field in this spectrometer confers some significant advantages. In particular, since no magnets are required, the mass of the device is reduced, and the potential interference of the magnetic field is removed. However, there may be an increased chance of electromagnetic interference (EMI) of other RF devices such as transmitters and receivers. For these reasons, and those of size, quadrupole instruments are the most popular form of mass spectrometer for flight experiments.

A modification to the two types of spectrometer described above has been made and applied to the OV1-21 satellite mission in LEO (*Philbrick et al., 1973b*). It was called a 'Velocity Mass Spectrometer' and the device is much simpler than the two spectrometers introduced before. In this device the normal mass analyser was replaced with a retarding energy analyser. The operation of the instrument relied upon the fact that, even though their velocities are nearly identical, different atmospheric species entering the ion source have different energies (see Table 3.1) by virtue of their different masses. When the species enter the ion source they become charged and pass into the energy analyser, a region of controlled electric field. The retarding electric field is swept through a range of values that encompasses the energies of the inbound ions. In this way, the satellite velocity can be used to separate the species by mass.

Species	Energy (eV)
H	0.3
He	1.3
O	5.3
N_2	9.3

Table 3.1 – Energies of typical atmospheric species at satellite velocity

Mass spectrometers have been flown on rockets (*Horowitz and LaGow, 1957; von Zahn, 1967; Offermann and Drescher, 1973; Offermann et al. 1981; Friedrich et al., 1977*) and on board vehicles in Earth orbit, such as the Space Shuttle (*Visentine and Leger, 1986; Koontz et al., 1995a; 1995b*), the Atmosphere Explorer (*Nier et al., 1973; Pelz et al., 1973*) and other satellites (*Philbrick and McIsaac, 1972; Philbrick, 1974; Philbrick, 1976*). They have also been used in the laboratory for compositional and time-of-flight analyses (*Cazaubon et al., 1996*).

The advantages of using mass spectrometers for *in situ* AO measurements are that direct measurement of AO number densities is possible (*Harris, 1996*); they can also be used to monitor the reaction products that result from AO/materials interactions (*Koontz et al., 1995a; 1995b*) and can be considered reusable. However, these devices tend to be heavy, bulky and frequently consume large amounts of power, which often precludes their deployment on microsatellite missions. Smaller devices have been made for application to interplanetary missions, but their

cost excludes application on most thermospheric research missions (*Niemann et al., 1980; Niemann et al., 1998*).

All mass spectrometers have an upper pressure limit for operation of around 10^{-4} mbar (*Roth, 1976*). Whilst this should not present a problem for space-based operations where the ambient pressure is far below this value (less than 10^{-7} mbar), it is of concern for sounding rocket applications where the atmospheric pressure may be above this limit. In this situation, differential pumping of the spectrometer entrance orifice would be necessary. In either case, pumping of the ion detector is necessary to remove collected ions.

The interpretation of atomic mass spectra is often complicated by the presence of doubly ionized species, and by behavioural differences of thermal and hyper-thermal oxygen atoms. In the laboratory, Harris found difficulty in achieving measurement accuracies of better than ± 50 % of number density (*Harris, 1996*). Also, AO tends to recombine on device surfaces (*Sjolander, 1976*), or react with contaminant layers adsorbed thereon, producing thermalized oxygen molecules (*Mauersberger et al., 1976*) and reaction products (*Cross et al., 1995*) that compound the difficulties of spectra interpretation. Recombination problems can, apparently, be limited by the use of titanium to form the internal surfaces of the device (*Philbrick and McIsaac, 1972*). Problems of thermalized oxygen atoms and reaction products can be alleviated by the employment of velocity mass spectrometers; since they are energy discriminating, such species do not complicate the scans.

To overcome some of these problems, cryogenically cooled mass spectrometers have been utilized. The equipment flown on rockets by several research groups employed supercritical helium to cool the ion source (*Offermann and Trinks, 1971; Scholz and Offermann, 1974; Trinks et al., 1978; Offermann et al., 1981*), whilst other groups used liquid nitrogen (*Philbrick et al., 1973b*). In this way, molecules and atoms colliding with the device walls were made to stick rather than reflect, thus preventing them from influencing the spectra. The mass penalties of this modification are self-evident, as is the problem of limited operational time due to the fixed quantity of cryogen that can be carried. No reports of space-based cryogenic mass spectrometers are found in the literature.

3.3.3 Catalytic probes

Catalytic probes offer a simple and sensitive way of measuring AO fluxes (*Kaufman, 1961*). When oxygen atoms recombine on a surface, a *heat of recombination* is released that warms the material. Most commonly, silver oxide is exploited to force recombination of AO because it has a high coefficient of recombination. In the most basic form of this sensor, the temperature of the

catalytic surface is used to indicate the number of atoms that are recombining on the surface. This number is then related to the magnitude of impinging AO flux.

Improvements to the above can be made by including a heater in the probe, along with the thermocouple or other temperature-measuring device. The probe is placed in the AO environment and the temperature at thermal equilibrium noted. The probe is then either removed from the flow, or the flow is ceased (if possible), and the heater used to warm the device to the temperature achieved during AO action. The power needed to maintain this temperature is then used to give the flux of atoms directly, using Equation (3.4).

$$F = \frac{P}{\eta A H} \tag{3.4}$$

Where:

F = AO flux (atoms.cm^{-2}.s^{-1})

P = Heater power (W)

A = Sensor area (cm^2)

η = Coefficient of recombination

H = Heat of recombination per atom (J.atom^{-1})

Single probe sensors have been operated in laboratory studies (*Kaufman, 1961; Satchell, 1993*) as have double probe sensors - one probe of which has no catalytic surface and is used to measure environmental energy losses (*Carruth et al., 1990*).

These sensors have been applied to sounding rocket missions (*Perov and Rakhmanov, 1977*) but no reference has been found to their application to LEO (or other orbit) studies. The lack of space-based applications of this technique is probably due to the small heat inputs from typical LEO AO fluxes - roughly 4 W.m^{-2} - compared to the solar input of ~ 1400 W.m^{-2}. Clearly, the effects of solar illumination dominate the recombination-related heat input - a problem exacerbated by self-eclipsing if the vehicle should be spin-stabilized, as are many microsatellites. Satchell (*ibid.*) reports that the probes also have long settling times, which would reduce the achievable time resolution. However, the sensors are lightweight and can be used to make many measurements - they are reusable.

3.3.4 Actinometers

The resistance of a thin, conducting film is a function of its thickness, length, width and the material from which it is fabricated. If the film is reactive with AO, a flux of this species will oxidize the material, reducing its thickness. Reduction of conductor thickness increases sample

resistance. Therefore, change of film resistance can be used as the measurand of AO exposure. This is the principle of the actinometer sensor, which appears to have been first proposed by Henderson and Schiff (*Henderson and Schiff, 1970*). A model to describe the response of an actinometer during AO oxidation was developed soon after conception by Thomas and Baker (*Thomas and Baker, 1972*).

Actinometer sensors have been flown on sounding rockets (*Henderson, 1974; Dickinson et al., 1980*), in LEO (*Cross et al., 1991; Gregory et al., 1993; Miller et al., 1997, Többen et al., 1998*), in GTO (*Harris, 1996; Harris et al., 1997a; 1997b*), and used in the laboratory (*Koontz et al., 1991a; Harris et al., 1994; Oakes et al., 1995; Chambers et al., 1996*) for measuring AO concentrations and conducting materials studies. In these applications, only two materials have been used for the active elements - carbon and silver.

Silver is used because it is readily and completely oxidized by AO (*Moore and Codella, 1988*). It is also reasonably cheap and easy to handle. At low AO fluences, silver actinometers exhibit a linear relationship between resistance increase and AO exposure. However, the formation of a stable oxide layer engenders a change in this response to a parabolic, diffusion limited regime (*Harris, 1996*). Even in the linear region, actinometers display a time-lag in their response - after AO impingement is terminated, the resistances of the films continue to increase (*Oakes et al., 1995*). This phenomenon is often called 'coasting'. Usually, the continuation of oxidation is explained by the diffusion of oxygen trapped in the surface oxide layer to the reacting metal interface.

Within the silver oxide, stresses develop due to volumetric differences between the metal and oxide systems. Thus, whilst silver oxide is stable in the vacuum environment of space, these stresses (in conjunction with thermal cycling) may result in flaking of the oxide layer. Consequently, virgin metal is exposed to AO bombardment. This process leads to unpredictable changes in the erosion rate of the silver. In addition, the catalytic properties of silver oxide may force the recombination of AO to molecular oxygen, in the same way that silver oxide surfaces are used in catalytic probes (Section 3.3.3). Recombination of AO to molecular oxygen is expected to result in lower diffusion and oxidation rates than with a wholly AO dominated system.

The use of carbon thin films would seem to overcome many of the problems encountered with silver, because oxides of carbon are volatile and thus diffusion limited regimes are not exhibited by sensors fabricated from this material (*Linton et al., 1993*). Unfortunately, there are other problems associated with carbon actinometers. Firstly, the erosion yield of carbon is dependent

on the form of the material (glassy, graphitic, diamond-like or amorphous) and so knowledge of the type of carbon used is essential to the correct interpretation of actinometer results (*Haenni et al., 1998*). Secondly, it has been widely accepted that carbon has a temperature-dependent erosion yield (*Arnold and Peplinski, 1986; Caledonia et al., 1994; Osborne, 1998b*), a problem that silver-based devices do not suffer. Thus, close control of the temperature of the carbon films must be maintained throughout the AO exposure experiment, increasing the mass and power requirements of the equipment.

The actinometer technique would appear to be relatively cheap and simple, and the apparatus can be made to be lightweight and to consume small amounts of power - properties that make the method ideal for application on microsatellite missions. For example, the first University of Southampton Atomic Oxygen Experiment (AOE-1) flown on the first Defence Research Agency (DRA) microsatellite, STRV-1a, consumed an average of only 2.3 W (heater on) and the total mass was just 0.36 kg for 12 actinometers (*Harris et al., 1998*). However, the sensors, like witness samples, are single use devices.

3.3.5 Quartz crystal microbalances (QCMs)

Essentially, a QCM consists of a small piezoelectric (quartz) crystal that is excited to oscillate at its natural frequency; the exact frequency is a function of the mass of the crystal and that of any coating applied to it. In the application of these devices to AO studies, one surface of the quartz crystal is coated with an AO-active material. When the device is exposed to oxygen atoms, the mass of the coating changes due to oxidation. Consequently, as the reaction proceeds, the frequency of crystal oscillation shifts. The area of the coating, its density, a mass-frequency calibration and the erosion yield of the material are then used to determine the AO fluence experienced. Alternatively, the rate of change of mass can be used to give the AO flux. Hence, QCMs can be considered to be witness samples, but with the capacity for *in situ*, real time mass measurement.

Carbon-coated QCM AO sensors (C-QCMs) have been operated on board a microsatellite (*Drolshagen and van Eesbeek, 1991; van Eesbeek, 1996*). They have also been employed in ground and space-based applications to investigate the action of AO on various materials (*Visentine and Leger, 1986; Caledonia et al., 1994; Koontz et al., 1995a; Oakes et al., 1995, Osborne, 1998b*); to investigate AO fluxes in ground-based sources (*Osborne, 1998a*) and to test materials intended for use as AO protective coatings (*Woollam et al., 1994*). No applications of QCMs to rocket campaigns have been found in the literature. Once again, like the witness sample, this is presumably due to the small fluences experienced during the short flight times.

QCMs suffer from few disadvantages, but one is the complicated electronics needed to measure and record the high frequency (typically 10 MHz) signals. Secondly, as with any technique that relies on the erosion of material during operation, QCMs can only be used until the coating either becomes completely eroded, or enters into a diffusion-limited regime. Thirdly, the quartz crystal can be temperature sensitive. However, it is possible to select a particular 'cut' of the quartz to reduce this sensitivity. Despite these precautions, it may still be necessary to temperature compensate the measurement crystal, increasing the mass and complexity of the equipment.

3.4 QUANTITATIVE TECHNIQUE COMPARISON

Inter-comparison of the techniques reviewed in this chapter would best be achieved by the use of a figure of merit, based upon characteristics common to each method and piece of equipment. It is therefore necessary to determine the essential properties of instruments for use in orbit. Microsatellite missions are frequently dominated by stringent constraints upon mass and power budgets. Thus, a technique to be utilized on board a microsatellite should be lightweight and require small power inputs from the vehicular power sub-system. The dimensions of the instrument should also be kept to reasonable values. The harsh space environment - introduced in Section 1.1 - requires that the equipment be rugged, so that during the lifetime of the mission, instrument stability can be assured. Depending upon the goals of the individual experiment, high instrument accuracy and, if the AO data is to be used for model input, the ability to make time-resolved measurements may be desirable. Lastly, it will always be better to apply a simple technique rather than a complicated one, since there are inherently fewer items that might fail. An instrument that possesses all these characteristics can be considered an 'ideal' sensor. It is now possible to construct a list of prerequisite properties for satellite-based AO sensors:

1) Low mass.
2) Small power consumption.
3) Small size (volume).
4) Simplicity is preferred.
5) Robust and stable.
6) High accuracy.
7) Time resolution.
8) Reusability.

A reliable figure of merit would include all the characteristics in the above list, so that it represents all of the design-drivers. It has proved impossible to develop such a generic figure, because the relative importance of each property is different for each mission considered. Additionally, many of the characteristics, like robustness and simplicity, are very difficult to

quantify and, as such, are not reported in the literature. The variety of techniques employed in thermospheric research poses further problems - parameters such as instrument accuracy, values of which are nearly always quoted, are given in a wide range of units that cannot be converted to a common system, precluding its inclusion in an analysis.

Hence, a comparison of the methods has been conducted using only three parameters: the mass of the experimental equipment (M), the number of sensors included in that mass (S) and the power consumed during operation (P). Frequently, it has been found that many of the journal papers and reports acquired by the author neglect to include even this basic information. Where this has been found to be the case, equipment representative of that used in AO studies has been used, even if its original purpose was not to make AO measurements. Obviously, this approach is not ideal, but the general conclusions should be unaltered - the mass of a photometer, for example, is fairly independent of the wavelength of light that it measures.

All information collected is presented in Tables 3.2.a (optical) and 3.2.b (non-optical), which can be found towards the end of this chapter. Figure 3.5 is a plot of the information contained in those tables. This log-log chart was generated by allocating each technique a set of co-ordinates: (M/S) and (P/S).

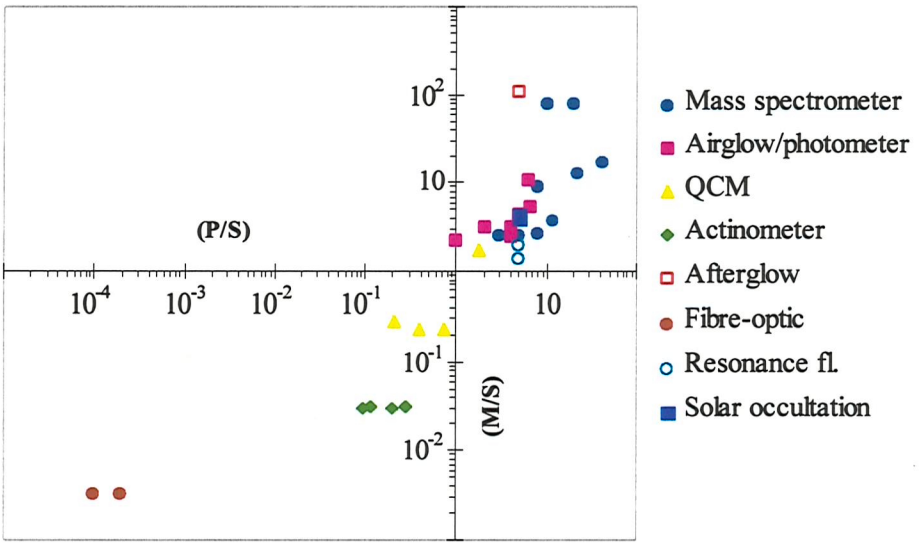

Figure 3.5 - Graphical representation of the information in Tables 3.2.a and 3.2.b

The further that a given instrument lies to the bottom-left of the chart, the more suitable it is for application to a mass- and power-limited mission. Figure 3.6 is a generalized version of Figure 3.5, which shows this quantitative relationship. On the basis of this judgement, the best overall technique reviewed in this chapter is the fibre-optic reflectance device proposed by Grunthaner (*Grunthaner et al., 1995*).

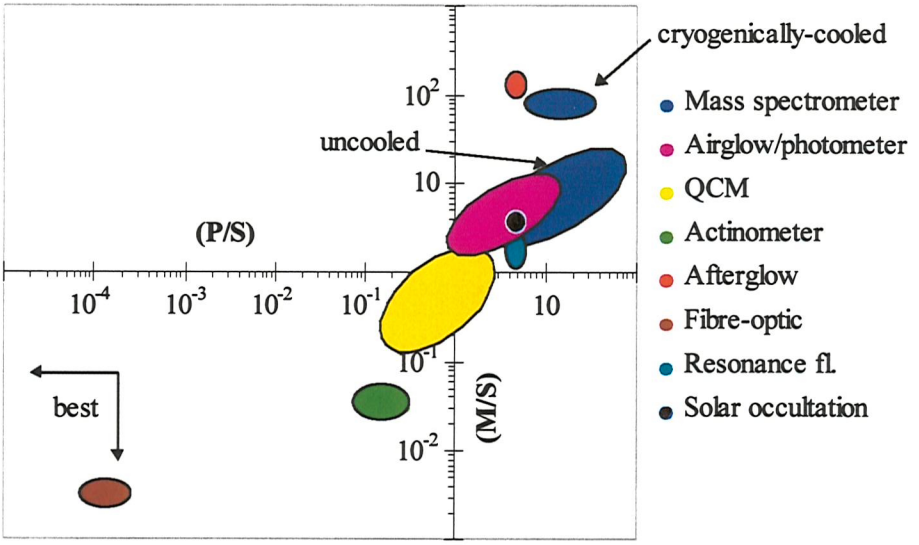

Figure 3.6 - Generalized plot of Figure 3.5

One of the ideal device properties is reusability - the ability to make repeated AO flux/fluence measurements. Any technique that relies on the irreversible oxidation of a material for its measurand will experience a limit on the number of AO fluence evaluations that it can perform. For example, the carbon layer of a C-QCM will eventually be completely eroded, thereby preventing further AO measurements. The fibre-optic device of Grunthaner is such a method and, therefore, despite the benefits of its small mass and power consumption, it cannot be considered for long term applications, where reusability is an important criterion. Unfortunately, no way of converting this method to a reusable technique has been found, hence, another method must be selected.

The next best approach, and one that is known to be suitable for application to microsatellite missions, is that of the thin-film actinometer (*Harris et al., 1998*). However, this device also relies upon the erosion of material, reducing its long-term usefulness. Yet, if a method of AO detection could be developed with similar characteristics to the actinometer sensor, in terms of small mass and power consumption, but one that also allowed repeated AO measurements to be made, then this device might be considered ideal. The possibility of such a device exists if the principles of semiconducting sensors are applied to the problem of *in situ* AO measurement. This is the topic of research presented in the remainder of this thesis.

Technique	Reference	Application	Mass, M (kg)	Power, P (W)	Number of devices, S	Comments
Airglow/photometer	Schenkel *et al.*, 1985	Satellite	9.5	6 - 12	3	1 x UV imager, 2 x photometers flown on the HILAT satellite.
	Bailey, 1998	Rocket	4.0 - 4.5	5	1	UV photometer and telescope also used for solar occultation.
	Shepherd *et al.*, 1973	Satellite	4.5	2	2	ISIS-II 630.0 nm photometer.
	Anger *et al.*, 1973	Satellite	4.8	8	2	ISIS-II 557.7 nm scanning photometer.
	Donahue *et al.*, 1973	Satellite	5.24	6.7	1	OGO-6 scanning green line photometer
	Clemesha, 1998	Rocket	107	61.5	10	MULTIPHOT, includes plasma probes.
Resonance fluorescence	Howlett *et al.*, 1980	Rocket	10	?	1	UV lamp and photomultiplier tube.
	Iwagami, 1999	Rocket	7 -10	10	2	1992 and 2000 rocket payloads.
Fibre-optic	Grunthaner *et al.*, 1995	Satellite	0.85	0.025 - 0.050	256	Mars '96 lander, reflectance change.
NO release - afterglow	Golomb *et al.*, 1965 Golomb and Good, 1972	Rocket	110	5.0	1	Predicted mass of NO (based on quoted tank volume) and supposed inclusion of a single photometer.

Table 3.2.a - A comparison of optical AO measurement techniques

Technique	Reference	Application	Mass, M (kg)	Power, P (W)	Number of devices, S	Comments
Mass spectrometer	Offermann, 1998	Rocket	80	10 - 20	1	Cryogenically cooled with helium.
	Niemann *et al.*, 1980	Satellite	3.8	12	1	Pioneer Venus instrument
	Niemann et al., 1998	Satellite	2.7	8	1	Nozomi instrument
	GSFC Laboratory for Atmospheres www pages	Satellite	13.2	22	1	Galileo instrument
		Satellite	17.3	41	1	Cassini GCMS
	Pavlenko, 1966	Rocket & Satellite	2.5	3 - 5	1	Radio frequency mass spectrometer suitable for rocket and satellite usage.
QCM	van Eesbeek, 1996	Satellite	0.557	0.419	2	C-QCMs flown on BREMSAT.
	Cant, 1990	Satellite	2	3.5 - 6.5	9	Mass & power figures are estimates only & based on old technology.
	Triolo *et al.*, 1984	Satellite	7	7	4	Temperature controlled QCMs used for contamination monitoring.
Actinometer	Harris *et al.*, 1998	Satellite	0.36	1.16 - 2.33	12	Silver film actinometers flown on STRV-1a.

Table 3.2.b - A comparison of <u>non-optical</u> AO measurement techniques

3.5 SUMMARY

This chapter has reviewed all the techniques reported in the literature that have been applied to thermospheric AO research. It was found that there was a clear division in the methods used to perform the measurements. The first group employed some form of optical measurement and included afterglow, airglow, resonance fluorescence and absorption, and reflection/transmission methods. Non-optical techniques such as mass spectrometers, C-QCMs, witness samples, actinometers and catalytic probes comprised the second group. Comparison of the methods showed that a fibre-optic reflectance device was the best available, in terms of small mass and power consumption per sensor. The non-reusability of this device appears to be its key disadvantage. Hence, an investigation of a reusable actinometer-style technique using semiconductor sensors was proposed to fulfil all the characteristics of an ideal space-based AO devices.

The next chapter is a brief guide to the topic of semiconductor physics, the intention of which is to enable the reader to fully understand the operation of semiconductor sensors.

CHAPTER 4

SEMICONDUCTOR PHYSICS

Semiconductors are, as the name implies, materials that conduct electricity more effectively than non-conducting insulators, but not as 'easily' as metals. The purpose of this chapter is to present an explanation of semiconductor physics, so that the various properties of semiconducting materials, and sensors based upon them, may be discussed in greater detail in later sections. An understanding of the electronic behaviour of semiconductors requires knowledge of quantum physics and Fermi-Dirac statistics - the relevant sections of these subjects are introduced where necessary.

4.1 ELECTRONS, POTENTIAL WELLS AND SCHRÖDINGER'S EQUATION

4.1.1 The classical view of atoms and electrons

Atoms consist of a small, dense nucleus - a collection of positive protons and chargeless neutrons - surrounded by a 'cloud' of electrons. In any free atom, the positive charge of the nucleus is balanced by the total negative charge of the associated electrons. Thus, overall, the atom is charge neutral. Frequently, it is sufficient to view the electrons as particles 'orbiting' the nucleus, in the same way that satellites orbit a planet - this is the 'classical' view of an atom.

However, in some circumstances, for example when one is interested in the energy distribution of the electrons, it is necessary to apply the *de Broglie* postulate that all matter can exhibit the same wave-particle duality as photons. With the application of this concept, electrons have to be considered as wave-like particles, and the classical description is no longer valid. It is the intention of the following discussion to develop a description of how electrons behave in isolated atoms and, subsequently, in multi-atom solids.

4.1.2 Energy of an electron in a potential well

In order to remove an electron from an atom, it is known that a net amount of energy must be supplied to that electron. In just the same way, a propulsive device must be used to boost the orbit of a satellite. Bodies in orbit around a planet reside in the gravitational potential well associated with the mass of the planet. The analogy shows that the electrons associated with an atom reside in a potential well associated with the charge of the nucleus. It would, therefore, appear possible to model a simple free atom by confining an electron inside an easily described potential well. The results from this model can then be used to gain an insight of the electronic energy levels within an atom.

The wave-like nature of an electron in an atom requires that Heisenberg's uncertainty principle and Pauli's exclusion principle must be applied and, so, the electron energies and positional distributions are described by quantum physics. In this description, electrons are not viewed as point-like particles but, rather, must be considered as wave functions that take the general form (*Somorjai, 1972*):

$$\psi(x) = A\exp(j\underline{k}x) + B\exp(-j\underline{k}x) \tag{4.1}$$

as solutions to the one-dimensional time-independent Schrödinger equation (*Smith, 1964*), which is given in Equation (4.2).

$$\frac{d^2\psi(x)}{dx^2} + \frac{8\pi^2 m}{h^2}(E - V)\psi(x) = 0 \tag{4.2}$$

The symbols in these two equations have the following definitions.

x = distance
A, *B* = constants associated with the boundary conditions of the problem
m = electron mass
h = Planck's constant
E = electron energy
V = potential experienced by the electron
$\underline{k}$ = is the wave-vector, given by Equation (4.3)

$$|\underline{k}| = 2\pi\left(\frac{2m}{h^2}(E - V)\right)^{\frac{1}{2}} \tag{4.3}$$

Furthermore, it can be shown that $|\psi(x)|^2 dx$ is the probability of finding an electron between x and x + dx (*Grieg, 1969*).

Now, model the potential in which the electron resides as a one-dimensional box of length L. Within this box the potential is taken to be zero (V = 0 in $0 \leq x \leq L$) but outside, the potential is considered to be infinite. Thus, as far as the electron is concerned, the box walls are impenetrable.

Inside the box, the general solution to Schrödinger's equation remains of the form in (4.1). However, because the electron is constrained by the potential, the wave function must vanish outside of the box. Therefore, at the walls of the box, the boundary conditions may be written:

$$\psi(L) = \psi(0) = 0 \tag{4.4}$$

Applying these boundary conditions to Equation (4.1) results in the solution:

$$\underline{k} = \pm n\frac{\pi}{L}, \quad n = 1,2,3,.....,\infty \tag{4.5}$$

Then, using Equation (4.3) and remembering that V = 0 within the walls, the energy of an electron in a one-dimensional box (or potential well) is given by:

$$E = \frac{n^2h^2}{8mL^2}, \quad n = 1,2,3,.....,\infty \tag{4.6}$$

So, it is evident that in a potential well, the energies that an electron may take are discrete and quantized into specific levels. Figure 4.1 is a diagrammatic plot of the result described by Equation (4.6), for the situation when the length of the box is on the order of atomic dimensions. Apparently, not only are the energy levels quantized, but they are also separated by broad forbidden gaps.

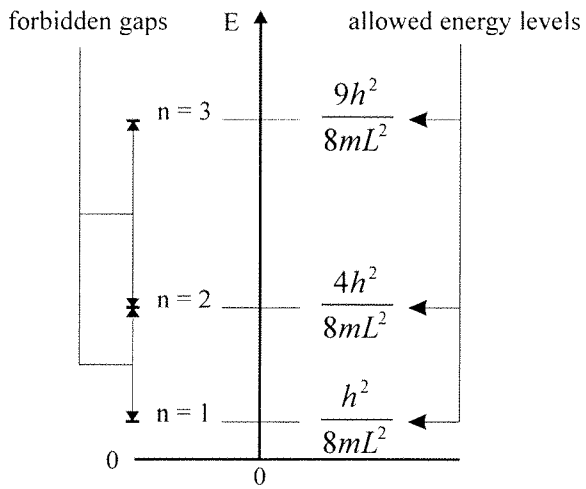

Figure 4.1 - The energy levels of an electron in a potential well.

Equation (4.6) also shows that the longer the box, the smaller is the spacing of the energy levels. This result indicates that a free electron has a continuous energy spectrum. For comparison to the result above, the energy of a free electron - that is one that is far removed from any potential - may be calculated from its velocity by the traditional kinetic energy equation:

$$E = \tfrac{1}{2}mv^2 \tag{4.7}$$

It is clear from Equation (4.7) that, indeed, a free electron may take any energy from zero to infinity - the amount is not restricted to certain values. The difference in energy structure between the two situations can only be caused by the action of the potential well upon the wave function describing the electron.

Thus, the key result from the discussion presented in this sub-section is that an electron caught in a potential well has quantized energy levels. Since electrons in real atoms are caught in the Coulombic potential well associated with the charge of the nucleus, it should be expected that electrons in real atoms also display such energy levels. Indeed, this is found to be the case (*Grieg, 1969*).

4.1.3 Electrons in solids

The previous section demonstrated that an electron influenced by one potential well had discrete and quantized energy levels. What happens when there is more than one potential influencing the electron?

In the case of two adjacent potentials separated by a small potential energy barrier, it can be shown (see for example the text by *Somorjai, 1972*) that the wave-vector of the problem is given by

$$\underline{k} = \frac{m\pi}{2a}\left\{1 \pm \frac{1}{2\alpha L}\left[1 + 2\exp(-2\alpha c)\right]\right\} \tag{4.8}$$

The meanings of the terms are unimportant to this work; the important point is that the $\underline{k}$ values for the electron are shifted to give two energy states. Consequently, at each of the energy levels calculated in the previous example, an electron influenced by two potentials is actually 'allowed' two energy states. Each pair of energy levels is still separated from those at higher, and lower, levels by a gap of forbidden energies.

This result is of importance because electrons in solids are influenced by many potential wells due to the periodic arrangement of the atoms therein. Thus, it is expected that the more potential wells that are present and influencing the electron, the more the energy levels divide. This finding has lead to the band theory of solids, which is the subject of the next section.

4.2 THE BAND THEORY OF SOLIDS

Figure 4.2 shows the quantum view of an isolated atom that was developed in the previous section. It can be seen that the nucleus of the atom sits at the bottom of a potential well, the shape

of which is dictated by the Coulombic potential energy of the electrons in the electric field of the nucleus. As already shown, the electron wave functions are confined to specific energy levels, and extend roughly as far as the boundary that is defined by the potential well. The energy levels nearest the nucleus are filled by the 'core' electrons, whereas the outer levels are filled by the conduction electrons. It is these outer electrons which are of interest in this chapter.

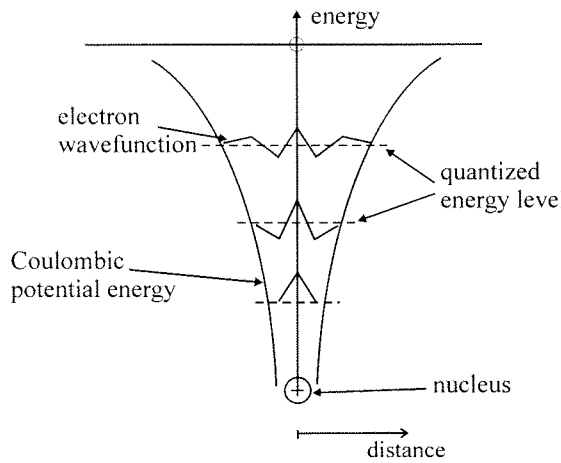

Figure 4.2 - The quantum view of an atom (after *Grieg, 1969*)

When atoms combine to make a solid, they reside in a closely spaced lattice structure. Since the energy of the solid must be lower than the individual atoms of which it consists, the potential wells of the atoms overlap and fall below the atomic value. Therefore, the arrangement of potential in this situation is analogous to that considered in Section 4.1.3. Figure 4.3 illustrates the case of two atoms.

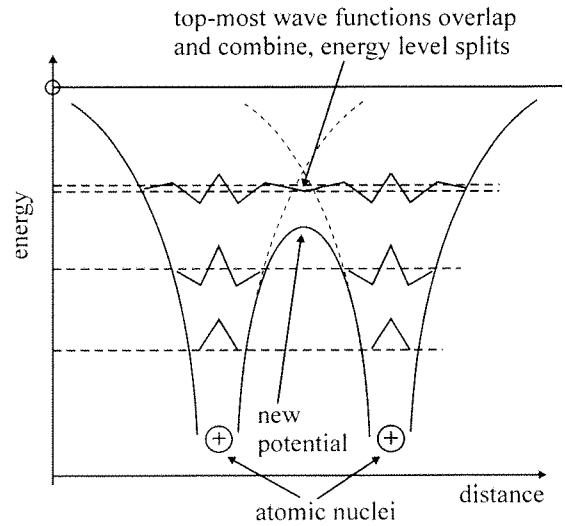

Figure 4.3 - The formation of a solid from two atoms

The overlapping of the potential wells allows the outer wave functions of the atoms - those that describe the conduction electrons - to combine. During the combination, the energy levels

described by the wave functions and Schrödinger's equation, split and spread, as shown in Section 4.1.3. For N atoms in the solid, the energy levels each split into N sub-levels. The allowed energy levels are then considered to form a 'band' of very closely spaced sub-levels, which are separated from higher and lower bands by a gap of forbidden energies.

Since electrons are spin-½ particles that obey the rules of quantum mechanics (fermions), the electrons associated with the solid fill the sub-levels in the bands in accordance with the Pauli exclusion principle. Therefore, each energy level may be occupied by no more than two electrons of different spin state at anyone time: one with spin 'up' and one with spin 'down'. Accordingly, the maximum number of electrons that may reside in each band is $2N$, twice the number of atoms present in the solid.

Two situations may arise when the electrons fill the energy bands, a process that occurs from the very lowest energy state towards the higher levels. The first is that the highest band is incompletely filled, with empty sub-levels towards the top of the band. The second is that the uppermost band is completely empty, whilst the band just below is completely filled. These two circumstances engender very different electrical properties within the solid materials in which they occur, and this is the topic of the next section.

4.3 METALS, INSULATORS AND SEMICONDUCTORS

4.3.1 Metals

Traditionally, the electronic structure of a metal is considered to consist of a sea of mobile electrons (*Sommerfeld, 1928*). The sea surrounds the discrete, positively charged ions from which the electrons originated. In this model, each electron may be viewed as shared by all of the ions, and not localized to any one ion in particular - the electrons are influenced by a potential that is equal and constant everywhere inside the metal. Metallic bonding results from the attraction of the ions for the sea of electrons, whilst conduction occurs by motion of the free electrons in the direction of an applied electric field.

Conduction in metals can also be explained by the band-theory of solids. When metal atoms combine to form a solid, the uppermost energy band - the conduction band - is incompletely filled with electrons. In principle, at absolute zero, the energy structure of the upper band of a metal is as that represented in Figure 4.4.a, with the electrons adopting the lowest energy states possible. Since all the lower bands are already completely occupied, Pauli's exclusion principle prevents any of the upper band electrons from 'falling' through the forbidden energy gaps into

lower bands. Hence, at zero Kelvin, the conduction electrons reside at the bottom of the conduction band and conduction is not possible.

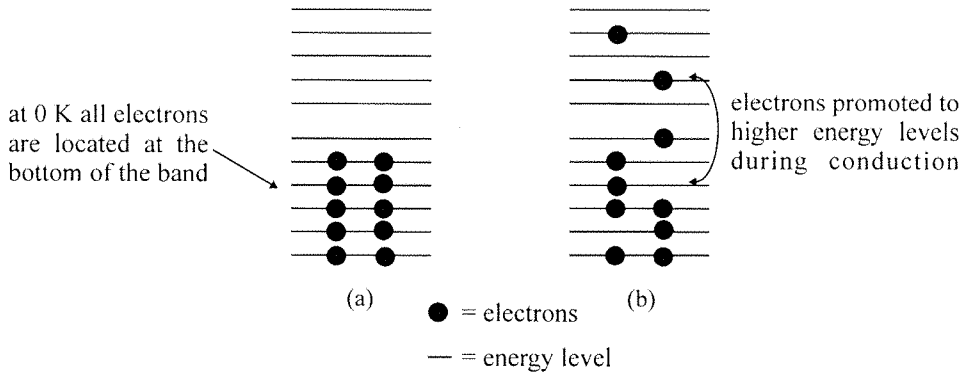

Figure 4.4 - The energy structure of metals: (a) at 0 K; (b) at T > 0 K

At higher temperatures, the electrons in the conduction band gain thermal energy through collisions, and are able to occupy sub-levels above those that they held at zero Kelvin. Promotion of these electrons to higher energies leaves some of the lower levels in the conduction band incomplete (see Figure 4.4.b). Electrical conduction is then allowed, because there are free levels into which electrons in the conduction band may be promoted by the application of an electric field.

Electrons in lower bands cannot be promoted to energy levels inside those bands, because all levels are completely filled. Also, the size of the energy gaps between the bands prevents electron promotion from lower into higher bands. Thus, the number of conduction electrons in a metal is essentially constant with temperature. However, the conductivity of metals decreases with increasing temperature, despite the increased thermal energy of the electrons, because electron scattering mechanisms - such as lattice vibration - begin to hinder the motion of the conduction electrons.

4.3.2 Insulators

The properties of insulator materials may also be understood by the band theory of solids. Insulators have an energy structure in which the lower energy bands are completely filled, whereas, the outer band is completely empty. Moreover, the filled lower band is separated from the empty upper band by the presence of a large energy gap, which is of the order of several electron volts, see Figure 4.5.

The energy gap in this group of materials is too large for significant thermal promotion of electrons from the lower band to the upper band - so all energy levels in the lower band remain

full. Again, Pauli's exclusion principle prevents promotion of any electrons into full levels and so electrical conduction cannot occur.

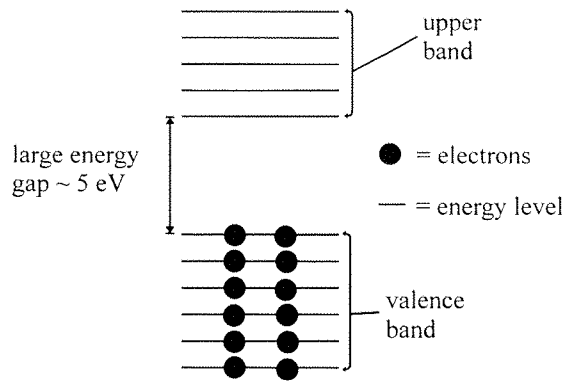

Figure 4.5 - The electronic structure of an insulator

The electronic structure of insulators and semiconductors are very similar. In fact, at low temperatures all semiconductors behave as insulators, whilst at high temperatures some insulators may exhibit semiconductor-like behaviour. There are two types of semiconductor, intrinsic and extrinsic.

4.3.3 Intrinsic semiconductors

Of the two classes of semiconductors, those of the variety called 'intrinsic' have an energy structure most closely resembling that of an insulator. The key difference is that the band gap is much smaller, perhaps one electron volt or less. The small gap means that, even at room temperatures, a significant number of electrons can be thermally excited from the lower (valence) band into the conduction band. When an electron is promoted to the conduction band, it leaves a partially filled energy level, or hole, in the valence band. Holes act as positively charged current carriers, so the overall conductivity of an intrinsic semiconductor is the sum of the conductivities arising from electrons in the conduction band, and holes in the valence band.

4.3.4 Extrinsic semiconductors

In extrinsic semiconductors, the majority of the conductivity arises not from the presence of valence band electrons in the conduction band, but from charge carriers originating from impurity atoms in the material. The impurity atoms may give rise to two different types of supplementary energy level within the band-gap of a semiconductor. Hence, there are two different types of extrinsic semiconductor.

Some impurities introduce donor levels just below the bottom of the conduction band of the semiconductor. Due to the very small energy gap between the bottom of the conduction band and

the donor level (perhaps on the order of a tenth of one electron volt), electrons from the donor atoms are easily promoted into the conduction band by thermal processes. Within the conduction band the majority of sub-levels are empty. Thus, upon application of an electric field, these electrons are able to conduct charge. The donor atoms are immobile within the semiconductor matrix and so, even though they are positively charged, they do not act as holes. The majority charge carriers in this type of extrinsic semiconductor are *n*egatively charged electrons; as a result they are referred to as *n-type* semiconductors.

Other impurities may introduce energy levels just above the valence band. These energy levels are frequently called acceptor levels, because they capture electrons that have sufficient energy to leave the valence band. Similar to the intrinsic semiconductors, removal of electrons from the once completely filled valence band leaves behind positively charged holes. Thus *p*ositive holes are the majority charge carriers in this type of extrinsic semiconductors, and they are referred to as *p-type* material.

The differences between n- and p-type semiconductors are shown, schematically, in Figure 4.6. In this diagram, the energy levels of the donors and acceptors are drawn as discrete levels, rather than as energy bands. This implies that the impurity atoms are assumed to be widely spread, so that their wave functions do not overlap.

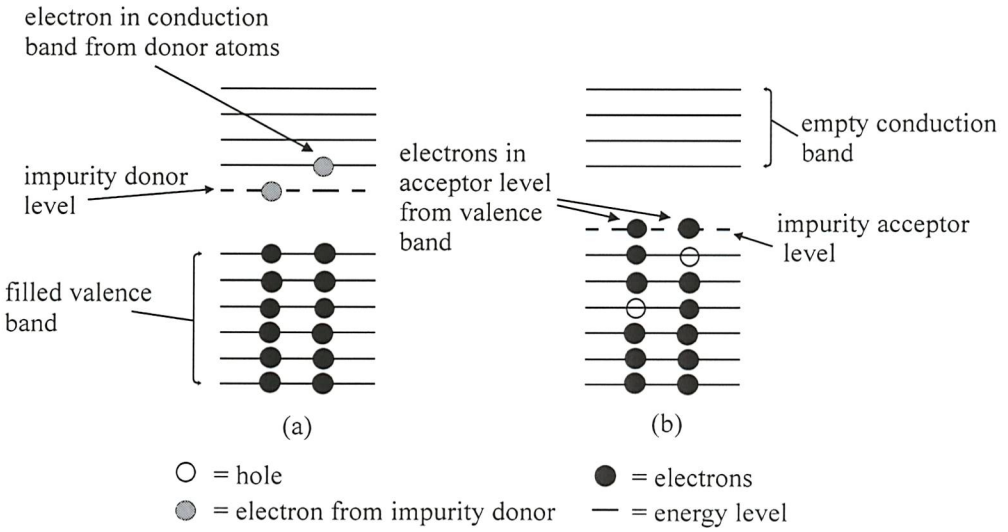

Figure 4.6 - Energy level diagrams of extrinsic semiconductors: (a) n-type; (b) p-type

Introduction of donor, or acceptor, energy levels in the electronic structure of a material can often induce that substance to demonstrate semiconducting behaviour. Additionally, this may occur in materials in which the native band-gap is too large for any significant intrinsic semiconduction. The impurities may either be foreign atoms that have been included in the matrix during

manufacture or, in a compound semiconductor, an above stoichiometry excess of one or more constituent atoms.

4.4 FERMI-DIRAC STATISTICS AND THE FERMI LEVEL

4.4.1 The Fermi level

It has already been stated that electrons in semiconductors must obey the Pauli exclusion principle, so only two electrons may occupy a given energy state. Thus, in a semiconductor at absolute zero (0 K), electrons occupy all energy levels from the ground-state (zero energy) to an upper value, which is commonly termed the Fermi energy or level. Above the Fermi level (ε_F) none of the energy states are occupied.

It is possible to define an occupation probability, n_j, which gives the mean number of particles in state j. For the absolute zero condition discussed previously, the Fermi-Dirac distribution is such that $n_j = 1$ for $\varepsilon_j < \varepsilon_F$ and $n_j = 0$ for $\varepsilon_j > \varepsilon_F$, so that all energy levels below ε_F are filled. This situation is represented diagrammatically in Figure 4.7.a.

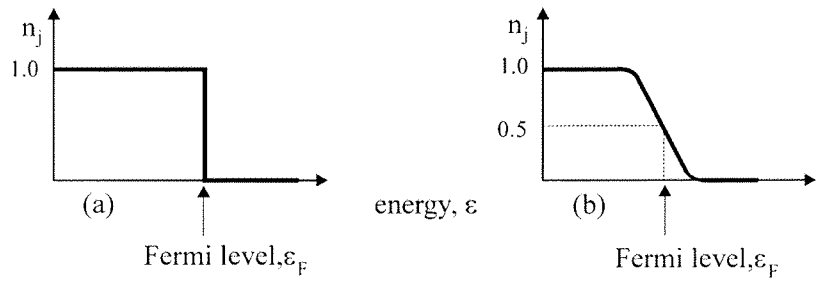

Figure 4.7 - Energy distribution of electrons: (a) at 0 K; (b) at T > 0 K

Above absolute zero (T > 0 K), the electrons at the top of the energy distribution - those that were near the Fermi level - can be promoted to higher, previously unoccupied energy levels. The development of the equation describing the dependence of n_j on ε_j is beyond the scope of this text, but is quoted for completeness:

$$n_j = \left(\exp\left\{ \frac{\varepsilon_j - \varepsilon_F}{kT} \right\} + 1 \right)^{-1} \tag{4.9}$$

With increasing temperature, the high-energy end of the Fermi-Dirac distribution loses the sharp cut-off that it had at 0 K and n_j drops from 1 to 0 over a finite energy range (see Figure 4.7.b). It is apparent from Equation (4.9) that at any temperature, when $\varepsilon_j = \varepsilon_F$, $n_j = ½$ - there is an equal probability that the energy level ε_F may or may not be filled by an electron. This is the

importance of the concept of the Fermi level, because it allows the definition of the most likely position of the top of the electron energy distribution - it acts as a reference level.

4.4.2 Fermi level in extrinsic semiconductors

In a purely intrinsic semiconductor, the number of electrons in the conduction band is equal to the number of holes in the valence band. In this situation, the Fermi level lies midway between the top of the valence band and the bottom of the conduction band. The position of the Fermi level in an intrinsic semiconductor is invariant with temperature, since electrons promoted to the conduction band will always leave holes in the valence band.

The situation is only slightly different for both n- and p-type extrinsic semiconductors. At absolute zero in n-type materials, when none of the donor atoms have lost electrons to the conduction band, the Fermi energy lies midway between the donor energy level and the bottom of the conduction band. As the temperature is increased, the number of electrons thermally excited into the conduction band increases, and the Fermi level falls to lower energies. However, the Fermi level does not fall indefinitely. The presence of the valence band places a limit on the lowest energy to which the Fermi level may fall. This energy is midway between the conduction and valence bands, just like an intrinsic semiconductor.

The arguments for p-type materials are very similar. In this case, at 0 K the Fermi level begins in a position halfway between the top of the valence band and the acceptor level. As the temperature increases, more and more electrons are promoted into the acceptor level. Consequently, the Fermi level rises to higher energies. Again, the presence of another band, in this case the conduction band, prevents the Fermi energy from increasing indefinitely and the same limit applies as to n-type materials, i.e. mid band-gap.

4.5 SEMICONDUCTOR CONDUCTIVITY AND TEMPERATURE

From the previous discussions, it should be clear that the conductivities of both intrinsic and extrinsic semiconductors increase with increasing temperature. This is in contrast to the behaviour of metals, where the conductivity falls with increasing temperature. The reason for the conductivity increase demonstrated by semiconductors is the creation of more and more charge carriers, be they electrons in the conduction band, holes in the valence band, or a combination of both.

For extrinsic semiconductors, there are three temperature-induced regimes of charge carrier density change (*Grieg, 1969*), which are shown in Figure 4.8. At absolute zero, none of the

donors in an n-type material are ionized. At slightly higher temperatures, some of the donor level electrons are promoted into the conduction band, so the carrier concentration (represented by n in Figure 4.8) in the sample increases. As the temperature is raised still further, the Fermi level falls, so more and more of the donors become ionized. Thus, the charge carrier concentration increases and, hence, so does the conductivity of the material. Eventually, however, all of the donors become ionized, and no more electrons can originate from this source. Above this temperature, the number of charge carriers remains constant and equal to the number of donor atoms, assuming single ionization of the donors. In this regime, the conductivity of the sample may alter - even though the charge carrier concentration is fixed - due to thermal-induced scattering of the charge carriers.

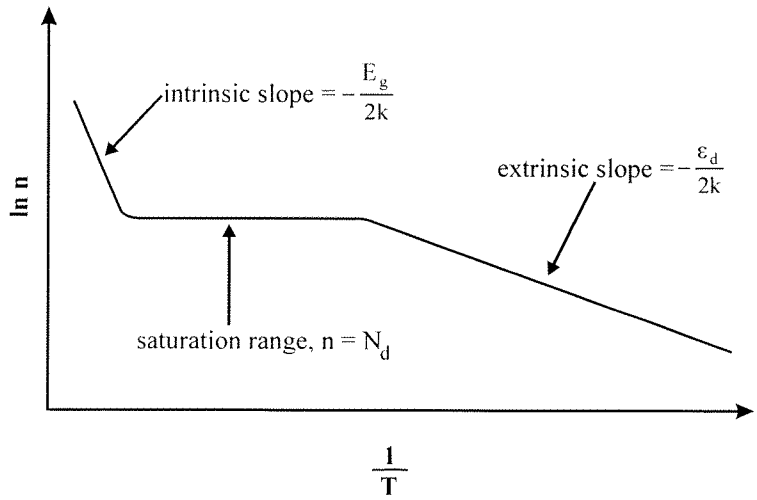

Figure 4.8 - Variation of carrier density, n, with temperature, T (after *Smith, 1964*)

At even higher temperatures, the number of electrons able to make the transition from the valence to conduction band becomes more and more significant; the behaviour of the semiconductor is becoming intrinsic in nature. Ultimately, at high enough temperatures, the semiconductor can be treated as purely intrinsic. At this point the Fermi level of the material will have reached its lower limit, midway between the two bands.

For an n-type semiconductor, the equation describing the number of charge carriers in the conduction band is given by Equation (4.10) (*Smith, 1964*):

$$n_e = \frac{1}{\sqrt{2}}(N_d N_c)^{\frac{1}{2}} \exp\left[-\frac{\varepsilon_d}{2kT}\right] \qquad (4.10)$$

Where:

n_e = extrinsic charge carrier concentration (m^{-3})

N_d = density of donor atoms (m^{-3})

N_c = effective density of states (m^{-3})

ε_d = donor level below conduction band (eV)

k = Boltzmann's constant ($J.K^{-1}$)

T = absolute temperature (K)

Equation (4.10) assumes that there are few acceptor levels in the n-type material.

In comparison, the charge carrier concentration of an intrinsic semiconductor varies according to Equation (4.11):

$$n_i = N_c \exp\left[-\frac{E_g}{2kT}\right] \tag{4.11}$$

Where:

n_i = intrinsic charge carrier concentration (m^{-3})

E_g = band gap of material (eV)

and the other symbols have their previously defined meanings.

Ignoring the contribution of holes to the conductivity of the extrinsic material - the absence of acceptors has been assumed and the band gap is large - the electron concentration, n_e, can be related to sample conductivity (σ), thus:

$$\sigma = n_e e\mu \tag{4.12}$$

Using Equations (4.10), (4.12) and $g = \frac{\sigma A}{l}$, it is possible to determine the variation of sample conductance (g) with temperature:

$$g = \frac{e\mu A}{l\sqrt{2}}(N_d N_c)^{\frac{1}{2}} \exp\left[-\frac{\varepsilon_d}{2kT}\right] \tag{4.13}$$

Where:

g = sample conductance (mhos)

= 1/sample resistance

e = electronic charge (C)

μ = charge carrier mobility ($m.s^{-1}.[V.m]^{-1}$)

A = cross-sectional area of sample (m^2)

l = distance between measurement electrodes (m)

Equation (4.13) assumes that the mobility (μ) of the electrons does not vary significantly with temperature. This assumption must be evaluated for each different material over the range of temperatures examined.

Lastly, by taking natural logarithms of both sides of Equation (4.13), it becomes apparent that the gradient of a ln(g) vs 1/T plot will be a straight line, the gradient of which will allow calculation of the donor level (ε_d) of the material.

$$\ln(g) = \ln\left\{\frac{e\mu A}{l\sqrt{2}}(N_d N_c)^{\frac{1}{2}}\right\} - \left(\frac{\varepsilon_d}{2k}\right)\frac{1}{T} \tag{4.14}$$

4.6 SEMICONDUCTOR SURFACES

All of the previous discussions have implicitly assumed that the semiconducting material is infinite in extent. However, real solids are not infinite, but are bounded by surfaces. Unsurprisingly, the break in symmetry associated with a surface influences the electronic structure of the underlying solid. Since semiconductor sensors actually utilize one or more properties of semiconductor surfaces in their operation, it will be instructive to examine the physics of these surfaces.

4.6.1 Surfaces - a break in symmetry

The band theory of semiconductors resulted from the solution of Schrödinger's equation for electrons within the periodic potential of an infinite solid. The solutions of the Schrödinger equation were discovered to be standing waves, which may only exist in this environment of symmetric, repeating potentials. However, the atoms at the surface of a real solid have fewer nearest-neighbours than the atoms within the matrix. Hence, surface atoms form an asymmetric pattern of potentials. Solution of Schrödinger's equation within this asymmetric environment leads to travelling wave solutions that may not penetrate into the bulk of the solid (*Prutton, 1987*). The travelling waves give rise to electron energy states that would not otherwise have existed in the solid. These energy states are called surface state wave functions, or surface states for short (*Somorjai, 1972*). A typical surface density of surface states is somewhat less than the number of surface atoms, around 10^{13} cm^{-2} (*Morrison, 1955*).

The energy levels of the surface states fall within the forbidden gap (band-gap) of the semiconductor (*Zangwill, 1988*). In fact, the surface states form their own band of allowed energy levels centred not far from the mid band-gap energy, which is below the Fermi level for n-type materials. Therefore, surface states capture electrons from the conduction band and trap them at the surface (*Somorjai, 1972; Prutton, 1987*). The electrons captured by the surface states are rendered immobile, so they can no longer contribute to the conductivity of the semiconductor. Overall then, the action of surface states is to reduce the conductivity of the semiconductor.

Impurity atoms, and particles adsorbed on the surface, reduce the surface state density from its usual level (*Somorjai, 1972*). On the other hand, features such as dislocations and extra native atoms in the near surface layers may actually increase the surface state concentration, by increasing the asymmetry and number of surface atoms (*Prutton, 1987*). In fact, any disturbance adding to the asymmetric potential at the surface is likely to give rise to surface states.

The importance of electron trapping by surface states depends very much upon the proportion of charge carriers removed from the conduction band of the semiconductor. The simple analysis below shows that the geometry of the semiconductor sample is an important factor in the extent of charge carrier depletion.

If the volume of an extrinsic semiconductor (with donor density N_d) is taken to be V, then the total number of conduction electrons available within it is given by N_dV. In contrast, if the density of surface states is N_a, and the surface area of the sample is A, the maximum number of electrons that can be trapped at the surface is N_aA. Hence, the proportion of charge carriers caught by surface states may be calculated as $\frac{N_aA}{N_dV}$ (*Morrison, 1955*). However, if the crystal is homogenous and isotropic, it may be assumed that V = Ad, where d is the thickness of the crystal. So, for fixed N_a and N_d, it is clear that the fraction of charge carriers trapped is proportional to $\frac{1}{d}$. Hence, the thinner the crystal, the more significant are the effects of electron removal from its surface.

For example, taking a typical extrinsic donor density of 10^{17} cm^{-3}, and the previously quoted trap density of 10^{13} cm^{-2}, it can be calculated that ~ 10 % of the electrons are localized by surface states when the semiconductor thickness is ~ 10 μm. Clearly, for crystals of linear dimension greater than this, the action of surface electron capture becomes difficult to detect. For thinner crystals the proportion of charge carriers removed is increased, enhancing the effect.

4.6.2 Band-bending and surface charge

When conduction electrons are captured by surface states, a 'layer' of negative charge forms on the surface of the semiconductor. As a result, a positively charged space charge layer (SCL) develops in the near surface regions of the material due to the presence of immobile, ionized donors. It is from these donors that the conduction band electrons originated (see Section 4.3.4). These two oppositely charged layers form a dipole or 'double layer' in which the ionized donors are compensated by the negative surface charge.

Thus, whilst the crystal remains charge neutral overall, an electric field within the SCL creates a voltage drop between the crystal interior and surface (*Prutton, 1987*). It follows that the potential energy of an electron must **increase** as it **approaches** the surface. Frequently, the region from which the mobile electrons have been removed is referred to as an 'exhaustion' or 'depletion' layer.

It is possible to examine the effect of the space charge upon the surface electronic band structure. Poisson's equation may be used within the SCL, where it takes the form (*Somorjai, 1972*):

$$\frac{d^2V}{dx^2} = -\frac{eN_d^+}{\varepsilon\varepsilon_0} \tag{4.15}$$

In Equation (4.15), ε is the dielectric constant of the material, ε_0 is the permittivity of free space (a constant), N_d^+ is the concentration of *ionized* donors, and the other symbols have their previously defined meanings.

Integrating (4.15) twice with respect to x yields (4.16)

$$V(x) = -\frac{eN_d^+}{2\varepsilon\varepsilon_0}(x - x_0)^2 \tag{4.16}$$

where the bulk potential at distance $x = x_0$ from the surface is assumed to be zero. At the surface, $x = 0$, (4.16) simplifies to:

$$V_s = +\frac{e}{2\varepsilon\varepsilon_0}N_d^+x_0^2 \tag{4.17}$$

This equation shows that the height of the surface potential, V_s, is proportional to the number of ionized donors in the SCL.

Perhaps unsurprisingly, the surface potential affects the electronic band structure of the solid. In fact, at the surface of the material, the conduction and valence bands are increased to higher energies by an amount proportional to the surface potential, in agreement with the hypothesis of a surface voltage drop. Both bands decrease towards their normal, bulk values with a shape in accordance to Equation (4.17). This situation is known as band bending and results whenever, and however, the surface of a semiconductor becomes charged. The situation is shown diagrammatically in Figure 4.9.

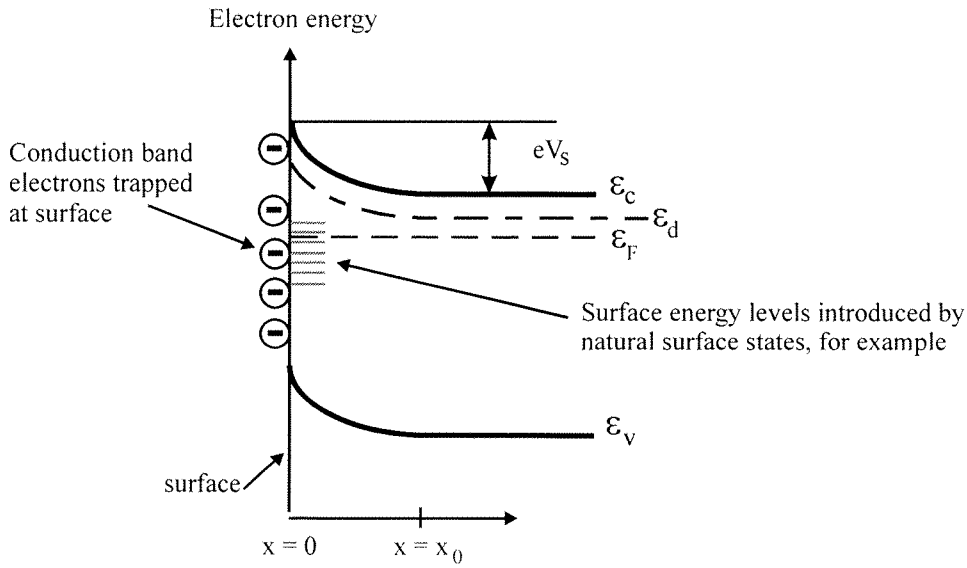

Figure 4.9 - Band bending of an n-type material due to surface charging

At the surface, the bending of the conduction band towards higher energies - away from the Fermi level - indicates that more energy is needed to promote an electron from the Fermi level to the conduction band, than it would in the bulk of the semiconductor (*Somorjai, 1972*). Thus, electrons are classically (that is energetically) forbidden from the regions of semiconductors affected by surface charging. In typical semiconductors, the penetration depth of the space charge layer is of the order 0.1 to 10 μm. The exact value depends upon the material dielectric constant, the number of charge carriers present and the surface charge density. Surface charging also increases the energy required for an electron to migrate from the bulk of a semiconductor to its surface, thereby restricting the number that can make this transition. This sort of limitation is referred to as a 'surface barrier', which in this case, is called a Schottky barrier.

It is possible for the surface of some semiconductors to become so highly charged that the resulting band curvature is sufficient for the top of the valence band to reach the Fermi level (*Cimino, 1963*). At this point, electrons can be removed directly from the valence band. Hence, some of the energy levels in the valence band become depleted of electrons and, thus, are only partially filled. Electron promotion within this band is then a possibility, and so the conductivity

of the semiconductor is increased by the presence of positively charged holes. In this case, the depletion layer is more correctly referred to as an '*inversion*' layer, because the electrical properties of the semiconductor surface swap from n-type to p-type or *vice versa*.

4.6.3 Restructuring

Many semiconductor surfaces undergo surface restructuring, even though they do not anneal well (*Zangwill, 1988*). Generally, surface restructuring or reconstruction occurs by atomic self re-arrangements and results in changes of surface atom position and symmetry. Energy considerations create the requirement that the final surface be of lower energy than that of the original, pre-restructured surface. Thus, the tendency is for surfaces to eliminate high-energy features like dangling (*unsaturated*) bonds, which are formed, for example, due to the reduced number of nearest neighbours or stacking faults. Reconstruction affects the electronic structure and behaviour of the semiconductor, and it may occur as a function of temperature or change in stoichiometry.

4.7 SUMMARY

This chapter has introduced the properties and equations that describe semiconductors. An understanding of these properties is vital if the operation of semiconductor sensors is to be clearly understood.

Examination of the properties of an electron in a potential well has shown that the energy levels that the electron may occupy are not continuous but, rather, discrete and quantized. Extension of the analysis to multi-potential systems demonstrated that the energy levels split into sub-levels in proportion to the number of potential wells present.

Thus, when atoms coalesce to form a solid, the energy levels of the atoms combine and split into bands, which fill according to the Pauli exclusion principle. Semiconductors - like insulators - have a forbidden gap in between a lower, completely filled valence band and an empty, upper conduction band. Semiconductor properties are governed by the effect that this gap has on the distribution of electrons. In the intrinsic semiconductor type, the band-gap is small enough so that at elevated temperatures electrons may be promoted into the conduction band from the valence band. The charge carriers in this type of semiconductor are both electrons and positively charged holes.

Extrinsic semiconductors, on the other hand, are influenced by the presence of impurities in the material. The impurities may either introduce donor levels just below the bottom of the

conduction band, or may create acceptor levels just above the valence band. Donor levels give rise to n-type material, whilst acceptor levels generate p-type. In both cases, the equations describing the behaviour of such materials are not concerned with the band gap energy, rather with the position of the donor or acceptor levels.

The concept of the Fermi level was introduced and was shown to represent the energy level at which the occupation probability is 0.5. Thus, the Fermi level is a way of defining the thermodynamic position of the top of electron energy distribution.

The variation of semiconductor conductivity with temperature was analyzed by the development of equations that described the change of electron density in the conduction band of an n-type material. It was postulated that the donor levels within such a material could be measured by examining the shape and form of the sample's conductance vs. temperature plot.

Finally, the effects of the presence of the semiconductor surface upon its electrical properties were investigated. It was shown that there exist special solutions to Schrödinger's equation at the surface, which are called surface states, and are capable of capturing electrons from the conduction band. As a result, the surface of the semiconductor becomes charged and, in a narrow region, forces the energy bands of the semiconductor to higher levels. This increase makes it difficult for electrons to move from the bulk of the solid to the surface, and in extreme cases, may even result in an apparent change of 'type' of the semiconductor surface.

Chapter 5 describes the operation of semiconductor gas sensors, and develops a model describing their operation.

CHAPTER 5

SEMICONDUCTOR GAS SENSORS

The object of this chapter is to elucidate the operation of semiconductor sensors. The descriptions below use the example of n-type semiconductor sensors for the measurement of AO fluxes, but the generic features and conclusions can be readily applied to other materials and species. A brief review of the historical development of these devices is used to highlight the differences between the various classifications of sensor. One form of sensor is found to be of special interest to the work in this thesis - the surface conductivity type. Since the responses of these sensors depend upon the interaction of gases with the semiconductor surface, the mechanisms associated with solid surface gas adsorption are described and modelled in detail. Using the results from the previous sections, a method of making quantitative AO flux measurements is proposed by the development of a ballistic-mode model. Finally, a review of the literature concerning previous employment of semiconductor AO sensors is presented to highlight the novelty of the current work.

5.1 HISTORICAL DEVELOPMENT OF SEMICONDUCTOR GAS SENSORS

In the early 1950s, Brattain and Bardeen discovered that the surface electrical properties of semiconductor materials were influenced by the nature and type of the surrounding atmosphere (*Brattain and Bardeen, 1953*). It soon became clear that the electrical properties of semiconductors were influenced by the atoms or molecules adsorbed onto their surfaces. From this realization, it was a small step from the application of semiconductors to the field of gas detection.

Two types of semiconductor gas sensor are in common usage today. The first, bulk conductivity devices, rely on the equilibration of volume stoichiometry with the ambient surroundings. Surface conductivity devices - the second type - use directly the influence of adsorbed species, or more correctly, chemisorbed species on the near-surface region of the semiconductor. Heiland, Morrison and Moseley have written in depth reviews of the operation of semiconductor sensors (*Heiland, 1982; Morrison, 1982; Moseley and Tofield, 1985; Moseley, 1991*).

Bulk-conductivity devices, a common example of which is the oxygen sensor used in engine management systems, are generally used at high (950 - 1100 K) temperatures. The high temperature is necessary for sensitive and rapid operation: the ambient atmosphere must be able to diffuse easily and readily into the semiconducting material. In general, the resistance of the sensor is used as the measurand of the gas partial pressure with which it is in equilibrium. A

typical bulk conductivity sensor response might be described by an equation of the form (*Moseley and Tofield, 1985*):

$$R = R_0 \exp\left(\frac{Q}{kT}\right)(p_p)^{\frac{1}{u}} \tag{5.1}$$

Where:

R = resistance of the sensor (Ω)

R_0 = base resistance (Ω)

Q = activation energy (eV)

k = Boltzmann's constant ($J.K^{-1}$)

T = temperature (K)

p_p = partial pressure of ambient species ($N.m^{-2}$)

u = an integer (value is equilibrium reaction dependant)

In general, inorganic materials, such as metal oxides, are used in this application because they remain stable at the required operational temperatures.

Changes of bulk stoichiometry do not (normally) occur in surface conductivity sensors. Instead, chemisorption reactions at the surface of the semiconductor influence its electrical properties by altering the charge carrier concentration and the material work function. Again, the resistance of the semiconductor sample can be used as the measurand of ambient gas concentration. This type of gas sensor is operated at lower temperatures (around 200 °C) than the bulk-conductivity type. Hence, heater power requirements are reduced. It is found that this temperature is sufficient to allow the number of chemisorbed particles to be in equilibrium with their concentration in the surrounding atmosphere, whilst additionally preventing the confusing influence of water vapour. Metal oxides have also been employed in these sensors (*Moseley and Tofield, 1985*), yet lower temperatures of operation allows the application of organic semiconducting materials (*Cranny et al., 1991*).

The sensors investigated in this study conform to the surface-conductivity type because their reduced power consumption is advantageous for operation in a space-based experiment (Section 3.4). Yet further power savings can be made because, in the absence of water in the space environment, the temperature required for operation in the current application can be reduced below normal values. To comprehend the *modus operandi* of these devices, an explanation of which is given in a subsequent section, it is essential to understand the way atoms and molecules interact with solid surfaces. It is therefore prudent to examine the physics of gas adsorption.

5.2 GAS ADSORPTION ON SOLID SURFACES

5.2.1 Physical description

A number of different outcomes may occur when a gaseous atom (or molecule) impacts upon a solid surface. Firstly, the atom may be reflected elastically, that is with no loss of energy. There are two ways in which this eventuality may occur - the particle may be specularly reflected, or its momentum may be redistributed in a diffraction-like mechanism. More usually, however, the particle will lose a fraction of its energy to the solid surface by exciting the atoms therein electronically or vibrationally. In this case, it departs with a lower energy than with which it impacted - an inelastic reflection.

If sufficient energy is lost to the solid in an in elastic collision, the atom may become temporarily bound - or *adsorbed* - upon the solid surface in a potential well. For a capture like this to occur, the amount of energy given up by they atom or particle must be at least equivalent to its component of kinetic energy perpendicular to the surface. Usually, the energy is dissipated by the excitation of lattice phonons in the solid adsorbent. Once caught in a potential well, energy considerations show that the atom or particle must thermally equilibrate with the solid, after which it oscillates at the bottom of the well.

The particle is then said to be *physisorbed*, a concatenation of the words physical adsorption, which is one of two possible adsorption mechanisms. Eventually though, through thermal excitation, the particle may gain sufficient energy to overcome the forces holding it to the surface, and it may then *desorb*. Desorption requires that the atom 'collect' an energy at least equal to the depth of the potential well in which it is trapped.

Physisorption is the weakest form of adsorption onto a solid. The key characteristic of this form is the deficiency of a proper chemical bond between the adsorbate and adsorbent. Instead, the force binding the particles to the surface is the weak - yet long range - van der Waals attraction, which is associated with fluctuating dipole moments of the adatom and its nearest neighbours in the adsorbent. The weak nature of this force means that the potential wells that 'capture' the atoms or particles are shallow. Typically, the binding energies of physisorbed species are less than 0.25 eV. However, because the van der Waals forces may extend many atomic dimensions, at low temperatures it is possible for adatoms to form many adsorbed layers, one on top of the next.

After some time in the physisorbed state, a particle may undergo an electronic or vibrational transition enabling it to overcome a small energy barrier, after which it resides in a much deeper potential well. The particle has been *chemisorbed* - a combination of the words chemical

adsorption. Thus, frequently, the physisorbed state acts as a precursor to the chemisorption process.

Langmuir was the first to examine and model the process of chemisorption on solid surfaces (*Langmuir, 1918*). He postulated that there could exist strong, short-range forces between adsorbed particles and the solid surface. In fact, the short-range forces are associated with surface chemical bonds. So, unlike physisorption, chemisorption involves the complete or partial transfer of charge from adsorbent to adsorbate. Thus, the differences between physi- and chemisorption are apparent; the strength of the forces holding the adatoms to the surface are far stronger in the latter than in the former. The short range of the chemical bonds associated with chemisorption places a limit on the number of adatoms that can be accommodated by this mechanism. As a result, it is frequently found that the extent of the adsorbed layers will be sub-monolayer.

Due to the energy release allied with charge transfer, the potential wells associated with chemisorption are much deeper than with physisorption. It follows that the energies of chemisorption are also much larger, commonly ranging from a few tenths of one electron volt to several electron volts, and the probability of desorption is thus much reduced. The rate of desorption is dependent on the strength of the forces holding the atoms to the surface and the temperature of that surface. If the forces are strong and the temperature low, the rate of re-emission is low and the surface becomes covered with a large number of particles. However, if the rate of desorption is large - small forces and high temperature - then the quantity of adsorbed material is small.

5.2.2 Model formulation

It is possible to formulate, from first principles, a model describing the dynamics of gas adsorption on a solid surface. The model described herein has been adapted for use in this thesis from the original works of Langmuir and Haberrecker *et al.* (*Langmuir, 1918; Haberrecker et al., 1967*), although the interpretation of the results from the model is different in this thesis.

Consider a general crystal that consists of planes of atoms in some orderly arrangement. The surfaces of the crystal represent a break in this pattern but there is a finite number of surface atoms in a given area. Thus, it is a reasonable suggestion that there will be a finite number of sites on the surface capable of retaining an adsorbed atom. If C is the density of crystal atoms at the surface, and a_∞ is the maximum density of adsorbed atoms that may ever reside on the crystal, then $\frac{a_\infty}{C}$ represents the fraction of surface sites that may be occupied by adatoms. Often,

$a_\infty << C$, so that the maximum number of adsorbed atoms is less than the number of surface crystal atoms.

If a(t) represents the density of adatoms on the crystal surface at a given time, t, then $\frac{a(t)}{C}$ is the fractional surface coverage of adsorbed atoms on the crystal at this time. Note that $a(t) \leq a_\infty$. Thus,

$$\left(\frac{a_\infty}{C} - \frac{a(t)}{C}\right) \tag{5.2}$$

is the fraction of unoccupied surface sites able to accept newly adsorbed atoms at time t.

Some atoms colliding with the surface will adsorb. A proportion, however, will reflect elastically, whilst others will reflect inelastically (see previous section). Let γ be the scattering coefficient, that is the fraction of impacting atoms that reflect. Then, if the flux of atoms is F, the number of atoms with energy suitable for adsorption is given by $(1-\gamma)F$. Hence, at time t, the rate of adsorption on the surface is determined by:

$$\left(\frac{a_\infty}{C} - \frac{a(t)}{C}\right)(1-\gamma)F \tag{5.3}$$

It is now necessary to describe the rate of atom re-emission from the surface. Langmuir supposed that there was a 'lifetime' associated with atom residency on the surface (*Langmuir, 1918*). If this lifetime is τ seconds, then the rate of atom re-emission is given by Equation (5.4).

$$\frac{a(t)}{\tau} \tag{5.4}$$

At equilibrium, the rate of atom adsorption must equal the rate of atom desorption and so the surface density of adatoms, a function of flux, may be found by equating Equations (5.3) and (5.4) and re-arranging for a(t). Surface-conductivity sensors frequently use elevated temperatures to ensure that this equilibrium is reached rapidly, so that the response time of the sensors is reduced. However, it is also possible to use this type of sensor at lower temperatures. In this case, the dynamic change of adatom density is used to infer the impinging flux of atoms, rather than the equilibrium density. The above model can also be used to describe the rate of atom adsorption.

In the non-equilibrium situation, the rate of change of surface atom density may be found by differencing Equations (5.3) and (5.4); the result of which is shown in Equation (5.5).

$$\frac{da(t)}{dt} = \left(\frac{a_\infty - a(t)}{C}\right)(1-\gamma)F - \frac{a(t)}{\tau} \tag{5.5}$$

Re-arranging (5.5) and integrating gives:

$$\int_0^a \left\{\frac{C\tau}{[a_\infty(1-\gamma)F\tau] - a(t)[(1-\gamma)F\tau + C]}\right\} da = \int_0^t dt \tag{5.6}$$

It is worth making a comment about the limits of the integration and their meaning. The zero-time point is defined as the start of adsorption on a clean surface. In this definition, 'clean' is taken to mean that there are no previously adsorbed atoms on the surface - all the allowed sites are free of atoms, i.e. a(0) = 0. In addition, during the time period 't' seconds, the quantities represented by F, τ, γ, C and a_∞ must remain constant if Equation 5.6 is to be valid.

The left-hand side of (5.6) can be evaluated by using the following standard form,

$$\int \frac{A}{B - Dx} dx = -\frac{A}{D}\ln(B - Dx) \tag{5.7}$$

which results in:

$$t = \frac{C\tau}{(1-\gamma)F\tau + C} \ln\left[\frac{a_\infty}{a_\infty - \left(1 + \frac{C}{(1-\gamma)F}\right)a(t)}\right] \tag{5.8}$$

Re-arranging Equation (5.8) for the surface atom concentration, a(t), gives:

$$a(t) = \left(\frac{a_\infty}{1 + \frac{C}{(1-\gamma)F\tau}}\right)\left[1 - \exp\left\{-t\left(\frac{(1-\gamma)F}{C}\right)\left(1 + \frac{C}{(1-\gamma)F\tau}\right)\right\}\right] \tag{5.9}$$

Where:

a(t) = adsorbed atom density at time t (atoms.cm^{-2})

a_∞ = maximum possible surface atom density (atoms.cm^{-2})

C = density of crystal atoms at surface (atoms.cm^{-2})

γ = scattering coefficient (-)

F = flux of impinging atoms (atoms.cm^{-2}.s^{-1})

τ = mean atom residency time (s)

t = time (s)

Equation (5.9) describes the time dependent adsorption of a gas onto a solid surface. It is clear that differentiating a(t) with respect to time (t) and evaluating the result at t = 0, gives:

$$\left.\frac{da}{dt}\right|_{t=0} = \left(\frac{a_\infty}{C}\right)(1-\gamma)F \tag{5.10}$$

Thus, the initial rate of adsorption of material on a clean, totally unoccupied surface is directly proportional to the intensity of the particle flux - an important result that will be used later. If the flux of particles continues to bombard the surface, Equation (5.9) shows that the rate of adsorption falls exponentially, until adsorption becomes balanced by desorption and the adatom density remains stationary. The next sub-section discusses this condition.

5.2.3 Ultimate density of adsorbed atoms

Several, general conclusions may be drawn from Equation (5.9) with regard to the ultimate number of adsorbed atoms. Firstly, when t is very large, the rates of adsorption and desorption will be balanced in the equilibrium state described earlier. If the number of adsorbed atoms at equilibrium is defined to be a_s, then it is clear that Equation (5.11) results from (5.9) by allowing $t \rightarrow \infty$.

$$a_s = \frac{a_\infty}{\left(1+\frac{C}{(1-\gamma)F\tau}\right)} \tag{5.11}$$

From this equation important conclusions may be drawn. Equation (5.11) may be simplified using the binomial expansion and neglecting terms of order 2 and higher, to give Equation (5.12).

$$a_s = a_\infty\left(1-\frac{C}{(1-\gamma)F\tau}\right) \tag{5.12}$$

Firstly, when $(1-\gamma)F\tau >> C$, which is the condition of validity of the binomial expansion of (5.11), it can be seen from Equation (5.12) that $a_s \rightarrow a_\infty$. In other words, at very high flux

intensities, the surface becomes saturated to its maximum value, independent of small changes in the flux level. In the converse case, when $C >> (1 - \gamma)F\tau$, Equation (5.12) is no longer valid, but it is possible to determine that a_s may be approximated by $\frac{a_\infty(1-\gamma)F\tau}{C}$. This result shows that at small flux intensities, the adsorbed atom saturation density is dependent on the magnitude of the flux. A sketch of Equation (5.11) demonstrates these last two conclusions, see Figure 5.1.

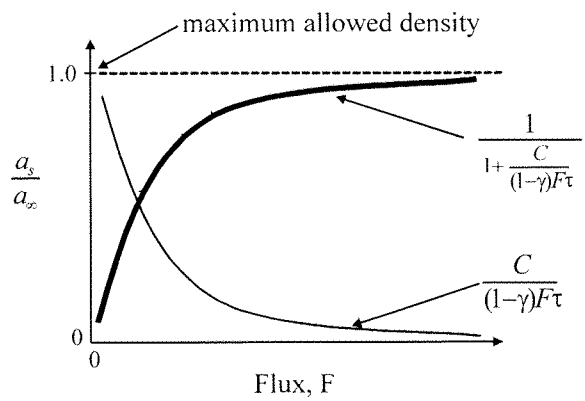

Figure 5.1 - A sketch of Equation (5.11)

At low flux levels, the saturation density is strongly dependent on the flux, and is smaller than the maximum that is allowed ($a_s < a_\infty$). At higher flux levels, the ultimate surface atom density becomes less dependent on the flux level, and tends towards the maximum density ($a_s = a_\infty$).

5.2.4 Desorption of adsorbed material

The previous section examined the saturation density of atoms on the solid surface. One important question, however, has not yet been answered by the model - what happens if the flux of impinging atoms should be ceased? Equation (5.5) shows that if the flux is reduced to a small value or zero ($F \rightarrow 0$), then the rate of change of surface atom density is given by:

$$\frac{da(t)}{dt} = -\frac{a(t)}{\tau} \tag{5.13}$$

Thus, the number of surface atoms falls at a rate proportional to the remaining number of atoms. The rate of desorption is also dependent on the residency time, τ. If τ should be large, the rate of desorption is slow. Large residency time occurs, as previously stated, in situations with large binding forces holding the atoms to the surface and/or when the temperature of the surface is low. Conversely, should the residency time be short, the rate of desorption will be high. This situation might occur, for example, when the forces holding the atoms to the surface are weak, or the temperature high.

5.3 OPERATIONAL PRINCIPLE OF SURFACE CONDUCTIVITY DEVICES

It is the intent of this section to elucidate the operation of surface-conductivity semiconductor sensors. The description below uses the example of n-type semiconductor sensors for the measurement of AO fluxes, but the generic features and conclusions can be readily applied to other species and materials. It will be shown that the action of oxidizing species - such as AO - on n-type semiconductors is very similar, if not analogous, to the behaviour of the surface states discussed in Sections 4.6.1 and 4.6.2.

5.3.1 Adsorption of atomic oxygen upon semiconductors

As described previously in this chapter, oxygen atoms impinging upon a semiconductor surface initially become physisorbed. Subsequently, due to the close proximity of the adatom and the surface atoms, the wave functions of the physisorbed oxygen atoms combine with those of the semiconducting substrate. The result of this mixing is that the physisorbed oxygen atoms contribute allowed energy levels within the forbidden gap of the material, around the Fermi level (*Sukharev and Myasnikov, 1984*). For example, it is reported in the literature that oxygen chemisorbed upon zinc oxide contributes an energy level 0.72 eV below the bottom of the conduction band (*Hartnagel et al., 1995*). So, the action of adsorbed oxygen atoms is akin to that of the natural surface states discussed in sub-sections 4.6.1 and 4.6.2. The energy levels depicted at the surface of the semiconductor in Figure 4.9, page 57, can thus arise from surface states or adsorbed material.

Energetically then, it is unsurprising that electrons from the conduction band 'fall' into these new, lower energy levels. In other words, the adsorbed oxygen atoms capture electrons and form charge centres on the surface of the material. Charge transfer to the oxygen atoms results in the chemisorption of the previously physisorbed adatoms. In this process, the oxygen adatoms are converted to oxygen ions and the bonds holding the adsorbed material to the semiconductor become ionic in nature. Hence, the likelihood of oxygen desorption is much reduced due to the high strength of these chemical bonds.

It is apparent that the chemisorption of AO denudes electrons from the conduction band of the semiconductor, and forms charge centres on its surface. In this manner, the adsorbed AO is behaving as the surface states of Chapter 4. As before, there are two implications of these phenomena. Firstly, the conductivity of the semiconductor sample is decreased by an amount proportional to the reduction of charge carrier density. Secondly, the negative charge at the surface develops a positive SCL, due to the ionized and immobile donors in the surface region of the semiconductor (*Heiland, 1982*). Band bending occurs as a result of the space charge (see Section 4.6.2) creating a depletion layer, from which conduction band electrons are forbidden. It

was stated in Chapter 4 that the typical thicknesses of this forbidden region is on the order 0.1 - 10 μm, the exact extent depends upon the number of oxygen ions as well as the properties of the semiconductor. Clearly, only a very narrow zone of the semiconductor is affected by surface atom adsorption.

5.3.2 Single crystal sensors

Single crystals of semiconductors can be used as gas, atom or free radical sensors and, in experimental studies, are generally preferred to other forms because of the simple nature of their surfaces. The semiconductor sample is provided with electrical contacts and, usually, some way with which to support it. Once exposed to the environment to be measured, the surface of the single crystal becomes covered with adsorbed atoms so that the electronic structure of the semiconductor is influenced as described previously. The magnitude of the conductivity decrease is proportional to the number of oxygen ions (in the case of AO) upon the surface of the crystal.

The thickness of the depletion layer formed during adsorption is often far smaller, possibly by several orders of magnitude, than the thickness of the single crystal. For example, in the work conducted by Gabriel (*Gabriel, 1997*), the crystals were 1 mm thick, whereas the maximum SCL thickness is likely to be 1 μm, 1000 times smaller. Given the thickness of the depletion layer, and its reduced conductance relative to the bulk, it is not surprising that the bulk material electrically shunts the surface. For this reason, the changes of conductivity occurring at the surface during adsorption may be difficult to detect with single crystal devices. This situation is schematically represented in Figure 5.2.a, in which the crosshatched area represents the depletion layer.

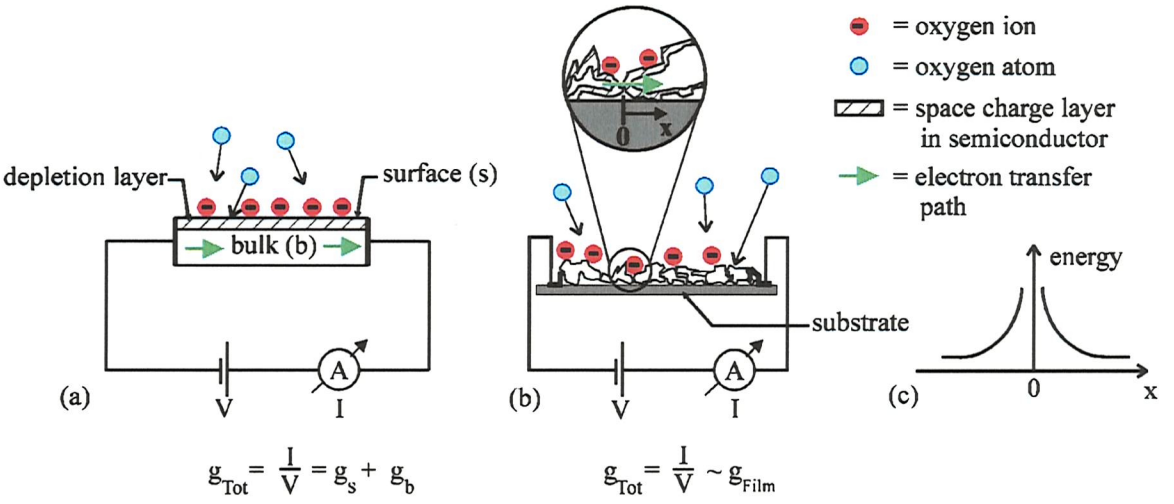

Figure 5.2 – Sensor comparison: (a) single crystal; (b) thin film; (c) potential barriers

Thus, in single crystal sensors, the major mechanism of conductivity decrease is the reduction of carrier concentration in the surface region affected by adsorption. The homogenous structure of

single crystals means that the depletion layer forms in a direction parallel to electron flow between the contacts, as shown. Therefore, the potential gradients associated with electron transfer across the SCL (depletion layer) are not significant in the operation of single crystal sensors. Employing thinner crystals increases the sensitivity of the sensor, by increasing the amount of material affected by adsorption (see Section 4.6.1), but the crystals become difficult to handle due to their fragility (*Morrison, 1982*). Such considerations would seem to preclude their use in simple space-rated experiments.

5.3.3 Thin film sensors

The behaviour of polycrystalline thin films should be contrasted to that of single crystals. Electron conduction paths in polycrystalline samples are tortuous; electrons move from crystallite to crystallite via grain boundaries, asperity contacts and narrow bridges (Figure 5.2.b). In thin films and sintered powders, such structural features have sizes similar to, or smaller than, the thickness of the depletion layers formed by the chemisorption of AO. So, large proportions - if not all - of the charge carriers in these small volumes are removed by depletion layer formation, a process enhanced by the typically large surface area to volume ratios of these films.

Thus, the differences between the single-crystal and thin film based sensors are readily apparent. In the former case, the number of charge carriers removed from the semiconductor is limited by the relative thicknesses of the depletion layer and crystal, whereas a thin film affected by AO adsorption is likely to suffer greater relative electron depletion, simply because of the small size of the structural features within the film (*Moseley, 1991*). This was demonstrated by physical argument in Section 4.6.1. Moreover, the potential barriers associated with the depletion layers limit electron motion from crystallite to crystallite, further reducing the conductivity of the sample. Figure 5.2.b demonstrates this effect graphically, whilst part (c) of the same figure shows the potential barrier experienced by an electron attempting to cross from one crystallite to another in the presence of two depletion layers.

However, similar to the single crystal devices, the magnitude of the conductivity change demonstrated by a thin film sensor is still proportional to the surface density of oxygen ions (*Sukharev and Myasnikov, 1987b*). Therefore, the conductivity change of the semiconductor allied to chemisorption can be used as the measurand in a flux-measuring device. The enhanced conductivity changes of thin film sensors are responsible for the increased sensitivity that they display over those fabricated from single crystals (*Morrison, 1982; Myasnikov and Gutman, 1986*). Presumably, this is the reason for their selection as today's gas sensors.

5.3.4 Advantages of semiconductor sensors

One of the benefits of semiconductor sensors is that the chemisorbed oxygen can be desorbed, and the original electronic properties of the semiconductor recovered, by 'regenerating' the sensor. This renewal is accomplished by heating the sample to modest temperatures (*Morrison, 1955; Yen, 1975*). During heating, the oxygen ions return the previously captured electrons to the semiconductor. In this way, the oxygen ions act like donor levels at the surface of the semiconductor, and the bonds holding them to the surface revert to the van der Waals type. The uncharged oxygen atoms then desorb once they have collected sufficient thermal energy from the surface.

Thus, the original - pre-exposure - conductivity of the semiconductor should be recovered and the surface sites liberated, allowing another measurement of AO flux in a subsequent exposure. Unlike many other commonly used AO sensors, such as C-QCMs and silver-film actinometers, semiconductor sensors are, in principle at least, reusable.

5.4 THE BALLISTIC MODEL OF SEMICONDUCTOR AO SENSORS

5.4.1 Model development

From the previous investigations and discussions, it is possible to develop a model to describe a mode of semiconductor sensor operation termed 'ballistic'. Section 5.2.2 showed that, when adsorption begins on a clean surface, the rate of change of surface atom density is related to the flux of impinging atoms by the following equation.

$$\left.\frac{da}{dt}\right|_{t=0} = \frac{a_\infty}{C}(1-\gamma)F \qquad (5.10)$$

Where:

F = flux of species, AO in present case (atoms.cm^{-2}.s^{-1})

γ = scattering coefficient (-)

a_∞ = maximum allowed surface density of adsorbed atoms (atoms.cm^{-2})

a = adsorbed atom density at time t (atoms.cm^{-2})

C = density of crystal atoms (atoms.cm^{-2})

Now, if $\frac{C}{a_\infty}$ is written as a^*, and (5.10) is re-arranged for F:

$$F = \frac{a^*}{(1-\gamma)} \left.\frac{da}{dt}\right|_{t=0} \tag{5.14}$$

However, as already shown, it is only those oxygen atoms upon the semiconductor surface that become ionized that affect the conductivity of the material. Thus, it is necessary to define and introduce an ionization coefficient, α, to represent the fraction of adatoms that become charged.

$$\alpha = \frac{[\text{ion}]}{[\text{adatom}]} = \frac{i}{a} \tag{5.15}$$

The square brackets in the above equation are used to represent the surface density of the enclosed species, and the ion density upon the surface is given the symbol i. So, (5.14) may be re-written:

$$F = \frac{a^*}{\alpha(1-\gamma)} \left.\frac{di}{dt}\right|_{t=0} \tag{5.16}$$

Since each ion localizes conduction band electrons, the charge carrier concentration within the semiconductor must reduce as a result of chemisorption. Upon ionization, each atom may capture κ electrons, hence, the rate of atom ionization is linked to the rate of surface electron density decrease by Equation (5.17). In this equation, the surface electron density - units electrons.cm^{-2} - is given the symbol n_s, whilst the minus sign demonstrates that as the ion density increases, the electron density decreases.

$$\kappa \frac{di}{dt} = -\frac{dn_s}{dt} \tag{5.17}$$

Substitution of (5.17) into (5.16) results in Equation (5.18), which is similar to that arrived at, via rather less rigorous routes, by a number of Russian authors (*Ryl'tsev et al., 1978; Livshits et al., 1981a; 1981b*) note, however, that the equations in these papers frequently appear to be dimensionally incorrect.

$$F = -\frac{a^*}{\kappa\alpha(1-\gamma)} \left.\frac{dn_s}{dt}\right|_{t=0} \tag{5.18}$$

Now, consider the semiconductor film to comprise a single, uniform crystal - such as may be formed, for example, by epitaxial deposition. Whilst this assumption is clearly a gross idealization of the films used in this study, which are expected to be polycrystalline (see Chapter 7), it is possible to justify its application in the development of this model.

During the initial stages of adsorption, when (5.18) is valid, the depletion layers will not be well developed. So, in these early stages, it is reasonable to neglect the effect of potential barriers upon the transfer of charge between the interior and the surfaces of the crystallites. Furthermore, charge carrier scattering associated with grain boundaries is independent of the effects of adsorption and, so, it is assumed to be a constant impediment to current flow. Therefore, these simplifications remove the need to model grain boundaries and potential barriers between the crystallites of a polycrystalline film. In this case, then, the single crystal film approximation does not appear to be so unfounded.

Previously, it has been shown that electrons are removed from a narrow depletion layer in the crystal, whilst the bulk of the material remains unaffected. If, however, the thickness of the film is assumed to be less than the ultimate extent of the depletion layer, it is clear that (in time) all of the film will be influenced by the adsorption of oxygen atoms. With this supposition, it is possible to suppose that the removal of charge carriers from the surface engenders a redistribution of the remaining conduction electrons over the whole film volume. In other words, if ΔN_s electrons are removed from the surface, the number remaining in the bulk changes by an equivalent amount, ΔN_b:

$$\Delta N_s = \Delta N_b = \Delta n_b V \tag{5.19}$$

$$\therefore \Delta N_s = \Delta n_b b l d \tag{5.20}$$

Where:

ΔN_s = number of electrons removed from semiconductor surface

ΔN_b = change in number of bulk carriers

Δn_b = change of bulk carrier density (electrons.cm^{-3})

$$= \frac{\Delta N_b}{V}$$

V = film volume (cm^3)

$= b l d$

b = breadth of film (cm)

d = thickness of film (cm)

l = distance between electrodes (cm)

Generally, the conductivity of a semiconductor is given by $ne\mu$ (Equation 4.12), where n is the charge carrier density, μ the mobility of the charge carriers and e the electronic charge. Therefore, if the change of film conductivity resulting from chemisorption is due only to a

change of charge carrier density, and not due to changes of carrier mobility (*Livshits et al., 1981a; 1981b*), then:

$$\Delta\sigma = \Delta n_b e\mu \tag{5.21}$$

Substituting for Δn_b from (5.20) gives

$$\Delta\sigma = \frac{\Delta N_s}{b/d} e\mu \tag{5.22}$$

If this change of conductivity occurred in time Δt then it is possible to write

$$\frac{\Delta\sigma}{\Delta t} = \frac{e\mu}{b/d}\frac{\Delta N_s}{\Delta t} \tag{5.23}$$

which, in the limit, $\Delta t \rightarrow 0$, reduces to

$$\frac{d\sigma}{dt} = \frac{e\mu}{b/d}\frac{dN_s}{dt} \tag{5.24}$$

$$\therefore \frac{dN_s}{dt} = \frac{b/d}{e\mu}\frac{d\sigma}{dt} \tag{5.25}$$

Now, recall that the flux of AO bombarding the surface is related to the rate of change of surface electron density, thus:

$$F = -\frac{a^*}{\kappa\alpha(1-\gamma)}\frac{dn_s}{dt}\bigg|_{t=0} \tag{5.18}$$

Since the surface electron density is related to the number of electrons at the surface (area = bl) by

$$n_s = \frac{N_s}{bl} \tag{5.26}$$

it is also possible to write

$$F = -\frac{a^*}{\kappa\alpha(1-\gamma)bl}\frac{dN_s}{dt}\bigg|_{t=0} \tag{5.27}$$

Hence, by substitution of Equation (5.25) into Equation (5.27), the following results (assuming of course that the dimensions of the film do not change during adsorption):

$$F = -\frac{a^*}{\kappa\alpha(1-\gamma)}\frac{d}{e\mu}\frac{d\sigma}{dt}\bigg|_{t=0} \tag{5.28}$$

The equation above needs to be recast into one that contains a parameter describing the sensor that can easily be measured, such as conductance. Conductivity (σ) is related to sample resistance (R) by the following two equations

$$\sigma = \frac{1}{\rho} \tag{5.29}$$

$$\rho = \frac{RA}{l} \tag{5.30}$$

Where:

ρ = sample resistivity (Ω.cm)

A = cross-sectional area (cm^2)

= bd

So,

$$\sigma = \frac{l}{Rbd} \tag{5.31}$$

Finally, by substitution of (5.31) in (5.28), and using the fact that conductance (g) is calculated from resistance by $g = \frac{1}{R}$, gives

$$F = -\frac{a^*}{\kappa\alpha(1-\gamma)}\frac{l}{be\mu}\frac{dg}{dt}\bigg|_{t=0} \tag{5.32}$$

Equation (5.32) shows that the flux of any oxidizing species chemisorbing on an n-type semiconductor sensor may be inferred directly from the rate of conductance change of that sensor, if recorded at a time close to the start of adsorption (*Sukharev and Myasnikov, 1987b; Osborne et al., 1999*). Additionally, the rate of change of sensor conductance is linearly dependent upon the flux of oxygen atoms. Henceforth, this equation will be referred to as the **ballistic equation** of sensor operation.

Note that, in the specific case of AO chemisorption, each oxygen atom captures but one electron from the solid, so $\kappa = 1$. Morrison postulates that singly charged AO, O^-, may capture another electron to form O^{2-} (*Morrison, 1955*). However, the same author admits that the experimental evidence for such a process is far from conclusive, and so no further treatment of this possibility will be made.

Clearly, the assumption that the film must be thinner than the maximum possible extent of the depletion layer places an upper limit upon the allowable thickness of the sensor film. It is also possible that this assumption is the reason for there being no apparent thickness term in Equation (5.32) as it might be expected there should be; this is because decreases of film thickness past the depletion maximum will have no beneficial effects on the magnitude of sensor response. The sensitivity increase associated with reduction of sensor thickness (Sub-sections 4.6.1 and 5.3.2) results from the ever-increasing proportion of the film (or single crystal) that is affected by adsorption. In other words, the ratio of depletion layer thickness to film thickness. If the entirety of the film is already affected by adsorption, there is no benefit in decreasing the film thickness any further.

5.4.2 Ballistic operation of a semiconductor sensor

The models and discussions presented to this juncture make it possible to outline the operation of an ideal, thin film semiconductor AO sensor. Figure 5.3 represents the change of sensor conductance with time during AO exposure and the subsequent renewal or regeneration phase.

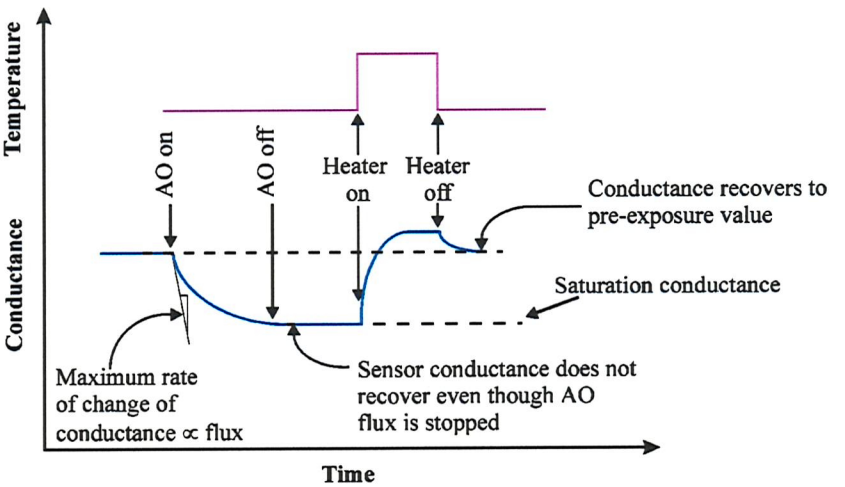

Figure 5.3 - Operational responses of an ideal semiconductor sensor

If such a sensor is in thermal equilibrium with its surroundings, and there is no flux of oxidizing or reducing species, then the conductivity of the sensor will remain stable at a fixed value. Immediately after initiation of AO exposure, however, the conductivity of the sensor begins to

decrease due to the reduction of charge carrier concentration, some of which are captured by chemisorbed oxygen atoms. The rate of change of adsorbed atom concentration is highest at the start of exposure - assuming the semiconductor surface was clean - hence, the rate of conductance change is also at its highest at this point. Application of Equation (5.32) allows the rate of sensor conductance change to be related to the unknown AO flux.

As the concentration of oxygen ions upon the surface increases with further AO exposure, the number of available adsorption sites falls and so more of the incident atoms are reflected from the surface. Thus, the rate of conductance decrease reduces. Eventually, the concentration of oxygen ions on the surface becomes stationary, and the sensor has saturated. At this point, the sensor conductance also ceases to decrease. Section 5.2.3 showed that this stationary concentration results either because the number of atoms adsorbed is equal to the number removed thermal desorption, or because all of the possible adsorption sites are filled.

However, another limit may also bring about this stationary concentration. Oxygen atoms may only become chemisorbed by the transfer of electrons from the semiconductor to physisorbed precursors. The band bending and surface barrier formation associated with the charged surface layers eventually prevents further transfer of electrons to the surface. At this time, no further oxygen adatoms may become chemisorbed and, so, the conductivity ceases to decrease. This type of charge-transfer limit is described by the Elovich rate equation (*Somorjai, 1972*). In any case, the sensor is said to have saturated and no further measurements may be made.

If the oxygen ion residency time is long (as expected from the high ionic bonding energy), when the AO flux is terminated, the concentration of adsorbed atoms will not fall significantly. Hence, the sensor conductance will not appreciably increase and may, in fact, remain constant. As discussed earlier, the chemisorbed atoms may then be removed from the surface by heating the sensor, which has the effect of reducing the adatom residency time. In this way, the sensor surface may be 'regenerated' for another measurement to be made. After cooling, the conductance of the sensor should recover to its pre-exposure value.

5.5 PREVIOUS APPLICATIONS OF SEMICONDUCTOR AO SENSORS

Several papers have been published in the literature regarding AO measurements with semiconducting sensors. Predominantly, single crystals have been used in ground-based studies. It is apparent from the literature that the material of choice for the sensor element is zinc oxide (ZnO). The structural and electrical properties of this material, which has also been used in this research, are investigated and reported in a later chapter of this thesis.

Nahr *et al.* appear to have been the first to publish results from single crystal devices tested in a thermal AO beam (*Nahr et al., 1971*). The small (3 mm diameter) Cu-doped, ZnO single crystal was connected into a measuring bridge circuit, the output of which was electronically differentiated and the results plotted on a chart recorder. The sensor was regenerated - heated to desorb oxygen ions - for another measurement by discharging a capacitor through the crystal. A secondary investigation demonstrated that the sensor signal was 10^2 to 10^3 times smaller when a molecular oxygen beam of the same flux was incident on the crystal. Thus, Nahr *et al.* found that even if the AO beam contained a significant quantity of O_2, its effect could be ignored.

Jacob also investigated the effects of AO on Cu-doped ZnO single crystals, amongst other materials (*Jacob, 1975*). A resistance bridge circuit using 4-point measurements was used to monitor the induced resistance change. Like the previous study, the output from the bridge was electronically differentiated and related to the AO flux. It was concluded that the rate of change of sample conductivity was proportional to the magnitude of the AO flux. The lowest flux intensity that could be measured was found to be about 10^{11} atoms.cm^{-2}.s^{-1}. As in the work by Nahr *et al.*, the sensors were regenerated by capacitor discharge.

Polycrystalline thin films of ZnO have also been used for thermal AO measurements (*Malinova and Myasnikov, 1969*). In fact, the technique has been used on board a sounding rocket for measuring lower thermospheric AO concentrations between 96 to 162 km (*Livshits et al., 1981a; 1981b; Gutman, 1995*). The thin films in this study were formed by the oxidation of zinc mirrors, which had been deposited onto a quartz substrate.

The analyser used for the rocket-based measurements consisted of an aperture equipped with a pulsed electromagnetic valve. During the flight of the rocket, the valve was briefly pulsed open and closed to allow exposure of the films to the external, AO containing environment. Whilst the valve was open, the change of sensor resistance was monitored. Once the valve was closed, the films were regenerated using a platinum heater on the reverse of the substrate. When the films had cooled to the ambient, working temperature, the valve was pulsed again to perform another measurement. This cycle was repeated many times in the flight of the rocket, therefore many measurements of the thermospheric AO flux were made. The measured AO fluxes, which were derived from the recorded resistance data using an equation similar to (5.32), were converted into number densities and plotted against the height at which the readings were performed.

The figure overleaf, which was adapted from the paper by Livshits *et al.*, shows the results generated by the rocket-based semiconductor 'analyser' equipment (*Livshits et al., 1981b*). Also shown in the figure, are curves generated by several other measurement techniques and a

thermospheric model. Whilst at first sight there appears to be good agreement between the results from the semiconductor sensors and those from other methods, the methods have been employed at very different times and at different geographic locations. For example, the best agreement to the results from the semiconductor sensor - taken above Volgograd in December 1979 - is with the resonance fluorescence curve 4 - taken above South Uist in November 1975. Whilst the season of the measurements is comparable, the epoch is not. In fact, there is a four-year difference, which is a significant proportion of the eleven-year solar-cycle. Such differences would seem to make the curves inherently incomparable, so it is difficult to comment on the relative accuracy of the equipment and technique.

Random errors in the technique are reported to be around 40 %, whereas systematic errors are a function of altitude and amount to approximately 50 % at 80 km to less than 1 % at 100 km (*Livshits et al., 1981a*). Nonetheless, it is possible to conclude from the paper by Livshits *et al.* that the method of semiconducting sensors seems to function properly at sounding rocket altitudes, enabling the lower thermospheric AO density to be determined. This conclusion lends credence to the aim of this research, which is to investigate the potential of these sensors for use in Earth orbit.

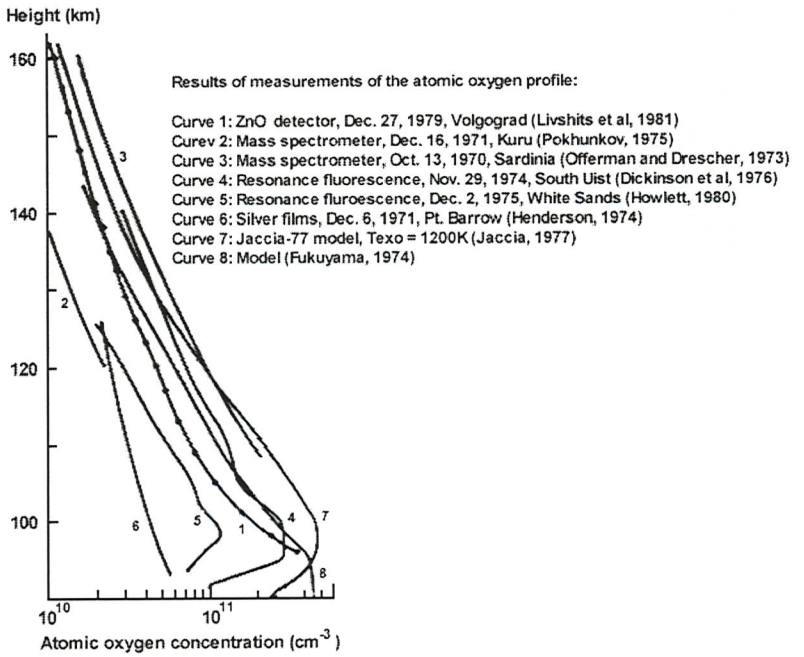

Figure 5.4 - Results from the rocket-based semiconductor sensor (after *Livshits et al., 1981b*)

More recently, Gabriel tested ZnO single crystals, without intentional dopants, in the atomic oxygen facility at the European space research centre, ESTEC (*Gabriel, 1997; Gabriel et al., 1998*). He found that ZnO crystals could be used to detect hyperthermal (~ 5 eV) oxygen atoms and that the crystals seemed to respond better at low temperatures. However, neither quantitative

measurements of AO, nor any comparisons of device response to models of sensor operation were made. One explanation of this enhanced response could be the effect of increased atom residency time upon the semiconductor surface (see Section 5.2). Increased residency time has the effect of allowing more atoms to stay adsorbed on the semiconductor surface for longer. If these atoms become chemisorbed, they will influence the electronic structure of the materials as indicated in Section 5.3.2 - more oxygen ions means a larger reduction of charge carriers, and hence a larger sensor response.

The work reported in this thesis is aimed at making a reusable AO detector, based upon the principles of ZnO gas sensors, for use in the space environment. No reports have been found in the literature of adaptations of ground or rocket-based equipment using these sensors for continuous use in the space environment. Thus, this is believed to be the largest area of novelty in this work. However, the testing of ZnO thin films in an hyperthermal AO beam is itself novel, as is the manufacturing route chosen for production of the thin films.

5.6 SUMMARY

This chapter has attempted to introduce the broad subject of semiconducting gas sensors. A brief historical review of these devices highlighted two types: the bulk conductivity device and the surface conductivity type. It is the surface conductivity variety that is most pertinent to the work described herein. These sensors are dominated by the effects of adsorbed gases and, so, a previously published model describing gas adsorption on solid surfaces was modified for use in this thesis. The model showed that, at the start of adsorption on a clean surface, the rate of change of adsorbed particle density is proportional to the flux of impinging particles. Moreover, particle saturation of the surface was demonstrated as being dependent on the level of flux at small intensities, but independent of magnitude at high flux intensities.

Operation of a surface-conductivity type sensor was then described in detail, with reference to the action of AO on ZnO single crystals and polycrystalline thin films. Chemisorption of atomic oxygen was found to remove charge carriers from the semiconductor, thereby forming depletion layers and reducing the conductivity of the sample. It was shown that thin films are more sensitive to surface adsorption than single crystals, because of the larger fraction of material that experiences electron depletion and due to the development of barriers to electron motion.

A quantitative method of using semiconductor sensors was presented by the development of a new ballistic model of operation. In this model, the rate of change of sensor conductance was shown to be linearly proportional to the level of flux, if the surface was initially clean.

Finally, the previous uses of ZnO AO sensors were discussed, and the novelty of this work made apparent. The following chapter reveals the design of the semiconductor sensors used in this research.

CHAPTER 6

THE SEMICONDUCTOR SENSOR DESIGN

The previous chapter discussed how semiconductor sensors function, and showed that ZnO-based devices could be used to perform thermal AO flux measurements. It is the intention of this chapter to describe the design of the ZnO sensors that have been used for the research reported in this thesis. Sensors of two designs have been fabricated - the second model to overcome difficulties noted with the first design. The manufacturing routes used to produce the sensors are also detailed. To begin with, this chapter opens with a description of the criteria that most influenced the generic design of the sensors.

6.1 INTRODUCTION

6.1.1 Project history

When the author began this research, testing by Gabriel had already demonstrated that single crystals of ZnO could be used as renewable hyperthermal AO sensors (*Gabriel, 1997*). Based upon this success, it was planned to test the principle in space by building a proto-flight experiment for inclusion on a microsatellite mission. Instead of using single crystal sensors, though, the satellite experiment was to employ sensors made from thin film zinc oxide. Thin film sensors were chosen because it was felt that they would be easier to incorporate into a flight-rated unit. It was one of the tasks of the author to design the thin film ZnO sensors.

The literature review and models presented in Chapter 5 revealed that the decision to utilize thin films was rather fortuitous. It is true that thin films can be deposited onto mechanically strong substrates, hence they are easier to package and handle than single crystal sensors. However, the major benefit of thin film sensors is that they are more sensitive than their thicker single crystal counterparts. This should have been the main reason for their selection.

6.1.2 Motivation of sensor design

The first step of the sensor design process was to isolate all the design drivers. Two of these criteria have already been established, namely that the sensor films must be deposited as thin films onto robust substrates.

Chapter 5 explained that the electrical conductance of an n-type material (like zinc oxide) is reduced by the adsorption of oxidizing species, for example atomic oxygen. Moreover, it was shown that the rate of change of sensor conductance, under certain conditions, is expected to be

linearly proportional to the level of AO flux. Clearly, the sensors must consist of a semiconducting material exposed to the AO environment. In addition, the sensors must be equipped with some method of making electrical contact to the semiconductor so that conductance measurements may be made.

The novelty of the semiconductor sensors is that they can be renewed. Thus, several AO flux measurements can be performed, rather than one as in the case of silver actinometer devices. The model of sensor operation presented in the previous chapter showed that regeneration of sensor properties occurs only at elevated temperatures. Therefore, it must be possible to heat the sensors. For this task, a heater is necessary.

Section 1.1 and Chapter 2 described the space environment in terms of its effects on materials. Recollection of this work shows that the materials from which the electrical contacts, the substrate and the heater are manufactured, must all be stable under the combined influence of oscillating temperatures, electromagnetic and particulate radiation, vacuum and atomic oxygen exposure. The condition of stability means that any material used should not be oxidized by AO and should also be non-contaminating. Additionally, good scientific practice dictates that some way of monitoring the effect of every component of the environment, other than AO, be included in the design of the sensors. In other words, a control device is required.

Thus, it is possible to compile a list of the pre-requisite properties, or design drivers, of a semiconductor AO sensor suitable for application in space:

1. Thin films of semiconductor must be used as the active element in the sensors.
2. The substrate upon which the films are deposited must be robust enough to withstand the stresses associated with launch and operation on a satellite.
3. The sensor films must be exposed to the AO environment.
4. The sensor films must be equipped with electrical contacts for conductance measurement.
5. Some way of heating the films must be incorporated in the design.
6. All materials used in the sensor must be stable and non-contaminating in the synergistic environments that exist in space and in ground-based AO facilities.
7. Given the wide variety of influences in the space environment, there should be some way of deconvoluting these effects from the influence of oxygen atoms.
8. The sensors should be small so that a reasonable number can be incorporated in a space flight experiment, but large enough so that handling problems are avoided.

Two different sensors have been designed using the above criteria. There are two common components of the design, namely the heater and the substrate. These parts will be described first, followed by detailed illustrations of the two sensor designs.

6.2 COMMON COMPONENT DESIGN AND MANUFACTURE

6.2.1 Heater

The style of heater chosen for the application in hand is a thick-film resistive element, formed directly onto the rear-face of the sensor substrate. Deposition of the heater directly onto the substrate confers several advantages over any other approach. Firstly, no adhesives need be used; the heater material itself forms the bond to the substrate, so the possibility of contamination is much reduced. Secondly, the thermal contact between the heater and substrate is improved, because there is no thermally insulating layer, like an adhesive, between the heater and substrate. Thirdly, because the heater may be fabricated from materials stable at high temperatures and in vacuum, it may be deposited onto the substrate before the ZnO thin films. This step reduces the amount of post-manufacture handling necessary to prepare the sensors and, therefore, further reduces the propensity of damage or contamination of the semiconductor films.

Consequently, it was decided that this style of heater would be adopted, rather than other options such as thermofoil heaters that require adhesive bonding, like that used on the first University of Southampton experiment, AOE-1 (*Harris, 1996*). The Thick Film Unit, of the Department of Mechanical Engineering at the University of Southampton, manufactured the heaters used in this project. The same unit was also responsible for the detailed design of the equipment needed to produce the various elements of the heaters.

A schematic of the heater can be found in Figure 6.1. There are two components of each heater, a resistive element in which electrical energy is converted to thermal energy, and electrical contacts to the resistor. The heater element consists of ruthenium oxide in a glass frit, whilst the electrical contacts are formed from a silver palladium alloy. All the materials are stable under conditions of vacuum, temperature and ultraviolet radiation. Even though the silver/palladium alloy may be oxidized by atomic oxygen, the substrate shields the contacts from AO exposure. In addition, the thickness of the tracks (~ 10 μm) is such that any oxidation-related thickness reduction is an insignificant part of the total. Hence, the track resistances should not change as a result of any AO reaction that might occur. A particular benefit of the silver/palladium alloy is that normal methods of soldering can be used to attach leads to the contacts. The heaters were deposited in two steps, both of which employed traditional thick-film manufacturing methods.

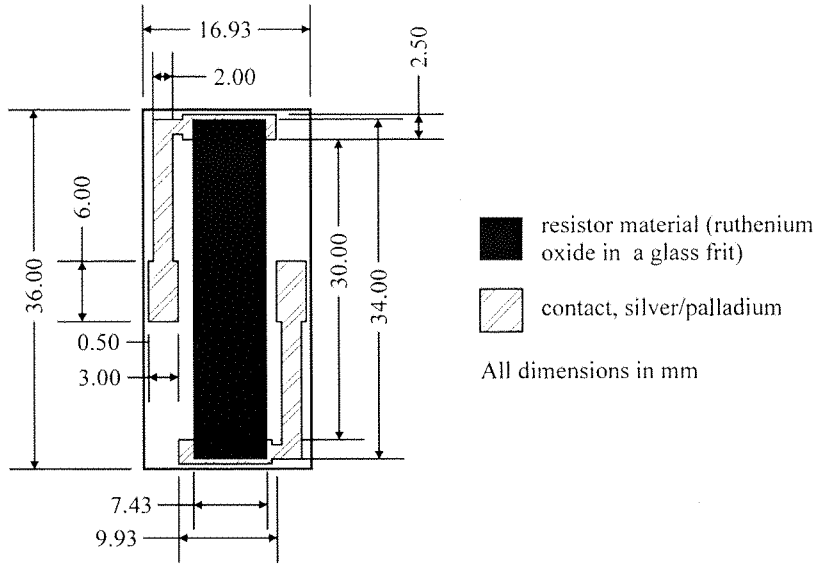

Figure 6.1 - Thick film heater

The first part of the heater to be fabricated on the substrate were the electrical contacts. Screen-printing was used to form 'wet' contacts on the substrate - the alloy comes in pre-mixed ink, which consists of silver and palladium powders mixed with solvents and resins to make it mobile. After printing, the ink was 'dried' for approximately ten minutes, during which time some of the solvents evaporated, increasing the viscosity of the ink. The substrates were then loaded into a furnace and fired at ~ 1120 K for one hour. In this time, the resins decomposed and the metals sintered to a robust, electrically conducting track bonded to the substrate.

Next, the resistor material that constitutes the major component of the heater was printed onto the substrate. Again, screen-printing was used. The screen was aligned with the substrate so that the resistor material overlapped both silver/palladium tracks. The resistor ink was a mixture of ruthenium oxide powder, glass frit, resins and solvents. Glass is included in the mixture to bind the oxide to the substrate, because the metal compound does not sinter at the firing temperature.

After cooling, the heater resistances were measured and trimmed to the desired value (384 Ohms, see Chapter 11) by removing some of the resistor material. A precision sandblasting tool was employed for this purpose.

6.2.2 Substrate

To some extent, the route adopted to form the heaters dictated the type of material that could be utilized for the sensor substrates. The high temperatures necessary to sinter the resistor and contact materials prevented the application of the first choice of substrate - glass. Originally, glass was chosen because it is widely available, cheap, chemically inert (with respect to AO),

electrically insulating and smooth. It was for these reasons that it was selected for the substrate of the silver film actinometers used in the AOE-1 (*Harris, 1996*).

However, the material of preference for the Thick Film Unit was alumina. Not only is this material stable at the high furnace temperatures, but it is also obtainable in thin sheets that would fit into the available screen-printing machine. There are further benefits of using alumina. Firstly, it is available (from Coors Ceramics Ltd.) in a thin film grade - the sheets of this grade have low surface roughness, ~ 0.076 μm (*Coors Tech Specs, 1995*). Secondly, the thermal conductivity of alumina is far higher than that of glass, 26 - 35 $W.m^{-1}.K^{-1}$ and 1.2 - 1.4 $W.m^{-1}.K^{-1}$ respectively, whilst still being electrically insulating. Higher substrate thermal conductivity results in more efficient use of heater power. Thirdly, alumina also satisfies the fifth design driver because it is inert with respect to AO and UV, and is not a source of contamination in a vacuum environment.

The standard alumina sheets processed by the Thick Film Unit are 50.8 mm square by 0.635 mm thick. It was found that this size of sheet was large enough to accommodate three reasonable sized sensor substrates. Hence, the supplier was instructed to laser-scribe the sheets, thereby making separation of the individual substrates easier. All of the manufacturing stages of the sensors - those of the heaters, ZnO films and contacts - were conducted with the alumina sheet as a whole. Thus, for example, three heaters were formed simultaneously on each alumina square.

6.3 FIRST SENSOR FORMAT

6.3.1 Sensor design

A schematic of the first AO sensor arrangement is given in Figure 6.2. Each substrate, with its own individual heater on the reverse, has four semiconducting films deposited on the centre-line. Chapter 7 describes the deposition process and studies the resulting film properties. All of the ZnO thin films are of dimensions 6 mm x 4 mm. However, thin (~ 2000 Å) gold films, which are used as electrical contacts, overlap the ZnO by 1 mm on both sides. This has the effect of reducing the exposed ZnO area to 16 mm^2. Gold was chosen for the contact material because it is inert to AO action, and is a good electrical conductor.

Two of the zinc oxide films are covered with silicon dioxide films of thickness 20 nm, which was deposited by RF sputtering of a silicon dioxide target in an argon atmosphere. This layer was formed upon the zinc oxide because silica is resistant to AO erosion (*Tagawa et al., 1997*), so if the layers are defect-free, they should prevent AO reaching the underlying ZnO. Silicon dioxide is also known to have a low coefficient of absorption in the UV (*Philipp, 1985*), so incident UV photons should have the same effect on the covered and uncovered semiconducting films. In this

manner, it is possible to prevent the action of atomic oxygen on the ZnO, whilst permitting other environmental influences to interact with the semiconductor. Hence, the silica-covered films can be used as the required control devices.

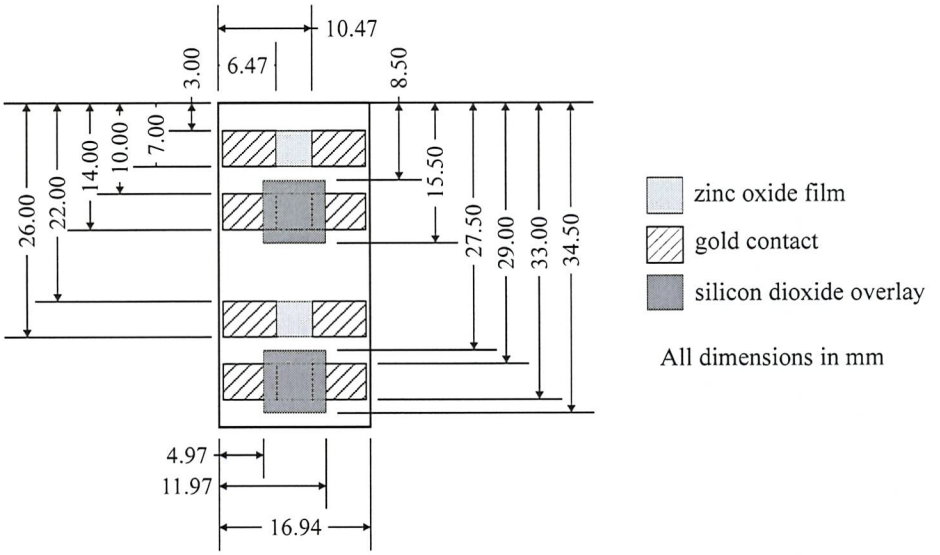

Figure 6.2 - Zinc oxide AO sensor design

Therefore, each substrate consists of four ZnO films - two exposed and two covered with silica. The figure shows that the ZnO films are gathered into groups of two, each group consists of one covered and one uncovered ZnO film, and is said to constitute a **sensor**. In other words, each sensor consists of one bare film to monitor AO, and a silica-covered film to enable deconvolution of other environmental effects. There are two such sensors on each substrate. It is evident in Figure 6.2 that there is a reasonable gap between the two sensors. The purpose of this gap is to allow sufficient space for a temperature sensor to be attached to the same surface of the substrate as the semiconductor films.

6.3.2 Sensor manufacture

After fabrication of the heaters on the alumina sheet, the substrates were sent to the School of Industrial Manufacturing Science, located at Cranfield University, so that the zinc oxide and gold films could be deposited. Both materials were deposited using traditional thin-film technology.

Before deposition of any films, the substrates were cleaned using the steps in the following list. All stages, excluding number 8, were conducted in ultrasonic baths.

1. Rinse in detergent and particle remover (Micro), 10% solution in distilled water.
2. Rinse in distilled water.
3. Wash in degreaser (Volasil 304).

4. Rinse in degreaser and distilled water.
5. Rinse with isopropyl alcohol (IPA).
6. Wash in IPA.
7. Rinse in IPA (analar grade).
8. Expose to analar grade IPA vapour in a re-flux column.

After removal from the hot IPA vapour, the substrates were loaded into clean boxes and placed into a vacuum chamber until required for processing.

Sensor manufacture began with the deposition of the metal oxide semiconductor films by RF sputtering of a ZnO target. Details of the sputtering conditions used, properties of the deposited films, and a characterization of the sputtering process, can be found in the next chapter. Three nominal thicknesses of ZnO film were deposited, namely 0.5 μm, 1.0 μm and 2.0 μm. Following deposition of the zinc oxide films, electron beam evaporation was used to deposit the gold electrical contacts. The last stage of sensor manufacture was the formation of the silicon dioxide overlays on two of the semiconductor films.

6.4 SECOND SENSOR FORMAT

6.4.1 Sensor design

The thin gold films used as electrical contacts in the first design were found to be very fragile - too fragile for application to a satellite mission. Additionally, the only reliable way to make electrical contact to the gold was to use a silver-loaded epoxy adhesive. Even though the manufacturer claims that the epoxy does not outgas under normal vacuum conditions, AO induced contamination must still be anticipated (see Sub-section 2.2.3). In order to overcome these difficulties, another sensor model was conceived. The new sensor was designed to eliminate the need for the fragile thin gold films and the requirement of silver-loaded epoxy.

Additionally, however, another design feature was included in this new model. The ballistic equation developed in Chapter 5 (Equation 5.32) stated that:

$$F = -\frac{a^*}{\kappa\alpha(1-\gamma)}\frac{l}{be\mu}\left.\frac{dg}{dt}\right|_{t=0} \tag{5.32}$$

All of the parameters in this equation, with the exception of b and l, are properties of the sensor material. In comparison, b - the breadth of the film, and l - the distance between the contacts, are dimension related. It is clear that, if all other terms are constants, the equation may be re-written:

$$F \propto \frac{l}{b} \left. \frac{dg}{dt} \right|_{t=0} \tag{6.1}$$

Evidently, to maximize the rate of change of sensor conductance under a given AO flux, the ratio b/*l* - a kind of aspect ratio - should be large. This can be achieved by having long contacts (large b), separated by small distance (low *l*).

The new contact design is shown in Figure 6.3. It can be seen that the pattern of the electrodes on the new sensor are more complicated than the simple thin films of gold used in the first model; the adopted layout is frequently called an interdigitated array. It has several benefits, particularly that the spacing of the contacts is just 300 μm while the integrated length is approximately 15.3 mm. Thus, the contacts have an aspect ratio of around 51, which is far larger than the first design, which has a ratio of 1. This aspect ratio makes the contact design ideal for use with low conductivity materials and/or for measuring small fluxes.

Like the first sensor, the electrode material is still gold-based, but is no longer in thin film form. Instead, the contacts have been formed using thick-film technology. Not only are the contacts produced in this fashion far more robust than the thin gold films, they may also be terminated with silver/palladium 'pads'. Like the heater contacts, electrical connection may be made to the pads by soldering. Hence, the two key problems of the first sensor design - fragility and potential of contamination - have been eliminated in this new model. Moreover, the contact arrangement should induce greater sensor sensitivity.

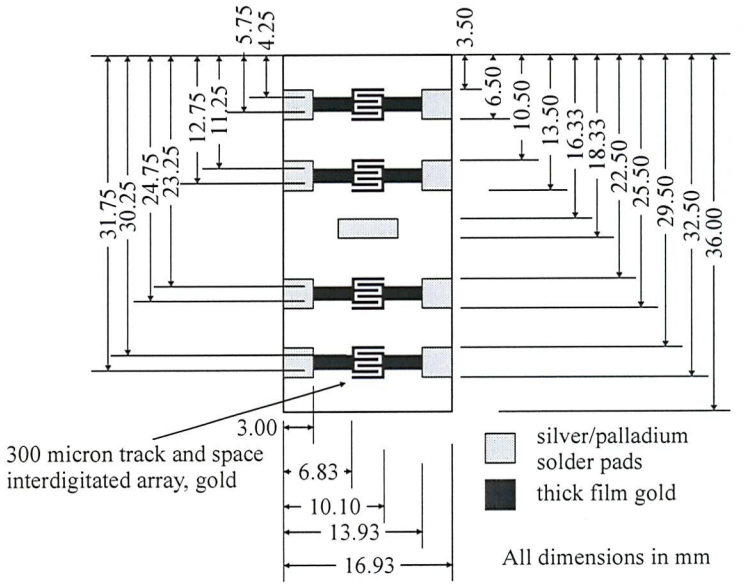

Figure 6.3 - The interdigitated array contact details

6.4.2 Sensor fabrication

Two variants of this sensor have been manufactured; the difference is based upon the type and thickness of the gold electrodes. The first employed gold ink, called a 'resinate', to form the electrode pattern. In the furnace, these inks reduce in thickness from around 25 μm as printed, to less than 1 μm when fired. In comparison, the second type used a gold ink called a 'cermet', which reduces in thickness from ~ 25 μm before firing to 8 - 10 μm afterwards.

The manufacture of the sensor was begun by deposition of the interdigitated electrodes. With the cermet ink it was sufficient to print and fire one layer. However, the large thickness reduction exhibited by the resinate required that two individual layers be printed and fired - the second directly on top of the first. After the electrodes were deposited, the silver/palladium solder pads were printed and fired in place. Finally, a heater with the same design as the first sensor model was formed on the reverse of the substrate, to complete the sensor.

Deposition of the ZnO and SiO_2 films was conducted in the same manner as that used for the first sensor model, however, several different ZnO thicknesses were deposited in this case. The ZnO films were reduced in size to 4 mm x 4mm so that they covered the interdigitated array, but the silica coverings were of the design described earlier. Again, each substrate has four zinc oxide films, split into two sensors. Each sensor consists of one bare ZnO film and one covered with silica. A silver/palladium pad was deposited in between the two sensors. This was included so that the temperature sensor might be affixed by soldering, completely eliminating the need for any polymer-based adhesive.

6.5 DEFINITION OF SENSOR NOMENCLATURE

Earlier in this chapter it was mentioned that three substrates were formed from a single alumina sheet by laser-scribed lines. Figure 6.4 shows a typical arrangement of the thin films on the sheet after deposition of sensors of the first design, however, a similar layout is observed for the interdigitated array devices. Thus, three sets of four ZnO films (six sensors) were deposited simultaneously. In this way, each set of four ZnO films should have similar electrical properties. The mask used to define the ZnO sensor films also had a pattern that allowed the deposition of a small 'witness' sample on some of the 'scrap' alumina that was not used in the sensor substrates.

Due to the large number of sensors manufactured in each deposition, and the two different styles of sensor, it will be helpful to define a nomenclature system for classification of individual sensors. The system used in this work has a format that allows the identification of:

- The contact type.
- The identity of the deposition in which the ZnO was formed.
- Which substrate a sensor resides upon (given that there are three in each deposition).
- The sensor (given that there are two per substrate).
- The covered or bare film of the sensor.

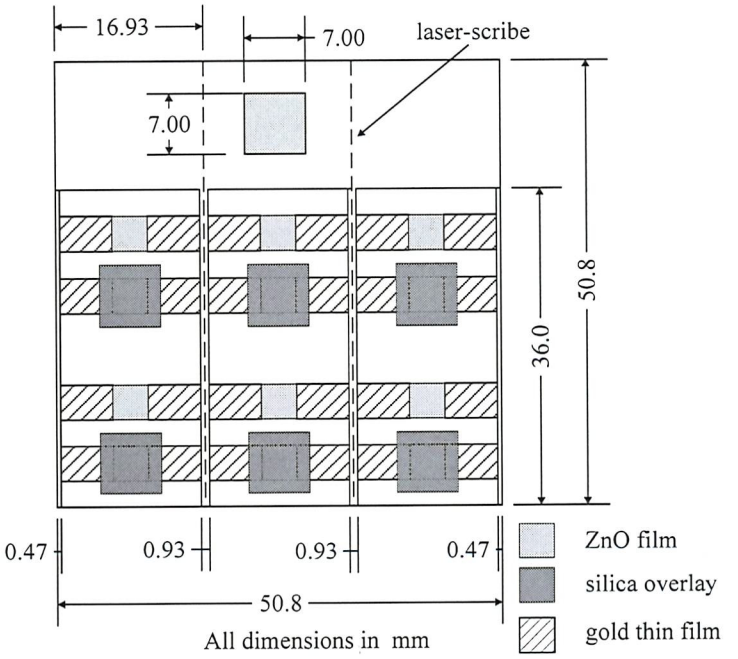

Figure 6.4 - The layout of semiconductor films on an alumina sheet

The contact type is defined by a two-letter prefix: 'TG' standing for 'thin gold'; 'CT', for cermet; and 'RT' for resinate. Next, is a two-number label identifying the deposition in which the films were formed; a complete list of depositions can be found in the following chapter. The labelling continues with a capital letter that identifies which one of the three positions the substrate was in during deposition. So, with reference to Figure 6.5 (overleaf), 'A' is used to represent the left-hand substrate, 'B' the middle, and 'C' the right-hand. To identify which sensor upon each substrate is under discussion, the sensors are given a number (1 or 2). Sensor number is determined according the figure below. Finally, the two zinc oxide films in each sensor are given a lowercase letter to enable distinction between the covered ('c') and bare ('b') elements.

For example, sensor TG08A1b is the bare ZnO film (b) of the first sensor (1), which was formed upon the left-hand substrate (A) during deposition number 08. The sensor uses thin gold (TG) films to make electrical contact to the semiconductor films. CT21B2c is the SiO_2 covered film (c) on the second sensor (2) of the middle substrate (B), formed in the twenty-first deposition to be conducted. The sensor has cermet electrodes (CT).

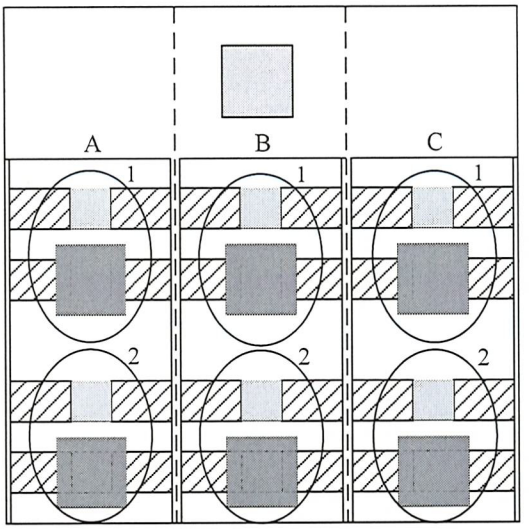

Figure 6.5 - Sensor nomenclature determination

6.6 SUMMARY

This chapter has described the design and fabrication route of two models of ZnO thin film sensor for use in the laboratory, and in a spaceflight experiment. In both types of sensor, a thick film, resistive heater was used because it reduced the chance of sensor contamination.

Sensors of the first model were formed solely by thin film technologies. Zinc oxide was deposited onto thin-film grade alumina using RF sputtering, whilst electrical contact to the films was achieved by evaporating overlapping gold films. Unfortunately, the gold contacts so formed were found to be fragile, and the method of attaching wires to them a potential source of contamination. Thus, a more robust second design was conceived. In this model, the electrodes used to measure the ZnO conductance were deposited using thick film methods. The gold electrodes were deposited in two thicknesses (< 1 μm and 8 - 10 μm), both with the same interdigitated pattern. The addition of silver/palladium solder pads enabled wires to be soldered directly onto the substrate, eliminating the need for the conductive adhesive used with the first model.

Each AO sensor is defined to consist of two ZnO films, one exposed to the environment, and one covered with silica. The covered control films are incorporated into the sensors to enable the affects of influences other than AO to be deconvoluted from the signals generated by the bare films.

The next chapter investigates the structural and electrical properties of the ZnO used in the sensors.

CHAPTER 7

ZINC OXIDE, A METAL OXIDE SEMICONDCUTOR

Several metal oxides - including those of nickel, cobalt, titanium, tin, cadmium and zinc - naturally exhibit semiconducting behaviour, or may be made to do so by the addition of dopants. Only one metal oxide semiconductor (MOS) material has been investigated in this study, namely zinc oxide. This chapter opens with a justification, in addition to its sensitivity to AO, for the selection of this substance. The following sections then describe the chosen ZnO fabrication route; the results of an empirical study of film structure and electrical properties of the sensors. Lastly, investigations of some other important properties of the ZnO films are reported.

7.1 INTRODUCTION

Zinc oxide occurs in nature as the mineral zinctite and has a stoichiometric chemical formula of ZnO. It is photoconducting, piezoelectric and luminescent amongst many other properties, which are too numerous to mention here. These properties have led to the employment of ZnO in a diverse range of scientific and technological applications. The piezoelectric property has been utilized in surface-acoustic-wave (SAW) filters and resonators, microsensors, microactuators and acousto-optic devices (*Song et al., 1995*). Under the bombardment of electrons, ZnO is luminescent, which has led to its application as a phosphor in fast-response cathode ray tubes (*Heiland et al., 1959*). It has also been used in UV sensors (*Fabricius et al., 1986*), and as a transparent electrode in solar cells (*Delahoy, 1998*).

A literature review in an earlier chapter showed that single crystals and thin films of zinc oxide demonstrate changing electrical properties upon exposure to oxygen atoms and, to a lesser extent, molecular oxygen. In point of fact, it is for precisely this reason that zinc oxide has been selected for the current study. However, there are other benefits for choosing this material. Hyperthermal atomic oxygen is a very reactive species, and so if a material is not inert to oxidation, or not fully oxidized before exposure, it will rapidly become so by AO action.

Research has also shown that other semiconductors, including silicon and germanium, demonstrate sensitivity to oxygen (*Jacob, 1975*), yet these materials may form impenetrable oxide barriers upon reaction with hyperthermal AO. Layers of this nature prevent interaction of the adsorbed oxygen with the electronic structure of the underlying semiconductor. Clearly, any material that might be oxidized to this extent cannot be used as a renewable AO sensor. So, the major benefit of zinc oxide is apparent, because it can be considered to be pre-oxidized and, hence, is expected to display stable stoichiometry under AO bombardment.

7.2 THE STRUCTURE OF ZINC OXIDE

7.2.1 Formation of single crystals and thin films

Zinc oxide is an ionic solid which crystallizes in the hexagonal wurzite lattice, with lattice constants a = 3.25 Å, c = 5.19 Å (*Heiland et al., 1959*). In this arrangement, the oxygen ions reside in a hexagonal close-packed (hcp) structure, whilst the zinc ions occupy half of the tetrahedral interstitial positions, as shown in Figure 7.1.

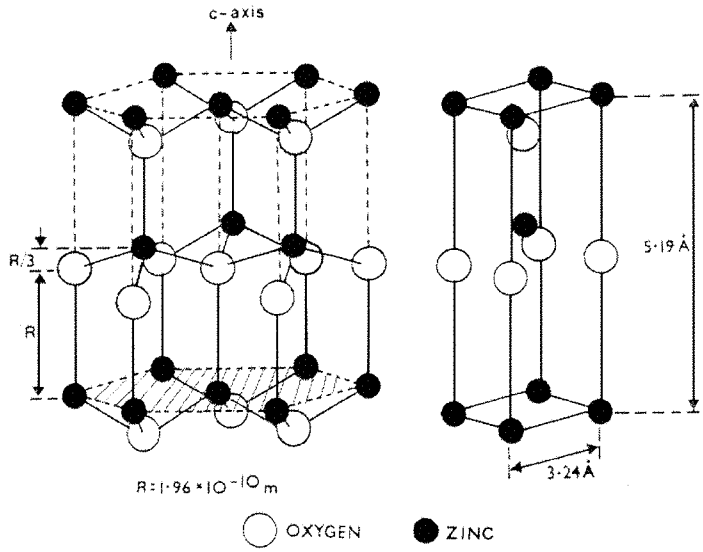

Figure 7.1 - The structure of a unit cell of zinc oxide (after *Chandler, 1980*)

Zinc oxide cannot be melted at atmospheric pressure because it sublimes and dissociates; this fact has lead to the development of some novel routes to produce pure samples of the material. Heiland *et al.* report that single crystals may be grown from the vapour phase at elevated temperatures (*Heiland et al., 1959*). They can also be grown by reacting zinc vapour with air or oxygen (*Scharowsky, 1953; Hutson, 1957*), by the hydrothermal method (*Laudise et al., 1964*), and by other routes (*Chandra et al., 1967*).

However, thin film ZnO has been selected as the sensitive element in the AO sensors, because the layers can be deposited directly onto mechanically strong substrates (see Chapter 6). Several methods for producing ZnO in thin film form have been found in the literature.

Polycrystalline, thin films of ZnO have been fabricated using a number of techniques. The sputtering method has been used in many forms. Radio frequency magnetron sputtering of ZnO targets with (*Nanto et al., 1984*), and without (*Schropp and Madan, 1989*) an applied, external magnetic field seem to result in films of high conductivity. In contrast, DC and RF sputtering of zinc targets in an oxygen-containing atmosphere generally lead to films of low conductivity (*Raimondi and Kay, 1970; Morgan and Brodie, 1982; Sundaram and Garside, 1984*).

Vacuum evaporation (*Niikura et al., 1969*), vapour transport (*Galli and Coker, 1970*) and spray pyrolysis (*Aranovich et al., 1979*) have also been employed to form thin films. Another two techniques using lasers have been developed in recent years: pulsed-laser deposition (*Craciun et al., 1994; Hayamizu et al., 1996*), and laser evaporation (*Maruyama et al., 1994*). Lastly, it is also possible to form zinc oxide layers by the oxidation of zinc thin films in an air or oxygen atmosphere (*Livshits, 1981a*).

It is usually found that ZnO thin films consist of two structural features: grains and crystallites (*Lad et al., 1980*). Grains are aggregates of several small crystallites and are often observed to form columnar structures upon the substrate. Generally, it is found that the crystallites - contained within the grains - are aligned with their c-axes (see Figure 7.1) normal to the plane of the substrate upon which the films are deposited.

7.2.2 Effects of deposition conditions

The sensors used in this research have been fabricated using RF magnetron sputtering of a zinc oxide target in an argon atmosphere with up to 10 % oxygen gas added. It is expected that films formed by this process will be polycrystalline in nature, thereby creating a high density of asperity contacts, bridges and necks, which engender sensitive detectors (Chapter 5).

An investigation of the sputtering conditions has shown that the resistivity of the deposited material is dependent upon the amount of oxygen gas included in the sputtering mixture. Figure 7.2, plotted in the standard logarithm-linear fashion, shows the dependence of ZnO resistivity upon the percentage content of oxygen in the sputtering mix. K. Lawson, of Cranfield University, kindly provided this data.

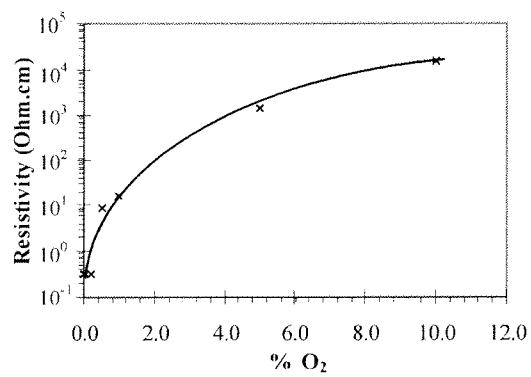

Figure 7.2 - The dependence of ZnO resistivity on % O_2 at 150 W RF power

Clearly, as the amount of oxygen in the sputtering gas is raised, the resistivity of the deposited material initially increases very rapidly. Further increases of oxygen concentration seem to affect

proportionally smaller resistivity increases. Deposition features similar to this have been reported by Barnes *et al.* and Sundaram and Garside (*Barnes et al., 1980; Sundaram and Garside, 1984*), but at much higher oxygen concentrations (10 - 100%). The increase of sample resistivity is traditionally attributed to changes of film stoichiometry, specifically increased oxygen content, which is associated with decreased interstitial Zn content.

Results from the investigation also show that the rate of ZnO deposition is a function of oxygen concentration. Figure 7.3 displays the measured deposition rates. Again, this dependency is a feature of ZnO deposition that has been observed previously (*Aita et al., 1980; Barnes et al., 1980*). It is evident from the graph that initially the deposition rate falls with increasing oxygen content in the sputtering gas. This observation is explained by the fact that, since oxygen is a 'light' element in comparison to argon, its sputtering yield (the amount of material ejected from the target per incident atom) is lower than that of argon. Increasing the concentration of oxygen therefore has the affect of reducing the number of sputtered atoms, and hence, lowering the deposition rate.

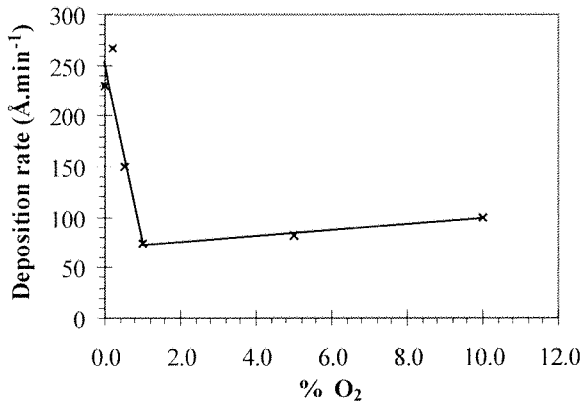

Figure 7.3 - The effects of O_2 concentration on ZnO deposition rate

However, as Figure 7.3 shows, the deposition rate recovers somewhat with further increases in oxygen concentration. Such a recovery was observed by Aita *et al.* (*ibid.*) and was interpreted as a consequence of increased target oxidation. Oxide targets generate higher yields of secondary electrons, which cause greater ionization of the sputtering gas, and hence a larger ion current is incident upon the target. Larger ion currents increase the sputtering rate, even though the amount of oxygen - with its lower sputtering yield - is increased. Oxidation of the zinc oxide target is possible, owing to the potential of non-stoichiometric removal of material from the target. Oxygen, being lighter than zinc, is likely to be preferentially removed, leading to a zinc rich target surface, prime for oxidation.

Several zinc oxide depositions have been performed. The table below summarizes the conditions used and also provides an identifier for each deposition, some of which have been used to fabricate AO sensors; where applicable, these devices will be described in more detail in subsequent chapters. All depositions were conducted at 150 W RF power. Gettered argon indicates the argon was effectively oxygen-free.

Sample	Thickness (μm)	Time (min)	% O_2 in Ar	Substrate bias (V)
TG05	1.00	40	gettered	-160
TG06	1.00	40	gettered	-160
TG07	2.00	80	gettered	-160
TG08	0.50	20	gettered	-160
TG09	0.50	20	gettered	-160
TG10	1.00	40	gettered	-160
TG11	2.00	80	gettered	-160
RT01/CT01	0.30	19	gettered	-160
RT02/CT02	0.30	25	gettered	-160
RT03/CT03	0.28	19	0.20	-158
RT04/CT04	0.32	33	0.50	-158
RT05/CT05	0.80	67	1.00	-159
RT06/CT06	0.32	30	5.00	-150
RT07/CT07	0.28	30	10.0	-153
RT08/CT08	0.32	20	1.00	-161
RT10/CT10	0.60	23	0.20	0
RT16/CT16	0.24	17	0.10	0
RT17/CT17	0.50	30	0.05	0
RT18/CT18	0.50	30	0.05	0
RT19/CT19	0.50	30	0.05	0
RT20/CT20	0.40	30	0.05	0
RT21/CT21	0.28	30	0.05	0

Table 7.1 - Deposition conditions of the ZnO samples

7.2.3 Structural investigations of thin films

Three thicknesses of zinc oxide have been studied with the aid of X-ray diffraction (XRD) because, as shown in Chapter 5, the structure of the semiconductor film defines the way in which the sensor responds. The ZnO films used were formed in depositions TG08, TG10 and TG11, and had nominal thicknesses of 0.5, 1.0 and 2.0 micrometres, respectively. The apparatus used to perform the measurements was a conventional Siemens D5000, θ - 2θ diffractometer, which employed Cu-$K\alpha_1$ radiation at a wavelength of 1.5406 Å. The scans were performed over a 2-θ range of 30.5 - 38.5° using a step size of 0.02°. Equipment such as this only detects the radiation reflected from crystal planes aligned parallel to the substrate surface. A schematic of the apparatus can be found in Figure 7.4.

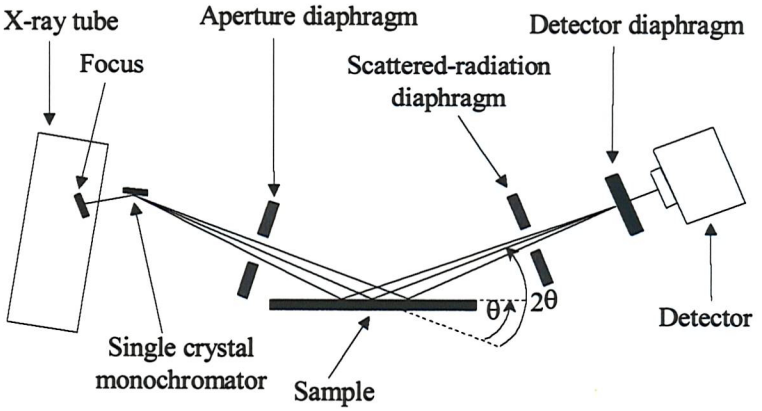

Figure 7.4 - Schematic of the Siemens D5000 diffractometer (after *Healey, 1999*)

Unfortunately, the alumina substrates upon which the films were deposited generated signals so strong that they 'swamped' the weaker ZnO reflections, preventing presentation of the complete scans. Instead, Figure 7.5 shows extracts from four XRD scans, one for each of the ZnO films and another for a control alumina sample, over the 2-θ range of 33.0 - 35.0°.

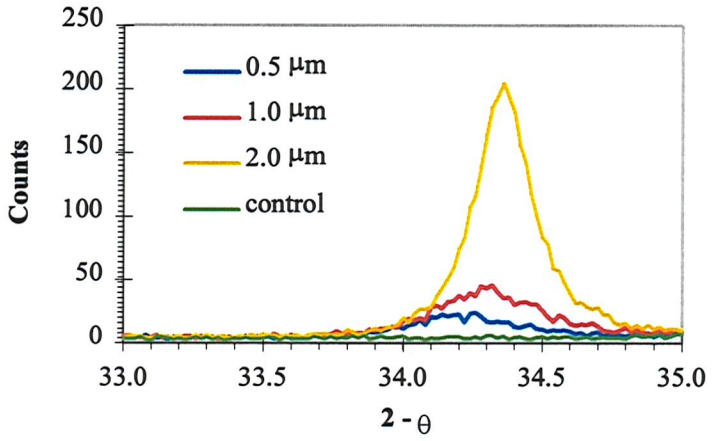

Figure 7.5 - XRD scans of ZnO on Al_2O_3

From the above graph, it is clear that each ZnO scan has a peak located somewhere between 34.0 - 34.5° - the exact position seems to depend upon the thickness of the film. It is reported in the literature that this peak is the ZnO (002) reflection. It appears that alumina does not generate a signal in this angle range, as demonstrated by the green curve labelled as 'control', so the observed reflections cannot be attributed to an effect of the alumina substrate. Also in Figure 7.5, it can be seen that the ZnO reflections become less intense with decreasing ZnO film thickness, presumably because there is less ZnO present to reflect the incident X-rays.

Therefore, all XRD scans performed show that the crystallite (002), or basal planes, are orientated parallel to the substrate surface. The (002) plane is the one crosshatched in Figure 7.1.

As a consequence of this preferential alignment, the c-axes of the crystallites must be perpendicular to the substrate plane, a conclusion which agrees with results from RF depositions reported in the literature (*Aranovich et al., 1979; Lad et al., 1980; Nanto et al., 1984*).

Using Bragg's law, Equation (7.1), the angular position of the peaks can be employed to determine the inter-planar spacing in the sample (*Bragg, 1913*).

$$o\lambda = 2d_{hkl} \sin\theta \tag{7.1}$$

Where:

o = order of reflection
= 1 (in this study)
λ = wavelength of radiation (Å)
= 1.5406 Å (in this study)
d_{hkl} = inter-planar spacing perpendicular to the substrate plane (Å)
θ = incident angle of radiation (°)

Table 7.2 gives the measured peak positions and inter-planar spacing of the thin films. For comparison, the same information for two unstressed powder samples is also presented.

Sample	Thickness (μm)	2-θ (°)	θ (°)	Spacing, d_{hkl} (Å)
TG08	0.5	34.26	17.13	2.615
TG10	1.0	34.32	17.16	2.611
TG11	2.0	34.36	17.18	2.608
Powder (*McMurdie, 1986*)	-	34.422	17.211	2.603
Powder (*Lad, 1980*)	-	-	-	2.602

Table 7.2 - XRD measurements of ZnO films

The data in Table 7.2 show that, as the ZnO film thickness increases, the inter-planar spacing falls towards the unstressed powder sample value. The fact that the spacing in all films is larger than the unstressed powders, indicates that the films are deposited with a residual tensile stress component parallel to the c-axis of the crystal (*Lad et al., 1980*).

Seemingly, the thicker films have reduced stress levels; there are two possible explanations of this observation. Firstly, it takes longer to deposit the thicker films. If significant substrate heating is encountered in this process, and there is evidence that it does (*Lawson, 1998*), the deposition time of the thicker films may be sufficient for the stresses to become partially relieved through annealing.

On the other hand, the reduction of apparent stress levels may be an artefact of the XRD measurement. When the first zinc oxide layers are deposited upon the alumina (Al_2O_3), there will be a mismatch between the crystal systems of the ZnO and Al_2O_3 - in fact this difference is likely to be the cause of the tensile stress. As the film grows in thickness during deposition, the upper layers of ZnO will be deposited onto ZnO, rather than Al_2O_3. Thus, it is expected that successive 'layers' in the film will experience a certain amount of stress relief, because the lattice mismatch developed at the film/substrate boundary will be dissipated with distance away from the interface. The thicker a film becomes, the more likely the X-ray radiation will be reflected from crystal planes further from the stressed Al_2O_3/ZnO phase boundary. Consequently, on average the crystallites will appear less stressed.

It is also possible to measure the full-width, half-maximum values (FWHM) of the (002) peaks. Full-width, half-maximum values give an indication of the crystallite size but, in general, are also affected by instrument errors, stacking-faults in the material, and non-uniform strains (*Warren, 1969*). It is reported in the literature, that the (002) peak width is not affected by stacking faults in the ZnO system (*Lad et al., 1980*). Thus, only crystallite size, strains and instrument defocusing affect the peak width. The author has no means of checking the instrumental broadening of the peak, so it is logical to assume it a small, constant error.

The standard Scherrer Equation (7.2) can be used to estimate the crystallite sizes, in the direction of the c-axis, from peak broadening information (*Warren, 1969*).

$$L = \frac{0.94\lambda}{B(2\theta)\cos\theta} \tag{7.2}$$

Where:

$B(2\theta)$ = FWHM (radians)

λ = wavelength of X-ray radiation (Å)

θ = peak position (degrees or radians)

L = average crystal dimension perpendicular to the reflecting planes (Å)

Table 7.3 presents the information necessary to calculate the average crystal sizes and the dimensions derived from Equation (7.2).

As expected, it is apparent that the crystallites in sample TG11 (2.0 μm film) are bigger than those in both the 1.0 μm and 0.5 μm films: as film thickness increases, so should the crystallite size. However, the 0.5 μm film crystallites are measured to be larger than those in the 1.0 μm

film - a rather unexpected result. This discrepancy might be caused by the inferred greater stress and, hence, strain in the thinner film. The stress causes the crystallites to be stretched in the measurement direction, distorting the 'true' size (see Table 7.2). The measured crystallites sizes seem to compare well with those published in the literature, which range from 140 Å to 450 Å (*Inaba et al., 1971; Hickernell, 1973; Maniv and Zangvil, 1978*).

Sample	Thickness (μm)	FWHM (x 10^{-3} rad)	θ (°)	L (Å)
TG08	0.5	6.5624	17.13	230.91
TG10	1.0	6.9639	17.16	217.64
TG11	2.0	4.0666	17.18	372.73

Table 7.3 - Crystallite size predictions

7.2.4 Electron microscopy investigations of deposited films

Figure 7.6 is a scanning electron photomicrograph of virgin substrate material. It can be seen that the alumina sheet is formed from connected nodules and globules of material. Literature from the manufacturer shows that the sheets of alumina are formed by slip-casting and furnace sintering (*Coors Tech Specs, 1995*). Therefore, the observed structure is commensurate with the manufacturing route of the substrate.

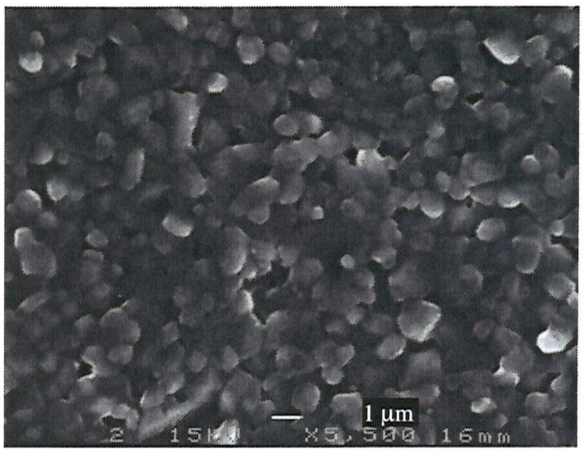

Figure 7.6 - Virgin alumina substrate

So, the surface of the substrate consists of many facets, each with a slightly different orientation. When ZnO is deposited onto the substrate, the crystallites will develop with their c-axis perpendicular to the **local** surface upon which they are growing. This orientation is not necessarily the same as the normal vector to the substrate plane. Moreover, since the local surfaces of the alumina globules are arranged randomly, the crystallite alignments will be scattered about a mean value relative to the normal vector to the substrate plane. This arrangement of locally random surface alignments will have increased the measured FWHM

values of the (002) reflection peaks, and hence, the crystallite size predictions made earlier may underestimate the true values.

Figure 7.7 parts (a) and (b) present photomicrographs of two ZnO films - thicknesses 1.0 and 2.0 μm - deposited on the standard alumina substrate like that of Figure 7.6. As suspected, the surface morphology of the ZnO thin films appear to be most greatly influenced by the underlying structure of the substrate. It is possible to see the nodular structure of the alumina, even in the thickest (2.0 μm) film. Indeed, the major difference between films of different thickness appears to be that the 'voids' between the alumina nodules become progressively filled with material the thicker the ZnO layer becomes.

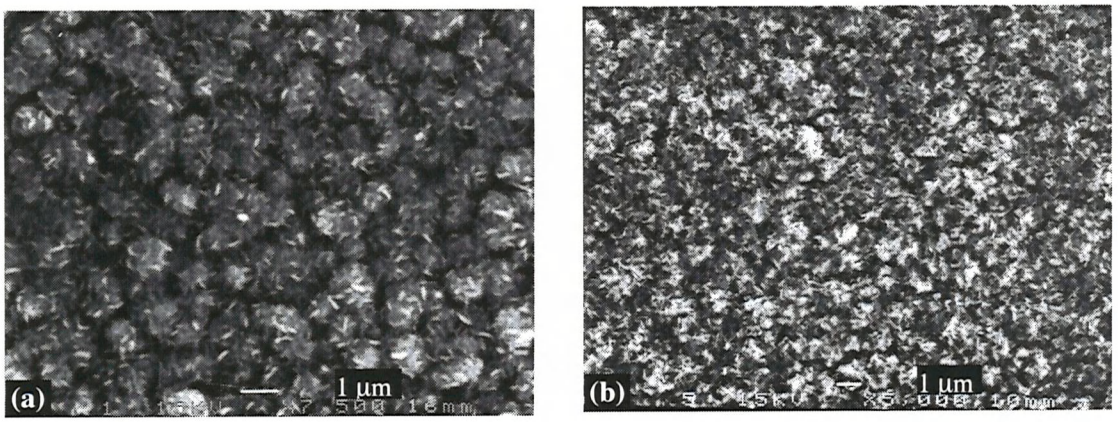

Figure 7.7 - ZnO deposited on alumina: (a) 1 μm ZnO; (b) 2 μm ZnO

There is another property of interest in the structure of the films. It can be seen that there are acicular-like features in both thicknesses of ZnO. Several of these features seem to bridge the gaps between adjacent nodules, and seem to exhibit no particular orientation. Given that these needle-like objects seem to be scattered over the surface, it is thought that they contribute to electrical conduction in the thin films. The random orientations of these features would seem to be a repercussion of the haphazard alignment of the alumina surface.

At first glance, the globular appearance of the ZnO films might seem rather disconcerting, perhaps even deleterious for the intended application as gas sensors. However, as established in Chapter 5, it is the small necks and bridges between adjacent grains of ZnO that confers high AO sensitivity on the ZnO thin films. Therefore, by this argument it would seem beneficial to promote the formation of as many links and connections between separate islands of ZnO as possible. It appears that the development of such structures may be enhanced by the discontinuous globular nature of the substrate material.

7.3 THE ELECTRICAL PROPERTIES OF ZINC OXIDE THIN FILMS

7.3.1 Current-voltage characteristics

All ZnO films tested in this thesis have gold contacts, whether they are fabricated from thin gold layers (TG prefix); gold cermet ink (CT prefix); or gold resinate ink (RT prefix). It is reported in the literature that gold forms a surface barrier on contact with ZnO (*Mead, 1965; Fabricius et al., 1986*). The ballistic equation of semiconductor sensor operation, presented in Chapter 5, requires accurate conductance measurements of the semiconductor films. If surface barriers exist between the sensor contacts and the semiconductor film, no accurate measurements of this kind can be made. Hence, it is required that all contacts onto the semiconductor films be Ohmic in nature. Thus, the first sensor electrical property investigation to be performed was measurement of the contact characteristics. The technique used to examine the nature of the contacts involved measurement of the I-V characteristics of each film.

Sensor substrates were individually mounted upon a thermo-electric heater/cooler inside a light-tight vacuum chamber, which was pumped through an orifice by an oil-filled diffusion pump. A proportional-integral-derivative (PID) controller was used to drive the heater/cooler. It was found that the controller could maintain the temperature of the samples to better than ± 0.1 K, based on the minimum scale reading of a temperature monitor. Previously, wires had been attached to the gold contacts of each sensor; these were connected to a multi-pin vacuum feed-through, enabling the films to be connected to equipment external to the vacuum chamber.

Before any measurements were made, all films were baked for several hours under *vacuo*. at a temperature of 373 K, until all of the film conductances were observed to be stable. During the bake-out, the conductance of all films was observed to increase, initially rapidly, and then more slowly. This behaviour is thought to be due to the slow desorption of species that influence the electronic structure of the zinc oxide (see Chapter 10 for a more in-depth study). Figure 7.8 shows a typical bake-out curve for the two bare 1.0 μm semiconductor films on substrate TG10A.

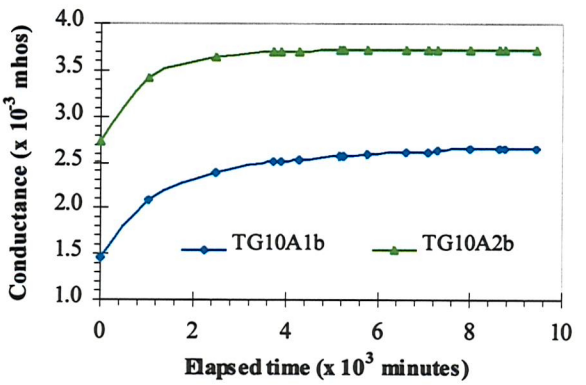

Figure 7.8 - 1.0 μm film conductance change with time at 373 K

Figure 7.9 is a schematic of the apparatus used for the I-V measurements. A precision DC voltage source (Time Electronics DC voltage calibrator type 2003S) was connected across the film under measurement, whilst the current flowing in the circuit was measured by a Keithley digital multimeter (model 179A). The voltage across the ZnO film was cycled once between +1.0 and -1.0 V in 0.05 V steps, so that 41 measurements were made in total. At each voltage setting, the current flowing in the circuit was recorded. This procedure was repeated three times for each of the films on the substrate. All measurements were performed in a dark vacuum chamber at pressures of less than 10^{-5} mbar and 314 K, to prevent any confusing influence of gases and photoconduction, and were only commenced once conductance stability of the films had been ensured. Only samples TG08A, TG10A and TG11A have been tested, because sensors from these depositions have been used in subsequent AO exposure experiments.

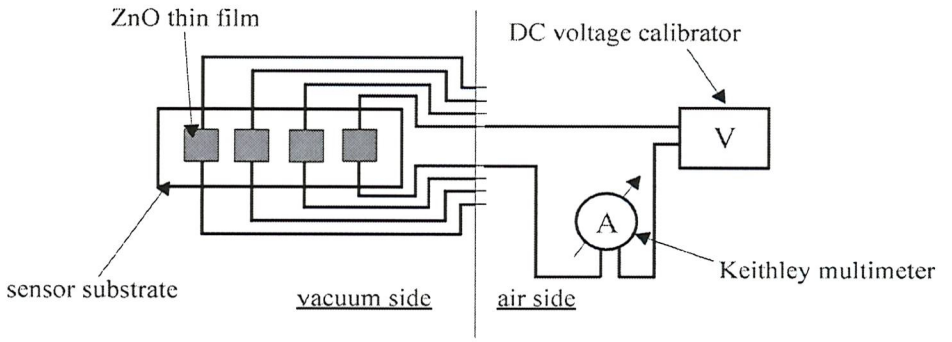

Figure 7.9 - Equipment used for I-V characteristic measurements

Since Ohm's law states that V = I.R, a linear current-voltage plot is sufficient to demonstrate Ohmic behaviour. Linear functions were fitted to the averaged data recorded from each film. The figure below shows a typical example of the type of plot generated.

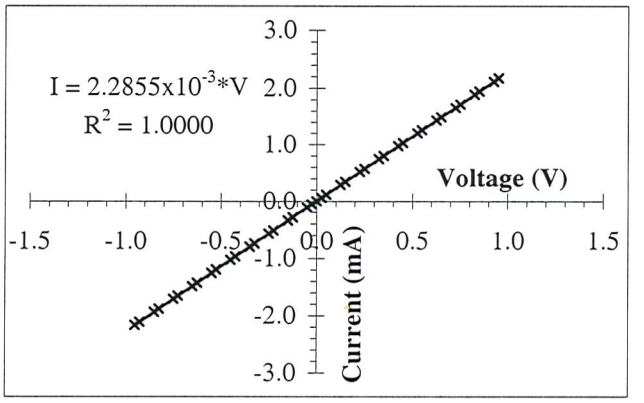

Figure 7.10 - Typical I-V plot at 314 K (for film TG10A1b)

It was found that the correlation coefficients of all linear functions were 0.9995 or above (41 data points), with many exactly 1.0000. Since all twelve ZnO films tested exhibited linear current-

voltage relationships, hence Ohmic behaviour, it is assumed that the gold-ZnO contacts are also Ohmic in nature. Thus, the reports of contact potentials between gold and zinc oxide appear not to be applicable to the devices described in this work, and any conductance measurements made will, therefore, accurately represent the true conductance value of the device under test.

7.3.2 The electronic structure of ZnO

Pure zinc oxide is an intrinsic semiconductor (*Hirschwald et al., 1981*), with a large band-gap of about 3.2 eV at room temperature. In comparison, the band-gaps of germanium and silicon are about 0.67 eV and 1.1 eV, respectively (*Callister, 1991*). However, under normal preparation conditions no intrinsic ZnO is formed, rather, the result is an n-type extrinsic semiconductor.

Many metal oxides exhibit semiconducting behaviour because of the presence of point defects in the material lattice, and ZnO is no different (*Jarzebski, 1973*). These defects are departures from stoichiometry and so, in general, can result from either a metal atom in an interstitial site, or an oxygen vacancy in the lattice. Both defects may introduce acceptor or donor levels in the electronic structure of the material (see Chapter 4 for definitions of these terms). Other substances - dopants - may also be added to the oxide, to introduce additional donor or acceptor levels.

The defects in ZnO responsible for the n-type behaviour are excess, interstitial zinc atoms and **not** oxygen vacancies (*Neumann, 1981; Bonasewicz et al., 1986*). Thus, the formula of zinc oxide should really be written $Zn_{1+\delta}O$, where δ is a small number representing the excess, interstitial zinc atom donors. Within the matrix, thermal processes ionize some of the interstitial zinc atoms - the resulting electrons occupy energy levels inside the conduction band of the material. It is important to note that because the excess zinc atoms are bound within the ionic crystal, they do not act as holes. Therefore, the only charge carriers in zinc oxide are electrons.

As more zinc atoms are added in interstitial sites, the conductivity of the ZnO sample becomes larger. It is clear that this relationship between the concentration of zinc donors and material conductivity is the explanation of the observed resistivity increase with oxygen content during sputtering (Section 7.2.2). Increased oxygen concentration in the sputtering mix reduces the density of interstitial zinc atoms, thereby reducing the number of donors in the matrix and, consequently, the number of available charge carriers.

It is commonly accepted that p-type zinc oxide has never been formed (*Eger et al., 1975*), even when the sample has been heavily doped with substances that act as acceptors (*Bonasewicz et al., 1986*). The lack of observable p-type conductivity, at normal conditions, has been attributed to

acceptor compensation by donors within the lattice (*Mandel et al., 1964*). However, there are two studies reporting evidence indicating that, under certain conditions, ZnO might undergo a change from n to p-type. The first investigation showed that, at elevated temperatures (573 - 1000 K), there was a marked alteration in the electrical properties of zinc oxide single crystals, which was attributed to a change of predominant charge carrier (*Chandra et al., 1967*). A second study found that, whilst under the influence of oxygen gas, zinc oxide powders would display behaviour explainable only by the presence of surface p-type material in the powder grains (*Cimano et al., 1963*).

7.3.3 Charge-carrier type study

It is possible to determine the type of charge carrier within a semiconductor by using the Seebeck effect (*Smith, 1964*). The Seebeck effect, which was discovered in 1821, is one of three distinct kinds of thermoelectric effect - the other two are also named after their discoverers, Peltier and Thomson. Seebeck found that a thermoelectric voltage was generated in a circuit containing two conducting materials, if the junctions between the materials were maintained at different temperatures. Moreover, if one of the conductors is a semiconductor, the sign of the thermoelectric voltage is indicative of the predominant charge carrier type within the semiconductor (*Tauc, 1962*). The magnitude of the thermoelectric voltage is proportional to the temperature difference between the hot and cold junctions, and the conductivity of the semiconductor.

The derivation of the equations describing the thermoelectric voltage is well beyond the scope of this investigation. Instead, the diagrams in Figure 7.11 demonstrate the application of the effect to the determination of the charge carrier type in a semiconductor sample.

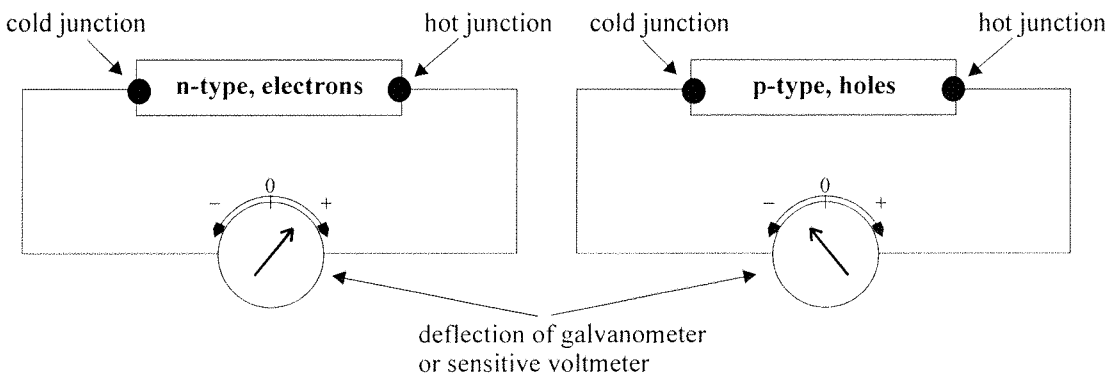

Figure 7.11 - Application of Seebeck effect to carrier type determination

Samples of ZnO from many of the depositions conducted to date have been tested in this manner. To perform the experiments, two probes were formed from long, thin pieces of copper wire. One of the probes was maintained at room temperature (~ 293 K), and was connected to the negative

terminal of a light-beam galvanometer. The other probe was connected to the positive terminal of the galvanometer and the free-end wrapped tightly around a soldering iron to heat it - a technique modified from that of Seeger (*Seeger, 1973*). Typically, the end of the hot probe was maintained at a temperature of approximately 470 Kelvin, as measured by a thermocouple. Due to the dimensions of the conductors, the end of the heated probe at the galvanometer was not significantly different to that of the unheated probe.

Both probes were then placed on the semiconductor sample under test, cold first and then hot. When the hot probe was placed on the material, the light spot on the galvanometer scale moved. The polarity of the thermoelectric voltage, hence direction of spot deflection, was checked against some semiconductor samples of known type[¶]. Consistent with the literature, it was found that the spot moved to the right when the sample was n-type and to the left when the sample was p-type. Table 7.4 summarizes the results gathered.

Sample	Thickness (μm)	Conductivity ($(\Omega.cm)^{-1}$)*	n-type	Voltage (relative)	AO sensors
TG05	1.00	100.000	Y	VS	-
TG06	1.00	5.556	Y	M	-
TG07	2.00	4.504	Y	S	-
TG08	0.50	1.835	Y	W	TG08A
TG09	0.50	0.055	Y	W	-
TG10	1.00	1.623	Y	S	TG10A
TG11	2.00	0.740	Y	S	TG11A
RT16	0.24	N/M	?	N/M	-
RT17	0.50	0.091	?	N/M	-
RT18	0.50	7.752	Y	S	-
RT19	0.50	0.032	Y	W	-
RT20	0.40	4.735×10^{-4}	?	N/M	-
RT21	0.28	2.585×10^{-3}	?	N/M	FM/FS
CT16	0.24	N/M	?	N/M	-
CT17	0.50	0.049	Y	W	-
CT18	0.50	1.324	Y	S	-
CT19	0.50	0.020	Y	VS	-
CT20	0.40	3.114×10^{-4}	?	N/M	FM/FS
CT21	0.28	1.702×10^{-4}	?	N/M	-

Y = yes; ? = not conclusive; N/M = not measurable VS = very strong (at least full scale deflection); S = strong; M = medium; W = weak; FM = flight model, FS = flight spare (see Chapter 11); * determined at room temperature.

Table 7.4 - Results of carrier type experiments

In this manner, most ZnO samples tested - including all those later tested in AO exposure experiments - were found to exhibit n-type behaviour. However, some samples did not demonstrate any deflection of the galvanometer spot, no matter to what sensitivity range the device was set. This lack of movement does not indicate p-type material, but rather that the

[¶] Samples kindly supplied by Dr Graham Ensell, Department of Electronics and Computer Science

thermoelectric voltage was too small to be measured. Indeed, there seemed to be a correlation with material conductivity - in general, the samples that did not generate a noticeable deflection seemed to be low conductivity ZnO.

7.3.4 Donor level analysis

Equation (4.14) showed that one way of determining the depth of the donor level below the bottom of the conduction band, is to measure the conductance-temperature characteristics of the zinc oxide. Since the magnitude of the donor level can be used to infer the donor species, this value is of importance in fully establishing the electrical characteristics of the semiconductor. For this reason an experimental investigation was conducted.

In this investigation, only those ZnO samples subsequently used as AO sensors have been examined. These samples are labelled TG08, TG10 and TG11, in Tables 7.1 and 7.4. Each sample in fact consists of four separate ZnO films on a substrate, numbered TG08A1b, TG08A1c, TG08A2b, and TG08A2c etc. Thus, twelve individual ZnO samples have been investigated, six bare zinc oxide films (b-series sensors) and six covered with silicon dioxide (c-series sensors).

The apparatus used to perform these measurements was relatively simple. Substrates were individually mounted on a thermo-electric heater/cooler inside a light-tight vacuum chamber, which was pumped through an orifice by an oil-filled diffusion pump. A proportional-integral-derivative (PID) controller was used to drive the heater/cooler. It was found that the controller could maintain the temperature of the samples to better than ±0.1 K, based on the minimum scale reading of a temperature monitor. Previously, wires had been attached to the gold contacts of each sensor. These were soldered to a multi-pin vacuum feed-through, enabling the films to be connected to equipment external to the vacuum chamber. A Keithley digital multimeter (model 179A TRMS) was used to make two-point conductance measurements of the samples.

All conductance measurements were performed in the dark, under vacuum and were taken at temperature intervals of 5 K from 373 K to 258 K, and then back to 373 K. The natural logarithms of the conductance were then plotted against the reciprocal of the temperature readings. A linear function was fitted to the data - Figure 7.12 shows a typical example - the gradient of the line was used to calculate the donor level, see Equation (4.14).

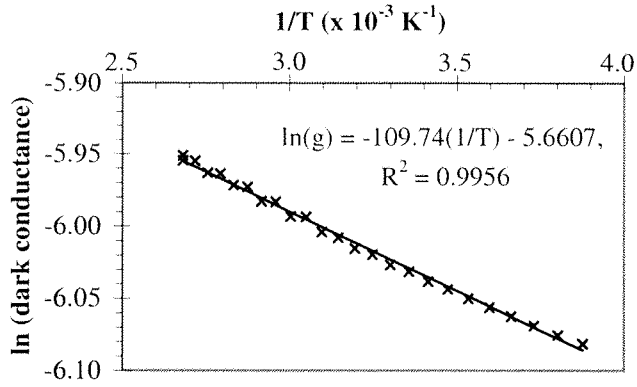

Figure 7.12 - An example plot used to calculate donor level from TG10A1b

The test was then repeated twice more for each film on the substrate. The substrate was then changed for the next, and the above process repeated. All donor levels measured in this way are recorded in Table 7.5. The columns headed ε_d #1, #2, #3 represent the results from the three measurements, whilst the ε_{mean} value is the mean donor level on each of the three substrates. The mean of all readings from all films is also presented.

Film	Thickness (μm)	ε_d (eV) #1	ε_d (eV) #2	ε_d (eV) #3	ε_{mean} (eV)
TG08A1c	0.5	0.056	0.056	0.054	0.070
TG08A1b	0.5	0.084	0.086	0.083	
TG08A2c	0.5	0.065	0.066	0.065	
TG08A2b	0.5	0.076	0.076	0.073	
TG10A1c	1.0	0.014	0.013	0.013	0.014
TG10A1b	1.0	0.019	0.018	0.017	
TG10A1c	1.0	0.012	0.012	0.011	
TG10A1b	1.0	0.014	0.014	0.013	
TG11A1c	2.0	0.032	0.030	0.028	0.033
TG11A1b	2.0	0.024	0.023	0.022	
TG11A1c	2.0	0.043	0.042	0.041	
TG11A1b	2.0	0.036	0.036	0.036	
Mean	-	-	-	-	0.039

Table 7.5 - Donor level experiment results

All the ZnO samples tested in this fashion were deposited using the same sputtering apparatus and conditions (see Table 7.1). Therefore, it is expected that the samples should all have similar compositions and electrical properties. It can be seen from the results presented in Table 7.5 that the measured donor levels are in relatively good agreement with one another. Also, the presence of a silicon dioxide layer appears to have no influence on the depth of the donor level. Yet there does appear to be a small spread of results within each film group and over the three groups as a whole. These variations are probably caused by random uncertainties in the method;

measurement errors; effects of carrier mobility change with temperature and slight differences in film structure resulting from heterogeneities during deposition.

The most probable donor level in the ZnO films examined is 0.039 ± 0.004 eV. The range of plausible values was generated using the formula $\pm\frac{\sigma}{\sqrt{n}}$, where σ is the standard deviation of the data and n is the number of readings (*Hey and Cox, 1996*). For comparison to this measured value, several published values of the donor level in ZnO are given in Table 7.6, along with the figure calculated herein. Donor levels at a depth of 0.02 to 0.05 eV are attributed to interstitial zinc. Given the simplicity of the technique and the assumptions made in the development of Equation (4.14), the agreement between published values and the figure that has been found in this work is encouraging.

Form	ε_d (eV)	Reference
Single crystal	0.02	*Chandra et al., 1965*
Not stated	0.03 to 0.035	*Hartnagel et al., 1995*
Thin film	**0.039 ± 0.004**	**This work**
Single crystal	0.043 to 0.045	*Hagemark and Chacka, 1975*
Single crystal	0.046	*Hutson, 1957*
Not stated	0.05	*van de Pol, 1990*
Single crystal	0.051	*Hutson, 1957*

Table 7.6 - Published values of donor levels

7.4 PHOTOCONDUCTIVITY OF ZINC OXIDE

In common with other semiconductors, ZnO exhibits photoconductivity. However, because of the large band gap (~ 3.2 eV), fundamental absorption occurs only within the UV region of the electromagnetic spectrum (*Mollwo, 1954*), see Figure 7.13. The marked decrease in absorption coefficient at around 370 - 380 nm is the edge of the fundamental absorption regime, and indicates the width of the band-gap of the material. For this reason, ZnO thin films have been used as UV detectors (*Fabricius et al., 1986*). Indeed, it is reported that when used as a pigment in paints, ZnO has the highest UV absorption of all those commercially available (*Sax and Lewis, 1987*).

Due to the large coefficient of absorption, photoconductivity in ZnO only occurs within the surface regions of the material (*Heiland, 1961*). In fact, the depth of photon penetration - approximately 0.1 μm - is roughly the same thickness as the region influenced by the presence of charged species on the semiconductor surface (see Chapters 4 and 5).

It appears that there are two regimes of photoconductivity in ZnO - one a fast, reversible process, the other a slow, irreversible process. When illuminated with band-gap light, the conductivity of the ZnO sample initially increases rapidly but, after a period of a few fractions of a second to a few seconds, the increase soon saturates. If the illumination is switched off, the conductivity of the sample returns to its pre-illuminated value and so no semiconductor properties are permanently altered. The literature shows that the fast effect is related to the double ionization of previously singly ionized interstitial zinc ions (*Mollwo, 1954*).

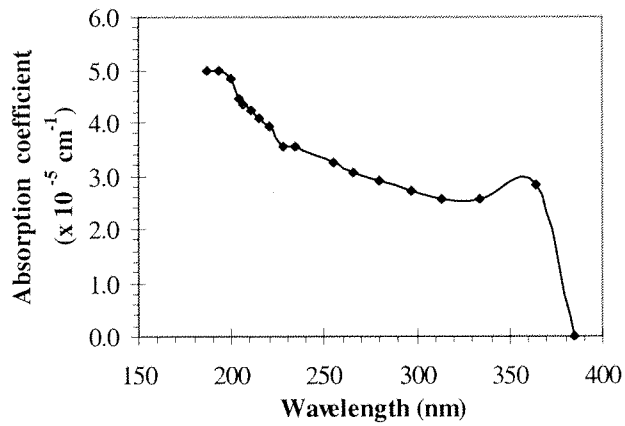

Figure 7.13 - Absorptance of ZnO (after *Heiland et al., 1959*)

Of more importance in this work is the slow, irreversible effect, which occurs with continued UV exposure. When a UV photon of energy larger than the band gap is absorbed in ZnO, an electron-hole pair is formed. The electron is promoted into the conduction band of the material, whereas the hole resides in the valence band. Frequently, the surface of ZnO is negatively charged due to the presence of chemisorbed oxygen (again, see Chapters 4 and 5). The negative charge has the effect of repelling conduction band electrons, but attracting positive valence band holes.

When the holes reach the ZnO surface, they combine with surface oxygen ions, thereby neutralizing them (*Mollwo, 1954; Collins and Thomas, 1958*). The neutral oxygen atoms are then only weakly physisorbed, rather than strongly chemisorbed, and may easily desorb. However, it is not only adsorbed AO that is photodesorbed, lattice-bound oxygen may also be removed by this process. Thus, the surface of a UV-illuminated ZnO sample becomes progressively richer with respect to Zn concentration. Hence, when the illumination is terminated, the conductivity of the sample is found to be higher than before irradiation. Although this effect is termed 'irreversible', if the surface is exposed to oxygen the original conductivity is eventually recovered.

It is also found that the number of photo-electrons produced per incident photon falls with accumulated photon flux (*Collins and Thomas, 1958*), as does the yield of photo-desorbed oxygen (*Cunningham et al., 1975*). It has been suggested that the ever increasing surface concentration of Zn is responsible for this apparent reduction of quantum efficiency (*Gilligan, 1967*).

7.5 ATOMIC DIFFUSION IN ZINC OXIDE

The diffusion of oxygen and zinc atoms in various forms of zinc oxide has been studied widely. A valuable review of the processes and investigations is given by Neuman (*Neumann, 1981*).

Description of the mechanics of diffusion is beyond the scope of this thesis, so only a few remarks will be made and formulas will be quoted without proof. The interested reader is referred to standard texts for further information (*Crank, 1956; Callister, 1991*). Diffusion in materials is often described by a diffusion coefficient, D. Usually the coefficient displays an Arrhenius-type temperature dependency:

$$D = D^0 \exp\left(\frac{-Q}{kT}\right) \tag{7.3}$$

Where:

D = diffusion coefficient ($cm^2.s^{-1}$)

D^0 = frequency factor ($cm^2.s^{-1}$)

Q = activation energy (eV)

k = Boltzmann's constant ($J.K^{-1}$)

T = absolute temperature (K)

Within a semi-infinite media, provided that the initial concentration is uniform and the surface concentration remains constant, it is possible to show that the time taken for a species to diffuse to a given distance can be approximated by:

$$\frac{x^2}{D} \tag{7.4}$$

Where:

x = diffusion depth (cm)

Neumann has tabulated several frequency factors and activation energies for both zinc atoms and oxygen atoms diffusing in stoichiometric ZnO (*Neumann, 1981*). The table below presents the averages of the values found in Neumann's review, which are widely scattered.

Species	D^0 ($cm^2.s^{-1}$)	Q (eV)
zinc	44.2	3.2
oxygen	1.63×10^{11}	4.11

Table 7.7 - Zn and O diffusion coefficients

The smallest crystallite size measured by XRD was found to be ~ 21.8 nm. It is therefore possible to calculate the time taken for oxygen and zinc atoms to diffuse through a distance of this magnitude. A typical upper temperature used in the AO exposure experiments performed (see Chapter 8) is 373 K, thus it is necessary to calculate the diffusion coefficients (D) for this temperature. Using Equation (7.3) the diffusion coefficients are found to be 5×10^{-45} $cm^2.s^{-1}$ and 2×10^{-42} $cm^2.s^{-1}$ for oxygen and zinc respectively.

Equation (7.4) can thus be used to estimate the time taken for diffusion through a given thickness of material. At the upper experimental temperature employed, it would take ~ 8×10^{32} s for oxygen to diffuse through a typical crystallite, and ~ 2×10^{30} s for zinc atoms to cover the same distance. Clearly, the diffusion of these species, even over very small distances, can be neglected in any reasonable experimental time-scale. Investigations of Morrison (*1955*) confirm that absorption, which would require atomic diffusion, is not responsible for the influence of oxygen on ZnO but, rather, it is the process of adsorption that is the dominant mechanism.

7.6 SUMMARY

This chapter has examined some of the key properties of zinc oxide - an n-type semiconducting metal oxide. RF sputtered ZnO films have been investigated using X-ray diffraction, SEM, thermoelectric, conductance-temperature and current-voltage methods.

The XRD analysis showed that the ZnO crystallites are aligned preferentially, with their c-axes perpendicular to the substrate surface. It was postulated, from inter-planar spacing measurements, that the thin films are deposited with a residual tensile stress component, probably caused by interfacial mismatch between the alumina substrate and the zinc oxide film. The XRD scans also allowed an estimate of the crystallite sizes within the polycrystalline layer. The size range found, 218 - 373 Å, agrees satisfactorily with values published in the literature.

Electron microscopy investigations revealed that, on a large scale, the ZnO surface morphology was mainly affected by the underlying structure of the alumina substrate. However, on a smaller scale, the structure of the films was found to consist of many bridging, small acicular features. It was postulated that the ZnO crystallites had grown perpendicular to the local alumina surface, and not perpendicular to the plane of the substrate. As a result, the XRD crystallite size measurements are probably underestimates of the true values.

Several electrical properties have also been investigated. Current-voltage measurements demonstrated that the gold-ZnO contacts on the AO sensors are Ohmic. The Seebeck effect was used to determine the conductivity type of several ZnO films. The experiments demonstrated that all ZnO films exposed in AO experiments are n-type material, as expected from the literature. Conductance-temperature investigations were performed to measure the donor energy level. The level, probably associated with interstitial zinc atoms, was found to lie 0.039 ± 0.004 eV below the bottom of the conduction band.

The photoconductivity of ZnO was examined by literature review. It was found that UV irradiation may stimulate oxygen desorption from the ZnO surface, enriching the composition with respect to Zn. Lastly, a brief examination of oxygen and zinc diffusion in ZnO showed that these processes are very slow and, at typical experimental temperatures, can be ignored in any reasonable time frame.

All of these investigations and studies result in one single, important conclusion - the ZnO films used for the work in this report are behaving as normal ZnO material. The next chapter of this thesis discusses the AO experiments that have been performed with six AO sensors.

CHAPTER 8

LABORATORY EXPERIMENTS

Six sensors of the type labelled TG, the design of which was introduced in Chapter 6, have been tested in a hyperthermal atomic oxygen facility. The purpose of this chapter is to describe the procedures used in the AO exposure experiments, which were designed to satisfy the research aims of this project. The text below includes details of the pre-experimental preparation; the equipment used to perform the AO exposures; the ancillary devices used to record sensor behaviour and the exposure conditions employed during the tests.

8.1 INTRODUCTION AND AIMS OF EXPERIMENTS

All of the ground-based AO exposure experiments described in this thesis have been conducted in a hyperthermal AO test facility called ATOX, which is located at the European Space Research and Technology Centre (ESTEC). In sympathy with the goals of this research, which were outlined in Section 1.4, the aims of the programme were to:

1. Test different thicknesses of ZnO semiconductor sensor.
2. Demonstrate that the ZnO thin films respond to AO exposure.
3. Determine whether degree of sensor response is dependent on the level of AO flux.
4. Test the effects of different regeneration temperatures.
5. Investigate the influence of molecular oxygen fluxes.
6. Examine the influence of UV irradiation.

In order to achieve these aims, it was necessary to perform a number of experiments. The sections below describe the equipment used and the way in which the tests were performed.

8.2 EQUIPMENT USED IN THE EXPERIMENTS

8.2.1 The atomic oxygen source

The ATOX facility is of the laser-induced breakdown variety, and is based on the operational principles pioneered by Caledonia *et al.* at Physical Science Inc. (*Caledonia et al., 1987; Osborne, 1998a*). A schematic of the AO source vacuum system is given in Figure 8.1.

The source comprises of three vacuum chambers. The first is called the sample compartment. This chamber is used as a 'load-lock', so that the samples to be exposed to AO may be loaded onto a sample tray without destroying the vacuum in the other chambers. Operation in this

manner speeds AO testing by reducing the necessary time to evacuate the chambers to vacuum. The sample compartment is evacuated by a turbo-molecular pump and typically reaches base pressures of ~ 10^{-6} mbar.

It is within the main chamber that the AO exposures are conducted under vacuum conditions. The large (150 L), main chamber is pumped simultaneously by turbo-molecular and cryogenic pumps. Base pressures are of the order of 10^{-9} mbar but, during AO exposures, the pressure varies around 10^{-6} mbar due to the gas load imposed by injection of molecular oxygen. Lastly, there is the nozzle compartment, which contains a copper nozzle that is used in the AO formation process. This compartment has its own pumping system for operation from atmospheric pressure. However, during AO exposures, it is evacuated by the same pumps as the main chamber.

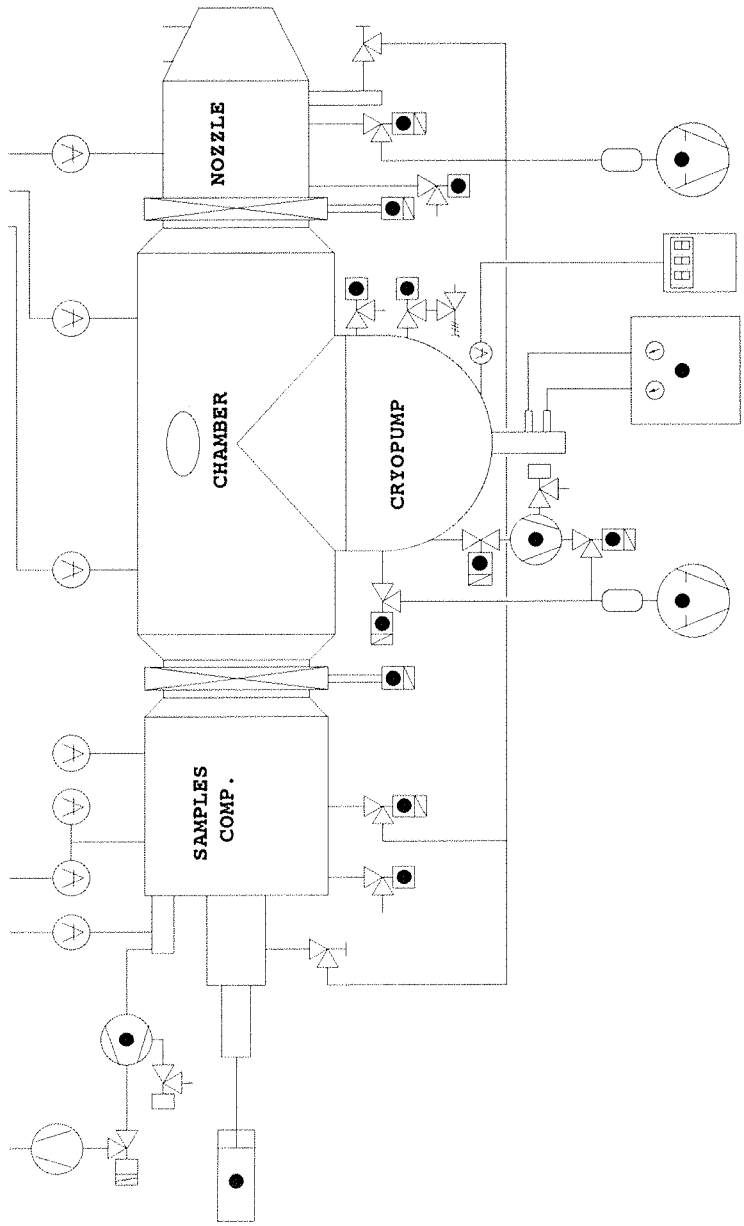

Figure 8.1 - ATOX vacuum system schematic

A pulsed, transversely-excited atmospheric (TEA), carbon dioxide laser is used as the energy source to form AO within the vacuum chambers of ATOX. Before the laser is fired, oxygen molecules are injected into the water-cooled nozzle by a fast acting electromagnetic valve. The amount of gas injected into the nozzle volume is measured by a flow meter. There are two methods with which to control the mass of oxygen injected into the nozzle. The first is to alter the length of time for which the valve is open, which is achieved by altering settings on the valve driver unit. Commonly, this will be set at about 475 μs with a line pressure of 21 bar. Secondly, the compressive force on the valve's two springs may be adjusted using a spanner on the valve body. Both of these adjustments may be made in 'real time' during an AO exposure.

When fired, the laser pulse is focussed at a point inside the nozzle where its energy is absorbed by the oxygen molecules, which dissociate and ionize to form a hot (> 20,000 K) plasma. Initiation of the plasma creates a blast-wave that accelerates the oxygen ions and electrons through the nozzle. During acceleration, the plasma cools and becomes frozen. However, the rate of cooling is slow enough to allow ion-electron recombination, yet fast enough to prevent slower atom-atom recombination processes. In this manner, a pulse of fast oxygen atoms is generated and directed in an expanding beam towards the sample tray.

In ATOX, atomic oxygen flux is controlled by altering the mass of oxygen injected into the nozzle (achieved by the two methods described above). During a test, the flux is principally, and subjectively, gauged by the chromacity of the oxygen plasma. In comparison to AO flux, oxygen atom velocity is adjusted by changing the mass of oxygen gas processed per laser pulse. This is achieved by altering the delay between the injection of molecular oxygen and the laser pulse, typical delay values are 370 – 470 μs. The mass of oxygen processed per pulse is also a function of amount injected into the nozzle, hence, AO flux and atom velocity are cross-coupled. Atom velocities can be controlled over the range 6 - 10 $km.s^{-1}$. Thus, the source can simulate LEO and GTO orbital conditions alike.

The sample tray is used to support the materials or devices under test, and its position relative to the nozzle can be adjusted. Continued expansion of the AO pulse, once it has exited the nozzle, means that AO flux falls with axial distance from the nozzle exit plane; the nozzle exit effectively acts as a point source. It is expected from gas-dynamic theory that the AO flux should decrease at a rate proportional to the inverse of the square of distance from the nozzle exit (*Roberts, 1998*). Recent empirical investigations of the decay of AO flux in ATOX by the author have confirmed this expectation (*Osborne, 1998a*). This is one way to change the AO flux experienced at the sample tray - a second method is to change the laser repetition rate. The laser can operate at a

maximum of 7 Hz and it has been shown that the time-averaged AO flux changes linearly with repetition rate (*Osborne, 1998a*).

The pulsed nature of the AO beam means that the arguments presented in Section 2.3.2, with regard to the inconsistency of LEO simulation due to the high instantaneous pulse flux, applies to this source.

Unfortunately, AO is not the only species to which the samples under test are exposed. There remains a small amount of undissociated, yet excited, molecular oxygen (*Caledonia, 1988*) and possibly oxygen ions and electrons (*Caledonia et al., 1994*). However, of particular concern is the uncontrollable presence of a high level of UV and VUV photon-radiation generated by the large plasma temperature. Sample illumination with this light may cause some synergistic problems and, in ATOX, it has been found that the UV/VUV illumination is several orders of magnitude higher than that experienced in orbit due to solar irradiation (*Weihs and van Eesbeek, 1994*).

8.2.2 Data acquisition system

The ATOX test facility also includes a data acquisition system. At the heart of the system is a Macintosh computer. The computer controls a switch unit via programmes written in the BASIC (beginners all-purpose symbolic instruction code) language. This unit can be configured with many separate input channels and is essentially no more than a relay-based multiplexing device. The output from the switch unit can be directed either to a Hewlett Packard Digital Multimeter (DMM), or to a frequency counter manufactured by the same company.

When the computer commands the switch unit to send a particular input to the measurement device, it also instructs either the frequency counter, or DMM to take a measurement. In the case of the DMM, the measurement may either be a resistance, a voltage or a current. Communication between the computer, the switch unit, the DMM and the frequency counter is through HPIB cables and protocols. The author wrote the programme employed to control the acquisition system in the tests detailed herein (see Appendix A1 for listing).

8.2.3 The sensor temperature controller

During all experiments, a custom-made temperature controller was used to control the temperature of up to three sensor substrates to within ± 0.5 Kelvin of a set point. However, this device did not just control the temperature of the substrates, it also provided output signals of the sensor's temperatures to the data acquisition system, so that these could be recorded. The output signals were voltages, which could be read directly by the DMM connected to the data

acquisition system. Another output channel was also provided by the controller, this was used to set the desired substrate temperature. Changes in temperature were achieved by altering the set point of the controller.

8.2.4 The sample holder

The size of the sample tray in ATOX was found to be sufficiently large for three sensor substrates to be exposed simultaneously. Thus, a jig - referred to as a sample holder in this text - was designed by the author to accommodate this number of devices. The holder was fabricated from a machineable glass-ceramic (MACOR) because this material is highly resistant to AO attack and is also vacuum compatible, even at high temperatures under the influence of UV irradiation.

8.3 EXPERIMENTAL PROCEDURES AND CONDITIONS

8.3.1 Design of AO exposure experiments

The first experimental aim, to investigate the effects of semiconductor thickness, required that sensors of different thicknesses be used in the same AO exposures. Hence, the tests were conducted with two sensors of each of the available ZnO thicknesses. At the time of the experimental programme, only sensors of the first model introduced in Chapter 6 had been manufactured. Thus, all sensors employed thin gold contacts. Sensors from depositions TG08, TG10 and TG11 were selected for the study, because they were felt to be representative of those manufactured to that time, and had no visually observable flaws in the semiconducting elements. The actual devices chosen were those on substrates: TG08A (0.5 μm), TG10A (1.0 μm) and TG11A (2.0 μm).

In order to achieve the remaining aims outlined in Section 8.1, it was necessary to perform several different experiments. The second aim simply required that the conductances of the sensor films be monitored in an AO flow. Thus, it was decided that this objective could be satisfied in the experiments needed to investigate the third goal, which was to determine if the level of AO flux and magnitude of sensor response were correlated. To establish whether or not this is the case, a sub-set of experiments were designed with different flux levels, but with all other conditions - such as exposure and regeneration temperatures - fixed. In experiments TF1 - 4 and TF6, the AO flux was varied by altering the sensor-nozzle distance, whilst maintaining constant laser repetition rate. In experiment TF5, another method of changing the magnitude of AO flux was employed, which was to alter the laser repetition rate at a constant sensor-nozzle distance.

The fourth aim was to investigate the effects of regeneration temperature. Hence, the sensors were exposed to approximately constant AO fluence in experiments TF6 - 10. Constant AO fluence level was achieved by fixing the AO flux (sample-nozzle distance and laser repetition rate) and the exposure time. The exposure temperatures were also fixed, whilst in each experiment a different regeneration temperature was employed.

Lastly, one experiment, TF11, was performed without the TEA laser firing into the chamber so that only molecular oxygen was incident on the ZnO films. This test was conducted as a control experiment suitable for achieving the fifth experimental aim.

During all AO exposures, the samples were irradiated by VUV photons from the oxygen plasma (see Section 8.2.1), so the influence of this illumination could be easily explored by examining the data from the SiO_2 covered film in each sensor. Therefore, no dedicated experiment was performed to achieve this goal. The table below summarises the purpose and methods used in each experiment.

Experiment ID	Purpose	Quantity varied	Fixed parameters
TF1	Flux study	AO flux (distance)	Regeneration and exposure temperature
TF2	Flux study	AO flux (distance)	Regeneration and exposure temperature
TF3	Flux study	AO flux (distance)	Regeneration and exposure temperature
TF4	Flux study	AO flux (distance)	Regeneration and exposure temperature
TF5	Flux study	AO flux (repetition rate)	Regeneration and exposure temperature
TF6	Flux study	AO flux (distance)	Regeneration and exposure temperature
TF7	Regeneration study	Regeneration temperature	AO fluence, exposure temperature
TF8	Regeneration study	Regeneration temperature	AO fluence, exposure temperature
TF9	Regeneration study	Regeneration temperature	AO fluence, exposure temperature
TF10	Regeneration study	Regeneration temperature	AO fluence, exposure temperature
TF11	Molecular oxygen exposure	Molecular oxygen flux	Exposure temperature

Table 8.1 - Summary of experiment design

8.3.2 Pre-experiment preparation

Before any experiments could be conducted, the sensors to be tested required some preparation. Since the manufacturer deposits six sensors on three substrates, joined as a single sheet of alumina, it was necessary to separate the chosen sensors from the other devices. The detachment

of the three sensor substrates (each with two sensors) is aided by the presence of the laser-scribed lines, which allow the substrate to be fractured in a definite location, when cantilevered over a sharp edge.

The next step of sensor preparation involved making electrical contact to the heater electrodes. This was achieved by soldering wires directly onto the thick film tracks. Simultaneously, a K-type thermocouple was affixed onto one of the solder pads. The purpose of the thermocouple (with a reader) was to enable the substrate temperature to be monitored during the following stage of sensor preparation.

To enable sensor conductance measurement, electrical connections to the gold contacts associated with each ZnO film were necessary. The internal wiring of ATOX was such that short (15 - 20 cm) leads could be used to connect the films to a multi-pin vacuum feed-through. All of the leads used were PTFE (polytetrafluoroethylene) insulated, and terminated with connectors suitable for use with the feed-through. This plastic was chosen in preference to any other because it has low outgassing rates, and is known to be one of the more AO resistant polymers (*Harris, 1996*). A two-part, silver-loaded epoxy adhesive (Epo-Tek H21D) was applied to the problem of making permanent connection to the gold films.

Once leads had been placed on all eight gold thin films of the two sensors, the adhesive was cured at an elevated temperature. Instead of placing the substrate in an oven, the thick-film heater was connected to a DC power supply, the voltage of which was increased until a substrate temperature of 120 °C was maintained. At this temperature, the adhesive required a curing time of 20 minutes.

The next stage of sensor assembly was to attach a second temperature-measuring device (AD590KF) to the front face of the alumina substrate. The heater controller used this device to monitor the temperature of the substrate, rather than the thermocouple. Constant-current temperature sensors, like the AD590, have one significant advantage over thermocouples: their outputs are not subject to voltage losses over long cable runs. Again, a small amount of silver-loaded epoxy was used to adhere the temperature sensor to the substrate. After curing the epoxy, the thermocouple was detached from the substrate. The two sensors were then ready for use.

All sensor substrates were prepared in this way and then attached to the sample holder. Figure 8.2 shows the sensors mounted on this jig. The silver-coloured material in irregular blobs is the conductive adhesive used to make electrical contact between the gold films and the PTFE

covered leads, all of which are also visible. The small, dark, rectangular components located in the middle of the sensor substrates are the AD590 temperature sensing integrated circuits.

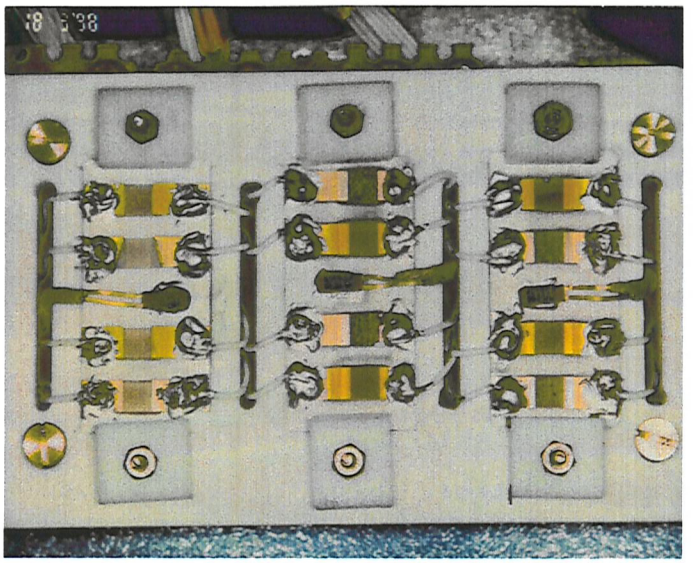

Figure 8.2 - ZnO substrates on sample holder L to R: TG08A; TG10A; TG11A

Subsequently, the sample holder was affixed to the ATOX sample tray, along with another AO sensor - a carbon-coated QCM (C-QCM). Following a check to see if all electrical connections were sound, the sample tray was mounted in the ATOX sample compartment. Figure 8.3 shows the sensors mounted on the sample tray in the vacuum chamber immediately prior to closing the compartment and pumping down to vacuum. In this figure, one can see that the sensor and AD590 leads have been bundled together - the bundle terminates at a connector attached to the vacuum feed-through.

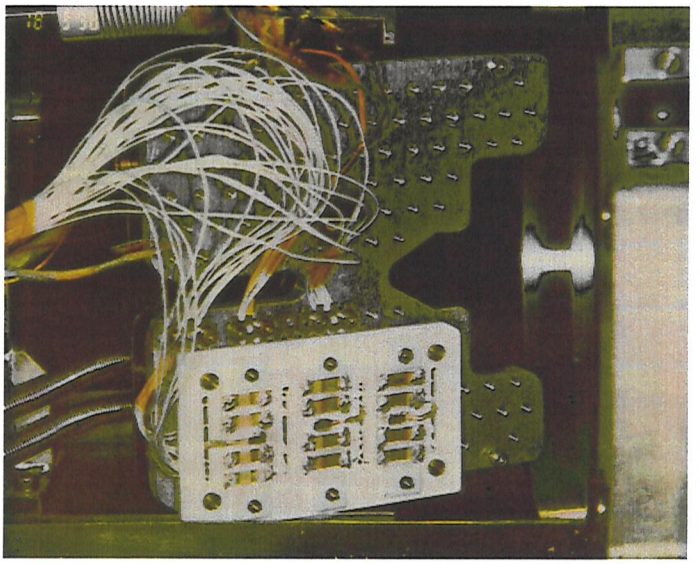

Figure 8.3 - Sensors mounted on sample tray inside ATOX compartment

Before the experimental programme was initiated, the films were baked at 323 K for 12 hours under vacuum (~ 10^{-6} mbar) to remove any contamination that may have adsorbed on the sensor surfaces during preparation, integration and installation. It also stabilized the conductance of the sensors.

8.3.3 Experimental procedure

Immediately prior to each AO exposure experiment, the films were heated or 'regenerated' at an elevated temperature for a given period under vacuum in the sample compartment. The temperature and duration of each regeneration phase are recorded in Table 8.2, which can be found at the end of this chapter. After cooling, the sensor holder was moved into position in the main chamber of ATOX. In this new position, the films were allowed to settle into thermal equilibrium with their surroundings, which was most significantly influenced by the cold (12 - 18 K) cryogenic pump. The position of the sensors relative to the nozzle was measured by the use of a scale previously marked on the ATOX rig by another researcher, believed to be accurate to ±1 cm.

Once a stable sensor temperature was noted on the data logger, AO exposure was commenced. The exposure temperature used in all of the experiments was set intentionally high, approximately 314 K. At lower temperatures, it was found that energy radiated from the oxygen plasma influenced the temperature of the substrates. With a high baseline temperature, the heater controller was able to maintain a stable temperature. The likely reason for this is that the temperature was controlled by active heat input but passive heat output; there was no active cooling of the sensors. At a low exposure temperature, any heat input from the plasma to the sensors would lead to a temperature rise that could only be compensated for by radiation and conduction away from the substrate. However, at higher exposure temperatures, the small heat input from the plasma could be compensated for by reduced heat input from the heaters.

The duration of AO exposure depended on the experiment being conducted. The tests to satisfy the second aim were continued until sensor saturation (see Chapter 5) was deemed to have occurred. Saturation was estimated by observing the recorded resistance values displayed on the computer screen. However, to investigate the influence of regeneration temperature, the AO flow was continued for a set time - in an attempt to generate a constant AO fluence in each experiment. After AO flow was ceased, the sensors were removed from the exposure chamber to the sample compartment, and heated to regenerate them before the next exposure.

In the last experiment, TF11, the laser was not allowed to fire into the vacuum chamber, thus no AO was created. In this case, only oxygen molecules were incident on the ZnO films. No direct

measure of O_2 flux was available during the experiment, although it is believed that the molecular oxygen fluxes experienced may be estimated as half of the incident AO flux under the same conditions of pulse rate and sensor-nozzle distance. The sensor was not regenerated after this experiment.

In all experiments, data was recorded by the data logger at the fastest rate possible, which was 20 seconds for a full sweep of 12 ZnO films; the C-QCM repeated at three times; 3 temperature sensors and the heater controller set-point temperature. Thus, the effective sample rate was 1 Hz, although each ZnO film was only monitored every 20 seconds. Clearly, a faster rate would have been desirable given that it is the ballistic rate of conductance change that is of importance to this work.

Table 8.2 provides all of the details of the AO exposure experiments performed. In all experiments, an independent measure of the AO flux was provided by the C-QCM, the temperature of this device was neither controlled nor monitored.

8.4 SUMMARY

Details of an experimental programme to test the ZnO-based semiconducting AO sensors have been presented in this chapter. All experiments were performed in the ATOX facility at ESTEC, the design and operation of which has been described. The sensors tested were of the design using gold thin films to contact the MOS elements. Preparation of the sensors for use in ATOX was detailed, as was the arrangement of the devices in the exposure facility. The experimental programme had six aims: to investigate the effects of semiconductor thickness; to gauge the response of the sensors to AO; to see if the sensor response was dependent on level of AO flux; to investigate the effects of regeneration temperature; to examine the influence of UV exposure and to determine the effects of molecular oxygen. Hence, several experiments were designed and performed to research these aims. Chapters 9 and 10 present analyses and discussions of the results gained from the programme described herein.

Experiment ID	Sensor-nozzle distance (cm)	Laser rate (Hz)	Oxygen flow rate (% of 500 mL.min^{-1})	C-QCM recorded AO flux (x10^{15} atoms.cm^{-2}.s^{-1})	Time in AO flux (min)	Average exposure temperature (K)	Approximate regeneration time (min)	Approximate regeneration temperature (K)
TF1	55	1	10.0 - 11.0	1.95820	22.00	312.9	720 +150	353 373
TF2	55	1	2.8 - 3.2	2.12618	22.00	312.6	150	373
TF3	75	1	2.8 - 3.0	0.90922	29.37	314.9	150	373
TF4	100	1	2.8 - 3.0	0.47048	30.00	316.0	148	373
TF5a	55	1	3.0 - 4.8	1.68481	20.20	313.2	632	373
TF5b	55	3	7.0 - 8.1	4.86014	13.00	313.4		
TF5c	55	5	9.9	7.85560	9.00	313.4		
TF6	65	1	2.7	1.41725	19.00	314.3	60	353
TF7	65	1	3.4	1.23385	19.00	315.4	60	373
TF8	65	1	4.0	1.12750	19.00	314.7	60	393
TF9	65	1	4.1 - 4.3	1.09544	19.00	314.6	60	416
TF10	65	1	4.5	1.14603	28.09	314.0	60	353
TF11a	65	1*	NR	0.0	10.00	313.4	Not performed	Not performed
TF11b	65	3*	9.0	0.0	5.00	313.4		
TF11c	65	5*	NR	0.0	5.00	313.5		

* denotes cold flow experiment, laser not operational; NR = not recorded

Table 8.2 - Experimental parameters

CHAPTER 9

ATOMIC OXYGEN RESULTS - ANALYSIS AND DISCUSSION

The atomic oxygen exposure experiments generated many results. The study below aims to examine solely those results directly connected to the action of atomic oxygen on the sensors, rather than those due to any ancillary effects like molecular oxygen and UV. Initially, results from sensors of three thicknesses of semiconductor are qualitatively compared to examine the influence of ZnO thickness upon sensor response. Several explanations for the observed differences in behaviour of the sensors are postulated, but only one description is found to adequately decipher all of the experimental observations. Subsequently, quantitative numerical analysis is conducted - using the ballistic model developed in Chapter 5 - to show how sensor response varies with magnitude of AO flux. Further characteristics of sensor operation are then determined. Finally, a practical use of the sensors is demonstrated by their application to a real AO flux measurement scenario.

9.1 ATOMIC OXYGEN INDUCED SENSOR BEHAVIOUR

9.1.1 Half-micrometre sensors

Figure 9.1 parts (a) and (b) display conductance data recorded from the two 0.5 μm sensors (TG08A1b and TG08A2b) exposed to AO in experiment TF1. Only the data from the two uncovered elements are given, along with the appropriate sensor temperature data. The arrows on the graphs indicate the moment at which the AO flow was commenced (24 minutes) - whence it was sustained for a total of 23 minutes. Prior to the initiation of AO flow, the conductances and, hence, temperatures of the two sensors changed rather markedly, particularly at about t = 4 minutes. This was due to the changing thermal environment that the sensors experienced as they were moved into the exposure chamber of ATOX, above the head of the cryogenic pump.

Immediately after initiation of AO flow, it is evident that the conductance of both sensors increased rapidly. After approximately 3.5 minutes of exposure the rate of conductance increase slowed down, so that at the time of AO flow cessation, the conductance of both sensors changed at a lower rate than at the start of exposure. Throughout the AO exposure it can be seen that there were a number of high amplitude oscillations in the conductance of both sensors, only some of which can be correlated to temperature excursions recorded by the AD590.

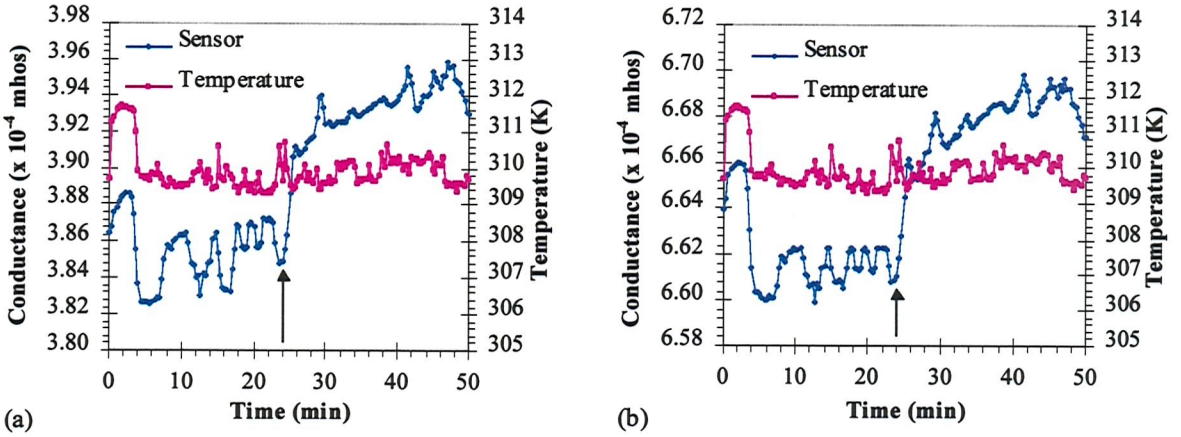

Figure 9.1 - Half micrometre sensor results from TF1: (a) TG08A1b; (b) TG08A2b

There is a remarkable similarity between the instantaneous conductance increase at the commencement of AO flow, and that experienced due to the temperature change already noted at t = 4 minutes. At the start of AO flow, no temperature excursions were recorded by the AD590, but it is accepted that this device may not be as responsive to changes in temperature (due to its thermal inertia and bonding effects) as the semiconductor films. Yet, if a sudden increase of substrate temperature was responsible for the jump in conductance, it should be evident in the silica-covered films that reside on the same substrate.

An examination of the data from TG08A1c and TG08A2c shows that these devices also experienced a conductance increase, but at a rate some ~ 4-5 times slower than the bare films. However, this change is attributed not to temperature alterations, but to the influence of UV (see Section 10.2) - if heating of the substrate did occur, the conductance gradients of all films thereon should be the same. Therefore, it can be concluded that temperature changes do not dominate the covered semiconductor sensors and, so, cannot be used to explain the sudden increase of conductance in the uncovered films. The only influence remaining that can explain the conductance increase at the start of exposure is the action of atomic oxygen.

The recorded behaviour is the exact opposite to that foreseen by the physical descriptions of AO sensor operation, and to the findings of other experimenters, both of which were presented in Chapter 5. These arguments stated that the conductance of the films should decrease as a result of electron depletion associated with oxygen chemisorption. Apparently, however, such a process did not occur. On the contrary, it seems as though the carrier concentration in the material actually increased as a result of AO action!

For comparison, Figure 9.2 consists of two graphs derived from the same sensors in the next experiment, TF2. Again, the arrows indicate the time at which the AO flux was initiated.

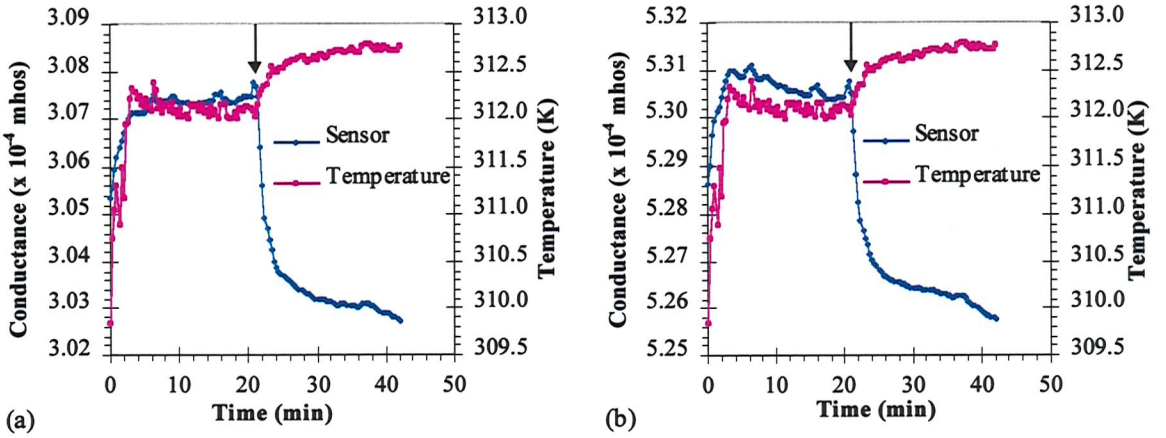

Figure 9.2 - Half micrometre sensor results from TF2: (a) TG08A1b; (b) TG08A2b

It is clear from these two graphs that, upon commencement of AO flux, the conductance of both sensors decreased. In each case the initial decrease was rapid. However, as exposure progressed, the rate of conductance reduction became slower until eventually, at around t = 36 minutes, the decrease seemed to halt completely. The small decrease of conductance apparent between t = 37 minutes and t = 42 minutes, when the AO flux was terminated, is attributed to a sudden increase of AO flux caused by an experimenter implemented change of the ATOX operating conditions. Such changes are frequently made during experiments in an attempt to compensate for pulse valve wear and laser output power variations. Since relative AO flux in ATOX is gauged by the chromacity of the oxygen plasma, it is sometimes difficult to prevent overcompensation of the changing parameters, which is exactly what appears to have occurred in this experiment.

Clearly, the overall response of the sensor to AO bombardment and its ensuing adsorption in exposure TF2 is just as anticipated in the previous chapters. Specifically, though, two features should be noted. Firstly, the decrease of sensor conductance immediately after the initiation of AO flux is the most rapid observed during the whole AO exposure. This observation agrees with the predictions of the theoretical model of sensor operation that was developed in Chapter 5, and the findings of other experimenters also described in that chapter.

Secondly, the rate of conductance change slowed with exposure until a saturation phase was observed, at which point the conductance did not seem to be changing further - the sensor curves in Figure 9.2 parts (a) and (b) both flattened to become nearly parallel to the abscissa at around 36 minutes. Notice also that, whilst the sensors were exposed to AO, the conductance data are free of any large-scale oscillations, unlike the results of TF1 (Figure 9.1). In all following experiments (TF3 - 10), the 0.5 μm sensors performed as they did in experiment TF2 - that is, with decreasing conductance in response to an impinging AO flux.

Therefore, the two half-micron, bare ZnO sensors TG08A1b and TG08A2b displayed a distinct change of behaviour at the beginning of the test programme. During the first experiment TF1 (the fluence of which was 2.584 x 10^{18} atoms.cm^{-2}), the sensors unexpectedly increased in conductance. In the next, and all subsequent experiments, the conductance of the sensors decreased upon exposure to AO - as expected. It seems as though some amount of AO exposure was necessary to 'condition' the sensors, after which they behaved in a fashion that is considered 'normal'.

9.1.2 One-micrometre sensors

The two 1.0 μm sensors also demonstrated erroneous conductance increases as a result of AO exposure in experiment TF1; this is exhibited in Figure 9.3. Once more, the conductance of the sensors increased most rapidly at the start of AO flow, thereafter the rate of change slowed. In the case of sensor TG10A1b, part (a) of the figure, the increase of conductance appeared to be smooth and monotonic, with no large-scale fluctuations. On the other hand, the results from TG10A2b in part (b) show that the conductance of this device increased erratically throughout the experiment - a pattern somewhat like an enhanced response of the two 0.5 μm devices in TF1.

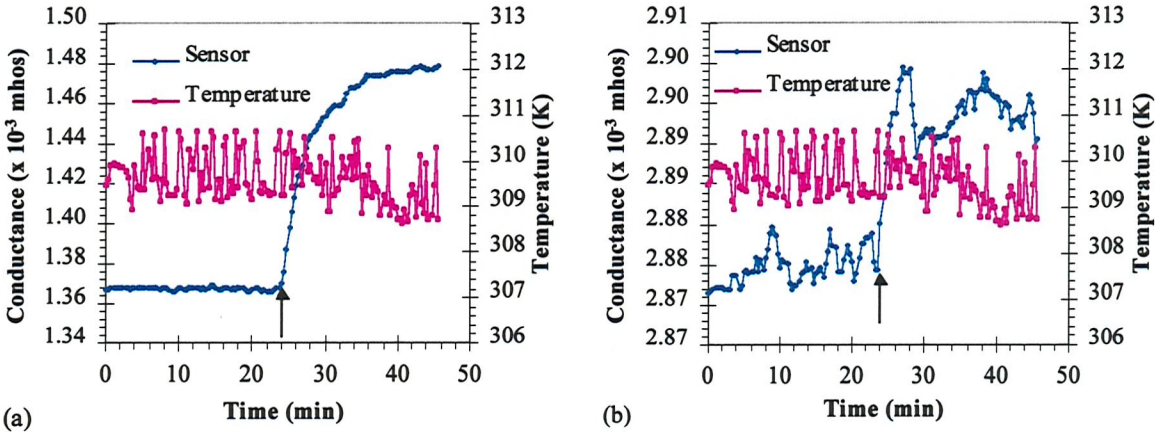

Figure 9.3 - One micrometre sensor results from TF1: (a) TG10A1b; (b) TG10A2b

In experiment TF2, the two sensors again demonstrated conductance increases during AO exposure. Once more, sensor TG10A1b's response was far smoother than that of TG10A2b. However, there was another difference between the two devices. Whilst the conductance of TG10A1b (Figure 9.4.a) increased monotonically, the conductance of TG10A2b (Figure 9.4.b) jumped to an initially high value and then recovered to just above that of its pre-AO exposure level. Neither of these responses was foreseen from the theory presented in Chapter 5, nor were they experienced by the 0.5 μm sensors, which reverted to the expected conductance decrease during AO exposure in TF2.

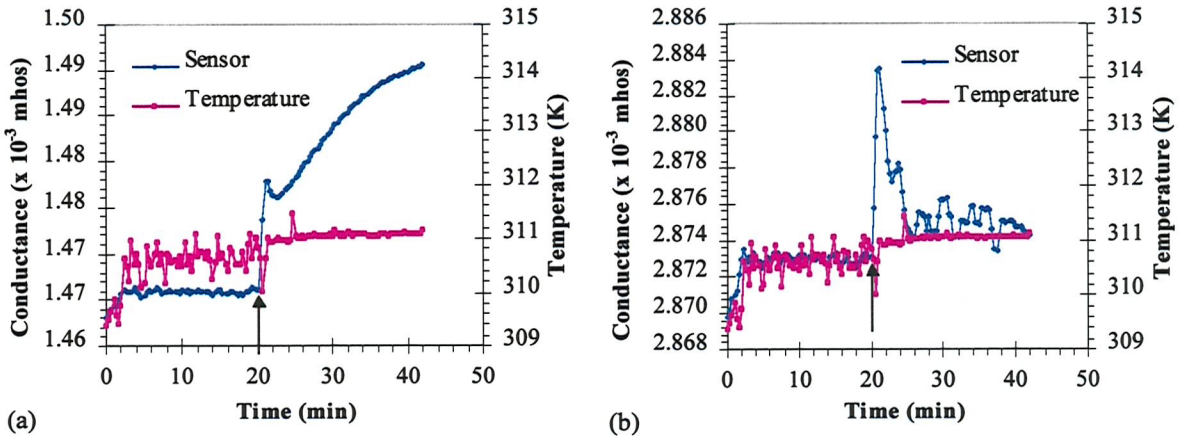

Figure 9.4 - One micrometre sensor results from TF2: (a) TG10A1b; (b) TG10A2b

In the next exposure (experiment TF3), the one micrometre sensor labelled TG10A2b adopted the correct behavioural response to AO impingement, whereas, TG10A1b performed in a manner similar to its own response in the previous experiment. Note that graphs from experiment TF3 are not presented in this thesis. However, by experiment TF4, both sensors responded according to theory, as shown in Figure 9.5 parts (a) and (b), TG10A1b and TG10A2b respectively. In these experiments, sensor conductance was found to increase immediately following the commencement of AO flux, an increase that is attributed to UV and VUV stimulated photoconductivity in the films, see Section 10.2. It can be seen from the figure below that the increase was temporary, and was followed by a period of conductance decrease caused by the action of AO on the sensors.

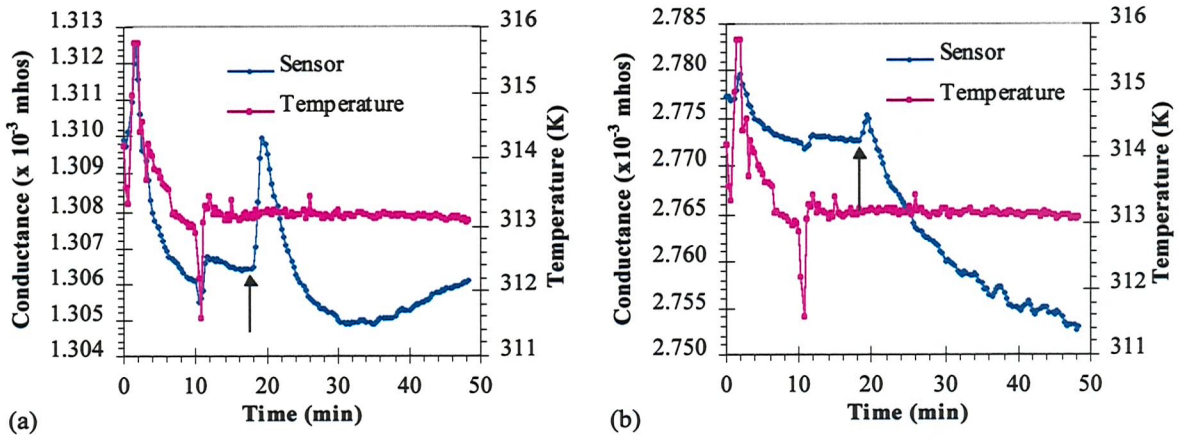

Figure 9.5 - One micrometre sensor results from TF4: (a) TG10A1b; (b) TG10A2b

There is a feature of operation of sensor TG10A1b to note from Figure 9.5.a. After sensor saturation at about 30 minutes, the conductance of the sensor increased once more, in spite of the continued flux of AO, which was terminated at 46.0 minutes. This response appears to be an intermediary phase between the, as yet, unexplained conductance increase, and the correct conductance decrease during AO exposure. Sensor TG10A1b acted in this manner for two

experiments (TF4 and TF5), before it adopted the normal monotonic and permanent conductance decrease during AO exposure in TF6, and all subsequent experiments. See for example Figure 9.6 below, which presents data from TG10A1b and TG10A2b in TF9. Clearly, in this experiment the behaviour of both 1.0 μm sensors is as expected from the theory introduced in Chapter 5.

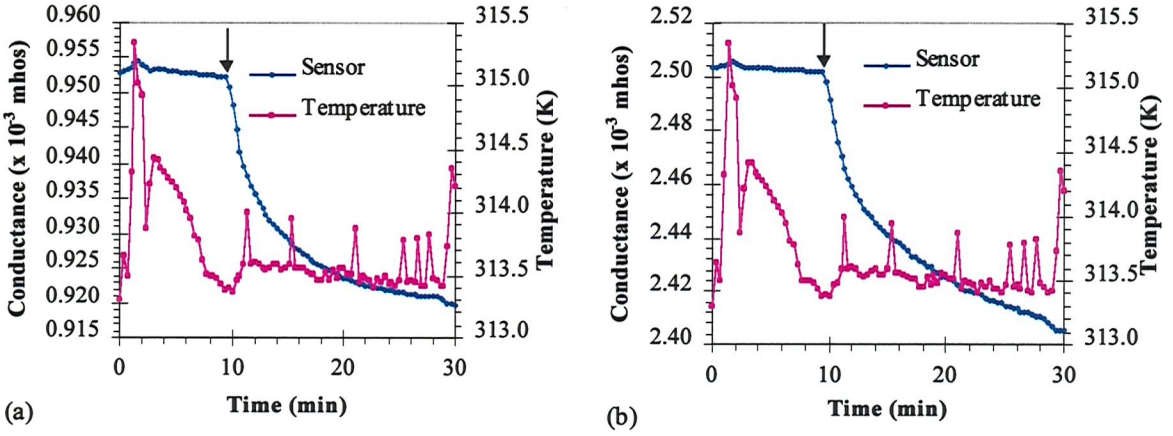

Figure 9.6 - One micrometre sensor results from TF9: (a) TG10A1b; (b) TG10A2b

Therefore, where the switch from abnormal to normal response was sudden in the case of the 0.5 μm sensors TG08A1b and TG08A2b, whence it occurred directly after TF1 with no intermediate stage, for the 1.0 μm devices the changeover from one response to another was found to occur through an intervening step. For example, sensor TG10A1b exhibited a spurious conductance increase in each of the first three AO exposure experiments. In the fourth experiment the behaviour of that sensor was normal to a certain extent, in that the conductance was observed to decrease. However, after sensor saturation, the conductance increased once more. The response from this device in experiment TF4 is an example of a short-lived intermediate stage in the change of sensor behaviour, for it only occurred in two experiments, after which normal response was observed in all remaining tests.

In a similar fashion, the second 1.0 μm sensor (TG10A2b) exhibited a transitional stage in experiment TF2, in which the conductance increased and then recovered somewhat. Only after this intermediate pattern did the behaviour change - in TF3 - to that normally anticipated. In all subsequent experiments, TG10A2b was found to respond to AO flux as theory and previous experiment expected.

In each of these two cases, as for the half micrometre sensors, a critical dose of AO was necessary to evolve sensor response from an unexpected conductance increase, to the envisaged conductance decrease. The dose of AO needed to condition the response of the 1.0 μm sensors seems to be larger than that for the 0.5 μm devices, since the latter changed response after TF1, whereas the former did not begin to swap until after TF3 - TF4. A more complete investigation of

the magnitude of AO fluence necessary to induce this conversion is given in Sub-sections 9.1.4 and 9.1.5.

9.1.3 Two-micrometre sensors

Results from the 2.0 μm sensors (TG11A1b and TG11A2b) showed a different pattern of behaviour. Both of these sensors demonstrated spurious conductance increases during each of the first five experiments akin to those shown by the thinner sensors. Then, in TF6, the responses of the 2.0 μm sensors were found to be similar to that of TG10A1b in experiment TF4. Plots of both 2.0 μm sensors' responses in TF6 can be found in the figure below, which should be compared to part (a) of Fig. 9.5.

However, after TF6 the responses of both sensors reverted to the erroneous conductance increase during AO bombardment that they demonstrated in TF1 - TF5. The 2.0 μm sensors responded in this fashion until experiment TF9, whence the reaction of the sensors once again adopted a style that closely resembles those in Figure 9.7.

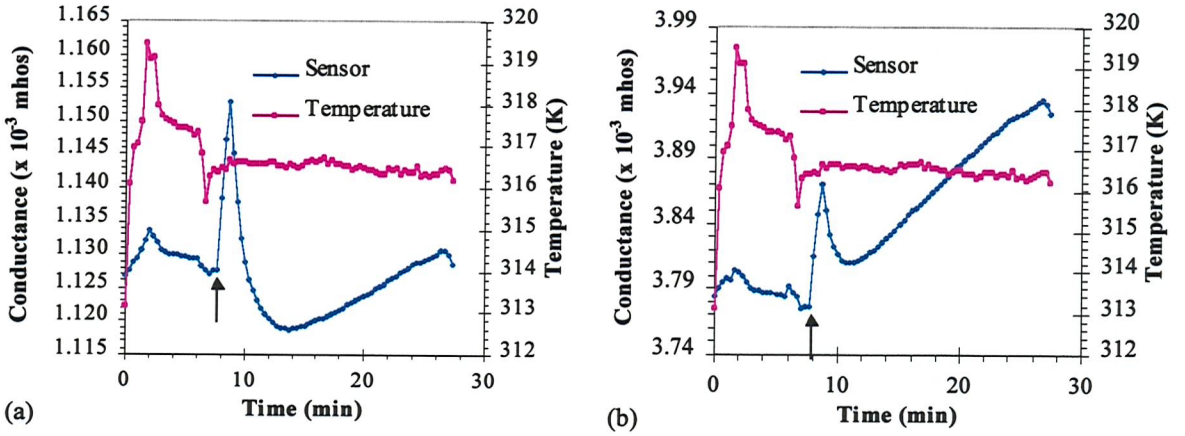

Figure 9.7 - Two micrometre sensor results from TF6: (a) TG11A1b; (b) TG11A2b

9.1.4 Summary of findings

It is clear from the previous discussions that all sensors responded in one way or another (normal or abnormal) to AO exposure, thereby satisfying the first aim of the experimental programme. To some extent, though, all sensors performed spuriously in the experimental programme, no matter what the thickness of ZnO from which they were fabricated. That is, the conductance of the sensors was found to increase during AO exposure - a reaction in contradiction to the theoretical expectations presented in Chapter 5. After a certain amount of exposure to AO, the response of each sensor was found to revert to that predicted, either directly, or through an intermediate stage. Thus, it is as though the sensors were 'burnt-in', or became conditioned by the impinging atomic

oxygen. Only in the case of the thickest sensors did the demonstrated reaction never fully change to the correct manner, perhaps because of insufficient accrued AO fluence.

Moreover, the dose - or fluence - of atomic oxygen needed to induce the conversion appears to be dependent upon the thickness of the ZnO. The 0.5 μm films swapped after TF1, a fluence of 2.584×10^{18} atoms.cm^{-2}. A fluence of between 5.391 to 7.840×10^{18} atoms.cm^{-2} was necessary to condition the 1.0 μm sensors (after TF2 and TF3), whilst the thickest devices (2.0 μm) first appeared to change response during TF6, after a dose of 17.91×10^{18} atoms.cm^{-2}. Although, in this latter case, the process never seemed fully complete. In fact, there seems to be a reasonably linear relationship between the film thickness and necessary fluence of AO, evident in the figure below.

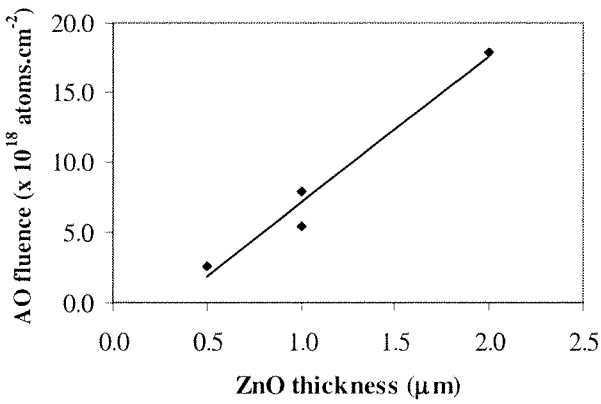

Figure 9.8 - The linear relationship between ZnO thickness and AO fluence necessary to condition sensor response

Several questions arise as a consequence of these findings. Firstly, why should all the ZnO sensors have displayed a phase during which the conductance increased under AO exposure? Secondly, why should this curious increase transmute into the correct conductance decrease? Finally, why should the AO fluence necessary to engender the change of response be, apparently, thickness dependent? The next sub-section will attempt to answer these questions.

9.1.5 Possible causes of erroneous sensor response

Several different explanations for the peculiar sensor behaviour have been investigated. The first was the possibility that the technique used to perform the conductance measurements in the experiments influenced the sign of the conductance change. As a multimeter was used in a 2-point mode to record the resistance of the thin films, the sensors cannot have been connected into the measurement circuit 'incorrectly'. Additionally, it was found through experiment that all of the gold films used to contact the ZnO sensors perform Ohmically, see Sub-section 7.3.1.

Therefore, contact effects cannot have caused the observed behaviour. Hence, the conductance increases cannot be attributed to the measurement technique employed.

Another explanation of the strange conductance decrease arises when it is recalled that ZnO is photoconductive. It has already been mentioned - see Section 8.2.1 - that, in ATOX, large amounts of UV and VUV are generated as a by-product of the AO formation process. Such electromagnetic radiation is quite able to stimulate photoconduction in ZnO (see Section 7.4), thus UV/VUV illumination of the sensors may result in the observed conductance increase, but only if atomic oxygen is prevented from reaching the semiconductor surface.

What material could act in this way? One possibility is that the sensors were covered with a contaminant layer, which was either deposited at the end of the manufacturing process, or resulted from post deposition and pre experiment preparation handling. If this layer is transparent, or at least translucent to short wavelength radiation, then enough UV/VUV may reach the ZnO to cause the observed conductance increase. Meanwhile, AO would be prevented from reaching the semiconductor because it would react after adsorption upon the contaminant.

After a certain amount of AO exposure, it is easy to envisage that the contamination may become completely eroded, thus no longer preventing oxygen action upon the sensor surface. At this point, the response of the devices would change from a UV/VUV induced conductance increase to an AO-dominated conductance decrease. If this hypothesis is correct, it is clear that the thickness of the contaminant layers - assuming that all were of the same composition - must be proportional to the thickness of the ZnO.

For a relationship between ZnO and contaminant layer thicknesses like this to exist, the blocking material must have been formed at the same time as the semiconductor. It is difficult to see how such a surface covering may result during deposition, indeed, discussion with the device fabricator has discounted this possibility (*Lawson, 1999*). Therefore, like the conductance measurement hypothesis above, a photoconductivity-contamination explanation is apparently not a feasible explanation of the observed results.

It is known that sensors fabricated from p-type material would respond with an increasing conductance upon AO bombardment. Adsorption of an oxidizing species creates extra holes in the material, thereby increasing the charge carrier concentration and, hence, the conductivity of the sensor. Yet, the bulk carrier type study of Sub-section 7.3.3 established that all ZnO films used in the AO flux experiments were n-type. Thus, the strange behaviour of the sensors cannot be due to the permanent presence of p-type ZnO, so another explanation has been sought.

A closely allied and potential explanation of the erroneous behaviour results from the possibility that an inversion layer existed at the surface of the semiconductor films. Section 4.6.2 showed that inversion layers result when the valence band is bent upwards to such an extent (by the action of surface charge) that its top reaches the Fermi level of the material. The surface of the semiconductor then behaves as though it was p-type, even though the bulk of the sample is inherently n-type.

Clearly, the semiconductor surface must become highly charged for an inversion layer to be formed. There are two potential sources of surface charging in the case in hand - electronic surface states, and gases adsorbed during manufacture and storage of the sensors. The consequences of each of these influences have been examined.

The presence of surface states upon the surface of the semiconductor leads to the development of surface charge (see Section 4.6) because they capture electrons from the conduction band of the material. The probability of there being a high density of surface states on the sensor surface is made greater by the method of manufacture chosen to form the films. During RF sputtering of the sensor elements, the crystallites of the films grow almost layer-by-layer due to the arrival of sputtered material at the evolving ZnO surface. Hence, the surface of the sensor is always formed from the last material deposited. At the end of sputtering, the apparatus is shut off suddenly, leading to a rapid cool-down of the ZnO film and substrate.

Therefore, at the surface, the last few atomic layers may have many trapped-in surface dislocations, stacking faults, included atoms and other distortions of the lattice that have not had time to anneal into a low-energy arrangement. Such features could promote the formation of surface states because they enhance the disruption of normal lattice symmetry. Once the surface states capture electrons from the conduction band, the conductivity of the material is reduced and the bands of the material bend upwards, to higher energies. This brings the top of the valence band closer to the Fermi level.

During manufacture of the sensors, the zinc oxide films experience excited plasma environments that may contain oxidizing species. For example, during deposition of the ZnO itself, the films will be bombarded by oxygen ions. Although the sputtering gas used in the deposition of the ZnO (Table 7.1) did not contain any intentional additions of oxygen, oxygen ions and atoms will be liberated from the oxide target and liberated from the chamber walls. Depositions TG08, TG10 and TG11 were conducted with a substrate bias of about -160 V, to limit the amount of oxygen reaching the developing films. However, it is conceivable that some high-energy oxygen atoms and ions, which did not get combined into the lattice, still reached the ZnO surface.

Additional oxygen may have been adsorbed on the ZnO during sputtering of the silica overlays. Whilst the bare ZnO films were shielded by a mask so that no silica would deposit upon them, since they were not hermetically sealed, it is possible that some oxygen - from the silica target - migrated to the bare semiconductor films and was adsorbed. It is also probable that during sputtering of the silica, the concentration of oxygen near the substrates was higher than during deposition of the ZnO, because of the extra oxygen contained in the dioxide.

Finally, the sensors were stored in normal laboratory atmosphere for a period of several weeks before usage. In this time, yet more oxidizing species (oxygen gas and carbon dioxide) may have become adsorbed on the surface. It has already been shown that, once adsorbed, oxidizing atoms and molecules will capture electrons from the material to form charge centres on the ZnO surface because they quickly become chemisorbed. It is reported that adsorption of any gaseous material removes the special conditions at the surface that allow the existence of surface states (*Somorjai, 1972*). However, if the combined densities of chemisorbed oxidizing material and surface states remain high, immediately prior to sensor use, the surfaces of the films will be highly charged.

Significant band bending may result from the presence of charge on the surface of the semiconductor. Therefore, due to the extreme manufacturing routes used and the associated propensity of oxidizer adsorption, it is proposed that inversion layers will exist at the surface of all tested sensors. Indeed, Cimino *et al.* found that simply storing zinc oxide at atmospheric pressure in oxygen was enough to form inversion layers in powder samples (*Cimino et al., 1963*). Since the environmental conditions experienced by the films in this study were harsher than those of Cimino *et al.*, the propensity of inversion layer formation may be increased. Once an inversion layer is formed, the surface of the ZnO would then behave as though it was p-type.

Thus, whilst it must still be considered conjecture, this model may explain why all sensors exposed to AO initially demonstrated an increasing conductance. Chemisorption of oxygen atoms in the experiments leads to the capture of electrons from the ZnO as normal but, paradoxically, this results in the formation of additional (hole) charge carriers due to the temporary p-type nature of the surface. So, instead of the conductance decreasing during AO adsorption, it actually increases. The first question about sensor behaviour seems to have been answered, but what could cause the experimentally observed change of sensor response?

During AO exposure, the impacting oxygen atoms become condensed upon the semiconductor surface in a physisorbed precursor state, and their impact energies are dissipated within the lattice by the production of phonons. Usually, the adsorption of gases occurs with relatively small impact energy - $\propto \frac{3}{2}\frac{kT}{e}$ - perhaps around 0.04 eV at room temperature (*Prutton, 1987*). In

contrast, the AO impact energy in these experiments was on the order of 5 eV. Whilst this energy is not enough to physically remove (sputter) ZnO from the surface, it may be enough - when combined with that released during the formation of chemical bonds - to force surface reconstruction and annealing. As a result, the features creating the surface states may be removed. In this fashion, the surface state density is reduced, and electrons are re-injected into the bulk. Hence, the component of band bending due to surface state electron capture is lost, or at least reduced.

In the period of regeneration heating between AO exposures, that is the elevated temperatures used to renew the sensors for another measurement, chemisorbed oxidizing species are released from the surface into the gas phase. Upon desorption, previously captured electrons are released back into the bulk of the semiconductor, and the amount of surface charge is decreased even further. Hence, the magnitude of band bending is also reduced.

Therefore, it is suspected that the processes of surface state removal, surface restructuring and oxidizer desorption gradually lead to an overall reduction in the density of charge centres on the surface of the semiconductor. If true, after several AO exposure and regeneration cycles, the number of charge centres remaining will be negligible and so the influence that they exert on the semiconductor sensor may be ignored.

At this point, the amount of band bending will be no longer sufficient to form an inversion layer (but maybe a depletion layer) and the semiconductor surface will adopt its inherent, n-type nature. Exposure to atomic oxygen will then lead directly to electron capture and conductance decreases as predicted by theory in Chapter 5. Thus, it appears that the observed change of sensor behaviour from the abnormal to the expected response may also be resolved by this model.

For confidence to be placed in this hypothesis, it should answer the remaining question of why the AO fluence necessary to engender the change of sensor behaviour should be thickness dependent. An examination of the surface of the ZnO shows it to be acicular in structure, see Figure 7.7 parts (a) and (b) on page 102. Thus, it seems reasonable to model the surface as a series of slender conical elements. With this assumption, the surface area of the films will scale approximately with the height of the cones which, in this case, is also the thickness of the film. So, the surface (rather than the plan or projected) area of the films is approximately proportional to film thickness.

Now, if there is a fixed (and finite) area density of surface states and adsorbed oxidizer, the absolute number of these electron-traps will thus also scale with film thickness. Hence, it would

seem a rational suggestion that the thicker a film, the higher the AO fluence and the more exposure/regeneration cycles that are needed to reduce the surface charge density to the point at which the inversion layer is lost. It is, of course, at this point that the sensor response reverts to that expected by theory.

Of all of the potential explanations of the peculiar sensor behaviour examined, only this last hypothesis appears to resolve convincingly all of the confusing and erroneous facets of observed sensor operation. However, it is worth re-iterating that it must still be regarded as conjecture and further experimental evidence is required before it should be considered fact.

It is likely that other researchers (including Gabriel, Nahr and Jacob) have never observed this effect because they employed single crystals of material in their AO detectors (*Gabriel, 1997; Nahr et al., 1971; Jacob, 1975*). Not only do single crystals have a much simpler surface than polycrystalline thin films, hence fewer surface states, but the surface area to volume ratio is far smaller. As described earlier (Chapter 4), surface effects have greater influence in thin films because reactions at the surface can influence the majority of the bulk material. Those researchers that used thin film zinc oxide AO sensors heated their devices to high temperatures (~ 500 - 600 K) in vacuum immediately prior to usage (*Livshits et al., 1981a*). It is believed that these temperatures are sufficient to remove any inversion layers that might be present.

9.2 NUMERICAL ANALYSIS OF SENSOR RESPONSE TO AO FLUXES

9.2.1 Goals of the analysis

The aim of this section is to illustrate how the raw conductance data recorded in the experiments can be reduced to usable information by the application of the ballistic sensor model. A supplementary objective is to demonstrate that there is some intrinsic sensor response proportional to the magnitude of AO flux, thereby satisfying the third aim of the experimental programme.

Experiments TF1 to TF6 were designed to allow such an investigation. Undeniably, the conditioning process and the sensor instability associated with it, means that data recorded from any sensor in this phase must be eliminated from the analysis. Thus, results from the 1.0 and 2.0 μm sensors in experiments TF1 - TF4 and TF1 - TF6 respectively, and from both the 0.5 μm sensors in experiment TF1, cannot be used. Additionally, data from TF5 has too much EMI-induced noise for a sensible interpretation of the results. Therefore, the analysis below will be conducted only with the data from the two half micrometre sensors (TG08A1b and TG08A2b) in

experiments TF2, TF3, TF4 and TF6. Whilst this results set is much reduced, it will serve the purpose of adequately demonstrating the application of the analysis technique.

9.2.2 Method and results of analysis

From the preceding sections, it is clear that the raw conductance data recorded during the experiments - such as that in Figure 9.2 parts (a) and (b) - requires post-processing to allow interpretation of the sensor responses. Several different data processing routes have been investigated; Appendix A2 contains a description of the underlying mathematics of the different routes and a description of the findings of the study. The method adopted below was found to be the optimum technique for reducing the data, both in terms of speed and consistency.

Reference to the ballistic model, Equation (5.32), shows that the rate of change of sensor conductance is proportional to the flux of AO engendering that change. Thus, it is necessary to find these rates of conductance change. In this work, a second order, central difference scheme was used to differentiate the data with respect to the time values logged by the computer data acquisition system. It was found that the maximum rate of change of sensor conductance always occurred just after the start of AO exposure. From this point forwards, this distinctive gradient value is termed the sensor **response**.

Table 9.1 presents the responses of the two 0.5 μm sensors and the AO fluxes to which the sensors were subjected. It is important to note that the C-QCM measured AO fluxes presented in the table below represent the time-averaged values, and not the instantaneous pulse fluxes generated within ATOX, which may be several orders of magnitude higher. Additionally, in this work, these flux measurements are treated as *reference values*, so that they can be used to calibrate the semiconductor sensors.

Test ID	AO flux (x 10^{15} atoms.cm^{-2}.s^{-1})	TG08A1b (x 10^{-6} mhos.min^{-1})	TG08A2b (x 10^{-6} mhos.min^{-1})
TF2	2.12618	-3.14918	-3.17870
TF6	1.41725	-1.29172	-2.15185
TF3	0.90922	-1.67097	-1.61903
TF4	0.47048	-0.92224	-0.95176

Table 9.1 - Sensor responses to AO flux

It is clear from the data in Table 9.1 that the magnitudes of response are, in some ways, dependent upon the level of AO flux to which the sensors are subjected. For example, high flux generates large response, whilst small flux generates small response. Also evident in the table is that the response of TG08A1b in TF6 (-1.29172 x 10^{-6} mhos.min^{-1}) seems to be half the magnitude of TG08A2b (-2.15185 x 10^{-6} mhos.min^{-1}) in the same experiment, and even below

the response of the lower flux experiment TF3 (-1.67097 x 10^{-6} mhos.min^{-1}). One possible explanation for the discrepancy is that there was an heterogeneity in the incident AO beam, such that the flux on TG08A1b was lower than that experienced by TG08A2b and the C-QCM. The existence of such features in the expanding AO plume have been observed optically by the author, and are believed to be caused by power distribution irregularities in the TEA laser beam used to form AO (*Matcham, 1998a*).

It is informative to plot graphs of sensor response versus AO flux, see Figure 9.9 (a) and (b) below. Part (a) of this figure has been derived from the data recorded from sensor TG08A1b, whilst part (b) is from TG08A2b. In both graphs, linear functions have been least squares fitted to the data points. In the case of TG08A1b, however, the response from experiment TF6 has been omitted from this process because, as noted above, it falls well below the trend indicated by the other values. The gradients of the functions represent the calibration factors of the MOS sensors (relative to the C-QCM), and are found to be -1.3171 x 10^{-21} (mhos.min^{-1}).[atoms.cm^{-2}.s^{-1}]$^{-1}$ and -1.3197 x 10^{-21} (mhos.min^{-1}).[atoms.cm^{-2}.s^{-1}]$^{-1}$ for sensors TG08A1b and TG08A2b respectively.

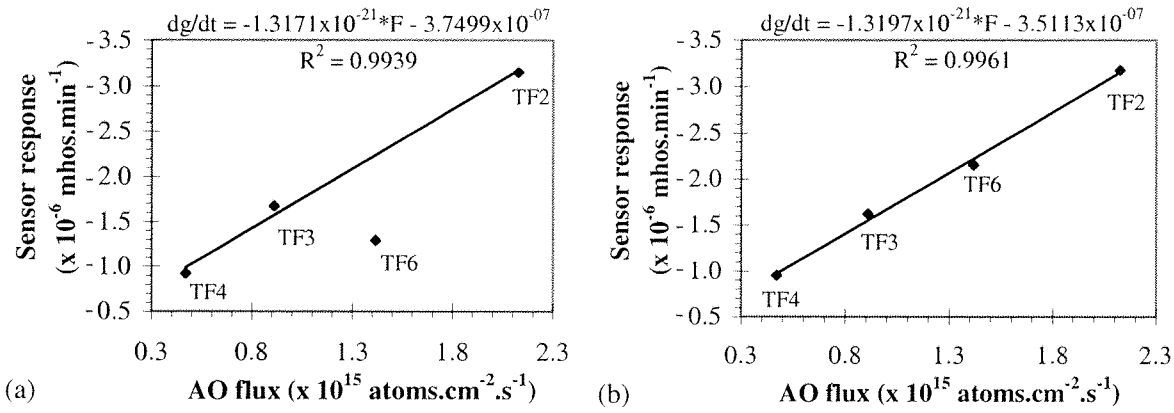

Figure 9.9 - Response of semiconductor sensors: (a) TG08A1b; (b) TG08A2b

Even though the number of results available is small, it is evident from Figure 9.9 that there is a linear relationship between the response of the ZnO sensors and the C-QCM detector. In fact, the high correlation coefficients of 0.9939 and 0.9961 indicate that there is little disagreement between the two measurement techniques, at least over the range of AO fluxes tested. Since the C-QCM measurements have been taken to be reference, it is possible to conclude that there is, indeed, a simple relationship between sensor response and AO flux. This linear response was first predicted from the ballistic-sensor model.

Other conclusions can be drawn from these graphs. The fact that best-fit equations for the two data sets are remarkably similar, suggests that ZnO sensors deposited simultaneously (or with identical conditions) respond in an alike manner, attesting to the manufacturing repeatability of

the technique. Also, the linear relationship and excellent correlation between the ZnO and C-QCM sensors confirms that semiconductor-based devices can be used to obtain quantitative and consistent measurements of AO fluxes (*Osborne et al., 1999*).

Each data point in the graphs of Figure 9.9 has been annotated with the experiment number. This information has been incorporated to indicate that the order of the experiment does not have an influence upon the measurement ability of the sensor films. For example, it may be supposed that the magnitude of sensor response associated with a given flux may fall with total AO exposure. Clearly, this is not occurring - if it had, the TF6 data point would have fallen at a position lower that it did, and almost certainly below that of TF4.

The next figure (9.10) shows the normalized responses of the semiconductor sensors plotted against the equivalent normalized AO fluxes. In this analysis the values were scaled by the maximum response of each device, obtained under the highest flux condition. The linear curve fit to the data shows that both sensors exhibit a gradient less than unity (0.8892 and 0.8906), indicating that the semiconductor devices are approximately 11 % less sensitive to AO than the quartz crystal microbalance. Like the curve fitting procedure used in Figure 9.9.a, the function fitted to the data in Figure 9.10.a does not take into account the data point from experiment TF6, an explanation of this omission can be found on page 140.

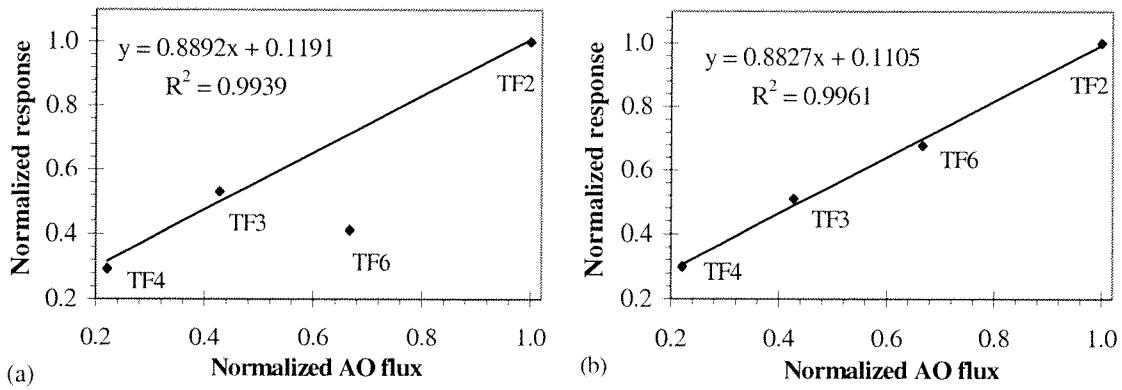

Figure 9.10 - Normalized sensor responses: (a) TG08A1b; (b) TG08A2b

Additionally, the presence of the intercepts in the equations of Figures 9.9 and 9.10 implies that there would be a ZnO sensor signal at zero AO flux. However, it must be recalled that a C-QCM detector was used to measure the AO fluxes. Hence, it may be some facet of this device, rather than the MOS sensors, causing this offset. It is possible to conduct a simple investigation of the apparent flux threshold.

The mass sensitivity of the C-QCM used in the experiments was 3.92 x 10^{-9} g.cm^{-2}.Hz^{-1}. If a minimum resolvable frequency change of 1 Hz is postulated for the C-QCM, this sensitivity gives a fluence resolution of 2.18 x 10^{15} atoms.cm^{-2} (assuming a carbon erosion yield of 1.0 x 10^{-24} cm^3.atom^{-1} and density 1.8 g.cm^{-3}). The intercepts of the linear functions in Figure 9.9 indicate that at zero C-QCM measured AO flux, the MOS sensors are still detecting a flux of approximately 2.7 x 10^{13} atoms.cm^{-2}.s^{-1}. It is apparent that the C-QCM would require around 80 seconds to register this flux. Hence, it seems that the flux resolution of the C-QCM sensor is limited by the mass sensitivity of the quartz crystal, unlike the semiconductor devices (*Osborne, 1999*).

The inference of such a flux threshold is realistic because the C-QCM relies on material removal as its measurand; carbon is removed by AO either in the form of carbon monoxide or dioxide. Delayed desorption of reaction products from the carbon surface may introduce the postulated lower resolution limit. For example, if the reaction products remained on the carbon surface for a significant time, they may partially mask the small changes of mass associated with carbon erosion at low AO fluxes. In comparison, the semiconductor sensor relies upon a change of conductivity as its measurand - a step that should proceed rapidly because of the high accommodation coefficient of AO on ZnO surfaces (*Ryl'tsev et al., 1978*). Assuming, of course, that the conversion of adsorbed neutral oxygen atoms to oxygen ions is a rapid step, and is therefore not rate limiting.

It is therefore concluded that the offsets in Figures 9.9 and 9.10 are an artefact of the C-QCM measurement - physical meaning: in this case, zero C-QCM 'signal' does not equal zero AO flux. As such, the positive offsets do no represent real coefficients of MOS sensor calibration, or a minimum resolvable flux for the semiconductor devices.

However, there may be another explanation for the observed offset. It may be that there is some other component of ATOX operation adding to the effect of hyperthermal AO on the semiconductor sensors. Vacuum ultraviolet, thermalized AO, temperature changes and molecular oxygen fluxes are all potential influences. Two of these effects - VUV irradiation and O_2 fluxes - will be investigated in the next chapter, whilst the effects of thermalized AO are postulated below.

9.2.3 Probable effect of thermalized AO

Unfortunately, no experimental investigations of the effects of thermal (or thermalized) AO have been possible. However, it is possible to hypothesise the magnitude of the likely influence that this species will have on the semiconductor sensors.

Section 5.2 demonstrated that adsorption of atoms impinging upon a surface requires that the atoms become caught in a potential well on the adsorbent. The same section went on to describe that the depth of the well must be at least equal to the component of the atom's kinetic energy perpendicular to the substrate. For adsorption of the hyperthermal AO used in this work, the potential wells on the ZnO surface must be approximately 5 eV deep. In comparison, for thermal atoms the wells are only required to have a depth of about 0.1 eV.

Energetic considerations show that it is likely that a surface be populated with many more adsorption sites of low-energy potential wells than those with high-energy wells (*Cranny, 1992*). Hence, it seems as though the adsorption of thermal energy oxygen atoms would be favoured over the adsorption of their hyperthermal counterparts. Since there are many more surface sites able to capture thermal atoms, it should be expected that the sensors would absorb thermal atoms quicker than hyperthermal atoms. Faster adsorption of oxygen atoms yields a higher rate of conductance change. Thus, under the influence of equivalent fluxes, the sensors may respond more strongly to low velocity, thermal atoms, than they do to high velocity or hyperthermal atoms.

The above discussion is equivalent to saying that γ, the reflection coefficient in Equation (5.32), is smaller for thermal atoms. Essentially, this means that fewer atoms are reflected from the surface of the sensor, which seems physically realistic given the lower energies of impingement of these atoms. Clearly, the sensor may thus exhibit an energy dependent response curve. Also, the number of atoms adsorbed at saturation is likely to be higher, so the change of conductance to this point will be larger with thermal atoms.

Moreover, since hyperthermal atoms cannot be adsorbed by low-energy potential wells, the adsorption of hyperthermal and thermal oxygen may occur simultaneously. So, in some ways, the adsorption of atoms of widely different energy is not mutually exclusive (one does not prevent the other). However, it would seem feasible that thermal atoms may be adsorbed in potential wells deep enough to accept hyperthermal atoms, hence, the presence of thermal atoms in a hyperthermal AO beam may restrict the adsorption of the higher energy species. Therefore, any thermalized AO present in the experiments reported herein will add indistinguishably, as postulated, to the effect of fast AO.

9.3 SENSOR SATURATION

The model of gas adsorption developed in Section 5.2 predicted that there was an ultimate surface density of adsorbed atoms and that, when this density is reached, no further adsorption takes place. Once the adsorbed atom density has reached this maximum value, the surface is said

to be *saturated.* Experimental evidence of sensor saturation was first presented in Section 9.1.1 (Figure 9.2) and Section 9.1.2 (Figure 9.6). Figure 9.11.a is an example of saturation taken from sensor TG08A2b in experiment TF6. As described previously, at the start of AO exposure (marked by first arrow), the rate of change of sensor conductance is high. With time, however, this rate falls and so the gradient of the conductance curve begins to level off. Eventually, the conductance changes no further and saturation has occurred.

One of the conclusions from the adsorption model was that there are two 'regimes' of saturation. The first was found to result in the surface density being dependent on the impinging flux. Thus, the larger the flux, the greater the number of adsorbed atoms per unit surface area and *vice versa.* In contrast, the saturation density in the second regime was shown to be independent of flux level. An analysis of the 0.5 μm sensor data from experiments TF2, TF3, TF4 and TF6 allows an investigation of the type of saturation to which the sensors have been operated. These early experiments must be used for the investigation, rather than the later ones, because the regeneration temperature was kept at a constant value throughout.

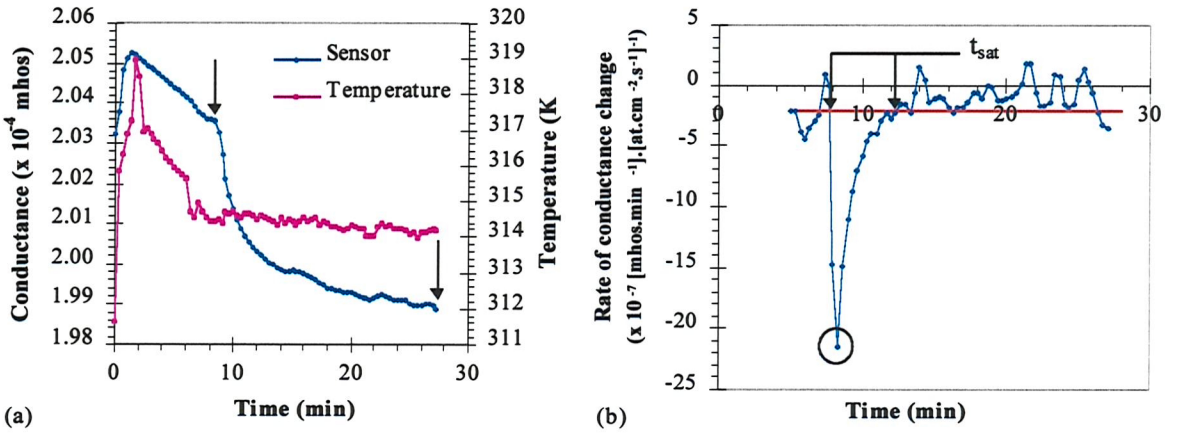

Figure 9.11 - Sensor saturation example (TF6): (a) raw data; (b) conductance gradient

In order to explore the saturation conditions experienced by the sensors, it is necessary to find a method that allows consistent determination of the sensor saturation fluence. It could be argued that the simplest way of determining the saturation fluence would be to decide when the conductance curve (such as that in Fig. 9.11.a) had become parallel to the abscissa. Such a decision is rather subjective and difficult to computerize. So, another technique has been adopted.

This method is based upon the gradient data used to derive the response value of the sensor, see Appendix A2. Part (b) of Figure 9.11 shows the gradient of the conductance curve in part (a). The circled peak of this curve is the sensor response to the AO flux. As expected from the earlier description in this chapter, the gradient values are initially high and then fall towards zero. A line

has been drawn on the graph of part (b) at a value 10 % of the maximum gradient recorded. The time to sensor saturation is taken as the elapsed time between the first and second intersection of the two curves, as indicated by the gap between the two arrows in the figure. The saturation fluence is then found by multiplying the time, t_{sat}, with the flux used during the experiment, i.e. $f_{sat} = F.t_{sat}$.

Table 9.2 shows the results of the saturation study for the four experiments TF2, TF3, TF4 and TF6. Clearly, this method does not determine the actual, absolute saturation fluence, but rather a characteristic value that neglects to take into account the amount of AO reflected during the exposure, and also underestimates the time to saturation. However, the values are easy to determine and, since a consistent approach has been used in all of the analyses, the results should be inter-comparable.

Exp.	AO flux (x 10^{15} atoms.cm^{-2}.s^{-1})	TG08A1b		TG08A2b	
		Time to sat (s)	AO fluence (x 10^{17} atoms.cm^{-2})	Time to sat (s)	AO fluence (x 10^{17} atoms.cm^{-2})
TF2	2.12618	187	3.98	187	3.98
TF6	1.41725	(356)	(5.05)	235	3.33
TF3	0.90922	279	2.54	273	2.48
TF4	0.47048	307	1.45	297	1.40

Table 9.2 - Sensor saturation fluences

Plots of these data can be found in Figure 9.12. Again, in plotting the curve for TG08A1b, the point associated with experiment TF6 has been ignored in the curve-fitting process (see Sub-section 9.2.2, specifically page 140, and Figures 9.9 and 9.10). Apparently, sensor saturation fluence is dependent on the AO flux impinging on the sensor surface. It is possible to conclude, therefore, that in these experiments the sensors have been utilized in the flux-dependent saturation regime. Moreover, the shape of the curves would seem to imply that the regime in which the devices have been operated is close to the flux independent stage; the curves appear to be of a shape akin to the 'shoulder' of the saturation curve in Figure 5.1.

Since the saturation fluence is dependent upon the magnitude of flux, it may be possible to use the time to saturation as another measure of the flux intensity. However, the non-linearity of the relationship between saturation fluence and flux would make the application of this method somewhat harder than the simple, linear conductance gradient method. For example, interpolation and extrapolation of the curves in Figure 9.12 is more difficult than the straight lines of Figure 9.9.

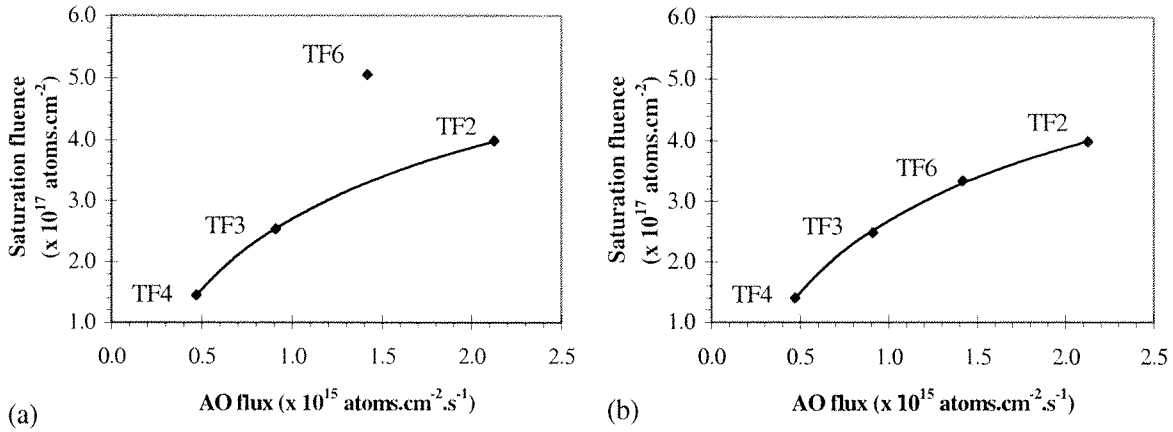

Figure 9.12 - Plots of sensor saturation fluences: (a) TG08A1b; (b) TG08A2b

It is interesting to note that the saturation fluence calculated for TG08A1b in TF6 is higher than the trend implies, and indeed higher than that achieved under the greatest flux employed in the experiments. Recall also, that in the same experiment this sensor's response fell well below the trend, and that this was attributed to a lower incident flux upon this sensor (Section 9.2.2). These two observations neatly dovetail, if the flux on TG08A1b were indeed lower during the experiment. Then, in this instance, the measured time to saturation would be far higher than expected from the accepted (C-QCM recorded) experiment flux. A large t_{sat} value, when multiplied by the experiment flux, thus yields greater apparent saturation fluence than otherwise anticipated. This conclusion acts as confirmation of the original postulate (see Section 9.2.2) that the AO flux upon this sensor was lower than the average experimental value experienced by the C-QCM and TG08A2b.

There is another fluence value that can be calculated, which is the AO fluence to peak sensor response. For all of the experiments conducted to date, the average time from initiation of AO flow to the time of peak sensor conductance change (maximum rate of change of sensor conductance) occurs around 2.33 data-logger time steps (46.6 s) after the start of AO exposure. This equates to a fluence of ~ 1.01 x 10^{17} atoms.cm^{-2}. Unfortunately, due to the slower than desired data acquisition rate, it is not clear if this quantity has any significance or if it is simply an artefact of the data processing and acquisition methods. However, it may be that a certain number of atoms must be adsorbed upon the semiconductor surface before the conductance change can be detected. Although, this hypothesis seems to be in contradiction with the condition that the ballistic equation of sensor operation (5.32) is only valid for totally unoccupied surfaces.

9.4 REGENERATION OF THE ZINC OXIDE SENSORS

9.4.1 General observations

One of the major benefits of the semiconducting sensor technique is that it is reusable, a property which confers significant advantages over the other devices (e.g. C-QCMs, actinometers and Kapton witness samples) that have been applied to the measurement of AO fluxes. Regeneration of the sensors, after exposure to AO, is accomplished by heating the semiconductor to elevated temperatures and then cooling. As a result, a recovery of the original, pre-AO exposure conductance should occur, see Figure 5.3. The literature shows that the sensor conductivity is renewed because the surface compounds formed during chemisorption (which are stable at low temperatures) breakdown, allowing desorption of the oxygen atoms and re-injection of the conduction band electrons.

Since regeneration of the sensors is a key characteristic of their operation, an experimental study was performed to investigate several of the process parameters and results. Since desorption of oxygen atoms is known to be energy dependent, a natural parameter to study is the sensor temperature at which regeneration takes place. It is also useful to study the completeness of the process, and if it has any effect on the subsequent measurement ability of the sensors. Experiments TF7 to TF10 were designed with just these enquiries in mind. Like the flux investigation of Section 9.1, any sensor behaving abnormally must be excluded from this analysis if a consistent study is to be performed. By TF6, the 1.0 micrometre sensors TG10A1b and TG10A2b were behaving correctly since they had been fully conditioned, as were the two half micron devices. However, TG11A1b and TG11A2b were still 'burning in' throughout these experiments, and so cannot be used. The remaining part of this section will examine some of the general features of sensor regeneration.

Figure 9.13 shows the results of a complete AO exposure and regeneration cycle for sensor TG08A2b in experiment TF4. This data was found to be typical of all of the experiments performed, and so will be used to describe the general features of sensor regeneration. The diagram shows the conductance of TG08A2b and the temperature of the substrate upon which it was deposited. The times at which AO flow was initiated (~ 18.5 min) and stopped (~ 48.5 min) are indicated by the arrows, annotated with the words 'on' and 'off' respectively. The decrease of sensor conductance due to AO impingement can be discerned. It appears as a small decrease purely because of the scale of the ordinate. After cessation of AO, at 50 minutes, the substrate heater was used to raise the temperature of the sensor to ~ 376 K, where it was maintained for around 140 minutes. This is the regeneration-heating phase.

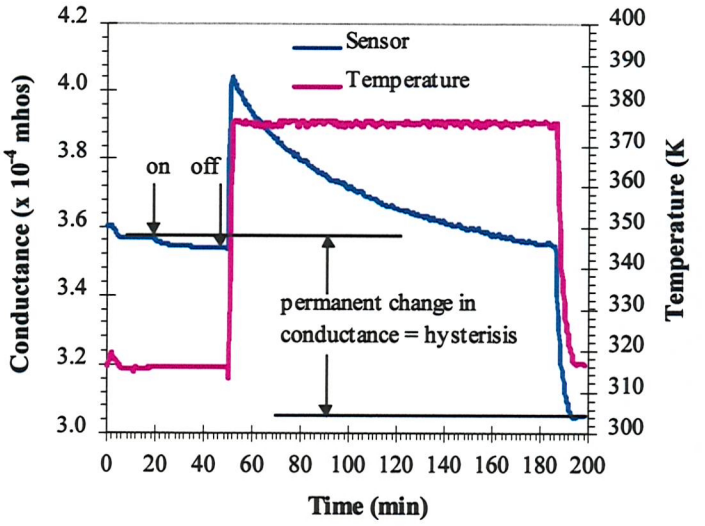

Figure 9.13 - Typical regeneration response

In response to the higher temperature, the conductance of the sensor increases, due to the thermal promotion of extra charge carriers into the conduction band of the ZnO (see Section 4.5). Whilst the temperature is maintained at 376 K, it can be seen that the conductance of the sensor decreased monotonically, indicating that the charge carrier density in the material was being reduced by one or more mechanism. At a time of 190 minutes, the temperature of the sensor was reduced to its pre-AO exposure value, so that a valid comparison could be made between conductance measurements performed pre-AO exposure and post-regeneration. During cooling, the charge carriers previously promoted into the conduction band drop back to the donor level, so the conductivity of the sensor fell rapidly.

It is clear from the figure that a permanent change in conductance occurred as a consequence of heating the sensor to elevated temperatures. Thus, the base conductance of the film is observed to decrease as a result of regeneration - from this point forward this change will be termed **hysterisis**. A single report of a similar phenomenon has been found in the literature, however, the effect was not studied empirically (*Malinova and Myasnikov, 1969*). Therefore, this investigation is highly novel. Close examination of the figure above shows that the magnitude of the permanent conductance change, the hysterisis, is equal (or thereabouts) to the reduction of conductance that occurred during the high temperature stage of operation.

All sensors exposed to AO flux showed a similar hysterisis, even those that were still well within the early conditioning phase. This result shows that hysterisis is not connected to the sign of response during AO exposure, but must instead be related to some property of the material from which the sensors are fabricated.

Several questions arise from these observations. Firstly, what causes the hysterisis? Secondly, can increased (or decreased) regeneration temperature and/or time be used to limit the amount of hysterisis? Finally, as discussed previously, what is the effect of hysterisis upon the measurement ability of the sensors?

9.4.2 Causes of regeneration hysterisis

The last section presupposed that the decrease of conductance during the high temperature refreshment of the sensor was due to the removal of charge carriers from the conduction band of the material. In some ways, this is very similar to the conductance decrease observed during AO exposure, which is indeed caused by electron depletion. However, there was no AO flux bombarding the sensors during regeneration, so this cannot have been the cause of the observed conductance decrease.

The apparent equivalence of the conductance decrease experienced during the elevated temperature stage and the start-to-end hysterisis, leads to the conclusion that whatever mechanism is causing the former, is also responsible for the latter. Solution of the problem of conductance decrease during heating will thus solve the problem of sensor hysterisis. In a similar fashion, it is hard to completely ignore the resemblance of the AO induced conductance decrease to that experienced by the sensor during heating.

The absence of investigative reports about hysterisis in the literature seems to indicate that all adsorbed oxygen is removed during regeneration. However, what if this were not the case? What if some of the chemisorbed oxygen remained upon the semiconductor surface? Clearly, the conductance would not recover to its pre-AO exposure value, but to somewhere in between that level and the minimum conductance that the sensor reached during AO exposure. This does not seem to explain the huge amount of observed hysterisis - roughly 13 times the conductance change during AO exposure. So, some other mechanism must be acting in addition.

One potential cause of the hysterisis is that the free zinc atoms, which are responsible for the semiconducting behaviour of ZnO, are becoming permanently oxidized. That is, instead of remaining in rather tenuous surface compounds, any undesorbed oxygen is becoming part of the ZnO matrix, forming proper (stronger) lattice-type bonds. Once the interstitial zinc has become immutably oxidized, it can no longer act as an electron donor and so the number of charge carriers is permanently reduced. The reduction of charge carrier concentration is manifested as a decrease of sample conductance. The oxygen atoms are thus caught in even deeper potential wells than they were when they were chemisorbed, and are thus unlikely to be desorbed by simple heating alone.

The previous description may explain what is causing the hysterisis, but not why the magnitude is so large. However, this answer is also at hand. When an oxygen atom becomes part of the ZnO matrix, it becomes doubly ionized, thereby removing two charge carriers from the bulk material, whereas, chemisorbed AO localizes but one electron. Moreover, it is not just the previously chemisorbed oxygen atoms that may be captured in this way, any physisorbed atoms may as well. Thus there is a high propensity for the inclusion of oxygen atoms in the ZnO material, and so for significant charge carrier removal. In this fashion, oxygen is being absorbed.

Section 7.5 showed that the diffusion of oxygen in stoichiometric ZnO could be ignored, even at the highest experimental temperatures, due to the vanishingly small diffusion coefficients. However, the ZnO that constitutes the sensors is unstoichiometric, with an abundance of interstitial zinc atoms. It is therefore understood that the diffusion of O in the sensors may be appreciably higher than calculated previously (*Lawson, 1999*).

In addition, the amount of oxygen *absorption* is unlikely to be restricted by the same Elovich limit as its adsorption because it will not create a space-charge region or limiting surface potential. Clearly accommodation of extra oxygen in the ZnO matrix, and the movement of any reacted interstitial zinc atoms to a lattice site may create extra stacking faults and other disorders at the surface. It has already been shown that these features create surface states, which will capture additional electrons.

Thus, it seems as though the incorporation of oxygen into the ZnO matrix by permanent oxidation of the zinc donors may adequately explain not only the cause of hysterisis experienced by the sensors, but also the large conductance change that characterizes it. Clearly, zinc oxide is not as stable under AO bombardment as first thought. Additionally, the incorporation of adsorbed oxygen into the semiconductor matrix may be partly responsible for the destruction of the surface inversion layer that existed in the early stages of sensor operation.

However, there is another potential source of sensor hysterisis, namely the residual stresses within the films discovered by XRD measurements (these are detailed in Section 7.2.3). It may be that as the films are heated during regeneration, atomic rearrangements occur which alleviate the stresses. If, during the course of these re-arrangements the number of interstitial zinc donors is reduced, then the conductivity of the semiconductor will also be decreased. Additionally, the stresses might help to aid the transport of adsorbed oxygen into the material. In this way, several mechanisms may act in co-operation to reduce the conductivity of the ZnO sensors.

Even though the conductance of the sensors is perpetually decreased in regeneration, Figures 9.9 and 9.10, and the discussion of Section 9.2, showed that they would still respond to AO fluxes in ensuing experiments. Thus, change of sensor base conductance does not appear to affect the ability of the sensors to measure AO flux. Indeed, examination of Equation (5.32) shows that it is the rate of change of sensor conductance that is dependent upon the flux. Consequently, increases in the base-line conductance of the semiconductor should have little or no influence on the response of the sensors.

9.4.3 Effects of regeneration temperature upon response

The previous section discussed the likely causes for the experimentally observed hysterisis, thereby answering one of the questions about regeneration. It is the intention of this section to examine the effects of regeneration temperature upon the measurement ability of the sensors. Results from experiments TF7, TF8, TF9 and TF10 can be used for this analysis; Table 9.3 gives the necessary data.

Exp.	Regen. temp. (K)	Sensor response per unit flux (x 10^{-22} [mhos.min^{-1}].[atoms.cm^{-2}.s^{-1}]$^{-1}$)			
		TG08A1b	TG08A2b	TG10A1b	TG10A2b
TF7	353	-3.9718	-1.3534	-2.2689	-58.5523
TF8	373	-7.7216	-4.3731	-15.4194	-60.2135
TF9	393	-20.0916	-12.2279	-110.7366	-276.1923
TF10	416	-3.7515	-4.2660	-9.1519	-18.1144

Table 9.3 - Data for investigation of regeneration temperature

In this table, the regeneration temperatures presented are those used at the end of the previous experiment. For example, the regeneration temperature that is shown under exposure TF7 was the temperature used at the end of the experiment immediately preceding TF7, i.e. TF6. Also, the sensor responses (which were calculated in exactly the same way as before) have been normalized by the fluxes that engendered them. This procedure was adopted to remove the influences of small variations of flux level that might have occurred from experiment to experiment. Plots of sensor response per unit flux versus regeneration temperature are shown in Figure 9.14, and there are two important points to consider.

Firstly, regeneration temperature has a clear effect on the magnitude of the response of each sensor in the next AO exposure. Indeed, it appears that there might be an optimum temperature (approximately 390 K) at which to regenerate the sensors, although it is accepted that the limited data set prevents firm conclusions. The optimum temperature seems to cause the ZnO sensors to respond more 'strongly' to a given flux than the other temperatures tested, which, if nothing else,

acts to highlight the need to treat the sensors consistently if accurate measurements are to be made.

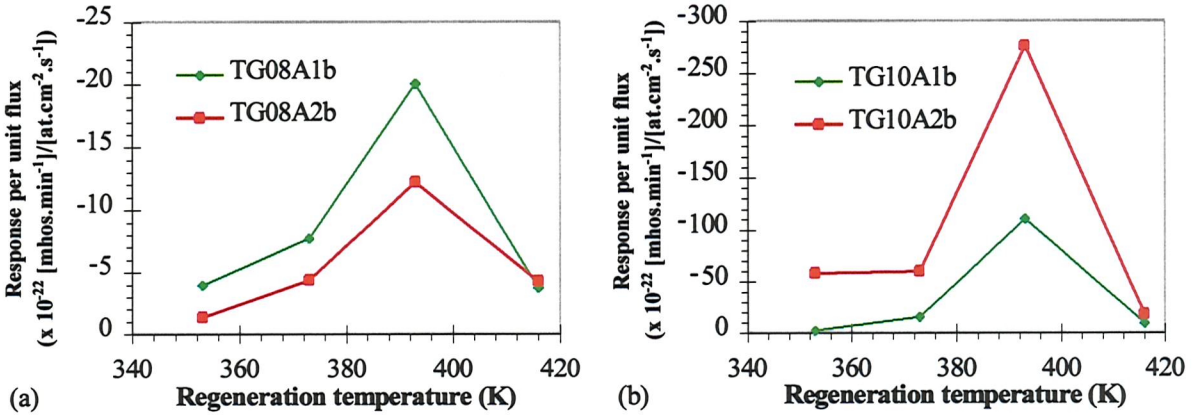

Figure 9.14 - Effect of regeneration temperature: (a) TG08A1b and TG08A2b; (b) TG10A1b and TG10A2b

Secondly, all sensors, no matter what the thickness of ZnO, appear to behave in a similar fashion, so that the optimum temperature is not dependent upon the thickness of the film. However, the response per unit flux calculated for the 1.0 μm sensors is generally higher by at least one order of magnitude than those of the 0.5 μm sensors. This occurs, not because the fluxes are lower, but rather because the gradient responses are larger. This is an unexpected result since it has been argued that the thinner sensors should be more sensitive than their thicker counterparts. Therefore, some explanation is required.

When the ballistic equation was derived (see Sub-section 5.4.1), it was assumed that the maximum extent of the depletion layer would be greater than the dimension of the semiconductor film. This device was used to enable the assumption of electron redistribution in the ZnO and, also, to remove the need to model surface potential barriers. In this way, since all of the film would be affected by adsorption, it would appear that the benefits of thickness reduction are also removed.

That model also assumed a homogenous, isotropic, regular thin film. The films used in the experiments do not conform to this requirement. Most importantly, they seem to have surface areas that scale with film thickness. So, whilst both the 0.5 and 1.0 μm films may be thinner than the dimension of the depletion layer, the thicker of the two has a larger surface area to volume ratio. Hence, under the influence of similar AO fluxes, the 1.0 μm sensors will be able to adsorb more atoms per unit time than the 0.5 μm devices. Therefore, the rate of electron depletion will be increased and so will the response of the sensors. Apparently, there may be a limit to the

performance enhancements of semiconductor sensors that can be achieved by thickness reduction.

9.4.4 Effects of regeneration temperature on hysterisis

The regeneration experiments performed (TF6 - TF9) also allow an examination of the influence of regeneration temperature on the conductance hysterisis experienced by the devices. It is easiest to think of hysterisis as a permanent change of conductance of the sample that results over the course of an experiment, i.e. the difference between the pre-AO exposure value and the post-regeneration value when measured at the same temperature. Therefore, the changes of sensor conductance from the start to finish of each experiment used in the regeneration study have been determined from the experimental data. All of the hysterisis values, in mhos, have been corrected for minor temperature differences that occurred during the measurement of the pre-AO exposure and post-regeneration conductances. This was accomplished by using conductance-temperature plots similar to that in Figure 7.12.

Since hysterisis is believed to be brought about by the irreversible oxidation of free zinc donors in the ZnO, the number of oxygen atoms on the surface may affect the total quantity of zinc oxidized. Thus, it was deemed necessary to eliminate any effects that the variations in AO exposure fluence may have had on the hysterisis values. This was achieved by normalizing the conductance hysterisis by the AO fluence accumulated in the experiments. Table 9.4 presents the calculated hysterisis per unit fluence values for the four experiments TF6, TF7, TF8 and TF9, whilst the graphs in Figure 9.15 are plots of these data versus the regeneration temperature used in the experiment.

Clearly, the graphs demonstrate that the amount of hysterisis any sensor experiences during regeneration is dependent upon the temperature to which it was heated. All sensors show a maximum hysterisis value at 390 K, though again the limited data set prevents firm conclusion that this is indeed the maximum value. It should be recalled that this temperature was also the one that provoked the maximum response from the sensors in the following exposure.

Exp.	Regen. temp (K)	Hysterisis per unit fluence (x 10^{-24} mhos.[atoms.cm^{-2}]$^{-1}$)			
		TG08A1b	TG08A2b	TG10A1b	TG10A2b
TF6	353	8.4065	11.6449	4.8423	-88.5236
TF7	373	12.6119	21.0831	112.4579	234.9418
TF8	393	16.9668	28.4252	237.3482	677.0874
TF9	416	4.8688	0.07563	-101.2215	76.4936

Table 9.4 - Regeneration hysterisis data

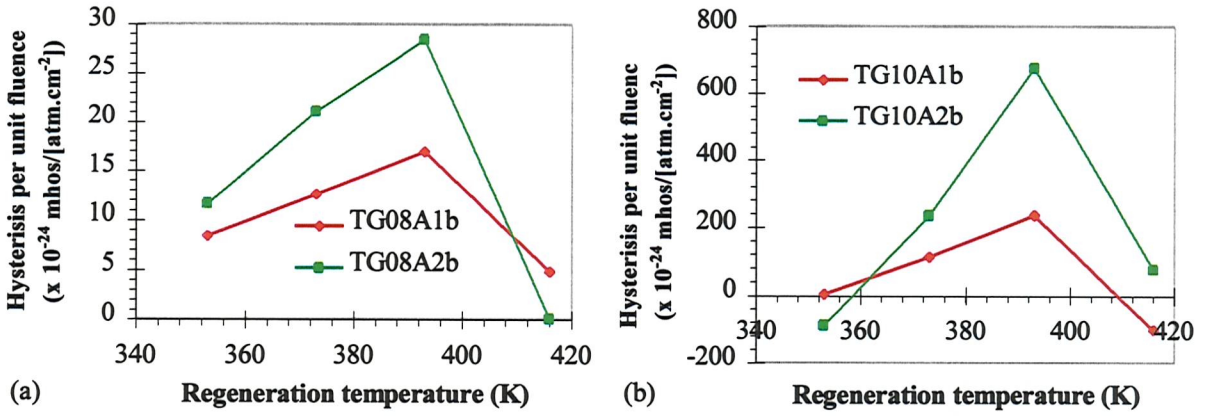

Figure 9.15 - Effect of temperature on hysterisis: (a) TG08A1b and TG08A2b; (b) TG10A1b and TG10A2b

These two results may not be coincidental; if hysterisis is indeed caused by the assimilation of adsorbed oxygen from the surface of the semiconductor, then the maximum hysterisis value is associated with the most absorbed oxygen. The greater the amount of oxygen absorbed from the surface, the 'cleaner' that surface becomes. Since clean surfaces have more adsorption sites free than not so clean surfaces, faster adsorption is possible in the next AO exposure, which thus engenders greater sensor response. So, high sensor response follows large regeneration hysterisis. This finding confirms an assumption used during the design of the experiments in Chapter 8, namely that sensors must always be regenerated under similar conditions (temperature and time), if consistent measurements are to be made.

There are some differences between the results of the two sensor thicknesses. The hysterisis values of TG08A1b and TG08A2b (the 0.5 μm sensors) are always positive, that is the conductance of the sensors always decreases as a result of regeneration. In comparison, one of the calculated hysterisis values for each of TG10A1b and TG10A2b (1.0 μm sensors) are negative, indicating that the conductance of the sensors actually increased, or recovered a little. No explanation has been found for this odd behaviour, and so it is assigned to measurement errors or artefacts of the temperature correction process.

Initially, the permanent change of conductance increases with increasing temperature, but all sensors reach a maximum hysterisis at about 390 K, after which the hysterisis falls to lower levels. The initial increase of hysterisis with regeneration temperature may be explained by the fact that higher temperatures excite more adsorbed oxygen atoms into reaction with surface interstitial zinc atoms. However, it is evident that further increases of temperature (beyond 390 K) reduce the amount of hysterisis. It is believed that these even higher temperatures lead to more

efficient AO desorption, rather than AO reaction. Hence, the quantity of Zn that is oxidized by adsorbed oxygen remaining on the surface is reduced.

9.4.5 Further discussion of regeneration phenomena

The continued presence of hysterisis, even at the most elevated temperatures used, indicates that some oxygen is still being captured in the ZnO. Indeed, it is reported in the literature that in order to fully remove adsorbed AO from ZnO surfaces, temperatures of the order of 500 - 800 K are required (*Malinova and Myasnikov, 1969; Nahr et al., 1971; Cunningham et al., 1975*). Eger reports that oxygen desorption from ZnO surfaces cannot be detected at temperatures in the range 473-573 K (*Eger et al., 1975*).

Unfortunately, no experiments could be performed at temperatures of these magnitudes because of material limits. Whilst the zinc oxide, alumina, silica and ruthenium dioxide are all stable to these temperatures, the solder used to connect the heaters to the temperature controller and the silver-loaded epoxy are not. Further investigations of hysterisis are important to this work, and should include higher temperature studies. A study of the evolved species would also be beneficial, but this would require some technique like mass spectrometry, which is difficult to arrange in ATOX.

Earlier discussion of Figure 9.13 revealed that the regeneration hysterisis seemed to result from the change of sensor conductance during heating at the elevated regeneration temperatures. The figure shows that the conductance change is rather slow, probably because of diffusion of oxygen along and into the surface. Hence, it appears that one method to limit the amount of hysterisis could be to rapidly heat and cool the device. Presumably, this is why Nahr *et al.* (*1971*) and Jacob (*1975*) used the flash heating technique of capacitative discharge to regenerate their single crystal sensors. This is also an area that warrants further investigation. Another benefit of this technique (over the resistive heater used herein) is that the heating energy is deposited directly into the ZnO film, increasing the efficiency of the process due to the reduction of conductive losses.

9.5 SEMICONDUCTOR AO SENSORS - THE SOLUTION OF AN AO FLUX PROBLEM

Until the author conducted accurate AO flux decay measurements in the ESTEC ATOX facility using C-QCMs, the axial variation of AO flux in that facility had not been quantified (*Osborne, 1998a*). These empirical measurements demonstrated that the rate of flux decay is inversely proportional to the square of distance between the sensor and nozzle exit, in agreement with gas-dynamic theory (see Sub-section 8.2.1).

The two 0.5 μm semiconductor sensors (TG08A1b and TG08A2b) have been employed to perform further measurements of the AO flux decay in the ATOX facility. Table 9.5 shows the results of this study - semiconductor sensor responses and the distances between the sensor and the nozzle exit plane (refer also to Figure 9.16 parts (a) and (b)).

Sensor-nozzle distance (cm)	TG08A1b (x 10^{-6} mhos.min^{-1})	TG08A2b (x 10^{-6} mhos.min^{-1})
55	-3.14918	-3.17870
65	-1.29172	-2.15185
75	-1.67097	-1.61903
100	-0.92224	-0.95176

Table 9.5 - Data enabling determination of the variation of AO flux in ATOX

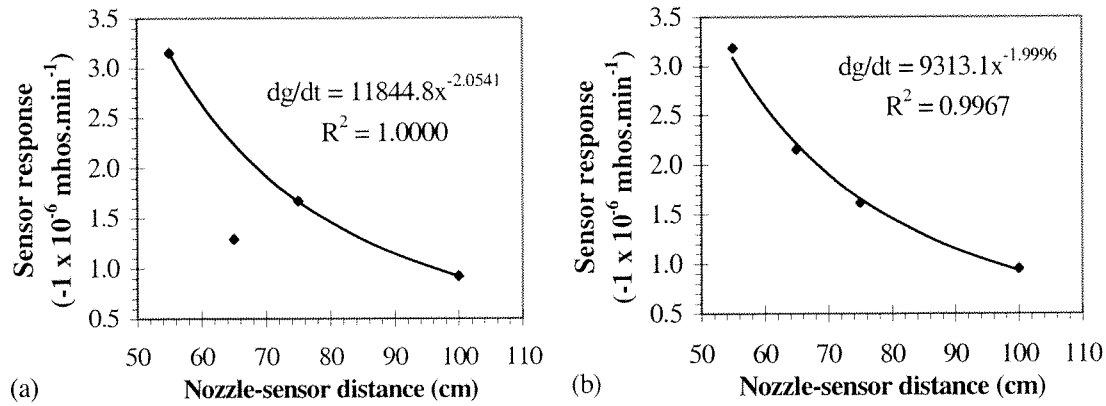

Figure 9.16 - Axial variation of AO flux in ATOX: (a) TG08A1b; and (b) TG08A2b

Since it has been previously shown that there is a linear relationship between ZnO sensor response and AO flux, the ordinates in Figure 9.16 (a) and (b) can be considered to be exactly analogous to the AO flux experienced at the indicated positions. Clearly, the AO flux falls with distance from the nozzle exit plane in a non-linear fashion. Power law functions have been least squares fitted to the data, ignoring the point at 65 cm generated by TG08A1b. The functions have indices of 2.0541 and 1.9996 for TG08A1b and TG08A2b respectively, whist the correlation coefficients are high at 1.0000 and 0.9967. It is apparent that the flux decay rates as measured by TG08A1b and TG08A2b are very close to the author's empirical result from the C-QCM study ($x^{-2.042}$) and to the gas-dynamic predictions of a x^{-2} relationship. This close agreement is yet another indication of the ability and usefulness of the semiconductor sensor technique.

9.6 SUMMARY

This chapter has analysed and discussed the results from the atomic oxygen exposure experiments. Six sensors of three thicknesses of ZnO were tested under exposure to hyperthermal

atomic oxygen. All sensors demonstrated a burn-in or conditioning response phase. During this stage, the conductance of the sensor was found to increase erratically rather than decreasing smoothly as expected from theory and in practise. Additionally, it was found that there existed a critical AO fluence after which sensor behaviour reverted to that considered normal, and that this fluence was film thickness dependent. All of the peculiar responses were adequately explained by the temporary presence of an inversion layer at the surface of the sensor, which forced a p-type sensor response until it was destroyed by surface state elimination and gaseous desorption or entrapment.

Due to the lengthy conditioning times of the 1.0 and 2.0 μm ZnO devices, the flux measuring ability of only the two half micrometre sensors was investigated in depth. It was shown that the sensor response - defined as the peak conductance gradient - was linearly proportional to the time-averaged flux engendering the conductance change. This finding is in agreement with the ballistic sensor model developed in Chapter 5, and allows simple conversion of the raw data into AO fluxes. This indicates the usefulness of ZnO-based AO sensors and the manufacturing repeatability of the devices.

Theoretical exploration of the differences between sensor response under the action of hyperthermal and thermal atomic oxygen showed that the sensors are likely to be more responsive to thermal atomic oxygen. Thus, it is believed, although it cannot be substantiated by experimental evidence, that the sensor will exhibit an energy-dependent response. This remains an area for future experimental investigation.

An investigation of the quantity of AO needed to bring about sensor saturation showed that the saturation process is flux dependent in the regime employed in the experiments. It was proposed that this dependency might be used as another measurand of AO flux.

A permanent conductance decrease was observed as a result of regenerating the ZnO sensors post AO exposure. This finding was not expected because heating the sensor should remove the adsorbed oxygen atoms. It was postulated that the hysterisis is caused by the irreversible oxidation of zinc donors in the zinc oxide lattice and may be prevented, or at least limited, by the use of higher regeneration temperatures of shorter times.

A novel exploration of the effects of regeneration temperature showed that it is most likely that there is an optimum temperature for the renewal of the films. If the sensor is heated to this temperature, the response in the next AO exposure experiment is maximized. However, there is also strong evidence that this temperature leads to the largest amount of sensor hysterisis -

defined as the change of conductance between the pre-exposure to post regeneration values. These two findings were unified by the idea that maximum hysterisis cleans the surface of the sensor to a greater extent than is achieved at any other temperature. The large number of free adsorption sites on the surface increases the rate of AO adsorption in the next exposure, hence the sensor response is also increased.

Two sensors were also used to perform measurements of the axial variation of AO flux in the ESTEC ATOX facility. The two rates of flux decay obtained were found to be close to theoretical prediction and to another empirical measurement. This last study confirmed, once more, the usefulness of the ZnO-detector technique. The next chapter examines the results from the silica-covered sensors and the data from the control experiments performed during the test programme.

CHAPTER 10

CONTROL EXPERIMENT RESULTS

Whilst the last chapter discussed all results allied to the direct action of atomic oxygen exposure on the ZnO sensors, it is the intention of this chapter to describe all of the other influences examined during the experimental programme. The first to be dealt with is the affect that molecular oxygen has upon the sensors - this was investigated in the control experiment TF11. Secondly, results from the silica-covered sensors are used to research the consequences of ultraviolet illumination. Lastly, although it is not a true control experiment, the various sensor behaviours demonstrated during outgassing are explored.

10.1 SENSOR RESPONSE TO MOLECULAR OXYGEN

10.1.1 Background

It should be expected that molecular oxygen will affect the conductivity of zinc oxide in a manner exactly analogous to that of single oxygen atoms. That is, O_2 should remove electrons from the conduction band of the semiconductor by introducing energy levels below the Fermi level. As before, this charge carrier depletion would be associated with surface charging and potential development and, as a result, band bending in a space charge region and reduction of material conductivity.

At first sight, it might appear that the affects of molecular oxygen and atomic oxygen would be indistinguishable. However, it has been reported previously in this work that several researchers have independently found the effect of molecular oxygen to be several orders of magnitude lower than that of atomic oxygen (see Chapter 5.5). In particular, Nahr *et al.* found that under the influence of equal fluxes of molecular and atomic oxygen, new ZnO single crystal sensors responded 10^2 to 10^3 times more weakly to oxygen molecules than atoms (*Nahr et al., 1971*). Moreover, the experiments performed by the authors showed that, when a sensor had been exposed to AO for 'some time', the sensitivity for molecular oxygen became too small to be measured.

Another investigation of the relative influences of molecular and atomic oxygen, using thin films of zinc oxide, is reported by Livshits *et al.* (*Livshits et al., 1981b*). In the ground state, the effect of molecular oxygen was found to be 50 % of its atomic counterpart when the fluxes are in the ratio $[O_2]/[O] = 10^6$. Thus again, it was found that the affect induced by molecular oxygen is far smaller than that of AO. However, the results are different when the molecular oxygen is in the excited state, $O_2(^1\Delta_g)$. With this species, the authors state that the changes in electrical

conductivity are equal when the fluxes are in the proportion $[O_2(^1\Delta_g)]/[O] = 35$. It would seem, the vibrational excitation of the molecules increases the influence of the oxygen on the semiconductor by several orders of magnitude.

Reasons for the differences between the responses of the sensors to molecular and atomic oxygen are difficult to ascertain. It is possible that molecular oxygen is adsorbed slower than AO because of the extra energy that must be supplied to dissociate the O_2 molecule into separate atoms (*Malinova and Myasnikov, 1969*). If this step has to occur before ionization, the rate of electron capture will be much reduced in comparison to the less energy demanding chemisorption of AO. It is also for reasons of energy that excited O_2 has a greater influence than its ground-state counterpart; the energy contained in the molecules due to their vibrational motion may reduce the extra energy required to split the molecules below that required for ground-state oxygen. Hence, the adsorption of excited molecules proceeds quicker than unexcited molecules.

Whilst the AO experiments performed in ATOX were conducted without any intentional flux of molecular oxygen, it is possible that some of the injected O_2 was not dissociated by the laser pulse, and so was incident upon the sensors (*Matcham, 1998a*). The mass spectrometry measurements of Cazaubon *et al.* revealed that the neutral molecular oxygen concentration in the AO beam of a laser-induced breakdown facility similar to ATOX was 9 % (*Cazaubon et al., 1996*). Moreover, Figure 2.1 shows that O_2 remains a significant component of the thermosphere, and is therefore important for spaceflight experiments. For these reasons, it was considered prudent to investigate the influence of molecular oxygen upon the ZnO sensors used in the AO experiments.

10.1.2 Experiment

An investigation of the influence of molecular oxygen requires a source of this species. In ATOX, the simplest way of generating a flux of O_2 is to pulse the electromagnetic valve without enabling the laser. In this case, the oxygen is not broken down, but simply expands through the nozzle and ultimately impinges upon the sensors. Experiment TF11 was performed with the apparatus in this configuration. During the experiment, the oxygen valve was pulsed at rates of 1, 3 and 5 Hz. No response was shown by the C-QCM during this exposure, as expected because carbon is stable in a molecular oxygen environment.

The velocity of the resulting ground state oxygen molecules is lower than that of any undissociated molecular oxygen in the AO beam. In fact, the nozzle exhaust speed should be close to the isentropic expansion velocity of the gas, measured as ~ 750 $m.s^{-1}$ in a facility similar to the one at ESTEC (*Cazaubon et al., 1996*). For comparison, measurements in the same facility

revealed that the remaining molecular oxygen in the AO beam attain a velocity of approximately 10 $km.s^{-1}$.

Whilst this experiment has been used to investigate the influence of molecular oxygen, in particular any undissociated molecules in the AO experiments, the simulation is clearly not quite accurate. As discussed above, the impact energy of the thermal molecular oxygen is low (about 0.093 eV) when compared to the ~ 16 eV of any undissociated molecules in the AO flow. If the response of the sensor displays an energy dependency, or an energy threshold, this experiment will not be suitable as a control. Chapter 9 predicted that, indeed, the sensor should be more responsive to lower energy oxygen atoms than to high-energy atoms. There is no reason why molecular oxygen should not follow the same trend. However, since the O_2 must dissociate before chemisorption, oxygen molecules of higher impact energy might well be more readily adsorbed, see previous sub-section.

Secondly, any remaining O_2 in the AO beam is unlikely to be in the ground state, but more likely to be vibrationally excited in the $O_2(^1\Delta_g)$, or other, state. Clearly, this is another deficiency of the experiment, because Livshits *et al.* (*1981b*) found that excited molecules engendered greater responses in the ZnO sensors than the ground state O_2 used here. Nonetheless, the technique used in this experiment represents the only method available to the author for exposing the sensors to oxygen under the same conditions of vacuum and flux as used in the AO tests.

10.1.3 Results of oxygen exposure

The easiest method to determine if the thin film ZnO sensors responded to molecular oxygen fluxes is to examine the gradients of the recorded conductance data. Figure 10.1 contains graphs of the gradient responses from the bare films in all six sensors. These gradients were calculated using the same routine as that applied to the AO exposure experiment data. In each graph of Figure 10.1, the times of O_2 flux initiation and flux increment are indicated by the positions of the arrows. Also included in the figures are the oxygen fluxes (units $molecules.cm^{-2}.s^{-1}$), which have been estimated as half the measured AO flux recorded under the same experimental conditions (sensor-nozzle distance and oxygen gas flow), but with the laser firing into the nozzle.

Initial observation of the figure below shows that none of the sensors demonstrated significant gradient responses - of the type seen during AO exposure - either with the initiation or increment of molecular oxygen flux. Figure 10.1 should be contrasted to Figure 9.11.b and those in Appendix A2, which were generated in the AO experiments. In these AO exposure graphs, the gradient response of the sensor allows easy identification of the time at which the AO flow was

initiated. No such features are observable in Figure 10.1, even though the oxygen fluxes are of an equivalent magnitude to the AO fluxes employed in experiments TF2 - 6.

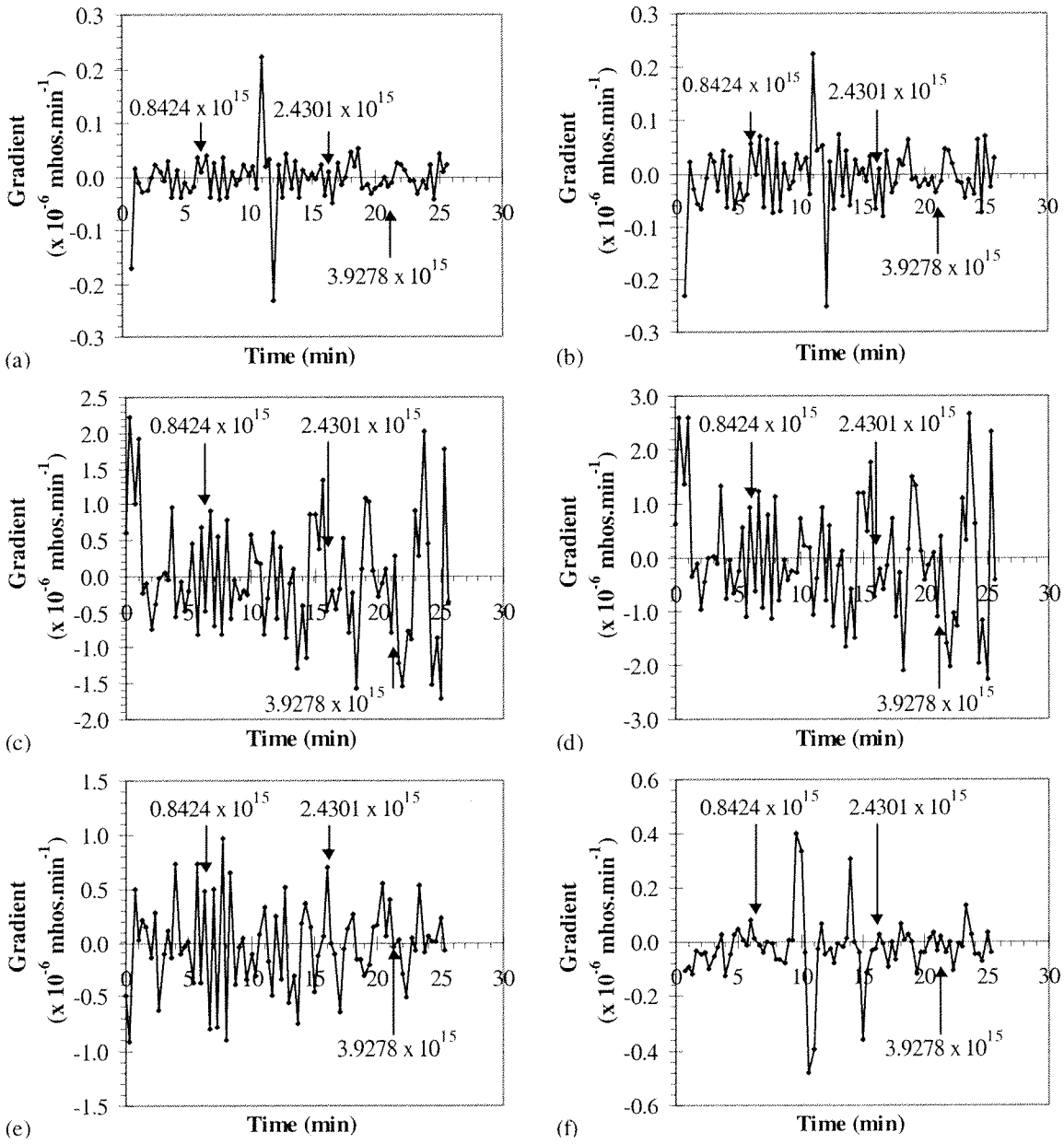

Figure 10.1 - Molecular oxygen responses of all six sensors: (a) TG08A1b; (b) TG08A2b; (c) TG10A1b; (d) TG10A2b; (e) TG11A1b; (f) TG11A2b

Detailed examination of the graphs in Figure 10.1 shows that frequently, upon initiation of O_2 flux, the conductance gradients are positive. It is expected that the gradients, like those found during the AO experiments, should be negative due to charge carrier depletion. Previously, when the laser was operated, these transient positive peaks were attributed to UV induced photoconductivity in the sensors. However, this cannot be the case under the influence of O_2, because there existed no source of UV illumination.

In fact, all the gradient responses of the sensors seem to be random and not correlated at all with the initiation, or increases, of molecular oxygen flux. Probable causes of the gradient changes are temperature oscillations and EMI induced noise. It is therefore possible to conclude that all of the sensors - no matter what the thickness of semiconductor - are insensitive to fluxes of ground state, thermal, molecular oxygen. These results compare well with the findings of other investigators, such as Nahr *et al.*, Livshits *et al.* and Gabriel (*Nahr et al., 1971; Livshits et al., 1981b; Gabriel, 1997*). Hence, with the recognized discrepancy of impact energy, it is also possible to conclude that it is unlikely that O_2 in the AO beam was contributing to the offsets noted in the sensor response plots of Figures 9.9 and 9.10. Therefore, these findings are further evidence in support to the hypothesis that the flux threshold is associated with the C-QCM and not the semiconductor sensors.

There is one last caveat that must be borne in mind when the statement is made that the sensors did not appear to demonstrate any response to O_2 fluxes, which is that all devices had previously been exposed to a significant fluence of AO. This fluence is calculated to be approximately 2.54×10^{19} atoms.cm^{-2} over experiments TF1 - TF10. Recall that Nahr *et al.* (*1971*) found that the O_2 induced response became immeasurable after 'some time' of AO bombardment. It is possible that the AO exposure during these experiments has forced such a change in the six sensors tested.

10.2 EFFECT OF UV ILLUMINATION

10.2.1 Origin of UV radiation in experiments

During operation of ATOX, a hot (~ 20,000 K) oxygen plasma is formed by laser-induced breakdown; this is ultimately the source of oxygen atoms. Unsurprisingly, the high temperature matter in the plasma emits high-energy photons. In addition, recombination and relaxation processes generate radiation in the visible and near infrared bands. Figure 10.2 demonstrates the wavelengths over which a blackbody at 20,000 K radiates.

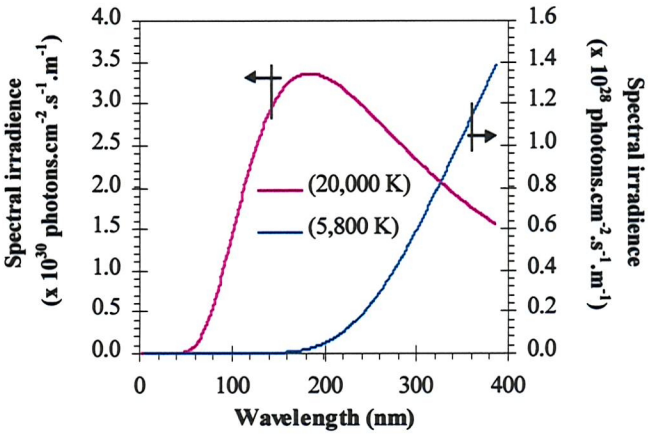

Figure 10.2 - The radiative emission of a blackbody at 20,000 K and 5,800 K

For comparison, the curve for a blackbody at 5,800 K - the effective temperature at which the sun radiates - is also plotted in this graph. Both curves were calculated using Planck's radiation law. It is evident that at 20,000 K the peak emission is in the UV part of the spectrum, at about 160 - 180 nm. In comparison, the peak emission for a sun-type body is at approximately 500 nm, well into the visible spectrum.

A method has been found to estimate the flux of UV and VUV photons at the various sensor positions used in the tests (*Weihs and van Eesbeek, 1994*). Assume that the plasma formed by the laser-induced breakdown of the oxygen gas in the nozzle is confined to a 1 cm diameter sphere. Then, because of the geometry of the nozzle, radiated photons can leave only through the front surface of the plasma. If the plasma is treated as a black body at 20,000 K, it radiates 7.6254×10^{23} photons.cm^{-2}.s^{-1} in the wavelength range 1 - 387 nm; this value can be calculated from the area under the appropriate curve in Figure 10.2. Hence, crossing the front face of the plasma there will be ~ 2.3956×10^{24} photons.s^{-1}, since photons radiated from the rear face of the sphere are assumed to reflect off of the nozzle surface. Note that the lower end of the considered wavelength range - 1 nm - is within the X-ray spectrum and, so, radiation of this wavelength should pass through the ZnO with little electronic interaction. The maximum wavelength range corresponds to the fundamental absorption edge of zinc oxide, see Section 7.4 and Figure 7.13.

If the assumption is made that the photons from the plasma spread out in a hemispherical - $\frac{1}{x^2}$ - fashion, it is possible to calculate the photon fluxes at all distances used in the experiments, see Table 10.1. From these data, it is then possible to calculate the number of photons experienced in each experiment, and also the programme total.

Distance (cm)	**Photon flux (x 10^{19} photons.cm^{-2}.s^{-1})**	**Photons per pulse (x 10^{14})***
55	12.6040	2.5268
65	9.0242	1.8048
75	6.7782	1.3556
100	3.8127	0.7625

* using an assumed plasma lifetime of 2 μs (*Weihs and van Eesbeek, 1994*)

Table 10.1 - Estimated UV fluxes at the experimental distances

The effect of UV irradiation on ZnO was first introduced in Chapter 5. Of particular concern were the reports in the literature that VUV illumination is associated with ZnO damage, in particular oxygen atom desorption. However, UV/VUV irradiation ($\lambda < 387$ nm) was also shown to induce photoconduction in the zinc oxide, a phenomenon that could easily perturb, or mask,

the conductance changes associated with oxygen chemisorption. The consequences of VUV illumination were therefore investigated by experiment.

10.2.2 Examination of experiment results

It is clear from the above that throughout every AO exposure experiment all sensors were illuminated by UV and VUV radiation. It is not possible to gain an insight of the effects of this irradiation by examination of the data from the bare ZnO sensors, because the conductance of these devices was simultaneously affected by AO action. However, in addition to one bare ZnO film, each sensor is equipped with a silica-covered ZnO element (see Chapter 6 for a detailed description of sensor design). The purpose of these films is to allow an investigation like that suggested earlier in this section.

The figure below (10.3) shows the affect of illumination upon the covered 0.5 μm film in sensor TG08A1c. The arrow indicates the time at which AO flow was commenced, and thus the point at which UV/VUV illumination began. Whilst the data presented is from experiment TF2, it is typical of the response of the covered 0.5 μm films in every experiment performed.

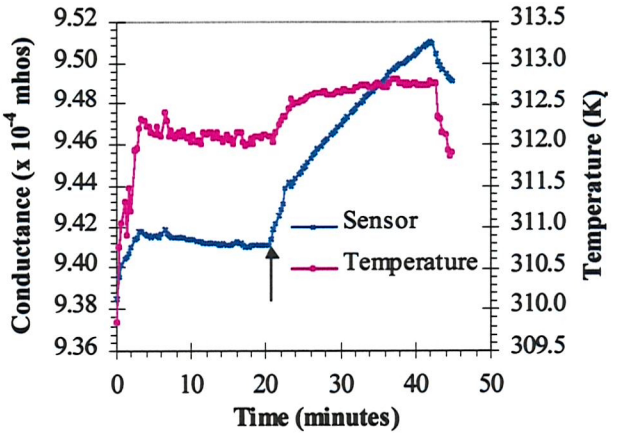

Figure 10.3 - Effect of UV illumination on TG08A1c during TF2

It is apparent from the figure that immediately after the initiation of AO, hence UV irradiation, the conductance of the semiconductor sensor increased. This increase was not caused solely by photoconduction, but also by a small temperature increase (of 0.5 K), which is also evident in the graph. The most probable cause of this temperature change is radiative heating of the sensor substrate. After this rapid conduction increase, a slightly slower one occurs. It is this increase that is brought about by UV illumination of the semiconductor. Notice that the data points are aligned almost linearly throughout this phase. The total increase of conductance caused by UV exposure is 7×10^{-6} mhos, or 0.74 % of the baseline conductance. Recall that during this experiment the

two uncovered films showed a decreasing conductance due to AO adsorption. Plots of their responses can be found in Figure 9.2.

The response of the 1.0 μm covered film TG10A1c, to illumination of the same intensity, is shown in Figure 10.4. Again, the time at which UV irradiation was commenced is marked on the graph by an arrow. The temperature of this substrate appears to have been more stable than the previous one. Hence, there is no rapid increase of conductance during the early stages of exposure. It is obvious from the shape of the sensor curve that its conductance increased non-linearly in time, a slightly different response compared to that of TG08A1c. The conductance of this sensor changed by ~ 7.4 x 10^{-5} mhos during TF2, which is 2.94 % of the starting value. Once again, the bare film data in this experiment can be found in Chapter 9, Figure 9.4 on page 130.

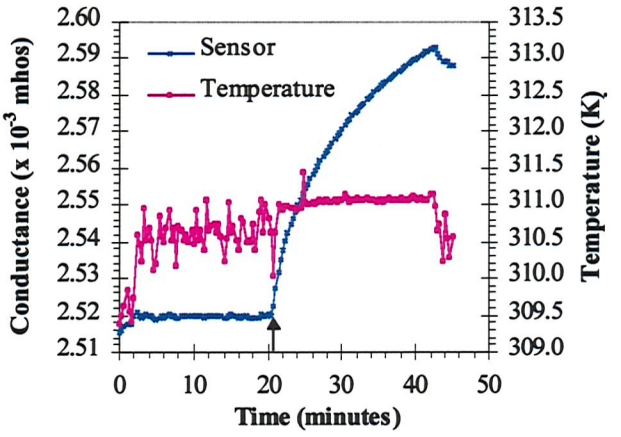

Figure 10.4 - Effect of UV illumination on TG10A1c during TF2

The next figure shows the response of TG11A1c (2.0 μm ZnO) again during the same experiment, TF2. Comparison of the conductance curve to the previous graphs shows that the increase of conductance is even more non-linear than that of TG10A1c and TG08A1c. Moreover, this device's (TG11A1c) conductance increased by the greatest amount: 5.6 x 10^{-4} mhos, or 38.10 % of the baseline. It is also worth noting that the responses of TG10A1c and TG11A1c look very similar to the response of the respective bare sensor films to AO impingement during the conditioning phase of sensor operation.

In all cases, the conductance increase of the semiconductor material is due to the formation of extra zinc donors in the surface lattice. These donors are formed by photodesorption of atomic oxygen, which increases the non-stoichiometry of the films and removes surface charge centres. Therefore, UV illumination is yet another mechanism acting to destroy the inversion layers present in the surfaces of the semiconductor - photodesorption of oxygen will reduce the amount of surface charge. It is also evident that the thicker sensors experienced the greatest conductance

increases as a result of UV illumination. Reasons for this occurrence are examined in a later section of this chapter. Another observation is that the UV illumination of the detectors causes a *positive* rate of conductance change, hence it cannot be used to explain the *negative* offsets noted in Figure 9.9 (page 140). This is yet further evidence that these features are C-QCM, and not MOS sensor, related.

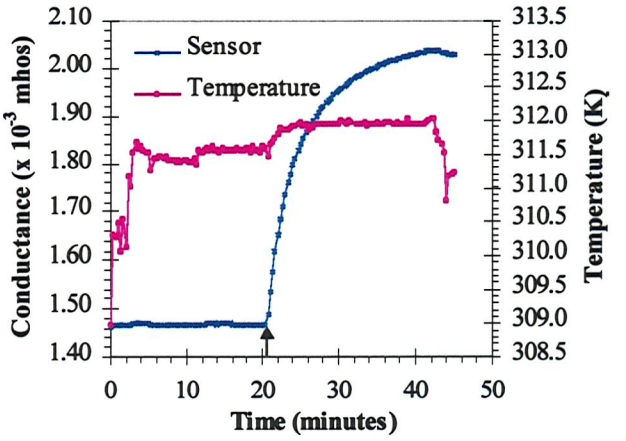

Figure 10.5 - Effect of UV illumination on TG11A1c during TF2

Zinc oxide demonstrates two regimes of photoconductivity, one of which is a fast, reversible change (see Section 7.4). The presence of this reversible mechanism leads to the expectation that the conductance of the sensor should recover some of the increase after the UV illumination has been terminated. Unfortunately, it is not possible to infer from the recorded data if the conductance of the films does in fact decrease in this manner. The regeneration-heating phase was commenced immediately after AO exposure stopped, so large temperature-induced conductivity changes mask any post-photoconductivity conductance recovery.

However, if the conductance change of TG08A1c (for example) is examined over experiments TF2 to TF6, it is found that there is only a very small overall increase in film conductance. Indeed, the start-to-end conductance change over the five experiments TF2 to TF6 is around 8×10^{-6} mhos, which on average is $\sim 2 \times 10^{-6}$ mhos/experiment. In comparison, there is a measured change of $3 - 7 \times 10^{-6}$ mhos during each individual experiment. Thus, if the UV effects were cumulative, it might be expected that the conductance of TG08A1c should change by between 15 and 35×10^{-6} mhos over the five experiments, far greater than what actually occurs.

The small change of film conductance over these five experiments (relative to that during each experiment) indicates that a form of conductance recovery is occurring after each experiment. It is known that some types of radiation-induced semiconductor damage can be annealed and recovered by heating (*Vendura, 1997*). Maybe the regeneration heating, which is conducted at

elevated temperatures, induces a recovery of conductance - in some way repairing the damage caused by UV. One possible mechanism is that photodesorbed oxygen atoms become trapped at the interface between the ZnO and SiO_2. During regeneration heating, these atoms will receive energy, thus allowing them to recombine with the free Zn to which they were originally bound, partially restoring the sample conductance.

In Chapter 9, it was proposed that the permanent oxidation of free zinc donor atoms is responsible for the regeneration hysterisis observed during sensor operation. Therefore, any process that creates additional zinc for later oxidation will enhance the magnitude of hysterisis. Hence, it is possible that the changes of ZnO surface stoichiometry - zinc enrichment - induced by VUV illumination contributes to the amount of hysterisis occurring during regeneration. This might explain why other researchers investigating the uses of ZnO sensors for thermal AO measurement have not reported any hysterisis. If the atom sources used by these researchers did not produce significant quantities of UV, little or no photo-stimulated stoichiometry changes would occur. It might then be postulated that the level of hysterisis would be much reduced.

10.2.3 Quantitative analysis of data

Graphs like that shown in Figures 10.3 - 10.5 have been plotted for each silica-covered sensor in almost every experiment. (*NB* some experimental data were found to be impossible to analyse because of the presence of excessive EMI-induced noise.) From these graphs, the rates of conductance change associated with UV illumination have been calculated. This was simple for those cases in which the conductance seemed to change linearly with time, for example Figure 10.3, but more complicated for those cases where the conductance changed non-linearly. In this event, average gradient values were found by measuring the gradient at three different times. Three linear approximations often matched - or fitted - the data very well.

Since the rate of conductance change demonstrated by a sensor is likely to be dependent upon the intensity of the VUV illumination, some way of deconvoluting changes of intensity with sensor-nozzle distance must be applied to the data. Therefore, for each experiment, the gradient values have been normalized by the calculated experimental photon flux (Table 10.1) engendering the conductance changes. The results of this analysis are presented in Table 10.2, in which a dashed cell indicates that the value could not be calculated.

Figure 10.6 shows plots of the normalized gradients versus the accumulated VUV fluence. It is clear that the general trend - for all six sensor films - is for the rate of change of sensor conductance to fall with accumulated VUV exposure. This is evidence of permanent VUV-induced damage of the MOS sensor material. Indeed, Gilligan reports that the quantum efficiency

of ZnO decreased by several orders after UV illumination to 10^{16} photons.cm^{-2} (*Gilligan, 1967*). In any case, ultraviolet illumination often induces ageing like that observed, for example optical transmittance of samples falls with accumulated UV photon fluence because of the formation of F-centres (*Matcham, 1998a*).

Exp	Dist (cm)	Time (s)	Photon flux (x 10^{19} cm^{-2}.s^{-1})	Photon fluence (x 10^{17})	Rate of conductance change (x 10^{-27} [mhos.min^{-1}].[ph.cm^{-2}.s^{-1}]$^{-1}$)					
					TG08A1c	TG08A2c	TG10A1c	TG10A2c	TG11A1c	TG11A2c
TF1	55	1320	12.6040	0.5324	6.9660	3.8702	47.0303	20.5285	508.6229	162.9676
TF2	55	1320	12.6040	1.0648	3.0705	1.7741	18.9257	11.6768	336.4592	76.8241
TF3	75	1777	6.7782	1.4502	1.6393	2.1076	15.3215	7.6225	220.6038	34.2388
TF4	100	1800	3.8127	1.6698	1.8412	0.9367	11.3654	7.2854	138.6399	18.0896
TF5a	55	1220	12.6040	2.1619	1.5868	0.9155	9.6756	5.2893	58.1825	24.0320
TF5b	55	780	12.6040	3.1057	1.1134	0.5510	5.1424	3.2794	11.2372	2.4590
TF5c	55	540	12.6040	4.1947	0.7823	0.3306	3.5262	2.0725	4.7898	9.3341
TF5d	55	200	12.6040	4.4367	-	-	-	-	-	-
TF5e	55	280	12.6040	4.5496	-	-	-	-	-	-
TF6	65	1140	9.0242	4.8788	0.3690	0.2586	7.7673	6.1754	62.1084	10.0210
TF7	65	1140	9.0242	5.2080	0.7779	0.2301	4.7491	5.3507	29.2655	5.9088
TF8	65	1140	9.0242	5.5372	0.7768	0.0875	3.9893	4.6858	29.3430	5.2043
TF9	65	1140	9.0242	5.8664	0.3324	0.0739	4.5544	4.4915	45.6677	9.2729
TF10	65	1689	9.0242	6.3541	-	-	-	-	-	-

Table 10.2 - Sensor UV exposure and rates of conductance change

It is interesting to note the relative magnitudes of the rate of change of sensor conductance due to UV exposure. In the case of the 0.5 μm sensors, TG08A1c and TG08A2c (Figures 10.6.a and b), the rates of conductance change are of approximate order 10^{-27} [mhos.min^{-1}]/[photon.cm^{-2}.s^{-1}]. For the 1.0 μm sensors (TG10A1c and TG10A2c) - (c) and (d) of the same figure - the rate is one order of magnitude higher, at about 10^{-26} [mhos.min^{-1}]/[photon.cm^{-2}.s^{-1}]. Lastly, for the thickest sensors, TG11A1c and TG11A2c shown in Figure 10.6 parts (e) and (f), it is larger still at approximately 10^{-25} [mhos.min^{-1}]/[photon.cm^{-2}.s^{-1}]. Therefore, it appears that the rate of UV/VUV-induced conductance change is semiconductor thickness dependent, like the steady-state increases described earlier. An exploration of one possible cause of this dependency is conducted below, although the results of this approach fail to provide an adequate explanation for this observation.

The figure also shows that the rate of conductance change demonstrated by all sensors seems to become more stable after about 4 x 10^{17} photons. It is suggested that after this photon fluence, the quantum efficiencies of the films cease to change rapidly.

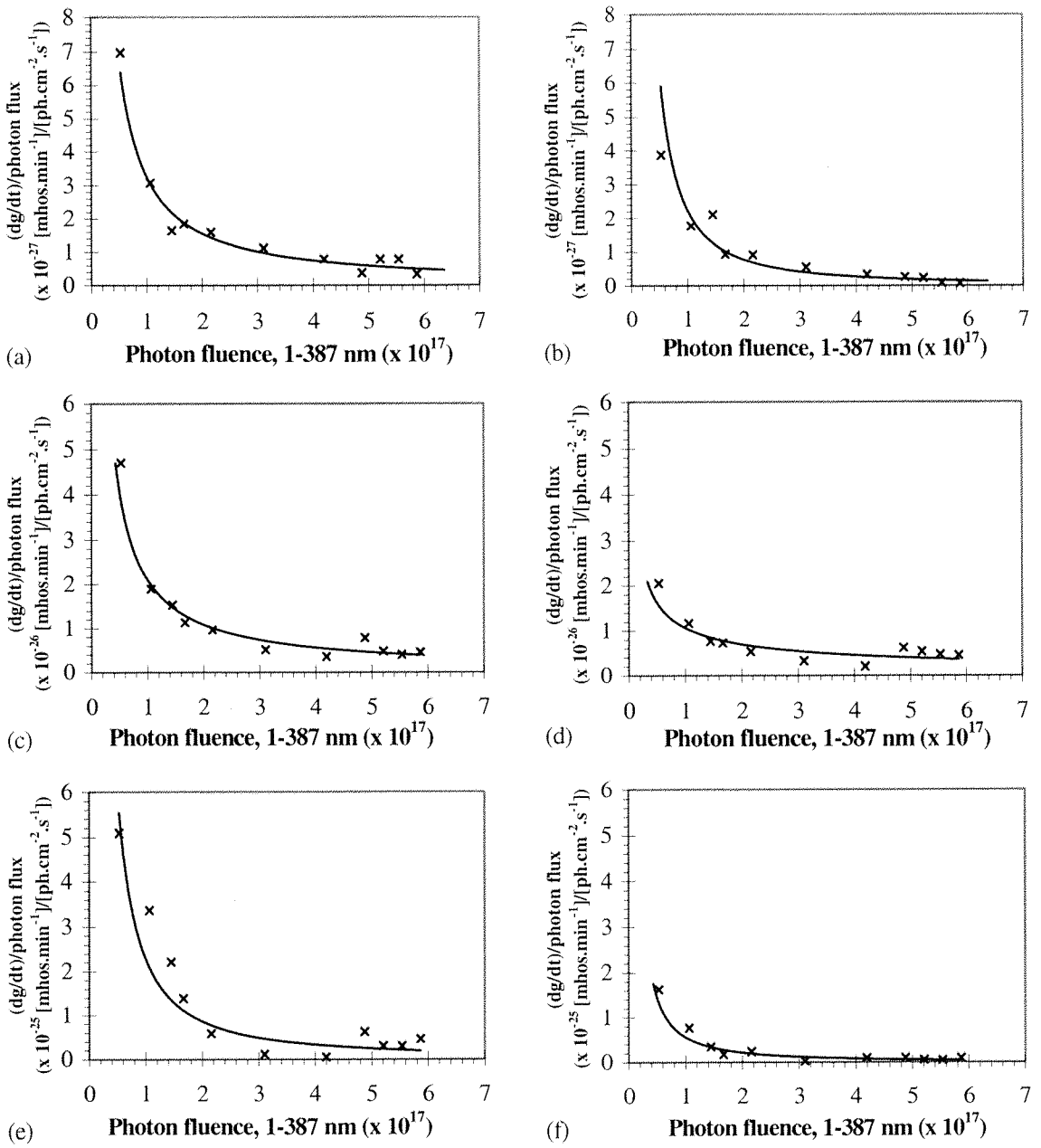

Figure 10.6 - Accumulated VUV effect: (a) TG08A1c; (b) TG08A2c; (c) TG10A1c; (d) TG10A2c; (e) TG11A1c; (f) TG11A2c

The size of the VUV-generated conductivity increase should be compared to the decrease brought about by AO exposure. This is best achieved by noting the rates of change of conductance caused by both AO and VUV action. For TG08A1c in TF2, the largest gradient due to photoconductivity is approximately $+0.4 \times 10^{-6}$ mhos.min^{-1}, compared to a change of the order of around -3×10^{-6} mhos.min^{-1} for AO recorded by TG08A1b. However, the ageing demonstrated in Figure 10.6 means that by experiment TF9, the UV-induced rate of change is reduced to about 0.3×10^{-7} mhos.min^{-1}, two orders of magnitude lower than the AO response of TG08A1b in the same experiment, which was measured to be -2.2×10^{-6} mhos.min^{-1}. Obviously, the thicker

sensors experience larger conductance changes due to UV illumination and, hence, the relative magnitudes of the UV-induced and AO-induced changes are different for these devices.

10.2.4 Investigation of semiconductor thickness dependency

The wavelength dependent absorptance of zinc oxide in the UV was presented in Chapter 7, Figure 7.13. Using data in this graph and Lambert's law, $I = I_0 e^{-\alpha x}$, it is possible to calculate the likely penetration depth (x) of the UV and VUV radiation. The figure below shows how this depth varies with wavelength of light, for 90% and 99% absorption ($\alpha = 0.90$ and 0.99, respectively).

As can be seen from the curves of the graph, the depth of UV penetration in ZnO is wavelength dependent. Towards the upper end of the range examined (387 nm), the radiation is able to travel to a thickness in excess of 100 μm before its intensity is reduced to 1% of its original value. With decreasing wavelength, the absorption depth reduces dramatically, reaching about 0.1 μm at 350 nm and remains at this value over much of the UV spectrum. Thus, it is clear that all of the incident UV and VUV will be absorbed in the near surface layers of all films, even in the thinnest of the ZnO sensors (0.5 μm). Hence, the previously observed thickness dependency in the rate of conductance change cannot be explained by increased photon absorption in the thicker layers. This phenomenon remains unexplained.

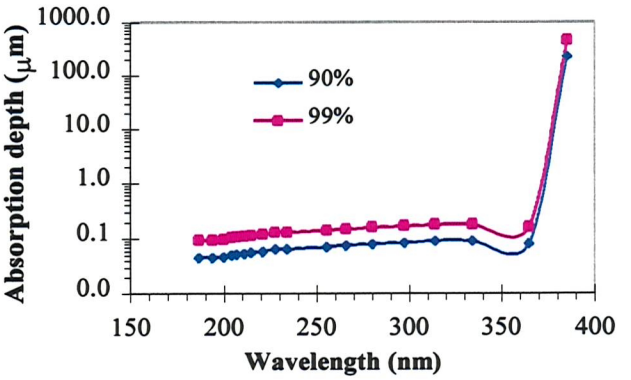

Figure 10.7 - The penetration depth of UV and VUV radiation in ZnO

10.3 OUTGASSING OF SENSORS

10.3.1 Experimental observations

Section 7.3.1 showed that the conductances of all sensors were found to increase as a result of heating the ZnO films to an elevated (but constant) temperature in vacuum. This result is attributed to the desorption, or outgassing, of gaseous species - such as oxygen - from the surface

of the zinc oxide. Upon adsorption, these molecules localize electrons from the conduction band and, hence, depress the conductivity of the sample. Thus, when the species thermally desorb, the electrons are returned to the material, and so the conductance of the sample increases. Typical outgassing curves are presented in Figure 10.8 (see also Figure 7.8).

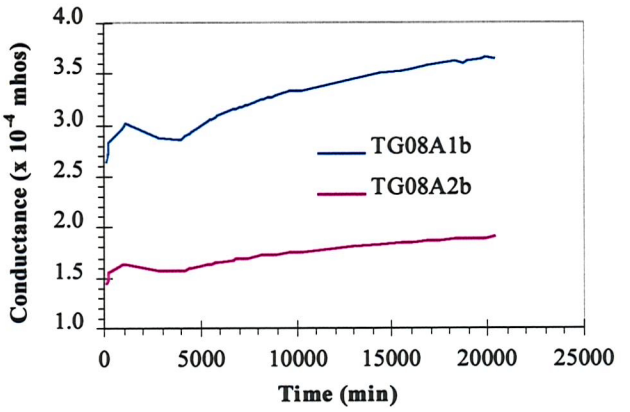

Figure 10.8 - Thermal outgassing, at 373 K, of two AO exposed sensors

In fact, this response is observed only from those devices that have been utilized in several atomic oxygen experiments and have then been stored in the laboratory atmosphere. A quite different reaction is observed for sensors that have never been exposed to atomic oxygen, but have been exposed to ambient air, for example see the plot shown in Figure 10.9.

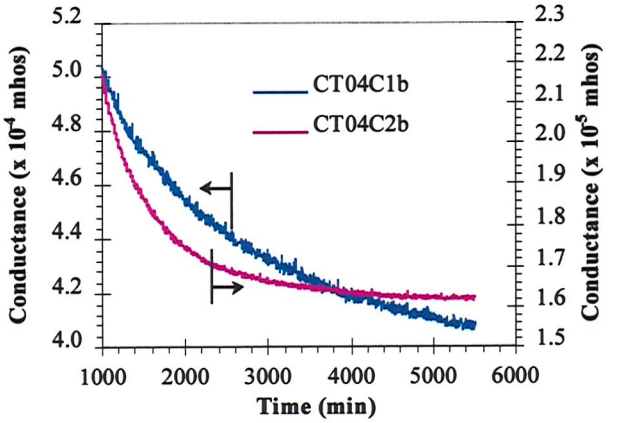

Figure 10.9 - Outgassing of two sensors, at 353 K, that have not experienced AO exposure

It is evident that the conductance of these unexposed (newly deposited) sensors decreases as a result of outgassing. The difference between the two sets of devices could not be clearer, even though they had been stored in the same fashion under laboratory air. The only conclusion to be drawn is that, in some manner, exposure to AO influences the effect of species desorption from the surface of the semiconductor.

10.3.2 Explanation of findings

The discussions presented in Chapters 4 and 9 indicated that the surfaces of newly manufactured semiconductor sensors are dominated by the presence of inversion layers, which result in the sensors demonstrating temporary p-type behaviour. Thus, upon the adsorption of oxidizing species, the conductivity of the semiconductor is observed to increase, because electrons are captured directly from the valence band, leaving behind positively charged holes that increase the total charge carrier density. After a certain number of AO exposure/regeneration cycles and AO fluence, the surface reverts back to its inherent n-type behaviour because the inversion layers have been destroyed.

Thus, a sensor that has never been exposed to AO will still have an inversion layer at the surface. During storage, adsorption of additional gases from the atmosphere will artificially increase the conductivity of the semiconductor by the introduction of holes in the valence band. When the sensor is subsequently heated under vacuum, for example immediately before the first exposure experiment, the adsorbed gases will desorb. Initially, the electrons originating from this process will fill the valence band, because this is the most energetically favourable site for them to go. Thus, outgassing of unexposed material will result in a decreasing total charge carrier concentration, hence decreasing conductance. This has been observed in practice, see Figure 10.9 for example.

However, once the valence band is fully occupied, continued baking of the films should then engender conductance increases. As further adatoms - those that were adsorbed during manufacture and storage - desorb, the electrons are liberated directly into the into the conduction band of the semiconductor, so the charge carrier concentration begins to increase. A reversal of this nature has never been observed, perhaps because the films have not been heated for the required time or to a high enough temperature.

In comparison, the destruction of the inversion layers by hyperthermal AO exposure and/or UV illumination engenders a very different response to outgassing. Again, during storage of exposed sensors, molecular oxygen and other oxidizing species become adsorbed on the semiconductor but, in this case, electron capture results in a decreased sample conductance. The likelihood of inversion layer formation in these samples is much reduced because surface annealing has permanently diminished the density of surface states. Therefore, the surface of the exposed sample always remains n-type.

During heating, the previously adsorbed species leave the surface, and re-inject their captured electrons directly back into the conduction band of the semiconductor. Hence, as observed during

experiment (Figure 10.8), the conductance of the exposed sensors always increases throughout the outgassing process.

10.4 SUMMARY

An investigation of the effects of thermal, ground state, molecular oxygen fluxes upon the thin film sensors used in the AO experiments has shown that the MOS devices are insensitive to this species. This study was performed in an attempt to demonstrate that any undissociated oxygen in the AO flux during the experiments would not influence the results from the sensors. However, the impact energy and excitation state of the molecular oxygen in the control experiment was found to be approximately 170 times lower than that of any undissociated oxygen that may have been present in the AO experiments. It was suggested that if the sensor displayed an energy threshold, or an energy dependency of response (as concluded in Chapter 9), then the simulation used might not be adequate. Unfortunately, no other was available.

Ultraviolet light, generated as a by-product of the AO formation process, was found to increase the conductance of the silica-covered sensors. Experiment showed that the thicker sensors experienced the largest and fastest increases of conductance as a result of UV irradiation. No explanation of this effect has been found, because it was demonstrated that all the incident UV light is absorbed in approximately 0.1 μm of ZnO - thinner than the least thick sensor.

The rate of increase of sensor conductance with UV photon fluence was found to decrease monotonically for all sensors tested. A damage mechanism involving photo-stimulated desorption of oxygen was suggested as the cause of this phenomenon. This decay means that, after around 4×10^{17} photons, the rate of conductance increase becomes a small, stable fraction of the magnitude of sensor response to AO flux. It was also postulated that the VUV-induced stoichiometry changes were, in part, responsible for a component of the regeneration hysterisis, and assists in the destruction of inversion layers.

Sensor behaviour during thermal outgassing was also examined. It was shown that unexposed sensors demonstrate a conductance decrease in this process, whereas AO-exposed devices experience conductance increases. The influence of surface inversion layers was postulated as the key cause of these features.

The next chapter describes the design of the spaceflight equipment. It also addresses the issues of sensor response discovered in this and the previous chapter that are pertinent to the operation of the spacecraft experiment.

CHAPTER 11

SPACEFLIGHT EQUIPMENT

The previous chapters have described the experiments and investigations that have been performed in order to satisfy the research aims presented in Chapter 1. However, the last aim, which was to build a space-rated experiment to demonstrate the use of ZnO-based, reusable AO sensors in Earth orbit, remains to be accomplished. It is the intention of this chapter to elucidate the design and construction of the spaceflight hardware conceived to fulfil this goal, and to attempt to predict the likely responses of the experiment once in orbit.

11.1 INTRODUCTION

11.1.1 Project history

The first University of Southampton atomic oxygen experiment, acronym AOE-1, was an actinometer-based experiment. The equipment was launched upon the maiden Space Technology Research Vehicle, STRV-1a. This spacecraft was one of a pair of microsatellites built and operated by the then Defence Research Agency (DRA). The AOE-1 was designed to demonstrate the feasibility of using silver thin film actinometers in GTO, both for AO sensing and material erosion studies. Results from the experiment have been reported widely elsewhere (*Harris, 1996; Harris et al. 1997a; 1997b; 1998*).

When the author joined the current project, it had already been decided to demonstrate the *in situ* operation of ZnO AO sensors on the third STRV satellite, STRV-1c. However, at that time, experiment definition was in an embryonic state and much work was required to research and design the flight hardware. Due to the limited time scales of the project, the flight hardware was developed concurrently with the characterization of the MOS sensors. The sections below describe the development, interface and intended operation of the spaceflight equipment.

11.1.2 The space technology research vehicles

Two spin-stabilized microsatellites - STRV-1a and 1b - were built in 1994 and launched into GTO as secondary payloads on an Ariane 44LP. The successful operation of these vehicles prompted the new Defence Evaluation and Research Agency (DERA) to build another two STRV units, 1c and 1d, again for operation in GTO.

The STRV-1c and 1d mission objectives are to (*Wells, 1999*):

1) Enhance the capabilities of future communications, navigation and surveillance space systems and reduce cost and risk by demonstrating the successful application of emerging technologies.
2) Execute a low cost, fast delivery microsatellite programme for flight-proving, accelerated life testing and prototyping against a comprehensive characterization of the space environment.
3) Promote international collaboration with the US, Canada and the European Space Agency and national collaboration with UK industry and universities.

Hence, the vehicles are equipped to accommodate many different experiments, each with specific, individual requirements. The architecture of the satellite bus is such that it provides a flexible interface for the experiments, and allows those units to be separately operated to maximize their scientific return.

The spacecraft platform is equipped with an on-board computer (OBC), which can be used to control the operation of simple experiments that do not have the mass, power or financial budgets for the inclusion of an internal processor. Experiments are commanded by the OBC using a digital command distribution unit (CDU). The OBC is used to switch experiments on and off, and to instruct them when to take data. It also allows telecommanding of experiment operations, so that various features of experiment and satellite operation may be altered during the course of the mission. Another property of the OBC is that it allows the operation of several software-based experiments, for example encryption algorithms and communication protocols.

An on-board data handling subsystem (OBDHS) receives the data from the experiments and prepares it for transmission to the ground station. The OBDHS incorporates several electronic interfaces for command and communication with the various experiments. Simple experiments can send data to the OBDHS via analogue or digital data acquisition unit (DAU) lines. However, the preferred digital OBDHS interface is RS-422/RS-232 international standard. An integral part of the OBDHS is an analogue to digital conversion unit. It is within this device that an 8-bit analogue-to-digital converter (ADC) digitizes the analogue data, before it is recorded and stored for transmission to the ground at the next down-link session.

Delivery of power to the experiments is also the responsibility of the satellite bus. Power is derived from a solar array and battery combination, so that operation may be achieved both in sunlight and, to a limited extent, in eclipse. Power is supplied to the experiments through the power conditioning and distribution subsystem (PCDS), which embodies separate isolation trip-switches for each of the experiments. Should an experiment exceed its allocated current, the trip-switch will fail, shutting down the experiment; the trip-switches may be remotely re-set from the

ground station. In addition, each experiment is isolated from the 28 V bus by the use of an inductively coupled DC-DC converter internal to the experiment hardware.

Satellite attitude is determined using slit sun-sensors and infrared Earth sensors. Nominally, the attitude of the satellite will be maintained with the spin axis orthogonal to the sun direction and within 10° of the orbit normal. A passive nutation damper is used to control the nutation of the vehicle, whilst the attitude is controlled using a magnetorquer and a xenon cold-gas thruster. The vehicle is also equipped with spin-up and spin-down xenon cold-gas thrusters to enable control of the spin rate of the spin-stabilized vehicles.

The last subsystem of importance to this work is the radio frequency communications subsystem (RFCS). This platform system is used for both the up-link of telecommands and the down-link of telemetry, which consists of satellite platform 'house-keeping' information and experiment data. The RFCS uses the S-band communications frequency for both of these purposes and standard ESA communication protocols. Communication sessions with the STRV satellites are scheduled to take place once every six orbits, or approximately every three days. They will be conducted through the DERA satellite operations centre and the DERA 12 m antenna located at West Freugh, Scotland, or the NASA Deep Space Network (DSN).

The details of the four STRV satellites are given in Table 11.1 below.

Vehicle	Mass (kg)	Size (mm) (X, Y, Z)	Power (W) *	Orbit (km) [i = 7°]	Exp.
1a	~ 50	450 x 450 x 395	35	280 x 38,000	8
1b	~ 50	450 x 450 x 395	35	280 x 38,000	6
1c	~ 112	580 x 680 x 600	66	564 x 35,890	13
1d	~ 112	580 x 680 x 600	69	564 x 35,890	9

* Power values quoted are beginning of life (BoL).

Table 11.1 - The STRV-1 series of microsatellites

The common structural design of the new STRV vehicles is shown in Figure 11.1, also indicated in this figure is the satellite co-ordinate reference system. The structure of the satellites comprises of an 'H' section formed by two shear walls bolted, at either end, to a fixed side wall. The 'H' section is then rigidly attached to a base (-Z) panel, upon which the interface to the launch vehicle is mounted. This part of the satellite is called the 'primary structure'.

Within the primary structure are support mechanisms for a number of shelves. It is on these shelves that the experiments, satellite bus subsystems and electrical harnesses are mounted. The shelves are designed to be removable from the structure so that, during assembly integration and

testing (AIT), the experiments can be mounted on the shelves, and then the shelves 'slotted' into the primary structure.

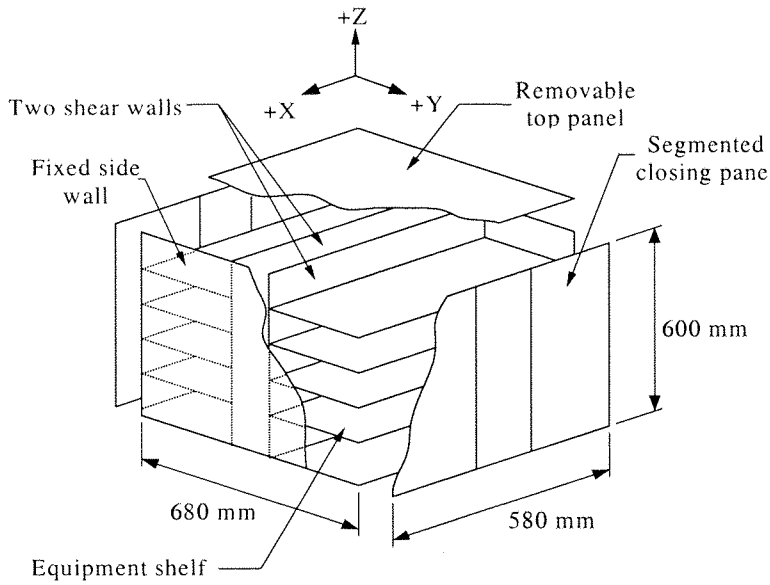

Figure 11.1 - The STRV-1c and 1d structure (after *Cant and Simpson, 1998*)

All shelves and panels are fabricated from flat composite panels. The face plates of the panels are manufactured from high stiffness, high thermal conductivity carbon fibres in a polyetheretherketone (PEEK) resin system. Separating the two face plates is perforated aluminium honeycomb core. The joints between all of the shelves and panels have been designed to maximize the thermal conductivity between the different structural elements.

Once integration of the internal shelves is complete, the satellite structure is finished by two closing panels, which are mounted on the ±Y faces of the satellite, and the removable top 'lid'. These three panels are used to support experiments that require exposure to the space environment, antennae, and satellite sensors like the Earth and Sun sensors. Additionally, the ±Y and ±X panels are used to carry the power generating solar arrays.

11.2 OVERALL DESIGN OF THE EXPERIMENT

The atomic oxygen experiment - 2 (AOE-2) is a payload of STRV-1c. Hence, the design of the AOE-2 was influenced by the budgets allocated to the experiment by DERA, the objectives of the AOE-2 experiment, and the experiences learned from the AOE-1 mission.

Tables 11.2.a and 11.2.b contain the budgets allocated to the AOE-2 by the DERA design team. The mass and size of AOE-2 are nominally the same as AOE-1, whilst the power and data allotments have been increased to accommodate the larger number of sensors and the higher

temperatures of operation in the new units. In common with nearly every microsatellite system, it is clear that the designated mass, power and size limitations place severe constrictions on the AOE-2.

Component	Mass budget (kg)	Size budget (mm) (X, Y, Z)
Sensor	0.1	50 x 34 x 93
Electronics	0.2	195 x 150 x 30
Harness	0.05	~ 150 mm length

(a)

Mode	Purpose	Power (W)	Data rate ($kb.s^{-1}$)	Data generated per operation (kb)
1	Measurement	3.0	5.0	15
2	Regeneration	3.0	1.7	11
3	Stand-by	0.0	0.0	0

(b)

Table 11.2 - The allocated AOE-2 budgets: (a) volume and mass; (b) power and data

The sensors of AOE-2 must be affixed to an outside surface of STRV-1c, so that they experience AO exposure. Hence, the experiment has been split into two units, which are electrically connected by a short harness. Division of the experiment into two separate assemblies allows easy integration of the experiment onto the cramped space vehicle, but at the cost of increased mass and susceptibility to electrical interference.

The unit exposed to the AO environment is called the sensor unit, abbreviation SU. It is designed to be affixed to the -Y closing panel of the satellite. This face will only experience periodic AO exposure, due to the stabilization-related rotation of the spacecraft about the Z-axis and due to the elliptical nature of the satellite orbit. The second component is called the electronics unit (EU), which contains all of the necessary electronic devices for power conditioning and isolation; sensor conductance measurement; sensor temperature control and temperature measurement; data transmission to the OBDHS and OBC interface. The EU resides upon a 'shelf' inside the satellite and has, where possible, been manufactured from space-rated radiation-hard components. The physical separation of the two units requires an inter-unit harness length of 150 millimetres.

Operation of the AOE-2 has been split into three modes. Similar to the ground-based experiments, two of the modes are required because the ZnO sensors are alternately exposed to AO and then regenerated. The third mode is required for stand-by operation between modes 1 and 2, so the experiment may be temporarily shut down to save power and data storage space.

The total design lifetime of AOE-2 is 200 days. The following sections describe the detailed design of both units.

11.3 THE SENSOR UNIT

11.3.1 Design of the unit

The purpose of the sensor unit is to mechanically support the AO sensors during satellite launch and operation in Earth orbit. However, given that the AOE-2 is divided into two units that are connected by a harness, the SU also includes electrical connections between the harness and the sensors.

Early on in the design phase of the experiment, it was decided to incorporate some silver film actinometer sensors into the sensor suite. These sensors serve two purposes. Firstly, they can be used to calibrate the responses of the ZnO devices, since their operation in space has been qualified by previous usage. Secondly, their presence allows some continuation of the silver-sensor work, which would have otherwise ceased. The design of the ZnO sensors and associated heaters has been detailed in Chapter 6; AOE-2 uses the robust sensor types CT and RT, rather than the fragile TG series. The silver actinometers are of the original design by Harris (*Harris, 1996*).

To aid visualization of the SU, an 'exploded' isometric diagram is presented in Figure 11.2 below, whilst a schematic of the sensor unit design can be found in Figure 11.3. Four ZnO sensors on two alumina substrates, and four silver actinometers on two glass substrates, are incorporated in AOE-2. The three substrates each have a dedicated AD590MF temperature sensor.

As Figure 11.2 shows, there are several individual components that constitute the AOE-2 SU. The sensors themselves are mechanically supported by a face plate. In the case of the ZnO sensors, the substrates are recessed slightly into the face plate and are affixed in place by the use of a NASA certified low-outgassing, pressure-sensitive adhesive (PSA#10). The face plate has been designed so that there is a void directly behind the ZnO sensors. In this way, the area over which heat may be conducted from the sensor is reduced - there is no material directly touching the sensor heaters. The efficiency of heater power transfer is thereby maximized. Each void behind the sensor is equipped with small vent holes, so that pressure differences between the front and back faces cannot arise during launch. Such pressure differences might have lead to damage of the sensor substrates, possibly completely destroying the operability of the sensors.

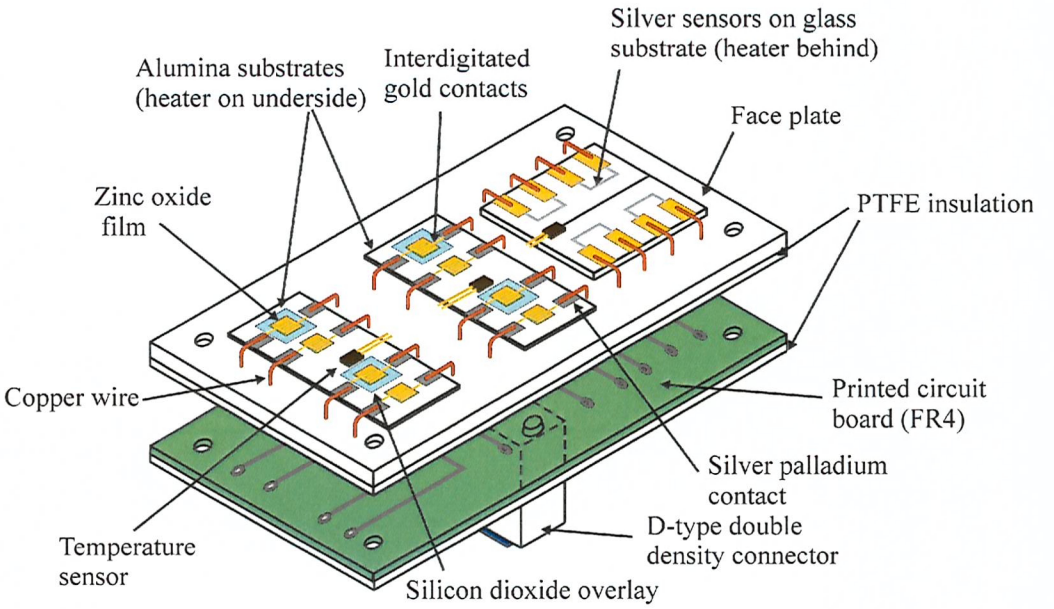

Figure 11.2 - Isometric drawing of the sensor unit

During the measurement phase, the silver actinometers are also heated to maintain a constant temperature. This is accomplished by using a 25.4 mm square thermofoil heater supplied by Minco. Due to the lower temperature requirements of the silver sensors, the heater is affixed directly onto the face plate and the silver sensor substrates directly onto the heater. Both bonds are made using the same pressure-sensitive adhesive used to affix the ZnO sensors to the substrate.

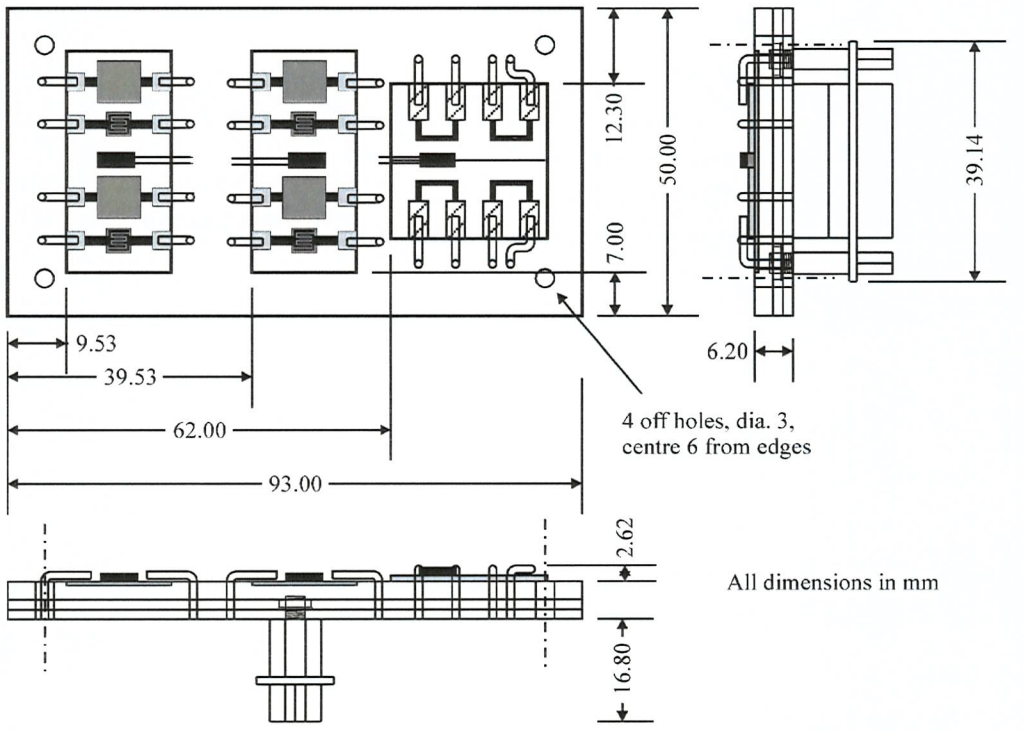

Figure 11.3 - Schematic of the AOE-2 sensor unit

Immediately behind the face plate is a sheet of PTFE polymer, the purpose of which is to insulate - thermally and electrically - the face plate and heaters from the next component, which is a PCB (printed circuit board).[Ψ] It is the PCB, in conjunction with a space-rated D-type connector (Positronics), which is used to connect the inter-unit harness to the different AO sensors, heaters and temperature sensors. Electrical contact between these elements and the PCB is achieved by the use of short lengths of 1 mm diameter copper wire, or multicore, insulated cable. The wires are soldered on the rear side of the PCB and are soldered to the ZnO sensors, heaters and temperature sensors. In comparison, silver-loaded epoxy (Epo-Tek H21D) is used to form the connection to the silver actinometers. The connector is fastened to the PCB by two bolts and the soldered pins, which avoided the need for a bracket to support it, thus reducing the mass of the sensor unit.

Behind the PCB is another PTFE component (not shown in Figure 11.3), which is designed to insulate the SU electrically and thermally from the conductive carbon fibre face plate of the spacecraft closing panel. The face plate, first insulation layer, PCB and second insulation layer are all bonded together using PSA#10 adhesive. The unit is mounted onto the satellite by the use of four M3 stainless steel bolts, supplied by DERA.

11.3.2 Material selection

The AOE-1 sensor unit used large amounts of polymers for sensor support and thermal insulation (*Harris, 1996*). Due to the potential contamination problems that this might cause (see Sub-section 2.2.3), it was decided to find another material which could replace polymer for the face plate, which is the component that will experience most AO exposure. The face plate material must have the following characteristics:

1) Vacuum compatibility.
2) UV and AO stability.
3) Electrically insulating.
4) Low density.
5) Machineable.
6) Thermally insulating.

A large search of materials revealed that ceramics were probably the best choice, only the brittleness of these materials was highlighted to be a potential problem. One available ceramic

[Ψ] The PCB was designed by Mr R. Stansbridge and Mr A. Wood of the Institute of Sound and Vibration Research, University of Southampton. It is manufactured to ESA standards from FR4 board.

composite material, MACOR, which is a machineable glass ceramic, met the property requirements and had previous spaceflight heritage on the Space Shuttle. So, the design of the SU was completed with this material in mind.

As discussed in the previous section, the layers providing electrical and thermal insulation have been fabricated from PTFE. It was felt safe to use this material for these components because they will experience little or no AO or UV exposure - they are shielded by the face plate. Hence, AO induced contamination is not a concern. The PCB material was fixed by the ESA specifications, but similar to the PTFE components, it should experience little AO bombardment and UV irradiation.

11.4 THE ELECTRONICS UNIT

11.4.1 Electronics unit design and functionality

Due to the mass and power limits placed on the AOE-2, it was necessary to design a very simple electronics unit (EU). In fact, the restrictions of mass, power and financial budgets prevented the inclusion of a central processing unit (CPU) to control experiment operations, such as data acquisition. Similar factors also prohibited the inclusion of an analogue-to-digital converter. Consequently, the satellite OBC is used to control the operation of AOE-2, and all data from the experiment is passed to the OBDHS via analogue DAU lines for digitization and storage. In this way the power and mass requirements have been kept to a minimum, but at the expense of experiment properties such as digital resolution, which is only 8-bit in STRV-1c.

Figure 11.4 is a schematic of the sensor measurement and temperature control electronics contained within the EU. For clarity, the power conditioning, filtering and isolation components have not been shown in the schematic. Mr R Stansbridge was responsible for the detailed design of the electronics, whilst the interface and functionality was conceived and designed by the author.

The simplest way of capturing the data from AOE-2 would be to connect each thin film to its own resistance measuring circuit, and to output its value - as a voltage - on a separate and individual analogue DAU line. Indeed, this was the design of the AOE-2 before the author joined the project. Unfortunately, the number of analogue DAU lines on STRV-1c is limited, thereby preventing the application of this method, which would require - at the very minimum - 12 of the 24 available lines, an unreasonable demand. Instead, a single DAU line has been used and all the resistance measurement data are sent to the OBDHS on this one line. The OBC instructs AOE-2 to select a single thin film through the use of four digital CDU lines. This is accomplished by

connecting the twelve - 8 off ZnO and 4 off Ag - thin films to a sixteen-way multiplexer. As shown in Figure 11.4, the four CDU lines (marked A, B, C & D) are used to address the inputs to the multiplexer.

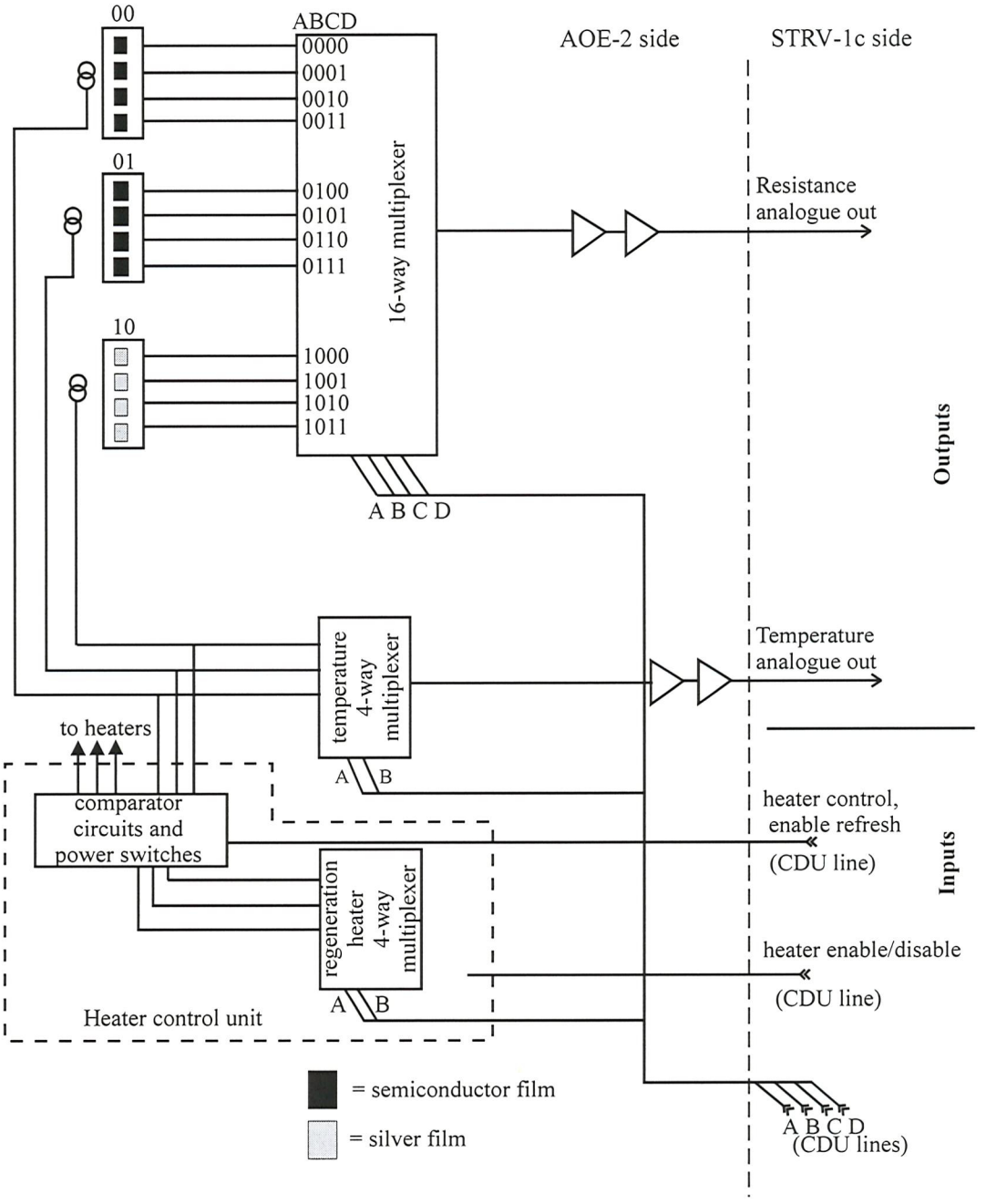

Figure 11.4 - Schematic of the AOE-2 electronics

To access the films, the 4 CDU lines are controlled in an address-system mode by experiment specific software resident in the OBC. The address of each film comprises of four bits and, so, can be represented as a 4-bit word, ABCD, for example 0010. The two most significant bits of the word (A & B) address a particular substrate: 00 is the first ZnO sensor substrate, 01 the second and 10 the silver-film substrate group. Each film on the selected substrate is then

addressed by the two least significant bits of the word (C & D): 00 is the first, 01 the second and so on. Using the four CDU lines in this manner provides a method for the OBC to index through all of the sensor films. If space and mass allowed, four additional sensor films could have been incorporated in AOE-2 due to the spare capacity of the multiplexer.

Once the OBC has selected a particular address on the CDU lines, the multiplexer connects the film in question to the resistance measurement circuitry. Resistances of all films (ZnO and Ag) are measured in the same manner, using a two-point technique. Mass considerations precluded the application of the preferable four-point technique. A constant current is passed through the selected film and, as shown by Ohm's law, a voltage drop - the magnitude of which is proportional to the resistance - is developed across the film. Thus, the resistance of the selected film may be inferred from the voltage measurement, if the voltage-resistance calibration is established.

Before being sent to the OBDHS, the small voltage (mV) is increased in magnitude by two amplifiers in series, so that it is in the 0 - 5 V range required by the ADC in the OBDHS. The amplifiers are also used as a buffer to prevent the input impedance of the DAU/OBDHS distorting the measured voltage. The pre-set gains of the two amplifiers, and the voltage range of the ADC, require that the conductances of the sensors remain in a fixed band. The size of the bands, and the resulting conductance resolution for each of the flight sensors, are presented in a later section.

Whilst this interface might seem unnecessarily complicated at first sight, it is hoped that - in addition to the reduction of DAU line usage - it will overcome the difficulties experienced by AOE-1[¶]. The first atomic oxygen experiment consisted of a number of actinometers that required resistance measurement. A clock and a simple input pulse from the OBC of STRV-1a were used to index a multiplexer through the silver films. The main problem experienced with this technique was that it was never certain which film was being measured, even though some 'marker' signals had been incorporated into the outputs. The address system used in AOE-2 should eliminate the problem, because the OBDHS records the OBC-commanded CDU line address. Therefore, it should always be possible to determine to which particular sensor the recorded output signal corresponds.

Since the semiconductor films are very sensitive to temperature, it is beneficial to record the temperature of the substrates simultaneously to the resistance measurements. For this reason, a

[¶] DERA had initially requested that the AOE-2 interface be a direct copy of that of AOE-1.

separate analogue DAU line is used to send the temperatures of the substrates to the OBDHS for digitization and storage. All temperature measurements are performed using more accurate versions of the AD590 devices - AD590MF - than used in the laboratory experiments (see Chapter 8). These devices supply a constant current, the magnitude of which is temperature dependent. Thus, if the current is passed through a resistance of known value, the voltage drop across the resistor is proportional to the temperature of the device. The voltage is amplified and buffered in the same fashion as the voltage signal from the resistance measurement circuit, before being sent to the OBDHS.

Each of the three sensor substrates has a dedicated AD590MF. Thus, similar to the resistance measurements, it is necessary to multiplex the outputs so that they can be sent along a single DAU line. To achieve this, a single 4-way multiplexer is used. The pins of this multiplexer that are used to select the desired input, are connected to the two CDU lines that constitute the two most significant bits (A and B) of the four-bit sensor address. Therefore, the same bits that are used to address the substrate are also used to access the temperature sensor associated with that substrate. For example, when the OBC commands address 0001, the resistance of the second film (01) on the first substrate (00) will be sent to the resistance output line by the 16-way multiplexer. Concurrently, the 4-way multiplexer will have connected the temperature sensor attached to the same substrate (00) to the temperature measurement circuitry, and its value will have appeared on the temperature DAU line. In this manner, the resistances of the films and their temperatures may be recorded simultaneously.

The temperatures of the sensor substrates are controlled autonomously by a heater controller, which is an integral device within the EU of AOE-2. The controller uses comparator circuits to compare the outputs from the three temperature sensors to pre-set values. If any of the temperatures are found to be below this set point, the heaters of the relevant substrate are supplied with current until the temperature reaches the required value.

Only the first mode of AOE-2 operation has a set-point temperature, which is fixed by placing certain resistance values in the comparator circuit during assembly. The resistors were chosen such that the set points for all three substrates are 298 K. However, as described previously, the temperature of the semiconductor sensors in the second mode of operation must be increased so that regeneration may be achieved. To realize this requirement, a fifth CDU line is used to switch all of the available power across the ZnO heaters in turn. This line is labelled 'heater control, enable refresh' in the previous figure. Another multiplexer is used to choose which semiconductor substrate is to be regenerated. Again, the OBC uses the two most significant bits of the four-bit address to select the desired substrate.

There is one last CDU line shown in Figure 11.4 - it is marked 'heater enable/disable'. The inclusion of this line allows the temperature control circuitry to be made inactive, while the rest of the EU may be left operational. This line can be tele-commanded low from the ground, to disable all of the heaters. Whilst this action would prevent operation of the semiconductor sensors (the primary goal of the mission), the silver actinometers would probably still function normally, achieving the secondary goal of the mission. Since the heaters drain the largest amount of current (see next section), the power consumption of AOE-2 with the heaters disabled is much reduced. This might enable operation of the experiment in the eventuality of a power supply problem, like that which occurred during STRV-1a operations (*Harris, 1996*).

11.4.2 Electronics power consumption and heater resistances

The power budget for AOE-2 was set at 3.0 W for both operational modes. Unfortunately, the efficiency of the DC-DC converter (Interpoint) is such that ~ 50 % of the allocated power is lost as heat in the EU. Thus, the maximum power that is available to drive the electronics and heaters is ~ 1.5 W. The heater power consumption dominates the drain of the electronics by several orders of magnitude, so that the power dissipated in the electronics may be neglected in any simple analysis.

The DC-DC converter supplies ±12 V and 0 V to three separate output 'rails'. The key operational feature of the semiconductor sensors is regeneration, which requires elevated substrate temperatures. Therefore, it was decided to select ZnO sensor heater resistances that would allow full dissipation of the available 1.5 W. During this mode of operation only one semiconductor heater is active at a time. It is easiest to power the heaters in the regeneration mode across the -12 V and +12 V rails, generating a maximum voltage drop of 24 V. A calculation using Ohm's law shows that the necessary heater resistance is 384 Ω. So, during heater manufacture (see Chapter 6), the resistances of the cermet heaters were deposited and trimmed to this value.

Mode 1 temperature control is accomplished using the +12 V rail. If both semiconductor heaters are active at the same time, an operational possibility, at 12 V the total power dissipation is 0.75 W. Hence, the actinometer heater may consume a maximum of 0.75 W, because it too may be operational concurrently with either one or both of the semiconductor heaters. At 12 V, the necessary resistance may be calculated to be 192 Ω. The nearest stock thermofoil heater manufactured by Minco has a resistance of 157 Ω, which means that the heater will actually draw 0.92 W. The ramifications of this increase are that the power drain of AOE-2 is actually slightly higher (~ 3.3 W) than the budget allocated by DERA, but this increase has been wavered and the necessary adjustments to the PCDU made.

11.4.3 Electronics unit box

The electronics unit resides internally in the STRV-1c vehicle. A box has been designed to prevent damage of the electronics, to protect them from EMI and, to a certain extent, shield them from radiation. A schematic of the assembled box can be found in Figure 11.5, below.

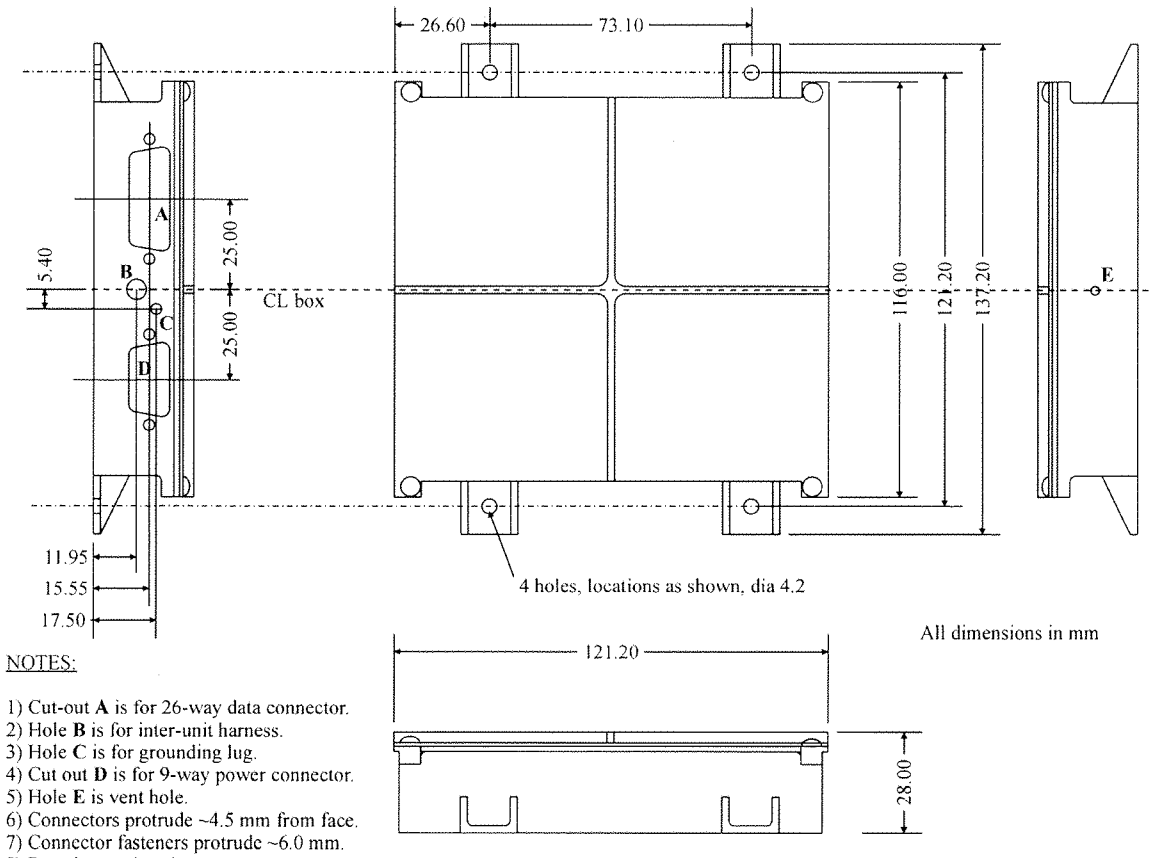

Figure 11.5 - Electronics unit box

The box and lid were designed so that they could be machined from solid aluminium ingots. The wall and base thicknesses are 1.6 mm, whilst the lid is 1.0 mm thick. The key design driver of the box was the strict mass budget.

It can be seen from the figure that one face of the box contains several apertures. The two large trapezoidal holes are machined so that the power and data connectors can protrude through the wall. The large central circular hole is for the inter-unit harness. The last hole on the front face is for a grounding-lug, one of the STRV-1c requirements. Venting of the box during launch is ensured by the presence of a hole on the rear side of the box. The box has been black anodized to improve its thermal radiative properties - this was a requirement specified by the STRV-1c design team.

11.5 MANUFACTURE AND TESTING OF UNITS

11.5.1 Engineering models

Engineering models (EMs) of both the SU and EU were built before the flight units to provide a test-bed enabling component fit-checks, electronic functionality checks and qualification testing. These units were built using components and materials representative of those that were subsequently used on the spaceflight equipment. The EMs were fully functional, apart from the lack of ZnO and silver thin films on the SU EM. Figure 11.6.a to d shows pictures of the two units.

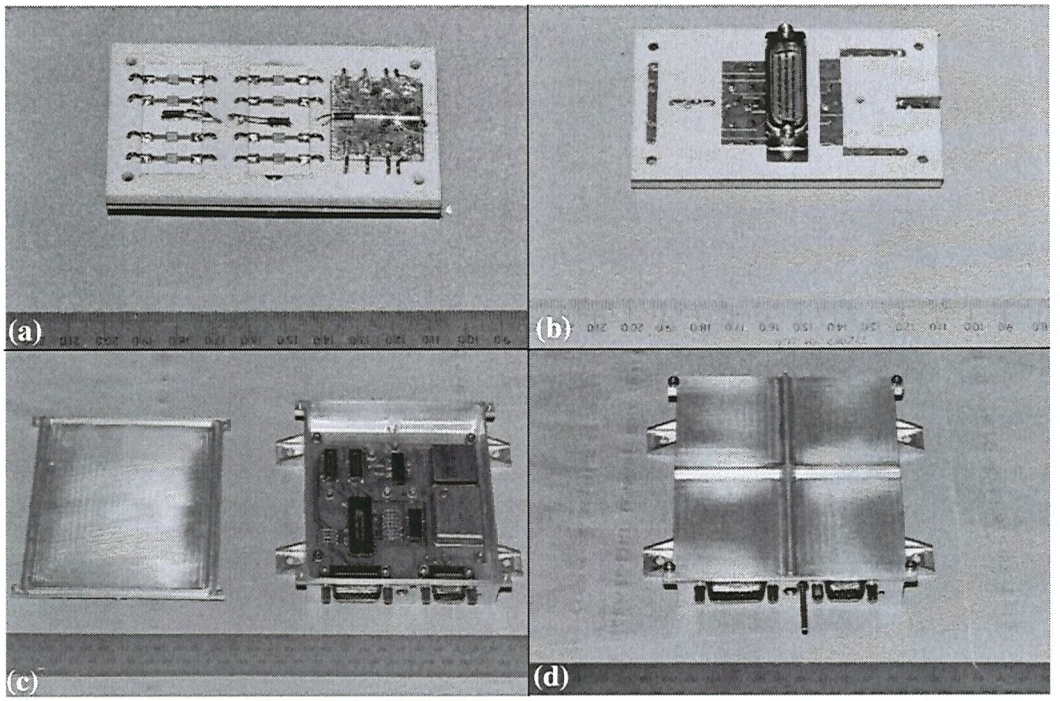

Figure 11.6 - The AOE-2 engineering models: (a) & (b) SU EM; (c) & (d) EU EM

Part (a) of Figure 11.6 shows the front (-Y) face of the AOE-2 sensor unit - it is this face of the spaceflight hardware that is exposed to AO. The sensor substrates and temperature sensors are clearly distinguishable in the figure. The D-type connector used to make electrical contact to the SU is visible in Figure 11.6.b. The remaining photographs show the EU, the first with the box lid off so that the +Z side of the electronics board is visible, part (c), and the second with the lid fastened down as if for flight, part (d). Note that the box had not been black anodized at the time of the qualification tests. During the qualification testing, the inter-unit harness was not attached to the EU EM. However, the power and data connectors are in place, to the right and left of the grounding lug respectively.

Table 11.3 shows the actual mass and size budgets achieved. The size of both units are within the DERA allocations, in fact the electronics unit box occupies a volume 47 % smaller than the

allotment. Even so, the total mass of the AOE-2 can be seen to be 0.374 kg, 0.024 kg over budget.

Component	Mass (kg)	Size (mm) (X, Y, Z)
Sensor	0.086	50 x 24 x 93
Electronics	0.264 (PCB 0.124, box 0.140)	137 x 121 x 28
Harness	0.024	~ 150 mm length

Table 11.3 - The achieved AOE-2 budgets

11.5.2 Qualification testing of engineering models

The launch environment that STRV-1c and AOE-2 will encounter is severe enough to warrant qualification testing of all experiment and platform subsystem engineering models. Such tests are accomplished by vibrating the EMs to levels more severe than will be experienced during launch, taking into account the likely transfer function of the satellite structure. DERA and Arianespace, the launch provider, have agreed a random vibration test specification that is designed to simulate the actual frequencies encountered by equipment during launch. Table 11.4 records the parameters of the random vibration test specification, whilst a plot of the power spectral density achieved in one of the AOE-2 EM tests is presented in Figure 11.7.

Frequency range (Hz)	Power spectral density ($g^2.Hz^{-1}$)	RMS value (g)
20-50	+6 dB.Oct^{-1}, 0.18 $g^2.Hz^{-1}$ at 50 Hz	16.4
50-500	0.18 $g^2.Hz^{-1}$	16.4
500-700	-3 dB.Oct^{-1}	16.4
700-2000	0.12 $g^2.Hz^{-1}$	16.4

Table 11.4 - Random vibration test specification

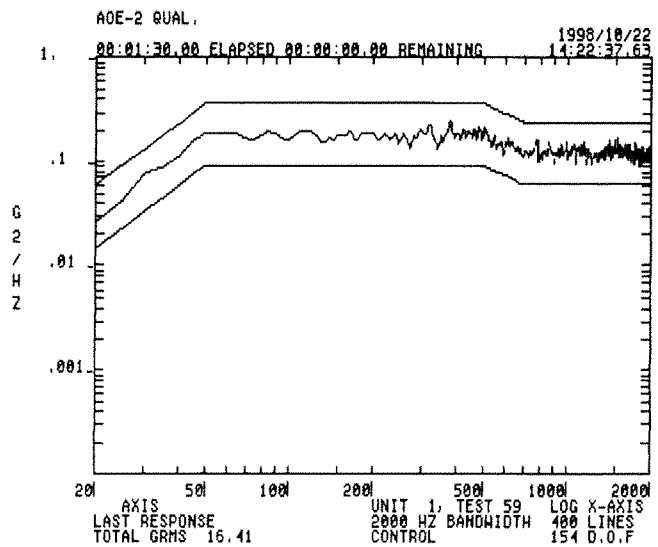

Figure 11.7 - Power spectral density plot from AOE-2 qualification test

The vibration test is performed separately in all three axes (x, y, z) to the levels detailed in Table 11.4. Immediately before and after every random vibration test, the units are subjected to a low-level sinusoidal sweep, at 0.75 g ± 3 dB over the frequency range 5 - 2000 Hz. The response of the EMs during these sweeps are measured by accelerometers, which detects characteristic unit resonances. Any structural damage that occurred as a result of the 16.4 g (RMS) qualification test is observed as a shift in the frequency of the unit resonant peaks. Also, it must be proved that the units remain functional after the random vibration test.

Both of the AOE-2 EMs were tested in this manner. Unfortunately, the first random vibration test performed resulted in significant damage to the MACOR face plate of the SU and also dislodged a component in the EU. It had been suspected that the MACOR component might cause problems (see Section 11.3.2). However, the electronics of the EU and all electrical connections within the SU remained in perfect working order.

The damage to the SU was manifested as through-thickness cracks in the brittle ceramic material, all emanating from stress raisers such as holes and section changes. Peculiarly, no shift in the unit resonances was observed as a result of these fractures. However, DERA ruled that such failures were not acceptable (because they increased the risk of unit fragmentation during launch) and so the sensor unit had to be redesigned. In fact, the only change made to the next EM of the SU was to abandon the use of the brittle MACOR ceramic, in favour of tougher PTFE. Whilst this material is likely to be more contaminating than the ceramic - although less so than many other polymers - it is also less susceptible to cracking.

The component that broke free in the electronics unit was found to be a surface-mount capacitor, the purpose of which was to smooth the voltage output from the DC-DC converter. It is believed that the solder connections of the component were substandard, and had failed through fatigue. Post failure analysis demonstrated that this component was not necessary for the successful operation of the unit, and so they were omitted from the next EM EU. Secondly, the new engineering model of the EU was coated with a conformal compound (Nu-Sil CV-1152 supplied by Polymer Systems Technology Ltd.) to prevent movement of the components.

The vibration qualification test of these two new EMs was performed to the same levels as the first. Both units passed, without any failures or problems and, so, these design alterations were adopted in the flight models.

11.5.3 Manufacture of flight models

After the successful completion of the second EM qualification test, the flight units were built to the same design specification. Two complete AOE-2 experiments have been made; one is called the flight model (FM) and the other, the flight spare (FS). The flight spare is just that - a spare - and will only be used if some fault is found, or damage inflicted upon the flight model during acceptance testing and integration to the satellite. The budgets for the flight model are detailed in Table 11.5.

It is evident that the mass budget allocated by DERA has been exceeded by 0.033 kg. DERA have agreed a waiver to allow this increase of mass. The small increase of excess mass between the first EM (Table 11.3) and the FM is due to the conformal coating applied to the FM EU PCB. It is worth noting that the power consumption of the FM is the same as the EM, at 3.3 W.

Unit	Mass (kg)	Size (mm) (X,Y,Z)
Sensor	0.086	50 x 24 x 93
Electronics	0.268 (PCB 0.126, box 0.142)	137 x 121 x 28
Harness	0.028	~ 150 mm length
TOTAL	0.383	not applicable

Table 11.5 - Budgets of the FM

There are three additional differences between the flight units and EM. Firstly, working AO sensors have been installed on the SU, instead of blank substrates. As mentioned previously, the ZnO-based AO sensors adopted for the flight equipment are those using thick film gold interdigitated arrays, because of the extra robustness that they offer. Indeed, no problems developed with the contacts or heaters during the EM qualification vibration test. Secondly, the inter-unit harness has been hard-wired to the EU PCB. The cables in this part of the EU are of a dual-wall construction, using cross-linked, vacuum-rated plastics (polyalkene and polyvinylidene fluoride). Cables of this form were DERA standard, and were supplied by Cabletec Ltd. Thirdly, the EU box was black anodised for thermal control reasons.

The actinometer sensors selected for use on the flight models consisted of thin silver films, deposited to a thickness of 1000 Å upon glass substrates. This thickness was chosen because it was thought to offer the best compromise between sensitivity, resistance and film structural stability during oxidation (*Harris, 1996; Harris, 1997c*). The same silver-loaded epoxy as used in the EM was employed to make electrical contact to the silver films, whilst the AD590MF temperature sensor was stuck to the substrate with PSA#10. The glass substrates of the silver

films were trimmed so that two silver sensors resided on a single piece of glass of dimension 12.5 mm x 27.0 mm. Two of these small substrates were mounted on top of the thermofoil heater.

Selection of the ZnO AO sensors was based upon several factors. It was decided to test sensors with both resinate (RT) and cermet (CT) contacts. Thus each SU built (FM and FS) comprised one resinate sensor substrate - two sensors - and one cermet substrate, again with two sensors. Choice of the actual substrates was influenced by the results from the laboratory research.

Experiment showed that the thinner the semiconductor film, the smaller the fluence needed to condition the sensor response. Also, thinner ZnO films were found to respond less to UV illumination than thicker films. Moreover, it is commonly accepted that the thinner a semiconductor film, the more sensitive it becomes to gas adsorption on its surfaces. However, inconclusive findings in Chapter 9 (Section 9.4.3) engender some doubt about the validity of this generalization in the case in hand. So, all of these considerations led to the conclusion that the most appropriate choice of sensors were those with the thinnest possible zinc oxide films.

Semiconductor sensor regeneration hysterisis has been attributed to the permanent oxidation of free zinc in the ZnO matrix. As previously discussed, this zinc acts as the electron donor in ZnO, and so material with reduced zinc concentration will be low conductivity. It was suggested in Chapter 9 that the amount of hysterisis displayed by a given sensor might be dependent upon the concentration of free zinc in the ZnO. Therefore, the conclusion is that sensors of low conductivity (low donor density) should be chosen to reduce hysterisis. However, anticipated difficulties such as the presence of noise on very low conductivity sensor measurements restricted the choice of sensors to those of 'reasonable' conductivity.

Hence, the above considerations led to the choice of sensors from depositions RT21 and CT20, see Tables 7.1 and 7.4. The semiconductor in deposition RT21 has thickness 0.28 μm, whilst that in CT20 has thickness 0.4 μm. Average sensor conductivity is low, at 2.585×10^{-3} $(\Omega.cm)^{-1}$ for RT21, and 3.114×10^{-4} $(\Omega.cm)^{-1}$ for CT20. The table below shows which substrates were used for the flight units.

Unit	Cermet	Resinate
FM	CT20A	RT21A
FS	CT20C	RT21B

Table 11.6 - Sensors used in the two AOE-2 flight units

These substrates were arranged in the same fashions on both the FM and FS. The CT sensors were mounted in the left-hand position on the SU, that is the substrate location furthest from the

silver actinometers. The RT sensors were mounted in the near centre-line position. The substrates were placed on the units so that the sensors have the following addresses, see Figure 11.8 and Table 11.7. *NB* Address 00 is that of the left-hand ZnO sensor substrate, whilst address 01 is that of the right-hand ZnO sensor substrate.

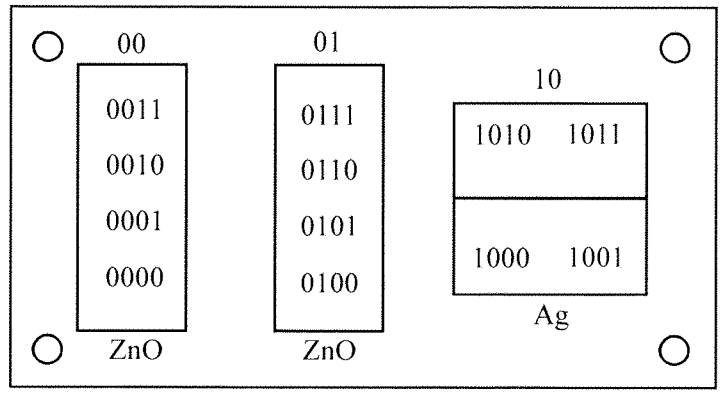

Figure 11.8 - Address locations of sensors

Address	FM	FS
0000	CT20A1b	CT20C1b
0001	CT20A1c	CT20C1c
0010	CT20A2b	CT20C2b
0011	CT20A2c	CT20C2c
0100	RT21A1b	RT21B1b
0101	RT21A1c	RT21B1c
0110	RT21A2b	RT21B2b
0111	RT21A2c	RT21B2c

Table 11.7 - The locations of the individual sensors on the FM and FS

As discussed previously, the resistance measurement circuitry requires that the sensor conductances remain in a pre-set band. Table 11.8 below contains the conductance ranges calculated from linear approximations for all sensors - ZnO and Ag - in the flight model. Table 11.9 presents the same information for the flight spare unit. Also included in the two tables are the resulting conductance calibration equations. These equations are given in terms of mho/V but, by virtue of the 8 bit ADC, they can be converted for use with digital bits by multiplying the 'gradients' 5/256.

Sensor	g_{min} (mho)	g_{max} (mho)	Calibration equation, V to g (mho)
CT20A1b	2.0391×10^{-7}	4.2650×10^{-7}	$g = -4.4968 \times 10^{-8} * V + 4.2875 \times 10^{-7}$
CT20A1c	3.8665×10^{-7}	6.0982×10^{-6}	$g = -1.3917 \times 10^{-7} * V + 1.0825 \times 10^{-6}$
CT20A2b	1.6280×10^{-7}	6.0982×10^{-7}	$g = -9.0309 \times 10^{-8} * V + 6.1434 \times 10^{-7}$
CT20A2c	1.0245×10^{-7}	1.3802×10^{-6}	$g = -2.5303 \times 10^{-7} * V + 1.3676 \times 10^{-6}$
RT21A1b	3.7650×10^{-7}	1.0975×10^{-6}	$g = -1.4566 \times 10^{-7} * V + 1.1048 \times 10^{-6}$
RT21A1c	2.5230×10^{-8}	7.1398×10^{-7}	$g = -1.3906 \times 10^{-7} * V + 7.2053 \times 10^{-7}$
RT21A2b	1.6468×10^{-7}	6.1062×10^{-7}	$g = -9.0088 \times 10^{-8} * V + 6.1512 \times 10^{-7}$
RT21A2c	1.5850×10^{-8}	1.4136×10^{-6}	$g = -2.8239 \times 10^{-7} * V + 1.4278 \times 10^{-6}$
Ag1	0.0158	0.0440	$g = -5.7019 \times 10^{-3} * V + 4.4295 \times 10^{-2}$
Ag2	0.0158	0.0440	$g = -5.6988 \times 10^{-3} * V + 4.4294 \times 10^{-2}$
Ag3	0.0158	0.0439	$g = -5.6931 \times 10^{-3} * V + 4.4228 \times 10^{-2}$
Ag4	0.0158	0.0439	$g = -5.6928 \times 10^{-3} * V + 4.4224 \times 10^{-2}$

Table 11.8 - Measurable conductance ranges and resolution of FM sensors

Sensor	g_{min} (mho)	g_{max} (mho)	Calibration equation, V to g (mho)
CT20C1b	2.0569×10^{-7}	5.2822×10^{-7}	$g = -6.5159 \times 10^{-8} * V + 5.3148 \times 10^{-7}$
CT20C1c	1.7150×10^{-8}	1.4144×10^{-6}	$g = -2.8227 \times 10^{-7} * V + 1.4285 \times 10^{-6}$
CT20C2b	2.0804×10^{-7}	5.2954×10^{-7}	$g = -6.4952 \times 10^{-8} * V + 5.3279 \times 10^{-7}$
CT20C2c	8.9800×10^{-8}	1.3866×10^{-6}	$g = -2.6198 \times 10^{-7} * V + 1.3997 \times 10^{-6}$
RT21B1b	9.1450×10^{-8}	1.3863×10^{-6}	$g = -2.6159 \times 10^{-7} * V + 1.3994 \times 10^{-6}$
RT21B1c	1.0510×10^{-7}	1.3906×10^{-6}	$g = -2.5970 \times 10^{-7} * V + 1.4036 \times 10^{-6}$
RT21B2b	9.9800×10^{-8}	1.4024×10^{-6}	$g = -2.6316 \times 10^{-7} * V + 1.4156 \times 10^{-6}$
RT21B2c	7.1830×10^{-7}	6.3133×10^{-6}	$g = -1.1303 \times 10^{-6} * V + 6.3698 \times 10^{-6}$
Ag1	1.60×10^{-2}	4.56×10^{-2}	$g = -5.9712 \times 10^{-3} * V + 4.5865 \times 10^{-2}$
Ag2	1.61×10^{-2}	4.56×10^{-2}	$g = -5.9570 \times 10^{-3} * V + 4.5860 \times 10^{-2}$
Ag3	1.61×10^{-2}	4.56×10^{-2}	$g = -5.9645 \times 10^{-3} * V + 4.5896 \times 10^{-2}$
Ag4	1.61×10^{-2}	4.56×10^{-2}	$g = -5.9521 \times 10^{-3} * V + 4.5878 \times 10^{-2}$

Table 11.9 - Measurable conductance ranges and resolution of FS sensors

11.5.4 Flight model acceptance tests

DERA demand that the flight units of all STRV-1c equipment undergo pre-delivery acceptance testing. These tests include: a lower level (than qualification) random vibration test in all three axes; dimension, mounting fit and mass check; power compatibility test; electrical interface functionality test; thermal vacuum test and test of the experiment specific software. The AOE-2 FM has passed all of these tests and, therefore, has been accepted for flight on STRV-1c.

Subsequently, the FM units have been delivered to DERA and integrated to the satellite. Figure 11.9, overleaf, shows the units mounted on the vehicle. Part (a) of the figure shows the AOE-2 EU mounted upon the shelf - centre unit of three - before integration into the satellite, the two units either side are the transmitters used in the RFCS. The second part of the figure shows the SU mounted on the -Y closing panel.

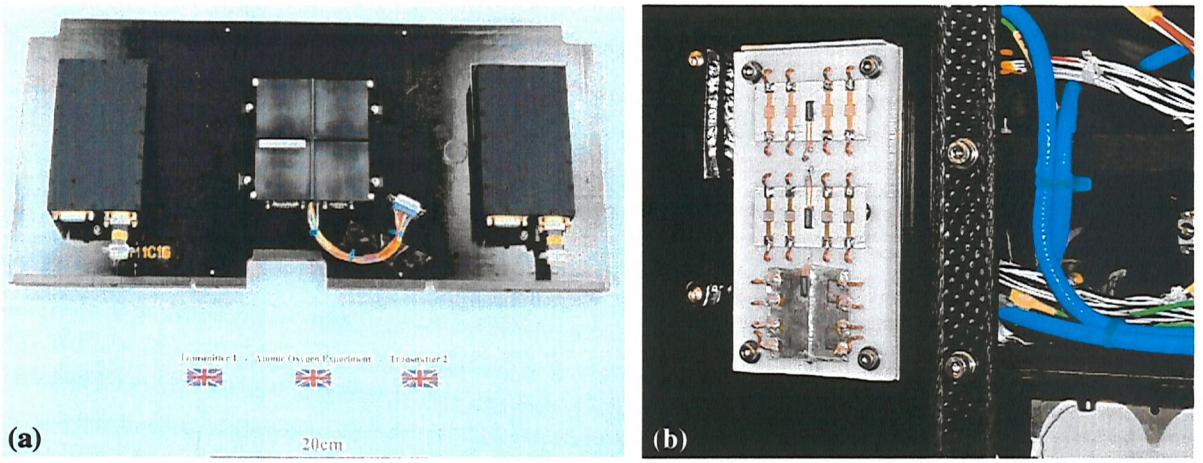

Figure 11.9 - AOE-2 and the satellite: (a) EU on shelf; (b) SU on closing panel[¤]

11.6 EXPERIMENT OPERATION

11.6.1 Mode 1 operation - AO measurement mode

Mode 1 is the AO measurement function of AOE-2. Thus, it is activated only when the sensor unit experiences AO exposure. For STRV-1c this occurs near perigee - the closest approach to the surface of the Earth - when the vehicle passes through the upper thermosphere. Section 11.7.2 describes the AO exposures that may be experienced and attempts to predict the responses of the sensors during a perigee pass.

Time-tagged OBC commands are used to ensure that mode 1 operation coincides with the perigee pass. Upon activation of mode 1, the OBC commands the 'heater enable' CDU line high, so that temperature control of the sensors is initiated. At the same time, the heater enable refresh line is held low so that regeneration heating may not occur. Then, the software running on the OBC commands a sweep of the thin films and temperature sensors so that their resistances and values can be recorded by the OBDHS. To accomplish this the OBC commands the CDU address lines in the sequence 0000, 0001, 0010 and then every address until 1011. At each address, the voltage value relating to the resistance of the selected element, and the temperature of the selected sensor, is sent to the OBDHS. Data is recorded by the OBDHS in the format shown in Table 11.10.

Extra information is inserted by software running on the OBC. The experiment start time is added to the first data set, whilst the start and end time of each sweep through the sensors is added to every data set. The CDU line status is also recorded so that the readings taken by the OBDHS can be associated to a particular sensor element or temperature sensor.

[¤] Photographs courtesy and copyright of DERA.

The CDU line address sequence (0000, 0001, ..., 0100, 0101, ..., 1011) is then repeated again one spin time later; the timing is triggered by the Earth sensor. It continues in this fashion every satellite spin until the time allocated for mode 1 operation has elapsed. Consequently, at down-link of the data, a large array made up of many sections like that in Table 11.10 will be returned to the ground segment and then disseminated to the University of Southampton.

Quantity	Memory (bytes)
Experiment start time	4
Number of samples	1
Reading start time	4
Sample 1 data : CDU line status	1
Sample 2 data : Temperature 1	1
Sample 3 data: CDU line status	1
Sample 4 data: Film 1 resistance	1
Sample 5 data: CDU line status	1
Sample 6 data: Film 2 resistance	1
Sample 7 data: CDU line status	1
Sample 8 data: Film 3 resistance	1
Sample 9 data: CDU line status	1
Sample 10 data: Film 4 resistance	1
Sample 11 data: CDU line status	1
Sample 12 data: Temperature 2	1
Sample 13 data: CDU line status	1
Sample 14 data: Film 5 resistance	1
Sample 15 data: CDU line status	1
Sample 16 data: Film 6 resistance	1
Sample 17 data: CDU line status	1
Sample 18 data: Film 7 resistance	1
Sample 19 data: CDU line status	1
Sample 20 data: Film 8 resistance	1
Sample 21 data: CDU line status	1
Sample 22 data: Temperature 3	1
Sample 23 data CDU line status	1
Sample 24 data : Film 9 resistance	1
Sample 25 data: CDU line status	1
Sample 26 data: Film 10 resistance	1
Sample 27 data: CDU line status	1
Sample 28 data: Film 11 resistance	1
Sample 29 data : CDU line status	1
Sample 30 data: Film 12 resistance	1
Reading end time	4

Table 11.10 - Mode 1 data format

The total duration of mode 1 operation is commandable from the ground. This facility was incorporated so that the AOE-2 could be operated in a flexible manner. The duration is determined by up-linking the start-time of Mode 1 and the total duration that the experiment is to be operational in this mode. Default values are loaded into the OBC before launch. These have

been chosen to be a total operating time of 30 minutes, split so that the unit is activated 20 minutes before perigee and deactivated 10 minutes post-perigee. The disparity between the times before and after perigee is to ensure that the sensors have warmed to a stable temperature before AO flux reaches its maximum intensity.

At the end of mode 1 operation, the OBC ceases to access the CDU address lines and also sets the heater enable line to low. The AOE-2 is then in its third 'operational' mode - the standby mode - so that it consumes no power until either the next mode 1 operation or until mode 2 is commanded by the OBC.

11.6.2 Mode 2 operation - sensor regeneration mode

Mode 2 is the semiconductor sensor regeneration phase of AOE-2 operation. It is activated only when the vehicle is well outside the thermosphere, so that no AO is incident on the sensors. A convenient (and well-determined) time to perform this activity is around the apogee of the orbit. Geostationary transfer orbit apogees are usually placed about 36,000 km above the surface of the Earth - far beyond the influence of the residual atmosphere.

In this mode, it is necessary to heat the semiconducting sensor substrates to a much higher temperature than in mode 1. This is accomplished by the 'heater control: enable refresh' CDU line, which is set high by the OBC. At the same time, the heater enable line is commanded high. The particular heater that is active in regeneration mode is determined by the two most significant bits of the four-bit word sent by the OBC to the AOE-2. The heater is supplied with power for a certain time, the value of which is commandable, like the duration of mode 1.

Once the two heater control CDU lines are set high, the first two bits (A & B) of the sensor address are latched, whereupon the heater multiplexer activates the required heater. At the same time, the last two bits of the address are sequenced through the series 00, 01, 10, 11 to index through the films, so that their resistances can be monitored. The temperature of the substrate is also recorded in this mode, as detailed previously. This sequence is repeated every spin rotation until the commanded time has elapsed. In mode 2, the data from each measurement sweep has the format shown in Table 11.11.

In this manner, the two semiconductor sensors on the first substrate (address 00) have been regenerated. It is then necessary to regenerate the sensors on the second alumina substrate, which has substrate address 01. This is accomplished in exactly the same manner as the first semiconducting sensor, except that the OBC latches the two most significant address bits with the

configuration 01. It is worth noting that the silver films do not require regeneration. So, in mode 2, the substrate with the address 10 - e.g. 1001 - will **never** be accessed.

Quantity	Memory (bytes)
Experiment start time	4
Number of samples	1
Reading start time	4
Sample 1 data : CDU line status	1
Sample 2 data : Temperature	1
Sample 3 data: CDU line status	1
Sample 4 data: Film resistance	1
Sample 5 data: CDU line status	1
Sample 6 data: Film resistance	1
Sample 7 data: CDU line status	1
Sample 8 data: Film resistance	1
Sample 9 data: CDU line status	1
Sample 10 data: Film resistance	1
Reading end time	4

Table 11.11 - Mode 2 data format

11.7 ASSESSMENT OF EXPERIMENT RESPONSES

Many of the findings of this research, which have been presented in the preceding chapters, have ramifications for the operation of AOE-2. It is the intention of this section to examine these implications.

11.7.1 Implications of laboratory-based results

Large sensor regeneration hysterisis causes some concern for the operation of AOE-2. Whilst every attempt has been made to eliminate the occurrence of hysterisis by the selection of low conductivity sensors, it may still occur to some extent. The method employed to measure the resistances of the sensors requires that the sensor conductances stay in a pre-set band, see Sub-sections 11.4.1 and 11.5.3. To ensure adequate resolution of the sensor signal, the band must be set as small as possible. Hence, if hysterisis occurs, the conductivities of the sensors could well decrease beyond the bottom of the range. At this point, no more measurements could be made.

Understandably, there are many factors that can affect the size of the required conductance range: namely the amount of hysterisis expected at each regeneration, the required resolution and the number of regenerations performed. However, at present it is not possible to predict the amount of regeneration hysterisis that will occur. Of necessity, therefore, the measurement bandwidth for all sensors of the EU has been made large (see Section 11.5.3) and, compounded by the 8-bit resolution of the DAU, the sensor resolution is thus rather low.

During the experiments described in this thesis, the temperature of the sensors was maintained as stable as possible by a temperature controller. The thermal environment of the exposure chamber was relatively constant, so sensor temperature control was a reasonably simple task. In comparison, the STRV-1c is a spin-stabilized satellite, which means that the AOE-2 will be subjected to discontinuous solar heating due to satellite self-eclipsing. The satellite will also be subjected to various eclipse seasons, further complicating the thermal environment of the experiment.

In orbit temperature fluctuations will affect sensor signals, due to the thermal coefficient of resistance of the semiconductor and, if the thermal deviations are large, the AO-related conductance response may even be masked by these changes. Unfortunately, thermal modelling of the experiment conducted to date has not resulted in any meaningful predictions of the temperature excursions that can be expected, mainly due to the lack of available data describing the behaviour of the host vehicle.

Atomic oxygen experiment - 2 will be subjected to other forms of radiation as well as the solar VUV, UV, visible and IR. The GTO path of STRV-1c takes the vehicle through the van Allen belts (high-energy protons and electrons) and it will also receive cosmic, X- and γ-rays. The effect of this radiation environment on the MOS sensors has yet to be determined theoretically or empirically.

11.7.2 Predicted sensor response to orbital AO environment

The results from the AO exposure experiments, which were reported in Chapter 9, enable a 'first-cut' prediction of the response of the ZnO sensors to the orbital AO environment likely to be encountered after launch. At the time of writing, the anticipated orbital elements of STRV-1c and 1d are those presented in Table 11.12. However, at that time these figures were still fluid due to on going launch negotiations and when, in due course, the AOE-2 data is analyzed, more exact orbital data will be required.

Parameter	Value
Apogee altitude (km)	35,890
Perigee altitude (km)	564
Inclination (°)	7
Argument of perigee (°)	178
Longitude of ascending node (°)	-133.01
Mean anomaly (°)	5.67
True anomaly (°)	45.27

Table 11.12 - Expected orbital parameters of STRV-1c and 1d

Evidently, the elliptical orbit described by the data in Table 11.12 takes STRV-1c through the upper thermosphere as it descends from apogee towards perigee and back to higher altitudes. Two parameters, in addition to the altitude of the vehicle, change during the descent towards, and climb-out from, perigee. The first is the spacecraft velocity, which near perigee may be approximately 10 $km.s^{-1}$. Secondly, as shown in Figure 2.1, AO number density increases with decreasing height. As a result, it is predicted that the AO flux experienced by the vehicle will increase towards perigee, peak at perigee, and then decrease as the vehicle returns to higher altitudes once more. Thus the vehicle and AOE-2 will experience periodic, rather than constant, AO exposure.

The probable variation of orbital fluxes during a single STRV-1c orbit have been simulated using the SYSTEMA[§] satellite design suite. In this analysis, orbital conditions expected to be typical of those that will be experienced after an assumed launch date of 1st March 2000 have been used - specifically 1st March 1989, which was at the end of solar cycle 22. This approach was necessary because data for the forthcoming solar maximum are not yet available for SYSTEMA. The resulting flux values are plotted in Figure 11.10; the predicted peak ram flux for the orbit described in Table 11.12 is 4.41 x 10^{13} $atoms.cm^{-2}.s^{-1}$. Moreover, in one orbit, AOE-2 mounted on the spinning satellite will accumulate a fluence of approximately 4.25 x 10^{15} $atoms.cm^{-2}$.

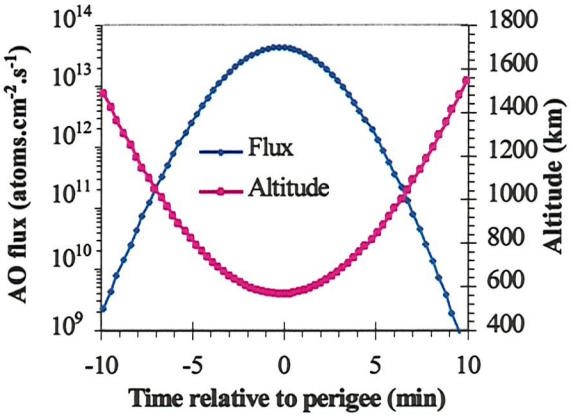

Figure 11.10 - The expected variation of AO flux and altitude for AOE-2

As described in Chapter 9, it was found in the laboratory that the conductance of ZnO sensors decrease when they are exposed to AO fluxes. Thus, it is expected that the conductance values of the sensors of AOE-2 will decrease during a perigee pass due to exposure to thermospheric oxygen atoms. During the laboratory experiments the time-averaged flux of AO was held at a constant value. However, as suspected, it can be seen from Figure 11.10 that the orbital AO flux

[§] SYSTEMA is a development of Matra Marconi Space, and was used under license to the University of Southampton.

is not constant, but increases and decreases before and after perigee by several orders of magnitude. No laboratory experiments were performed to simulate this situation, so in the following discussion it will be assumed that the shape of the orbital AO flux 'pulse' is a flat-topped square wave, the upper magnitude of which is described by the ram flux values detailed earlier. Without doubt, this model is an oversimplification of reality, but it will suffice in this basic examination of the likely experiment behaviour.

Therefore, during the pass through the thermosphere, the conductance of the sensors will decrease in a fashion very similar to that observed in the laboratory experiments. The experiment and STRV-1c OBDHS record the decrease subject to the resolution of the DAU. Figure 11.11 describes graphically how the change of conductance might look due to a single perigee pass. In drawing this figure, it has been assumed that the effective AO flux above 1,000 km is so low as to be negligible in comparison to the peak at perigee, and a smoothed curve has been plotted through the digitally resolved conductance data.

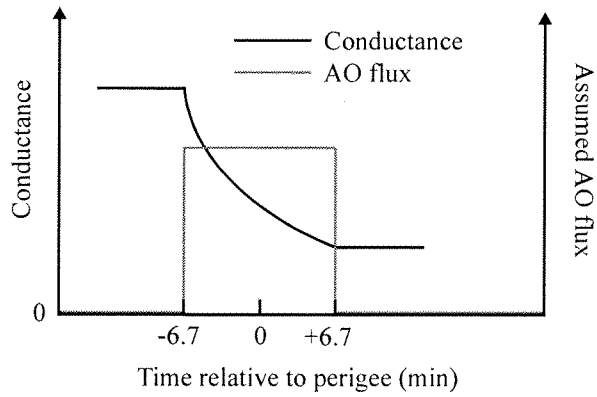

Figure 11.11 - A representation of a signal from AOE-2

Several features in this figure are noteworthy. Firstly, an altitude of 1,000 km correlates with approximately 6.7 minutes before and after perigee. Secondly, as soon as the AO flux 'begins' - taken to be when the spacecraft reaches altitudes lower than 1,000 km - the conductance of the sensor starts to decrease, and continues to do so monotonically throughout the perigee pass. Lastly, it is shown in the schematic that the conductance abruptly ceases to decrease at + 6.7 minutes after perigee. Such a cessation of conductance decrease may occur either because the vehicle has exited the AO containing region (example indicated in figure), or because the conductance change has exceeded the full 256 bits of the DAU. Sensor saturation may or may not occur before one of these eventualities.

Just as for the data recorded in the laboratory, differentiating the conductance curve with respect to time - at the start of exposure - leads to a rate of change of conductance value $\left(\frac{dg}{dt}\right)$ that is characteristic of the flux engendering the decrease. One of the advantages of operating the sensor in the ballistic fashion is thus understandable, because in this mode it does not matter whether or not the sensor has saturated. In either case, it is still possible to calculate a parameter that can be related to the flux experienced. Hence, saturation is not a necessary requirement for correct sensor function, which allows experiment operation over shorter duration than that necessary for saturation to occur.

Data presented in Table 11.8, which concerns the FM EU conductance conversion factors, can be used to estimate the maximum rate of conductance change that may be detected by AOE-2. The average conductance bandwidth of the FM is $\Delta g_{ave,max} = 7.3627 \times 10^{-7}$ mhos, and this value represents the **maximum** change of conductance of a sensor that may be recorded, i.e. the total 0 - 5 V DAU range. However, to continue this analysis it is necessary to define a time over which the conductance of a sensor may alter by this amount.

It was described in Sub-section 11.6.1 that the OBDHS acquires data from AOE-2 once per rotation of the satellite, a time determined by Earth sensor pulses. Thus, it would seem that the shortest resolvable time over which a given sensor may change throughout its complete conductance bandwidth is one spin time. The default spin stabilization of STRV-1c requires that it rotate at 5 rpm, hence, the maximum rate of conductance decrease that may be measured by AOE-2 is $5.\Delta g_{ave,max}$. Using the average bandwidth quoted above, the maximum rate may be calculated to be $\left(\frac{dg}{dt}\right)_{ave,max} = -3.681 \times 10^{-6}$ mhos.min^{-1}, to use the unit for sensor response adopted in this work. Clearly, faster spin rates - which may be implemented by DERA - would increase this value linearly.

Using the calibration curves generated for the 0.5 μm sensors, this rate of conductance change may be converted to a maximum measurable flux value. For example, the calibration curve of TG08A1b, which can be found in Figure 9.9 part (a) is:

$$\left(\frac{dg}{dt}\right) = (-1.3171 \times 10^{-21}) * F - 3.7499 \times 10^{-7} \qquad (11.1)$$

where F represents flux in atoms.cm^{-2}.s^{-1} and the rate of conductance change is in mhos.min^{-1}.

Therefore, invoking Equation (11.1) and using the $\left(\frac{dg}{dt}\right)_{ave,max}$ value calculated before reveals that the maximum measurable flux is approximately 2.51 x 10^{15} atoms.cm^{-2}.s^{-1}. To perform this calculation requires that Equation (11.1) be linearly extrapolated to flux values higher than those used to generate the results from which it was derived. Comparing this maximum flux to the predicted ram flux calculated for the orbit of STRV-1c (4.41 x 10^{13} atoms.cm^{-2}.s^{-1}), shows that the AO fluxes likely to be experienced are comfortably below the upper limit. Indeed, this upper flux limit correlates with an approximate number density of 3 x 10^{9} cm^{-3}, which Figure 2.2 shows is reached at around 220 km, far below the perigee of the satellite.

Defining an equivalent minimum measurable rate of conductance change, hence lowest resolvable AO flux, is far harder. If a similar approach to that above is adopted, it could be assumed that the smallest conductance change is that contained in one bit of the 256-bit bandwidth. As before, it is then necessary to define a time over which this conductance change must be recorded. It is this part of the analysis that is difficult: should the time of one mode 1 operation, for one perigee pass or for one orbit be used? In fact, without knowing the stability of the instrument and without a measure of how other components of the spacecraft environment will affect the sensors, an estimate will be nothing more than pure conjecture.

However, assuming instrument stability and no sensor deterioration or other environmental influence, in principle it may be possible to detect very low fluxes. The opportunity to operate the experiment in another fashion results from the ability to telecommand the length of mode 2, or regeneration, operation. In the case above, it would be necessary to regenerate the sensor at apogee so that another measurement maybe made during the next perigee pass. This would be especially important if the sensor had saturated, or had exceeded its full bandwidth in a single pass. If the AO flux is very low, however, it may take several orbits for a conductance change even of one bit to accumulate. Clearly, if the experiment were regenerated after each sweep through the thermosphere, such an accumulation would never be registered.

So, in the case of low flux measurement, it would be necessary to command mode 2 duration to zero minutes. In this manner, the sensor response curve, like that drawn in Figure 11.11, is constructed not with the data from a single perigee pass, but from many. Only after sufficient data is gathered to assemble a curve that can be differentiated in the manner described at length throughout this thesis, should the experiment be commanded to regenerate the sensors - by re-setting the mode 2 time to a non-zero value.

Operation of the experiment in this cumulative fashion is rather similar to the exposure of sensors in ATOX. In this experimental facility, the sensors experience several pulses of oxygen atoms per data acquisition. Therefore, the response of the sensors is accumulated over several discrete AO pulses. In the same way, AOE-2 will experience pulses of AO every time it passes through the thermosphere, and so the response of the sensors may be determined over several data acquisitions. In this description, a data acquisition is defined to be each orbit, or each group of orbits, in which a one-bit change of conductance occurs. The time scales are radically different, but as long as the sensors remain stable - no coasting or self-regeneration - throughout the quiescent apogee pass, the analogy should hold. No experimental evidence of coasting has been observed in the tests conducted during this research. However, there is a report in the literature of atomic hydrogen sensors displaying such a phenomenon after cessation of hydrogen impingement (*Sukharev and Myasnikov, 1987a*). It is not obvious what will occur in the case of atomic oxygen.

There are advantages and disadvantages to operating the experiment in this fashion. The key advantage is that it extends the minimum detectable flux to far lower values than might be otherwise possible in a single-measurement-per-orbit scenario. However, this is also the source of the major disadvantage, in that accumulating the response of the sensors over many orbits will reduce the time and spatial resolution of the measurement.

During the mission lifetime of AOE-2, the perigee height of STRV-1c will experience a net increase or decrease and periodic fluctuations due to the effects of solar-lunar perturbations. Unfortunately, DERA have not yet been able to acquire sufficient information from Arianespace to determine the likely outcome for STRV-1c. Such changes have clear implications for the operation of AOE-2. An increased perigee height will reduce the AO flux and total exposure experienced per orbit, lowering the sensor response and, possibly, increasing the number of orbits to response detection. Alternatively, decreased perigee height leads to higher fluxes and fluences, increased sensor responses and reduced number of orbits to peak response. Changes of flux like these may require AOE-2 to be operated in both of the manners described previously.

The results of these calculations must be treated only as examples of the type of analysis that will have to be performed on real data from AOE-2. The FM AO sensors are thinner than those used in the laboratory to derive Equation 11.1, so the sensitivities they display will be different. The results presented in Chapter 9 also showed that the magnitude of sensor response is a function of the temperature used in the previous regeneration, thus, the level of heating used at the previous apogee must be monitored carefully. Additionally, the sensor response to flux calibration incorporates the measurement errors, specifically the offset of the C-QCM device (see Sub-

section 9.2.2). Therefore, it would be prudent to characterize the two remaining sensors deposited simultaneously with the FM/FS sets - or after FM launch the FS itself - using a different measure of AO flux, like a mass spectrometer.

11.7.3 Effect of other thermospheric species

The thermosphere does not only contain atomic oxygen, but also many other species. Molecular oxygen is an important constituent, but the results of the oxygen calibration experiment indicate that this species does not influence the ZnO sensors, even at large fluxes. Section 10.1 describes these findings. Hence, it is not believed that orbital fluxes of O_2 will adversely effect the responses of the sensors.

There are other gases in the thermosphere, such as nitrogen, argon and helium, see Figure 2.1 on page 6. These materials are inert to zinc oxide and so should not engender a sensor response (*Myasnikov, 1975*). However, there remains a component of particular concern - atomic hydrogen (AH). These atoms are known to influence zinc oxide sensors (*Pospelova and Myasnikov, 1967; Myasnikov, 1975*). Whereas AO is an electron acceptor, AH is an electron donor. Hence, it is to be expected that direct action of AH will induce conductance increases in n-type materials. So, under the influence of AH, ZnO-based sensors will demonstrate rates of conductance change opposite in sign to those generated by AO. Indeed, it is reported in the literature that equal fluxes of AO and AH engender sensor responses of the same magnitude, but of opposite sign (*Westley, 1999*). Therefore, it is prudent to examine the quantity of AH that might be encountered in orbit. Unfortunately, SYSTEMA does not calculate atomic hydrogen fluxes, so the comparison will have to be made simply from relative number densities.

Figure 11.12 shows the relative concentration of atomic hydrogen to atomic oxygen over the altitude range 100 to 1000 km. Curves for solar maximum, mean and minimum conditions have been calculated using the MSISE-90 model (*Hedin, www resources*).

The STRV-1c is due to be launched close to solar maximum, hence, this is the curve of most interest in the above figure - it is the lowest of the three lines. It is clear that, at solar maximum, the number density of AH is several orders of magnitude lower than that of AO, at all altitudes examined. In particular, at the predicted perigee height of 564 km, the ratio [AH]/[AO] can be seen to be about 2×10^{-4}. Thus, at perigee, it is expected that sensor response will be affected by approximately $+3.42 \times 10^{-12}$ mhos.min^{-1} due to AH. This effect can clearly be ignored relative to the predicted response due to AO, which is calculated to be -4.33×10^{-7} mhos.min^{-1} using the perigee flux value and Equation (11.1). At higher altitudes, for example on the way to perigee, the relative influence of AH is greater, but always less than 100 times that of AO, up to 1000 km.

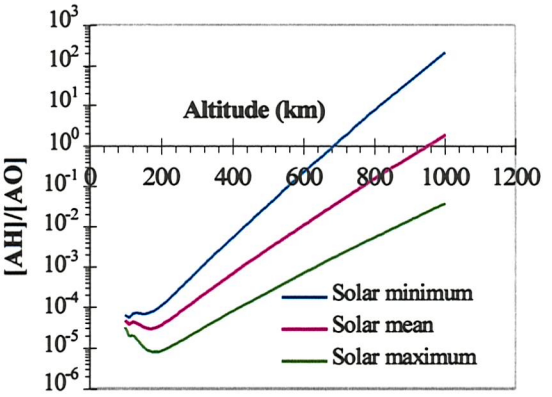

Figure 11.12 - Relative densities of atomic hydrogen and atomic oxygen

The above discussion was concerned with the relative effect of AO and AH on 'clean' ZnO surfaces. However, review of the literature shows that the effect of AH is markedly different when there is material pre-adsorbed onto the semiconductor surface (*Morrison, 1955*). In particular, chemisorbed oxygen affects AH adsorption; there are two proposed mechanisms that result from the possibility of two forms of charged oxygen atoms:

$$H + O^- \rightarrow OH^- \quad \text{(I)}$$

$$H + O^{2-} \rightarrow OH^- + e^- \quad \text{(II)}$$

Type (I) adsorption of hydrogen occurs at less than 353 K and proceeds without change of semiconductor conductivity because trapped electrons remain trapped. In comparison, type (II) AH adsorption occurs at higher temperatures (> 353 - 393 K) and results in conductivity increases of the semiconductor due to the released electron. However, type (II) adsorption of AH requires the presence of doubly ionized oxygen - the existence of which has never been empirically proven as a result of AO adsorption upon ZnO (*Morrison, 1955*).

It is expected that the ZnO sensors of AOE-2 will be covered with adsorbed oxygen before exposure to AH, because prior to launch they have been stored in an oxygen containing environment, and during launch they will experience AO exposure. Hence, the direct influence of AH upon the sensors will be avoided in favour of the two adsorption mechanisms (I) and (II). Since perigee exposure temperatures are expected to be ~ 298 K, and the existence of O^{2-} on ZnO is in doubt, in practice it is likely that the mechanism of AH adsorption will be type (I). Clearly then, since this mechanism does not involve the release of electrons, AH exposure experienced during perigee passes will not affect the ZnO devices and AO measurement should proceed as if AH were not present.

11.7.4 Impact of solar ultraviolet irradiation

During operation of the experiment on orbit, it will be exposed to a large amount of VUV and UV radiation. Investigations described in Chapter 10 have shown that these radiations can adversely affect the semiconductor material used in the sensors; it causes sensor conductance increases during illumination and alters the surface composition. The experimental results seem to indicate that regeneration heating helps induce a recovery of the sensor conductance.

Observations from the experiments also showed that the thinner the ZnO film, the less it was affected by UV irradiation. Partly for this reason, the thinnest possible films were selected for use in the flight equipment.

In addition, it was found that the rate of change of sensor conductance per incident UV photon decreased with accumulated photon fluence. Around 4×10^{17} photons are necessary to induce this reduction of sensitivity in the films. It is possible to estimate both how long it will take to accumulate this fluence in GTO, and the likely rates of conductance change thereafter.

Assume the Sun radiates as a black-body at 5,800 K. From curves like that in Figure 10.2, it is possible to calculate the flux of photons reaching the Earth in the wavelength range of $1 \leq \lambda \leq 387$ nm, to be approximately 2.44×10^{16} photons.cm^{-2}.s^{-1}. Hence, on a spinning satellite, 4×10^{17} photons will be accumulated in a single sensor in 321 seconds, or just over 5 minutes. Thus, almost immediately after launch the sensors will become insensitive to UV irradiation induced composition changes.

After that time, a typical normalized rate of sensor conductance (for a 0.5 μm film) will be around $+5 \times 10^{-28}$ [mhos.min^{-1}].[ph.cm^{-2}.s^{-1}]$^{-1}$, which at the predicted UV flux will induce an absolute rate of conductance change of ~ $+1.22 \times 10^{-11}$ mhos.min^{-1}. Since the flight model sensor films are thinner than that used to generate this estimate, the actual values will be lower than those calculated here (see Chapter 10). The UV-induced rate of change of conductance is some three orders of magnitude lower than that expected to be caused by AO flux - clearly negligible, even though this rate may add to the influence of AH.

11.7.5 Sensor unit damage estimate

In Chapter 1 it was reported that surfaces in the near Earth environment experience hypervelocity impacts of man-made debris and natural micrometeoroids. An impact on a sensor may lead to operationally significant damage, or perhaps complete destruction. However, it is believed that an impact on the SU face plate will not lead to damage of the sensors because cracks in this unit should not propagate into the mechanically isolated sensor substrates. Clearly, the sensor

elements of greatest susceptibility are the thin and thick films - the silver and zinc oxide films and their associated contacts. Given the brittle nature of alumina and glass, it is believed that even impacts of small particles would lead to catastrophic fracturing of the sensor substrates. Such fracturing would lead to breakage of the films, preventing electrical resistance measurements and, hence, failure of the experiment.

It is possible to estimate the probability of a hypervelocity impact on the AOE-2 sensor unit. Unfortunately, it has been impossible to find measurements or predictions of the flux of micrometeoroids and debris particles in GTO. Instead, the damage estimate will be implied from probabilities derived from measurements taken in circular low Earth orbits.

Laurance and Brownlee have estimated the flux of particles that had impacted the Solar Maximum Mission satellite during the 4.5 years that it resided in its 500 - 570 km circular orbit (*Laurance and Brownlee, 1986*). Their measurements showed that the flux of particles that generated craters of diameter of ≥ 0.2 μm was ~ 10^{-2} $m^{-2}.s^{-1}$. Li used the debris and micro-meteoroid model of Anderson and Smith to calculate the flux of particles (diameter ≥ 62.5 μm) in a 500 km circular orbit inclined at 28.5°, and found it to be 5.4 x 10^{-7} $m^{-2}.s^{-1}$ (*Anderson and Smith, 1994; Li, 1995*).

The large differences in the flux estimates is explained by the size difference of the impacting particles - the smaller the particles, the more frequent the impact. These two different size ranges are of particular interest because it is thought that the smallest particles should only damage the sensor films, whereas the 62.5 μm particles are ~ $1/10^{th}$ of the alumina substrate thickness, so it is believed that their impact may lead to fracture failures of these components.

From these fluxes, it is possible to generate a range of damage probabilities for the sensors. Each ZnO sensor substrate has an area of ~ 6.1 x 10^{-4} m^2. Table 11.13 contains the estimated times for impacts on a single ZnO sensor substrate for the particle size ranges detailed earlier.

Particle size range (μm)	Cumulative flux (impacts.$m^{-2}.s^{-1}$)	Time to impact on single ZnO sensor (days)
≥ 0.2	~ 10^{-2}	1.9
≥ 62.5	~ 5.4 x 10^{-7}	35.2 x 10^3

Table 11.13 - Estimated time to particle impact on a ZnO sensor

The data presented in the table shows that an impact of particles greater than ~ 0.2 μm is likely to occur on a ZnO sensor approximately every 2 days. Thus, in the mission lifetime of 200 days, around 100 impacts are to be expected. However, the majority of these impacts will involve very

small particles that may have a negligible effect on the operation of the sensor unit. In comparison, the impact of dimensionally significant particles ($\geq 1/10^{th}$ substrate thickness) is far less likely, just one impact every 96 years, or a 0.6 % chance of an impact per sensor in the mission lifetime. Overall, though, the number of expected impacts on the SU sensors must be factored by the number present. Since there are two ZnO sensor substrates, the time to impact must be halved and probability doubled. If the Ag sensor substrate is included in the analysis, the probability of an impact of a particle of size larger than or equal to 62.5 μm on any of the sensor substrates is 1.7 % over the entire mission lifetime.

Obviously, these figures must be treated with caution. They have been calculated from data recorded from orbits (LEOs) very different to the one that STRV-1c will occupy in GTO. Due to the large LEO orbital debris population, it is believed that the estimates presented herein may well over estimate the flux of these particles that will be experienced by AOE-2 (*Swinerd, 1999*). However, the micrometeoroid flux should be reasonably similar at LEO and GEO altitudes (*McBride, 1999; McBride and McDonnell, 1999*).

It is also difficult to say what size of particle will cause operationally significant damage to the sensors, especially since micrometeoroids tend to do more damage - for a given mass - than debris because of their higher impact velocities. Given these uncertainties, this analysis reveals that an impact of some form on the sensor unit is rather likely. It should be borne in mind that the AOE-1 experiment on STRV-1a remained fully functional throughout its 150 day operational lifetime, and it is therefore assumed that no significant impacts occurred on this unit. Since this observation is for an orbit very similar to that due to be occupied by STRV-1c, it may be a better indication of the GTO debris and micrometeoroid environment than the predictions made previously.

11.8 SUMMARY

This chapter has described the atomic oxygen experiment designed to demonstrate the feasibility of reusable ZnO AO sensors in Earth orbit. The experiment is called AOE-2 and incorporates semiconductor and silver thin film atomic oxygen sensors. It has been shown that the key design drivers for the experiment were the limited mass and power budgets allocated by DERA to AOE-2, 0.374 kg and 3.3 W respectively. The experiment has been integrated to the STRV-1c microsatellite, which is scheduled for launch in early 2000.

The experiment is split into two units for easy mounting and integration with the satellite. The sensor unit contains the sensors - four ZnO-based devices and four silver thin films - and is designed to be affixed to an outer, AO exposed satellite surface. The second part is the

electronics unit, which resides inside an aluminium box internal to the satellite. In order to reduce the mass and power consumption of the experiment, the satellite's on board computer is used to control all operations. For the same reason, the data generated by the experiment is digitized and stored by the on board data handling subsystem of the satellite platform.

The operation of the experiment in both of its modes of operation has been described in detail, as has the interface of the units with the satellite electronic, data and structural subsystems. Functional engineering models of the experiment have been manufactured and successfully vibration tested to the qualification levels demanded by DERA and Arianespace. Following the completion of the qualification testing, flight units of the experiment were built. These units have been tested by DERA and, owing to the successful outcome of the acceptance testing, the units have been delivered and integrated to STRV-1c.

Lastly, the ramifications and implications of the findings of ZnO sensor testing for the operation of the AOE-2 have been examined, and the expected orbital responses of the sensors assessed. It has been shown that there may be two methods in which to operate the experiment; a one-measurement-per-orbit scenario and another, where the sensor response is accumulated over the course of several orbits. Other environmental influences, such as atomic hydrogen and solar UV, were shown to have a negligible impact on the operation of the experiment. However, it is predicted the sensors of AOE-2 will experience some form of debris or micrometeoroid impact during its design life-time. These impacts may or may not have operational significance.

CHAPTER 12

CONCLUSIONS AND SUGGESTIONS FOR FUTURE WORK

12.1 CONCLUSIONS

Near-Earth space has been shown to be a hazardous environment in which to operate satellites. Of particular concern for vehicles resident in low Earth orbit are the effects of atomic oxygen in the thermosphere. Atomic oxygen is erosive towards many commonly used spacecraft materials, especially polymers and some metals, such as silver. Erosion of these materials can affect the performance of satellite systems. Hence, it is necessary to understand the AO environment and to perform *in situ* measurements of AO number densities.

Satellite- and rocket-based AO measurement techniques have been reviewed. Most are heavy, have high power requirements, or are able to effect but one measurement. These characteristics have prevented the application of many of the techniques to microsatellite missions. A new pseudo-quantitative, graphical comparison of all reviewed techniques demonstrated that a better method might be created by the fusion of actinometer and semiconductor gas sensor technologies. In this manner, it was thought possible to create a lightweight, lower power and, most importantly, reusable technique.

A theoretical model was developed in order to understand the operation of semiconductor sensors when applied to the task of AO measurement. It was found that adsorption of AO upon n-type materials decreases sample conductivity by electron capture. Moreover, the model showed that the rate of sensor conductance change is proportional to the flux of impinging AO, enabling easy determination of these fluxes. With continued exposure, the semiconductor surface eventually becomes saturated, whereupon no more atoms are adsorbed. If the sensor is heated, the model showed that the adatoms would be desorbed, thus refreshing the sensor for further measurements.

Semiconductor sensors of two designs were conceived and fabricated, both using thin film zinc oxide - an n-type metal oxide semiconductor. Each sensor was formed from two elements: one a bare ZnO film, the other a ZnO film covered with silica. The purpose of the bare film is to record the influence of AO, whilst the covered film is a control device, to enable deconvolution of the effects of other environments. The films are deposited on an alumina substrate, upon the reverse of which is a thick-film heater for temperature control. Where possible, all materials used in the sensors were chosen to be stable in the synergistic environments likely to be experienced in laboratory tests and in space.

The zinc oxide was deposited by RF sputtering. A study of the deposition process showed that the resistivity of the deposited material increased with the amount of oxygen in the sputtering plasma. X-ray diffraction investigations of the ZnO films showed that they consisted of crystallites of size between 218 - 373 Angstroms, and that the crystallite c-axes were always aligned normal to the substrate plane. All material was found to be n-type by the Seebeck effect. In addition, the ZnO was found to have a donor level 0.039 ± 0.004 eV below the conduction band, probably associated with interstitial zinc donors. The contact formed with gold thin films was observed to be Ohmic, allowing consistent conductivity measurements to be made.

Several sensors were tested in a hyperthermal, ground-based, atomic oxygen exposure facility, the first time such experiments have been performed with thin film, semiconductor-based sensors. Differences were noted in the responses of sensors of different semiconductor thicknesses. All sensors were found to require a certain AO fluence to condition their surfaces, but the thicker the film, the higher the necessary AO fluence. It was postulated that this thickness dependency was caused by a relationship between thickness and effective surface area.

Before conditioning was complete, sensors exposed to AO would increase in conductance, in contradiction to the expectations of the model. After conditioning was complete, however, the sensors all demonstrated decreasing conductances with AO exposure. This change of response was explained by the presence of an inversion layer at the semiconductor surface, which was destroyed by annealing of the semiconductor material during repeated AO exposure/regeneration cycles. Some devices changed from one response to the other via an intermediary stage. In the transition, the conductances would first decrease, but then revert to the erroneous increase as time of exposure progressed.

Detailed investigations of the responses of two half-micrometre sensors demonstrated that, as predicted, the rate of conductance change is proportional to the level of AO flux. The calibration coefficients of the two sensors were found to be very similar, which indicates the manufacturing repeatability of the devices. Also, this study showed that - in agreement with the mathematical model - the sensors exhibited a saturation limit. The AO fluence to saturation was found to be dependent on the level of flux engendering it, and the possibility of using the time to saturation as another measure of AO flux was presented.

The two half-micrometre sensors were also used to determine the flux decay in the atomic oxygen exposure facility. The results of this study showed that the flux decreased in an inverse square manner. Not only did the semiconductor sensor results agree with those of another sensor, but also with gas-dynamic expectations.

Additional, unique experiments were conducted to investigate sensor regeneration, a previously un-studied stage of sensor usage. These tests showed that regeneration was not occurring as anticipated. Instead of the conductance of the sensors recovering to its pre-exposure value upon heating to elevated temperature, it decreased even more than during AO exposure. This permanent decrease was called hysterisis, and is believed to be caused by the permanent oxidation of the zinc donors in the zinc oxide matrix. Evidence of a time-dependent factor in the regeneration hysterisis was presented, which indicated that the shorter the regeneration heating phase, the better. Results from the regeneration study indicated that there is an optimum temperature at which to perform this process, because heating to this temperature maximises the response of the sensor in the next AO exposure. However, it also appears that this temperature leads to the largest amount of sensor hysterisis. Yet higher temperatures of regeneration and shorter regeneration times were proposed to limit the amount of hysterisis. Unfortunately, material limits associated with the sensor design prevented these investigations from being performed.

During AO exposure, all sensors were exposed to VUV fluxes. Data from the silica-covered films were analyzed. The conductances of all silica-covered ZnO films were observed to increase during the experiments as a result of UV/VUV induced photoconductivity. The thinner ZnO films were found to be less sensitive to UV/VUV exposure than the thicker films. Regeneration heating was found to anneal the majority of the conductance changes, thus only a small permanent increase resulted during each experiment. The rate of conductance increase of the silica-covered ZnO films was observed to decrease with accumulated VUV photon fluence. This phenomenon was attributed to the documented damage caused by VUV stimulated oxygen desorption. Therefore, illumination-induced conductivity changes can be ignored after a certain accumulated total.

Molecular oxygen exposures were conducted with the sensors. Although the oxygen was thermal and ground state, rather than hyperthermal and vibrationally excited, like any residual component in the AO beam, the simulation was used to determine if the sensors would respond to this species. No response was observed from any of the films, despite the fluxes being of a similar order of magnitude to the oxygen atom fluxes used in the AO experiments. Hence, it was concluded that the devices display no measurable sensitivity to unexcited, molecular oxygen.

A proto-flight experiment was designed and built to demonstrate the operation of these renewable sensors in Earth orbit, and is believed to be the first application of such a technique in this environment. The experiment has been designed for inclusion on the STRV-1c microsatellite. The interface and operation of the unit on the satellite was explained in depth. Results from the

laboratory experiments were used to demonstrate the way in which the satellite experiment could be operated and the form of the ensuing data analysis.

The low weight, low power consumption and reusability of the sensors developed during this project confer significant advantages on this experiment that other equipment simply does not possess. Thus, the goal of combining the reusability of semiconductor sensors with the properties of actinometers has been achieved. No other AO sensor has the same combination of properties as the one resulting from this research. The flight hardware has been delivered to the satellite manufacturer and has been successfully integrated onto the vehicle. Launch is anticipated in spring 2000.

12.2 SUGGESTIONS FOR FUTURE WORK

The previous section of this chapter has concluded the research performed by the author. Although all of the goals of the initial research programme have been achieved, more questions have arisen as a result of the findings and, in some cases, due to inadequacies of the investigations possible in the time scale of this work. Therefore, the project described herein is best viewed as the basis for future investigations, rather than as a definitive study. As a result, several suggestions for future research are proposed below.

1) Further research is required to fully characterize the ZnO sensor responses, in particular their repeatability. For example, the effects of different exposure temperatures, AO energy, and a greater range of AO fluxes. This study will require more AO exposure experiments, which could be conducted in the ESTEC ATOX facility.

2) The ESTEC ATOX source is pulsed, and there remain some doubts about the influence of large bursts of AO and UV fluxes on the sensor response. Therefore, it would be better to investigate the response of the sensors in a continuous, hyperthermal exposure facility.

3) One of the key problems of sensor operation found to this juncture is the large amount of sensor hysterisis associated with regeneration. It is proposed that the effects of increased regeneration temperature and decreased regeneration time be investigated. Other authors have used flash heating of the films, using the discharge of capacitors to supply energy directly into the semiconductor. In this manner, the temperature limits imposed by the materials used to fabricate the sensor could be overcome, because only the sensor element would be heated to any extent.

4) It was suggested in Chapter 9 that there may be a relationship between ZnO conductivity and the amount of sensor hysterisis experienced during regeneration. Thus, a regeneration study should include sensors of different ZnO conductivity to confirm or refute this supposition.

5) It is not yet known how the sensors respond to thermal or thermalized atomic oxygen. Therefore, sensor response should be examined when subjected to a flux of thermal AO atoms. Whilst not an issue for satellite-based operation, it might be for ground-based sources where the AO may reflect inelastically from chamber surfaces, and to qualify the sensor for use in thermal atom facilities, which are still used for material erosion studies.

6) It would also be interesting to investigate other semiconducting materials, especially those of p-type. Since p-type materials experience an increase of conductivity during AO exposure, their response is opposite that of n-type semiconductors. Hence, if a resistance-bridge circuit were formed with one arm of the bridge containing an n-type sensor, and another a p-type device, the output signal from the circuit would be the sum of both of the responses. In this way, it might be possible to detect small fluxes, which were undetectable with a single element sensor. Additionally, p-type materials will not suffer from Elovich-type limits on the quantity of AO that they can adsorb, allowing longer duration measurements than the n-type sensors developed by this research.

7) In addition to investigating other materials, it would be beneficial to investigate other forms of zinc oxide. Currently, depositing the semiconductor is the most expensive stage of sensor fabrication. Using thick films, which can easily be screen printed at the same time as the electrodes, would substantially reduce the costs of sensor production. However, the ramifications of such a change upon sensor sensitivity and response would have to be studied carefully.

8) Whilst the influence of VUV and UV has been examined by experiment, there are still uncertainties about the effect of particulate and ionizing radiation such as γ-rays and fast electron and protons. Given the unknown effects of this radiation, large doses of which may be experienced by the flight equipment, some ZnO devices should be exposed to these radiations to measure any decay or change of sensor property. Facilities for conducting radiation exposure exist at ESTEC (γ-rays) and at ONERA/CNES (e^- and p^+).

9) After the launch of STRV-1c, results from the atomic oxygen experiment will require analysis. This will require a software programme, which has yet to be written.

10) If it is intended to continue the efforts to develop the semiconductor sensors as AO measurement devices for Earth orbit, a great deal of effort should be put into developing the sensor measurement electronics and interface equipment. Improvements to the AOE-2 flight hardware could be the inclusion of a dedicated ADC, improved sensor measurement technique so that greater conductance changes can be accommodated, and an overall reduction in the power and mass of the electronics.

11) Application of the technique to lower orbits, where the fluxes of atomic oxygen are higher would allow an *in situ* test more akin to that achieved in the laboratory. The opportunity for conducting such a test exists with the inclusion of semiconductor sensors on the materials exposure and degradation experiment on the European technology exposure facility (MEDET on EuTEF).

'*The greatest sin is ignorance, not to know.*' **Rudyard Kipling**.

REFERENCES

Ahmadjian, M. and Jennings, D.E., (1995), "Analysis of STS-39 Space Shuttle Glow Measurements," *Journal of Spacecraft and Rockets*, 32, no. 3, pp 507-513.

Aita, C.R., Purdes, A.J., Lad, R.J., and Funkenbusch, P.D., (1980), "The Effect of O_2 on Reactively Sputtered Zinc Oxide," *Journal of Applied Physics*, **51**, no. 10, pp 5533-5536.

Alet, I., (1997), "Eleven Years of Ageing of SSM Teflon on the Sunsynchronous Orbit – SPOT," *in Proceedings of the 7th International Symposium on Materials in a Space Environment*, Toulouse, France, pp 283-286, 16th-20th Jun. 1997. ESA SP-399.

Allen, M. and Yung, Y.L., (1981), "Vertical Transport and Photochemistry in the Terrestrial Mesosphere and Lower Thermosphere (50-100 km)," *Journal of Geophysical Research*, **86**, pp 3617-3627.

Anderson, B.J. and Smith, R.E., (1994), "Natural Orbital Environment Guidelines for Use in Aerospace Vehicle Development," *NASA Technical Memorandum 4527*, Marshal Space Flight Center.

Anderson, J.G., (1975), "The Absolute Concentration of $O(^3P)$ in the Earth's Stratosphere," *Geophysical Research Letters*, **2**, no. 6, pp 231-234.

Anger, C.D., Fancott, T., McNally, J., and Kerr, H.S. (1973), "ISIS-II Scanning Auroral Photometer," *Applied Optics*, **12**, no. 8, pp 1753-1766.

Aranovich, J., Oritz, A., and Bube, R.H., (1979), "Optical and Electrical Properties of ZnO Films Prepared by Spray Pyrolysis for Solar Cell Applications," *Journal of Vacuum Science and Technology*, **16**, no. 4, pp 994-1003.

Arnold, G.S. and Peplinski, D.R., (1985), "Reaction of Atomic Oxygen with Polyimide Films," *AIAA Journal*, **23**, no. 10, pp 1621-1626.

Arnold, G.S. and Peplinski, D.R., (1986), "Reaction of High-Velocity Atomic Oxygen with Carbon," *AIAA Journal*, **24**, no. 4, pp 673-677.

Arnold, G.S., Peplinski, D.R., and Cascarano, F.M., (1987), "Translational Energy Dependence of the Reaction of Atomic Oxygen with Polyimide Films," *Journal of Spacecraft and Rockets*, **24**, no. 5, pp 454-458.

Bailey, S. M., (1998), Hampton University, USA, (formally at the Laboratory for Atmospheric and Space Physics, University of Colorado), personal communication.

Baird, J.K., (1998), "Low-Earth-Orbit Atomic Oxygen Erosion of Polymer Surfaces," *Journal of Spacecraft and Rockets*, **35**, no. 1, pp 62-65.

Banks, P.M., Williamson, P.R., and Raitt, W.J., (1983), "Space Shuttle Glow Observations," *Geophysical Research Letters*, **10**, no. 2, pp 118-121.

Banks, B.A., Rutledge, S.K., and Brady, J.A., (1988), "The NASA Atomic Oxygen Effects Program," *in Proceedings of the 15th Space Simulation Conference*, Williamsburg, VA, USA, pp 51-65, 31st Oct. - 3rd Nov. 1988. NASA-CP-3015.

Banks, B.A., Rutledge, S.K., Auer, B.M., and DiFilippo, F., (1990), "Atomic Oxygen Undercutting of Defects on SiO_2 Protected Polyimide Solar Array Blankets," *in proceedings 119th TMS Annual Meeting and Exhibition*, Anaheim, CA, USA, pp 16-33, 18th-22nd February, 1990.

Barnes, J.O., Leary, D., and Jordan, A.G., (1980), "Relationship Between Deposition Conditions and Physical Properties of Sputtered ZnO," *Journal of the Electrochemical Society*, **127**, no. 7, pp 1636-1640.

Bedingfield, K.L., Leach, R.D., and Alexander, M.B., (1996), "Spacecraft System Failures and Anomalies Attributed to the Natural Space Environment," *NASA reference publication 1390*, 43 pages.

Blair, P., Jr., Carroll, W., Jacobs, S., and Leger, L.J., (1971), "Study of Thermal Control Surfaces Returned From Surveyor III," *AIAA Paper*, AIAA-71-479.

Bonasewicz, P., Hirschwald, W., and Neumann, G., (1986), "Influence of Surface Processes on Electrical, Photochemical and Thermodynamical Properties of ZnO Films," *Journal of the Electrochemical Society: Electrochemical Science and Technology*, **133**, no.11, pp 2270-2278.

Bourde, J., Renard, P., Sabbathier, G. de, and Drolshagen, G., (1994), "Improved Analysis Tool for the Computation of Spacecraft Erosion due to Atomic Oxygen," *in Proceedings of the 6th International Symposium on Materials in a Space Environment*, Noordwijk, The Netherlands, pp 271-276, 19th-23rd Sep. 1994. ESA SP-368.

Bragg, W.L., (1913), "The Diffraction of Short Electromagnetic Waves by a Crystal," *Proceedings of the Cambridge Philosophical Society*, **17**, pp 43-57.

Brattain, W.H. and Bardeen, J., (1953), "Surface Properties of Germanium," *The Bell System Technical Journal*, **32**, no. 1, pp 1-41.

Butler, M.A. and Ricco, A.J., (1988), "Chemisorption-Induced Reflectivity Changes in Optically Thin Silver Films" *Applied Physics Letters*, **53**, no. 16, pp 1471-1473.

Butler, M.A. and Ricco, A.J., (1989), "Reflectivity Changes of Optically-Thin Nickel Films Exposed to Oxygen," *Sensors and Actuators*, **19**, pp 249-257.

Caledonia, G.E., Krech, R.H., and Green, B.D., (1987), "A High Flux Source of Energetic Oxygen Atoms for Materials Degradation Studies," *AIAA Journal*, **25**, no. 1, pp 59-63.

Caledonia, G.E., (1988), "Laboratory Simulations of Energetic Atom Interactions Occurring in Low Earth Orbit," *Rarefied Gas Dynamics: Space-Related Studies*, Muntz, E.P., Weaver, D.P., and Campbell, D.H., (eds), *Progress in Astronautics and Aeronautics*, **116**, pp 129-142.

Caledonia, G.E., Krech, R.H., and Oakes, D.B., (1994), "Laboratory Studies of Fast Atom Interactions With Materials," *in Proceedings of the 6th International Symposium on Materials in a Space Environment*, ESTEC, Noordwijk, The Netherlands, pp 285-290, 19th-23rd Sep. 1994. ESA SP-368.

Callister, W.D., (1991), "Materials Science and Engineering," 2nd Edition, pub John Wiley and Sons, Inc., NY, USA, 1981, 791 pages.

Cant, A., (1990), "Atomic Oxygen Experiment – A Feasibility Study," Final Year Undergraduate Report (unpublished), Department of Aeronautics and Astronautics, University of Southampton, Southampton, UK.

Cant, A. and Simpson, H., (1998), "STRV-1c & d Satellite Architecture Design Document," DERA Space Department, DERA Farnborough. Project reference: **1CD/MGT/SPEC/0092/3.0**.

Carruth, M.R., Jr., DeHaye, R.F., Norwood, J.K., and Whitaker, A.F., (1990), "Method for Determination of Neutral Atomic Oxygen Flux," *Review of Scientific Instruments*, **61**, no. 4, pp 1211-1216.

Cazaubon, B., Paillous, A., Siffre, J., and Thomas, R., (1996), "Five-Electron-Volt Atomic Oxygen Pulsed-Beam Characterization by Quadrupolar Mass Spectrometry," *Journal of Spacecraft and Rockets*, **33**, no. 6, pp 870-876.

Chambers, A.R., Harris, I.L., and Roberts, G.T., (1996), "Reactions of Spacecraft Materials With Fast Atomic Oxygen," *Materials Letters*, **26**, pp 121-131.

Chandler, P.E., (1980), "The Oxidation of Zinc and Gas Adsorption onto Zinc Oxide, Zinc and Oxidised Zinc Surfaces," Ph.D. Thesis, University of Southampton, Southampton.

Chandra, P., Tare, V.B., and Sinha, A.P.B, (1967), "Optical and Electrical Properties of Zinc Oxide Single Crystals," *Indian Journal of Pure and Applied Physics*, **5**, no. 1, pp 6-9.

Cimino, A., Molinari, E., and Cramarossa, F., (1963), "Oxygen Chemisorption and Surface p-type Behaviour of Zinc Oxide Powders," *Journal of Catalysis*, **2**, pp 315-323.

Clemesha, B. R., (1998), Instituto Nacional de Pesquisas Espaciais, personal communication.

Cogger, L.L. and Murphree, J.S., (1980), "The Latitudinal and Seasonal Variation of Atomic Oxygen Deduced from Observations of the E-region OI 557.7 nm Airglow," *Space Research*, **20**, pp 115-120.

Collins, R.J. and Thomas, D.G., (1958), "Photoconduction and Surface Effects with Zinc Oxide Crystals," *Physical Review*, **112**, no. 2, pp 388-395.

Coors Tech Specs, (1995), "Thin Film Substrates, Technical Specifications," 42-4-1095, available from Coors Ceramics Electronics Ltd., Glenrothes, Scotland, UK.

Craciun, V., Elders, J., Gardeniers, J.G.E., and Boyd, I.W., (1994), "Characteristics of High Quality Zinc Oxide Thin Films Deposited by Pulsed Laser Deposition," *Applied Physics Letters*, **65**, no. 23, pp 2963-2965.

Crank, J, (1956), "The Mathematics of Diffusion," pub. Clarendon Press, Oxford, UK, 1956, 347 pages.

Cranny, A.W.J., Atkinson, J.K., Burr, P.M., and Mack, D., (1991), "A Comparison of Thick- and Thin-Film Gas-Sensitive Organic Semiconductor Compounds," *Sensors and Actuators B*, **4**, pp 169-174.

Cranny, A.W.J., (1992), "Sensor Array Signal Processing for Cross-Sensitivity Compensation in Non-Specific Organic Semiconductor Gas Sensors," Ph.D. Thesis, University of Southampton, Southampton, UK.

Cross, J.B. and Blais, N.C., (1988), "High-Energy/Intensity CW Atomic Oxygen Beam Source," *Rarefied Gas Dynamics: Space-Related Studies*, Muntz, E.P., Weaver, D.P., and Campbell, D.H., (eds), *Progress in Astronautics and Aeronautics*, **116**, pp 143-156.

Cross, J.B., Koontz, S.L., and Hunton, D.E., (1995), "Flight Mass-Spectrometer Calibration in a High Velocity Atomic Oxygen Beam," *Journal of Spacecraft and Rockets*, **32**, no. 3, pp 496-501.

Cross, J.B., Koontz, S.L., and Lan, E.H., (1991), "Atomic Oxygen Interaction with Spacecraft Materials: Relationship Between Orbital and Ground-Based Testing for Materials Certification," *in Proceedings of the 5th International Symposium on Materials in a Space Environment*, Cannes, France, pp 369-384, Sep. 1991. ISBN 2-85428-293-0.

Cunningham, J. Finn, E., and Samman, N., (1975), "Photoassisted Surface Reactions Studied by Dynamic Mass Spectrometry," *Faraday Discussions of the Chemical Society*, **58**, pp 160-174.

Cuthbertson, J.W., Langer, W.D., and Motley, R.W., (1990), "Atomic Oxygen Beam Source for Erosion Simulation," *in Proceedings 119th TMS Annual Meeting and Exhibition*, Anaheim, CA, USA, pp 16-33, 18th-22nd Feb. 1990. (See also Cuthbertson, J.W., Langer, W.D., and Motley, R.W., (1992), "Reflection of Low Energy Plasma Ions from Metal Surfaces," *Journal of Nuclear Materials*, **196-198**, pp 113-128.)

Danilov, A. D. and Istomin, V.G., (1970), "Chemistry of the Ionosphere," pub. Plenum Press, New York, USA, 1970, 296 pages.

de Groh, K.K. and Banks, B.A., (1994), "Atomic-Oxygen Undercutting of Long Duration Exposure Facility Aluminized-Kapton Multi Layer Insulation," *Journal of Spacecraft and Rockets*, **31**, no. 4, pp 656-664.

Delahoy, A.E., (1998), Energy Photovoltaics (EPV) Inc., NJ, USA, personal communication.

Dickinson, P.H.G., Bolden, R.C., and Young, R.A., (1974), "Measurement of Atomic Oxygen in The Lower Ionosphere Using a Rocket-Borne Resonance Lamp," *Nature*, **252**, pp 289-291.

Dickinson, P.H.G., Twiddy, N.D., and Young, R.A., (1976), "Atomic Oxygen Concentrations in the Lower Thermosphere," *Space Research XVI*, pp 301-305.

Dickinson, P.H.G., Bain, W.C., Thomas, L., Williams, E.R., Jenkins, D.B., and Twiddy, N.D., (1980), "The Determination of the Atomic Oxygen Concentration and Associated Parameters in the Lower Ionosphere," *Proceedings of the Royal Society of London*, **A 369**, pp 379-408.

Domingo, V., (1993), "The Sun – Its Role in the Environment of the Near Earth Space," IN DeWitt, R. N., Duston, D., and Hyder, A. K., (eds.), "The Behaviour of Systems in the Space Environment," *Nato ASI Series – Series E: Applied Sciences*, **245**, pp 67-101.

Donahue, T.M., Guenther, B., and Thomas, R.J., (1973), "Distribution of Atomic Oxygen in the Upper Atmosphere Deduced from OGO-6 Airglow Observations," *Journal of Geophysical Research*, **78**, no. 28, pp 6662-6689.

Donahue, T.M., Anderson, J.G., Rawlins, W.T., Kaufman, F., and Hudson, R.D., (1977), "Apollo-Soyuz $O(^3P)$ and $N(^4S)$ Density Measurement by UV Spectroscopy," *Geophysical Research Letters*, **4**, pp 79-82.

Drolshagen, G. and van Eesbeek, M., (1991), "Atomic Oxygen Fluence Detector for BREMSAT: Scientific and Technical Description," *in Proceedings of the 5th International Symposium on Materials in a Space Environment*, Cannes, France, pp 405-409, Sep. 1991. ISBN 2-85428-293-0.

Eger, D., Goldstein, Y., and Many, A., (1975), "Oxygen Chemisorption and Photodesorption Processes on ZnO Surfaces," *RCA Review*, **36**, pp 509-530.

Fabricius, H., Skettrup, T., and Bisgaard, P., (1986), "Ultraviolet Detectors in Thin Sputtered ZnO Films," *Applied Optics*, **25**, no. 16, pp 2764-2767.

Friedrich, V.H., Offermann, D., Trinks, H., and von Zahn, U., (1977), "The Cryo Mass Spectrometer in the Winter Anomaly Campaign," *Journal of Geophysics*, **44**, pp 139-146.

Gabriel, S.B., (1997), "The Feasibility of Zinc Oxide as a Detector For Atomic Oxygen," *Final report under ESTEC contract no. 11702/95/NL/PB.*

Gabriel, S.B., Osborne, J.J., Roberts, G.T., and Chambers, A.R., (1998), "Development of a Renewable Atomic Oxygen Sensor for Low Earth Orbit," *Journal of Spacecraft and Rockets*, **35**, no. 3, pp 413-415.

Galli, G. and Coker, J.E., (1970), "Epitaxial ZnO on Sapphire," *Applied Physics Letters*, **16**, no. 11, pp 439-441.

Garrett, H.B., Chutjian, A., and Gabriel, S., (1988), "Space Vehicle Glow and Its Impact on Spacecraft Systems," *Journal of Spacecraft and Rockets*, **25**, no. 5, pp 321-340.

Gilligan, J.E., (1967), "The Induced Optical Properties of Zinc Oxide," *AIAA Paper*, AIAA-67-214.

Gilmore, D.G., (ed.), (1994), "Satellite Thermal Control Handbook," pub. The Aerospace Corporation Press, El Segundo, California, USA, 1994.

Goeckner, M.J., Bennett, T.K., and Cohen, S.A., (1997), "A Source of Hyperthermal Neutrals for Materials Processing," *Applied Physics Letters*, **71**, no 7, pp 980-982.

Golomb, D., Rosenberg, N.W., Aharonian, C., Hill, J.A.F., and Alden, H.L., (1965), "Oxygen Atom Determination in the Upper Atmosphere by Chemiluminescence of Nitric Oxide," *Journal of Geophysical Research*, **70**, no. 5, pp 1155-1173.

Golomb, D. and Good, R.E., (1972), "Atomic Oxygen Profiles over Churchill and Hawaii from Chemical Releases," *Space Research*, **12**, pp 675-683.

Good, R.E., (1976), "Determination of Atomic Oxygen Density from Rocket Borne Measurement of Hydroxyl Airglow," *Planetary and Space Science*, **24**, pp 389-395.

Green, B.D., (1988), "The Spacecraft Glow: A Review," *in Proceedings of the 4th European Symposium on Spacecraft Materials in a Space Environment*, Toulouse, France, pp 477-491, 6th-9th Sep. 1988. ISBN 2-85428-228-0.

Greer, W.A.D., Stark, J.P.W., and Pratt, N.H., (1995), "Surface-Induced Luminescence in a High-Velocity Rarefied Atomic Oxygen Flow Regime," *Journal of Geophysical Research*, **100**, no. A5, pp 7821-7828.

Gregory, J.C., Miller, G.P., Pettigrew, P.J., Raikar, G.N., Cross, J.B., Lan, E., Renschler, C.L., and Sutherland, W.T., (1993), "Atomic Oxygen Dosimetry Measurements Made on STS-46 by CONCAP-II," *in Proceedings of the Long Duration Exposure Facility Third Post Retrieval Symposium*, Williamsburg, Virginia, USA, pp 957-970, 8th-12th Nov. 1993. NASA-CP-3275 Part III.

Greig, D., (1969), "Electrons in Metals and Semiconductors," pub. McGraw-Hill, London, UK, 1969, 167 pages.

Grunthaner, F.J., Ricco, A.J., Butler, M.A., Lane, A.L., McKay, C.P., Zent, A.P., Quinn, R.C., Murray, B., Klein, H.P., Levin, G.V., Terhune, R.W., Homer, M.L., Ksendov, A., and Niedermann, P., (1995), "Investigating the Surface-Chemistry of Mars," *Analytical Chemistry*, **67**, no. 19, pp A605-A610.

GSFC (Goddard Space Flight Center) Laboratory for Atmospheres web page at http://webserver.gsfc.nasa.gov/java/missions.html

Gulino, D.A., (1988a), "Solar Dynamic Concentrator Durability in Atomic Oxygen and Micrometeoroid Environments," *Journal of Spacecraft and Rockets*, **25**, no. 3, pp 244-249.

Gulino, D.A., (1988b), "Atomic-Oxygen Durability of Impact-Damaged Solar Reflectors," *Journal of Spacecraft and Rockets*, **25**, no. 1, pp 39-44.

Gumbel, J., (1997), "Rocket-borne Optical Measurements in the Middle Atmosphere," Ph.D. Thesis, Stockholm University, Stockholm, Sweden.

Gutman, E.E., (1995), "Semiconductor Gas Sensors and Problems of the Earth's Ozonosphere," *Sensors and Actuators B*, **23**, pp 209-214.

Haberrecker, K., Mollwo, E., Schreiber, H., Hoinkes, H., Nahr, H., Linder, P., and Wilsch, H., (1967), "The ZnO-Crystal as Sensitive and Selective Detector for Atomic Hydrogen Beams," *Nuclear Instruments and Methods*, **57**, pp 22-28.

Haenni, W., Baumann, H., Comninellis, Ch., Gardini, D., Niedermann, P., Perret, A., and Skinner, N., (1998), "Diamond-sensing Microdevices for Environmental Control and Analytical Applications," *Diamond and Related Materials*, **7**, pp 569-574.

Hagemark, K.I. and Chacka, L.C., (1975), "Electrical Transport Properties of Zn-Doped ZnO," *Journal of Solid State Chemistry*, **15**, pp 261-270.

Harris, I.L., Chambers, A.R., and Roberts, G.T., (1994), "The Laboratory Testing of Silver and Polymeric Material in Atomic Oxygen Flows," *in Proceedings of the 6th International Symposium on Materials in a Space Environment*, ESTEC, Noordwijk, The Netherlands, pp 195-200, 19th-23rd Sep. 1994. ESA SP-368.

Harris, I.L., (1996), "Space and Ground-Based Studies of Orbital Atomic Oxygen Effects Using Silver Film Detectors," Ph.D. Thesis, University of Southampton, Southampton, UK.

Harris, I.L., Chambers, A.R., and Roberts, G.T., (1997a), "Preliminary Results of an Atomic Oxygen Spaceflight Experiment," *Materials Letters*, **31**, pp 321-328.

Harris, I.L., Chambers, A.R., and Roberts, G.T., (1997b), "A Low Cost Microsatellite Instrument for the *In Situ* Measurement of Orbital Atomic Oxygen Effects," *Review of Scientific Instruments*, **68**, no. 8, pp 3220-3228.

Harris, I.L., (1997c), Jet Propulsion Laboratory, Pasadena, California, USA, personal communication.

Harris, I.L., Chambers, A.R., and Roberts, G.T., (1998), "Results from the Space Technology Research Vehicle 1a Atomic Oxygen Experiment," *Journal of Spacecraft and Rockets*, **35**, no. 5, pp 647-652.

Harris, N.S. (1989), "Modern Vacuum Practice," pub. McGraw-Hill Book Company, Maidenhead, UK, 1989, 315 pages.

Hartnagel, H.L., Dawar, A.L., Jain, A.K., and Jagadish, C., (1995), "Semiconducting Transparent Thin Films," pub. Institute of Physics Publishing, Bristol, UK, 1995, 358 pages.

Haruvy, Y., (1990), "Risk Assessment of Atomic-Oxygen-Effected Surface Erosion and Induced Outgassing of Polymeric Materials in LEO Space Systems," *ESA Journal*, **14**, pp 109-119.

Hayamizu, S., Tabata, H., Tanaka, and Kawai, T., (1996), "Preparation of Crystallized Zinc Oxide on Amorphous Glass Substrates by Pulsed Laser Deposition," *Journal of Applied Physics*, **80**, no. 2, pp 787-791.

Hays, P.B., Carigan, G., Kennedy, B.C., Shepherd, G.G., and Walker, J.C.G., (1973), "The Visible-Airglow Experiment on Atmosphere Explorer," *Radio Science*, **8**, no. 4, pp 369-377.

Healey, A.M., (1999), "The Synthesis and Characterisation of Potential High Capacity Ion Exchange Materials ", Ph.D. Thesis, University of Southampton, Southampton, UK.

Heath, D.F., (1959), Dissertation, The John Hopkins university, USA.

Hedin, A. E., (www resources),

1) http://nssdc.gsfc.hasa.gov/space/model/atmos/msis.html
2) http://nssdc.gsfc.nasa.gov/space/model/models/msis.html

Hedin, A.E., Reber, C.A., Newton, G.P., Spencer, N.W., Brinton, H.C., Mayr, H.G., and Potter, W.E., (1977), "A Global Thermospheric Model Based on Mass Spectrometer and Incoherent Scatter Data MSIS-2: Composition," *Journal of Geophysical Research*, **82**, no. 16, pp 2148-2156.

Hedin, A.E., (1988), "Atomic Oxygen Modelling in the Upper Atmosphere," *Planetary and Space Science*, **36**, no. 9, pp 907-920.

Heiland, G., Mollwo, E., and Stöckmann, F., (1959), "Electronic Processes in Zinc Oxide," *Solid State Physics*, **8** pp 191-323.

Heiland, G., (1961), "Photoconductivity of Zinc Oxide," *Journal of Physics and Chemistry of Solids*, **22**, pp 227-234.

Heiland, G., (1982), "Homogeneous Semiconducting Gas Sensors," *Sensors and Actuators*, **2**, pp 343-361.

Henderson, W.R. and Schiff, H.I., (1970), "A Simple Sensor for the Measurement of Atomic Oxygen Height Profiles in the Upper Atmosphere," *Planetary and Space Science*, **18**, pp 1527-1534.

Henderson, W.R., (1974), "Atomic Oxygen Profile Measurements," *Journal of Geophysical Research*, **79**, pp 3819-3826.

Hersom, C.H., (1997), Instrument Services Lab, Institute for Space and Terrestrial Science, Ontario, Canada, personal communication.

Hey, A.J.G. and Cox, S.J., (1996), "Data Handling for Research Students 1996," Postgraduate School Handbook, Faculty of Engineering and Applied Science, University of Southampton.

Hickernell, F.S., (1973), "DC Triode Sputtered Zinc Oxide Surface Elastic Wave Transducers," *Journal of Applied Physics*, **44**, no. 3, pp 1063-1071.

Hirschwald, W., Bonasewicz, P., Earnst, L., Grade, M., Hofmann, D., Krebs, S., Littbarski, R., Neumann, G., Grunze, M., Kolb, D., and Schulz, H.J., (1981), "Zinc Oxide", Chapter 3, *Current Topics in Materials Science*, **7**, Kaldis, E., (ed), pub. North Holland Publishing Company, Amsterdam, The Netherlands, 1981.

Hofland, G.B. and Weaver, J.F. (1994), "Performance Characteristics of a Hyperthermal Oxygen Atom Generator," *Measurement Science and Technology*, **5**, no. 3. pp 201-204.

Howlett, L.C., Baker, K.D., Megill, L.R., Shaw, A.W., Pendleton, W.R., and Ulwick, J.C., (1980), "Measurement of a Structured Profile of Atomic Oxygen in the Mesosphere and Lower Thermosphere," *Journal of Geophysical Research*, **85**, no. A3, pp 1291-1296.

Hutson, A.R., (1957), "Hall Effect Studies of Doped Zinc Oxide Single Crystals," *Physical Review*, **108**, no. 2, pp 222-230.

Inaba, R., Ishiguro, T., and Mikoshiba, N., (1971), "Preparation and Properties of RF Sputtered Films of ZnO as an Ultrasonic Transducer," *Japanese Journal of Applied Physics*, **10**, no. 11, pp 1493-1406.

Iwagami, N., (1999), Department of Earth and Planetary Physics, University of Tokyo, Japan, personal communication.

Jacob, A., (1975), "Detection of Atomic Oxygen and Atomic Hydrogen Beams by Semiconductors," *Journal of Applied Physics*, **46**, 12, pp 5116-5121.

James, B.F., Norton, O.W., and Alexander, M.B., (1994), "The Natural Space Environment: Effects on Spacecraft," *NASA Reference Publication 1350*, 25 pages.

Jarzebski, Z.M., (1973), "Oxide Semiconductors," pub. Pergamon Press, Oxford, UK, 1973, 285 pages.

Kaufman, F., (1961), "Reactions of Oxygen Atoms," *Progress in Reaction Kinetics*, **1**, no. 1, pp 1-39.

Kessler, D.J., (1992), "Orbital Debris Environment for Spacecraft in Low Earth Orbit," *NASA Conference Publication 10077*, pp 74-80.

Kinnersley, M., Stark, J., and Swinyard, B., (1988), "Development of and Initial Results from a High Fluence, High Velocity Atomic Oxygen Source," *in Proceedings of the 4th European Symposium on Materials in a Space Environment*, Toulouse, France, pp 701-710, 6th-9th Sep. 1988. ISBN 2-85428-228-0.

Kita, K., Imamura, T., Iwagami, N., Morrow, W. H., and Ogawa, T., (1996), "Rocket Observation of Atomic Oxygen and Night Airglow: Measurement of Concentration with an Improved Resonance Fluorescence Technique," *Annales Geophysicae*, **14**, pp 227-237.

Koontz, S., Leger, L., Albyn, K., and Cross, J., (1990), "Vacuum Ultraviolet Radiation/Atomic Oxygen Synergism in Materials Reactivity," *Journal of Spacecraft and Rockets*, **27**, no. 3, pp 346-348.

Koontz, S., King, G., Dunnet, A., Kirkendahl, T., Linton, R., and Vaughn, J., (1991a), "The International Telecommunications Satellite (INTELSAT) Solar Array Coupon (ISAC) Atomic Oxygen Flight Experiment, Techniques, Results and Summary," *in Proceedings of the 5th International Symposium on Materials in a Space Environment*, Cannes, France, pp 331-348, Sep. 1991. ISBN 2-85428-293-0.

Koontz, S.L., Albyn, K., and Leger, L.J., (1991b), "Atomic Oxygen Testing with Thermal Atom Systems: A Critical Evaluation," *Journal of Spacecraft and Rockets*, **28**, no. 3, pp 315-323.

Koontz, S.L., Leger, L.J., Rickman, S.L., Hakes, C.L., Bui, D.T., Hunton, D.E., and Cross, J.B., (1995a), "Oxygen Interactions with Materials III – Mission and Induced Environments," *Journal of Spacecraft and Rockets*, **32**, no. 3, pp 475-482.

Koontz, S.L., Leger, L.J., Visentine, J.T., Hunton, D.E., Cross, J.B., and Hakes, C.L., (1995b), "EOIM-III Mass Spectrometry and Polymer Chemistry: STS-46, July-August 1992," *Journal of Spacecraft and Rockets*, **32**, no. 3, pp 483-495.

Kudryavstev, N.N., Mazyar, O.A., and Sukhov, A.M., (1994), "Generation of Atomic Oxygen Beams (Review)," *Instruments and Experimental Techniques*, **37**, no. 1, part 1, pp 16-26.

Lad, R.J., Funkenbusch, P.D., and Aita, C.R., (1980), "Postdeposition Annealing Behaviour of RF Sputtered ZnO Films," *Journal of Vacuum Science and Technology*, **17**, no.4, pp 808-811.

Langmuir, I., (1918), "The Adsorption of Gases on Plane Surfaces of Glass, Mica and Platinum," *Journal of the American Chemical Society*, **40**, pp 1361-1403.

Laudise, R.A., Kolb, E.D., and Caporaso, A.J., (1964), "Hydrothermal Growth of Large Sound Crystals of Zinc Oxide," *Journal of the American Ceramic Society*, **47**, no. 1, pp 9-12.

Laurance, M.R. and Brownlee, D.E., (1986), "The Flux of Meteoroids and Orbital Space Debris Striking Satellites in Low Earth Orbit," *Nature*, **323**, no. 11, pp 136-138.

Lawson, K, (1998), School of Industrial Manufacturing Science, Cranfield University, personal communication.

Lawson, K, (1999), School of Industrial Manufacturing Science, Cranfield University, personal communication.

Leger, L.J., (1982), "Oxygen Atom Reaction with Shuttle Materials at Orbital Altitudes," NASA-TM-58246, May 1982.

Leger, L.J., (1983), "Oxygen Atom Reaction with Shuttle Materials at Orbital Altitudes – Data and Experiment Status," *AIAA paper*, AIAA-83-0073.

Leger, L.J., Visentine, J.T., and Kuminecz, J.F., (1984), "Low Earth Orbit Atomic Oxygen Effects on Surfaces," *AIAA Paper*, AIAA-84-0548.

Leger, L.J., Visentine, J.T., and Schliesing, J.A., (1985), "A Consideration of Atomic Oxygen Interactions with Space Station," *AIAA Paper*, AIAA-85-0476.

Leger, L.J., Koontz, S.L., Visentine, J.T., and Cross, J.B., (1988), "Laboratory Investigations Involving High-Velocity Oxygen Atoms," *in Proceedings of the 4th European Symposium on Spacecraft Materials in the Space Environment*, Toulouse, France, pp 393-404, Sep. 1988. ISBN 2-85428-228-0.

Lehn, W. and Hurley, C., (1974), "Skylab DO-24 Thermal Control Coatings and Polymeric Films Experiment," *AIAA Paper*, AIAA-74-1228.

Li, L., (1995), "A Fibre Optic Sensor for Monitoring Atomic Oxygen Erosion of Polymer Matrix Composites," Master's Thesis, Department of Aerospace Studies, University of Toronto, Toronto, Canada.

Linton, R.C., Vaughn, J.A., Finckenor, M.M., Kamenetzky, R.R., DeHaye, R.F., and Whitaker, A.F., (1993), "Orbital Atomic Oxygen Effects on Materials: An Overview of MSFC Experiments on the STS-46 EOIM-3," *AIAA paper*, AIAA-93-4102.

Livshits, A.I., Gutman, E.E., Myasnikov, I.A., Fursa, V.M., Padeev, V.I., Romanovski, Yu.A., and Kriman, E.I., (1981a), "Atomic Oxygen Analyser with Semiconductor Sensors for Researching the Upper Atmosphere of the Earth," *Pribory I Tekhnika Eksperimenta*, no. 3, pp 177-180.

Livshits, A.I., Gutman, E.E., and Myasnikov, I.A., (1981b), "Measurement of the Atomic Oxygen Profile in the Lower Thermosphere by the Method of Semiconducting Detectors," *Kosmicheskie Issledovaniya*, **19**, no. 3, pp 415-420.

Malinova, G.V. and Myasnikov, I.A., (1969), "The Effect of Chemisorption of Atomic Oxygen on Conductivities of Semiconducting Oxides I. Pyrolysis and Photolysis of Oxygen," Kinetics and Catalysis, **10**, no. 2, pp 263-268.

Mandel, G., Morehead, F.F., and Wagner, P.R., (1964), "Self-Compensation-Limited Conductivity in Binary Semiconductors. III Expected Correlations with Fundamental Parameters," *Physical Review*, **136**, no. 3A, pp A826-A832.

Maniv, S. and Zangvil, (1978), "Controlled Texture of Reactively RF-Sputtered ZnO Thin Films," *Journal of Applied Physics*, **49**, no. 5, pp 2787-2792.

Martin, A.R., and Proudfoot, G., (1988), "Spacecraft Material Oxygen Erosion Simulation Using Ion Beams," *in Proceedings of the 4th European Symposium on Spacecraft Materials in a Space Environment*, Toulouse, France, pp 415-424, 6th-9th Sep. 1988. ISBN 2-85428-228-0.

Maruyama, K., Sasaki, G., Endo, S., and Kamata, K., (1994), "Formation of ZnO Films by CO_2 Laser Evaporation at Atmospheric Pressure on Glass and Organic Substrates," *Journal of Materials Science Letters*, **13**, pp 1737-1739.

Matcham, J.S., (1998a), Matcham Technical Services, UK, personal communication.

Matcham, J.S., (1998b), "Ground-Based Laboratory Atomic Oxygen Calibration Experiments," *ESA/ESTEC D-TOS-QMC Report 98/039*, June 1998. See also: Matcham, J.S., (1998), "Ground Based Laboratory Atomic Oxygen Calibration Experiments," Ph.D. Thesis, University of Southampton, Southampton, UK.

Matlis, S., Vered, R., Lempert, G.D., Marom, G., and Lifshitz, Y., "Scanning-Tunnelling-Microscopy Measurements of the Initial Erosion of Graphite by Hyperthermal atomic Oxygen and Neon," *Composites Science and Technology*, **48**, no. 1-4, pp 301-305.

Matthews, T., (1993), IN DeWitt, R.N., Duston, D., and Hyder, A.K., (eds.), "The Behaviour of Systems in the Space Environment," *NATO ASI Series – Series E: Applied Sciences*, **245**, pp 183-204.

Mauersberger, K., Kayser, D.C., Potter, W.E., and Nier, A.O., (1976), "Seasonal Variation of Neutral Thermospheric Constituents in the Northern Hemisphere," *Journal of Geophysical Research*, **81**, no. 1, pp 7-11.

McBride, N., (1999), Unit for Space Sciences and Astrophysics, The School of Physical Sciences, The University of Kent, Canterbury, UK.

McBride, N. and McDonnell, J.A.M., (1999), "Meteoroid Impacts on Spacecraft: Sporadics, Streams and the 1999 Leonids," *Planetary and Space Science*, **47**, pp 1005-1013.

McDonnell, J.A.M., (1993), "The Near Earth Particulate Environment," IN DeWitt, R. N., Duston, D., and Hyder, A. K., (eds.), "The Behaviour of Systems in the Space Environment," *NATO ASI Series – Series E: Applied Sciences*, **245**, pp 117-146.

McMurdie, D. (1986), *Powder Diffraction*, BIB, pp 76.

Mead, C.A., (1965), "Surface Barriers on ZnSe and ZnO," *Physics Letters*, **18**, no. 3, pp 218.

Miller, G.P., Pettigrew, P.J., Raikar, G. N., and Gregory, J.C., (1997), "A Simple, Inexpensive, Hyperthermal Atomic Oxygen Sensor," *Review of Scientific Instruments*, **68**, no. 9, pp 3557-3562.

Mollwo, E., (1954), "Electrical and Optical Properties of ZnO," *in Proceedings of the Conference on Photoconductivity*, Atlantic City, USA, pp 509-528, 4th-6th Nov. 1954.

Moore, W.M. and Codella, P.J., (1988), "Oxidation of Silver Films by Atomic Oxygen," *Journal of Physical Chemistry*, **92**, pp 4421-4426.

Morgan, J.H. and Brodie, D.E., (1982), "The Preparation and Some Properties of Transparent Conducting ZnO for Use in Solar Cells," *Canadian Journal of Physics*, **60**, pp 1387-1390.

Morrison, S.R., (1955), "Surface Barrier Effects in Adsorption, Illustrated by Zinc Oxide," *Advances in Catalysis*, **7**, pp 259-301.

Morrison, S.R., (1982), "Semiconductor Gas Sensors," *Sensors and Actuators*, **2**, no. 4, pp 329-341.

Moseley, P.T. and Tofield, B.C., (1985), "Semiconductor Gas Sensors," *Materials Science and Technology*, **1**, pp 505-509.

Moseley, P.T., (1991), "New Trends and Future Prospects of Thick- and Thin-Film Gas Sensors," *Sensors and Actuator B*, **3**, pp 167-174.

Myasnikov, I.A. and Malinova, G.V., (1964), "Semiconductor Probes Responding Separately to Free Radicals and Molecules," *Doklady Physical Chemistry*, **159**, no. 4, pp 1083-1085.

Myasnikov, I.A., (1975), "Semiconductor Active-Particle Detectors in Physical Chemical Research," *Zhurnal Vses. Khim. Ob-va im. Mendeleeva*, **20**, no. 1, pp 19-32.

Myasnikov, I.A. and Gutman, E.E., (1986), "Physico-Chemical Basis for Detection of Active Particles and Gas Molecules by Means of Semiconductor Metal Oxides," *in Proceedings of the 2nd International Meeting on Chemical Sensors*, Bordeaux, France, pp. 243-246, 1986.

Nahr, H., Hoinkes, H. and Wilsch, H., (1971), "New Method for the Detection of Atomic Oxygen Beams," *The Journal of Chemical Physics*, **54**, no. 7, pp 3022-3025.

Nanevicz, J. E. and Adamo, R. C., (1980), "Occurrence of Arcing and its Effect on Space Systems," *Progress in Astronautics and Aeronautics*, **71**, pp 252-275.

Nanto, H., Minami, T., Shooji, S., and Takata, S., (1984), "Electrical and Optical Properties of Zinc Oxide Thin Films Prepared by RF Magnetron Sputtering for Transparent Electrode Applications," *Journal of Applied Physics*, **55**, no. 4, pp 1029-1034.

Neumann, G., (1981), "On the Defect Structure of Zinc-Doped Zinc Oxide," *Physica Status Solidi B – Basic Research*, **105**, pp 605-612.

Niemann, H.B., Booth, J.R., Cooley, J.E., Hartle, R.E., Kasprzak, W.T., Spencer, N.W., Way, S.H., Hunten, D.M., and Carignan, G.R., (1980), "Pioneer Venus Orbiter Neutral Gas Mass Spectrometer Experiment," IEEE Transactions on Geoscience and Remote Sensing, **GE-18**, no. 1, pp 60-65.

Niemann, H.B., Harpold, D.N., Feng, S., Kasprzak, W.T., Way, S.H., Atreya, S.K., Block, B., Carignan, G.R., Donahue, T.M., Nagy, A.F., Bougher, S.W., Hunten, D.M., Owen, T.C., Bauer, S.J., Hayakawa, H.J., Mukai, T., Miura, Y.N., and Sugira, N., (1998), "The Planet-B Neutral Gas Mass Spectrometer," Earth, Planets and Space, **50**, pp 785-792.

Nier, A.O., Potter, W.E., Hickman, D.R., and Mauersberger, K., (1973), "The Open-Source Neutral-Mass Spectrometer on Atmosphere Explorer -C, -D and -E," *Radio Science*, **8**, no. 4, pp 271-276.

Niikura, I., Watanabe, H., and Wada, M., (1969), "Contact of ZnO Thin Films with Rhodamine B Dye," *Japanese Journal of Applied Physics*, **8**, no. 6, pp 755-758.

Oakes, D.B., Krech, R.H., Upschulte, B.L., and Caledonia, G.E., (1995), "Oxidation of Polycrystalline Silver Films by Hyperthermal Oxygen Atoms," *Journal of Applied Physics*, **77**, no. 5, pp 2166-2172.

Offermann, D. and Trinks, H., (1971), "A Rocket Borne Mass Spectrometer with Helium Cooled Ion Source," *Review of Scientific Instruments*, **42**, no. 12, pp 1836-1843.

Offermann, D. and Drescher, A., (1973), "Atomic Oxygen Densities in the Lower Thermosphere as Derived from *In Situ* 5577-A Night Airglow and Mass Spectrometer Measurements," *Journal of Geophysical Research*, **78**, no. 28, pp 6690-6700.

Offermann, D., Friedrich, V., Ross, P. and von Zahn, U., (1981), "Neutral Gas Composition Measurements Between 80 and 120 km," *Planetary and Space Science*, **29**, no. 7, pp 747-764.

Offermann, D., (1998), University of Wuppertal, Germany, Physics Department, personal communication.

Osborne, J.J., (1998a), "An Investigation of the Effects of Sample Distance and Laser Repetition rate on the Flux in the Atomic Oxygen Facility at the European Space Research and Technology Centre (ESTEC)," *ESA/ESTEC D-TOS/QMC report 98/038*, June 1998.

Osborne, J.J., (1998b), D-TOS/QMC report in preparation for ESA/ESTEC.

Osborne, J.J., Roberts, G.T., Chambers, A.R. and Gabriel, S.B., (1999), "Initial Results From Ground-based Testing of an Atomic Oxygen Sensor Designed for Use in Earth Orbit," *Review of Scientific Instruments*, **70**, no. 5, pp 2500-2506.

Packirisamy, S., Schwam, D., and Litt, M.H., (1995), "Review Atomic Oxygen Resistant Coatings For Low Earth Orbit Space Structures," *Journal of Materials Science*, **30**, pp 308-320.

Pavlenko, V.A., Zarkhin, V.I., Rafal'son, A.E., and Slutskii, M.E., (1966), "High-Sensitivity Radio Frequency Mass Spectrometer for Research on the Ionic and Neutral Composition of the Upper Atmosphere," *Kosmicheskie Issledovaniya*, **4**, no. 3, pp 457-462.

Pelz, D.T., Reber, C.A., Hedin, A.E., and Garigan, G.R., (1973), "A Neutral-Atmosphere Composition Experiment for the Atmosphere Explorer -C, -D, and -E," *Radio Science*, **8**, no. 4, pp 277-285.

Perov, S.P. and Rakhmanov, A.S., (1977), "Atomic Oxygen Concentration Measurements by a Rocket Near the Mesopause," *Space Research*, **18**, pp 261-264.

Peters, P.N., Linton, R.C., and Miller, E.R., (1983), "Results of Apparent Atomic Oxygen Reactions on Ag, C and Os Exposed During the Shuttle STS-4 Orbits," *Geophysics Research Letters*, **10**, no. 7, pp 569-571.

Peters, P.N., Gregory, J.C., and Swann, J.T., (1986), "Effects on Optical Systems from Interactions with Oxygen Atoms in Low Earth Orbits," *Applied Optics*, **25**, no. 8, pp 1290-1298.

Philipp, H.R., (1985), "Silicon Dioxide (SiO_2), Type α (Crystalline)," pp 719-748 and 749-763, IN Palik, E.D., (ed), "Handbook of Optical Constants of Solids," pub. Academic Press, Boston, USA, 1985, 804 Pages.

Philbrick, C.R. and McIsaac, J.P., (1972), "Measurements of Atmospheric Composition near 400 km," *Space Research*, **12**, pp 743-749.

Philbrick, C.R., Narcisi, R.S., Good, R.E., Hoffman, H.S., Keneshoa, T.J., MacLeod, M.A., Zimmerman, S.P., and Reinisch, B.W., (1973a), "The ALADDIN Experiment - Pt II, Composition," *Space Research*, **XIII**, pp 441-448.

Philbrick, C.R., Narcisi, R.S., Baker, D.W., Trzcinski, E., and Gardner, M.E., (1973b), "Satellite Measurements of Neutral Composition with a Velocity Mass Spectrometer," *Space Research*, **13**, pp 322-325

Philbrick, C.R., Faucher, G.A., and Trzcinski, E., (1973c), "Rocket Measurements of Mesospheric and Lower Thermospheric Composition," *Space Research*, **13**, pp 255-260.

Philbrick, C.R., (1974), "Satellite Measurements of Neutral Atmospheric Composition in the Altitude Range 150 to 450 km," *Space Research*, **14**, pp 151-156.

Philbrick, C.R., (1976), "Recent Satellite Measurements of Upper Atmospheric Composition," *Space Research*, **16**, pp 289-295

Pippin, H.G., Torre, L.P., Linton, R.C., and Whitaker, A.F., (1989), "Materials Resistance to Low Earth Orbit Environmental Effects," *in Proceedings of the 34th International SAMPE Symposium*, Reno, Nevada, USA, pp 1143-1151, 8th-11th May.

Pollard, E., (ed), (1994), "The Oxford Paperback Dictionary," 1st ed., pub. Oxford University Press, Oxford, UK, 1994, 938 pages

Pospelova, I.N. and Myasnikov, I.A., (1967), "Adsorption of Hydrogen Atoms on Zinc Oxide and Its Effect on Electrical Conduction. II Experimental investigation," *Russian Journal of Physical Chemistry*, **41**, no. 8, pp 1064-1067.

Prutton, M., (1987), "Surface Physics," 2nd ed., Oxford Physics Series, pub. Oxford University Press, Oxford, UK, 1987, 138 pages.

Raimondi, D.L. and Kay, E., (1970), "High Resistivity Transparent ZnO Thin Films," *Journal of Vacuum Science and Technology*, **7**, no. 1, pp 96-99.

Rancourt, J., Kamerling, M., and Monaco, D., (1991), "Title unknown," *in Proceedings of the 22nd IEEE Photovoltaic Specialists Conference*, Las Vegas, Nevada, USA, pp 1518, 7th-11th Oct. 1991.

Reddy, M.R., (1995), "Review Effect of Low Earth Orbit Atomic Oxygen on Spacecraft Materials," *Journal of Materials Science*, **30**, no. 2, pp 281-307.

Reddy, M.R., Srinivasamurthy, N., and Agrawal, B.L., (1992), "Effect of the Low-Earth-Orbit Atomic-Oxygen Environment on Solar-Array Materials," *ESA Journal*, **16**, pp 193-208.

Renarde, P., (1994), Matra Marconi Espace, personal communication to Dr I. Harris, relayed to author.

Roberts, G.T., (1998), University of Southampton, personal communication.

Roth, A., (1976), "Vacuum Technology," pub. North Holland Publishing Company, Amsterdam, The Netherlands, 1976, 496 pages.

Rousslang, K., Crutcher, R., and Pippin, H.G., (1992), "Results of Examination of Silvered Teflon from the Long Duration Exposure Facility," *in Proceedings of the First LDEF Post-Retrieval Symposium*, pp 847-859. NASA CP-3142 (part 2).

Ryl'tsev, N.V., Gutman, E.E., and Myasnikov, I.A., (1978), "Interaction of Atomic Hydrogen and Oxygen Beams with Various Surfaces," *Russian Journal of Physical Chemistry*, **52**, no. 7, pp 1042-1043.

Satchell, J., (1993), "Atomic Oxygen Detector," *Superconductor Science and Technology*, **6**, pp 379-380.

Sax, N.I. and Lewis, R.J., (eds), (1987), "Hawley's Condensed Chemical Dictionary," pub. van Nostrand, Reinhold, Holland, 1987, 1288 pages.

Scharowsky, E., (1953), "Optische und Electrische Eigenschaften von ZnO-Einkristallen mit Zn-überchuß," *Zeitschrift für Physik*, **135**, pp 318-330.

Schenkel, F.W., Ogorzalek, B.S., Larrabee, J.C., LeBlanc, F.J., and Huffman, R.E., (1985), "Ultraviolet Daytime Auroral and Ionospheric Imaging from Space," *Applied Optics*, **24**, no. 20, pp 3395-3405.

Scholz, T.G., and Offermann, D., (1974), "Measurement of Neutral Atmospheric Composition at 85-15 km by Mass Spectrometer with Cryoion Source," *Journal of Geophysical Research*, **79**, no. 1, pp 307-310.

Schropp, R.E.I. and Madan, A., (1989), "Properties of Conductive Zinc Oxide Films For Transparent Electrode Applications Prepared by RF Magnetron Sputtering," *Journal of Applied Physics*, **66**, no. 5, pp 2027-2031.

Seeger, K. (1973), "Semiconductor Physics," pub. Springer-Verlag, New York, USA, 1973, 514 pages.

Sharp, W.E., (1980), "Absolute Concentrations of $O(^3P)$ in the Lower Thermosphere at Night," *Geophysical Research Letters*, **7**, no. 7, pp 485-488.

Shepherd, G.G., Fancott, T., McNally, L., and Kerr, H.S., (1973), "ISIS-II Atomic Oxygen Red Line Photometer," *Applied Optics*, **12**, no. 8, pp 1767-1774.

Silverman, E.M., (1995), "Space Environmental Effects on Spacecraft: LEO Materials Selection Guide," *NASA Contractor Report 4661*, no. 1.

Sjolander, G.W., (1976), "Atomic Oxygen-Metal Surface Studies as Applied to Mass Spectrometer Measurements of Upper Planetary Atmospheres," *Journal of Geophysical Research*, **81**, pp 3767-3770.

Slemp, W.S., Santos-Mason, B., Sykes, G.F., Jr., and Witte, W.G., Jr., (1985), "Effects of STS-8 Atomic Oxygen Exposure on Composites, Polymeric Films and Coatings," *AIAA Paper*, AIAA-85-0421.

Smith, J., (1972), "Apollo-Nine Thermal Control Coating Degradation," *NASA TN D-6739.*

Smith, R.A., (1964), "Semiconductors," pub. Cambridge University Press, Cambridge, UK, 1964, 496 pages.

Sommerfeld, (1928), "Zur Elecktronentheorie der Metalle auf Grund der Fermischen Statistik," *Zeitschrift für Physik*, **47**, pp 1-60.

Somorjai, G.A., (1972), "Principles of Surface Chemistry," pub. Prentice-Hall, New Jersey, USA, 1972, 283 pages.

Song, Y., Kim, E.S., and Kapila, A., (1995), "Thermal Stability of Sputter Deposited ZnO Thin Films," *Journal of Electronic Materials*, **24**, no. 2, pp 83-86.

Stark, J.P.W. and Kinnersley, M.A., (1988), "Development of a Low-Power, High Velocity Atomic Oxygen Source," *Rarefied Gas Dynamics: Space-Related Studies*, Muntz, E.P., Weaver, D.P., and Campbell, D.H., (eds), *IN Progress in Astronautics and Aeronautics*, **116**, pp 156-170.

Stark, J.P.W. and Gabriel, S.B., (1997), "The Spacecraft Environment and its Effect on Design," IN Fortescue, P. and Stark, J., (eds.), (1997), "Spacecraft Systems Engineering," 2nd Edition, pub. Wiley, Chichester, UK, 1997, 581 pages.

Stevens, N.J., (1990), "Method of Estimating Atomic Oxygen Surface Effects in Space Environments," *Journal of Spacecraft and Rockets*, **27**, no. 1, pp 93-95.

Sukharev, V.Ya. and Myasnikov, I.A., (1984), "Electrical Conduction in Sintered Semiconductor Films With an Open Work Structure During the Adsorption of Active Gases," *Russian Journal of Physical Chemistry*, **58**, no. 3, pp 418-420

Sukharev, V.Ya. and Myasnikov, I.A., (1987a), "Theoretical Foundations of the Semiconductor Sensor Method of Analysis of Active Gases. II Effect of Adsorption on the Electrical Conductivity of Sintered Polycrystalline Adsorbents," *Russian Journal of Physical Chemistry*, **61**, no. 2, pp 159-165.

Sukharev, V.Ya. and Myasnikov, I.A., (1987b), "Theoretical Foundations of the Semiconductor Sensor Method of Analysis of Active Gases. III Quantitative Detection Methods," *Russian Journal of Physical Chemistry*, **61**, no. 3, pp 301-311.

Sundaram, K.B. and Garside, B.K., (1984), "Properties of ZnO films Reactively RF Sputtered Using a Zn Target," *Journal of Physics D: Applied Physics*, **17**, pp 147-153.

Swinerd, G.G., (1999), Department of Aeronautics and Astronautics, University of Southampton, personal communication.

Tagawa, M., Ema, T., Kinoshita, H., Umeno, M., Ohmae, N., and Minton, T. K., (1997), "Oxidation of Room Temperature Silicon (001) Surfaces in a Hyperthermal Atomic Oxygen Beam," *in Proceedings of the 7th International Symposium on Materials in a Space Environment*, Toulouse, France, pp 225-229, 16th-20th June 1997. ESA SP-399.

Tauc, J., (1962), "Photo and Thermoelectric Effects in Semiconductors", pub. Pergamon Press, Oxford, UK, 1962, 248 pages.

Tennyson, R.C., (1991), "Atomic Oxygen Effects on Polymer-Based Materials," *Canadian Journal of Physics*, **69**, pp 1190-1208.

Thomas, R.J. and Baker, D.J., (1972), "Silver Film Atomic Oxygen Sensors," *Canadian Journal of Physics*, **50**, pp 1676-1681.

Thomas, R.J. and Young, R.A., (1981), "Measurement of Atomic Oxygen and Related Airglows in the Lower Thermosphere," *Journal of Geophysical Research*, **86**, no. C8, pp 7389-7393.

Többen, H.H., Ringel, G.A., Schmitt, D.R., Weißbrodt, P., Schrenk, M., Raupach, L., and Hacker E., (1998), "In Flight Exposure Experiment SESAM," *in Proceedings 2nd European Symposium on the Utilization of the International Space Station*, ESTEC, Noordwijk, The Netherlands, 16th-18th Nov. 1998. ESA SP-433.

Torr, M.R., Hays, P.B., and Kennedy, B.C., (1977) "Intercalibration of Airglow Observatories with the Atmosphere Explorer Satellite," *Planetary and Space Science*, **25**, pp 173-184.

Trinks, H., Offermann, D., von Zahn, U., and Steinhauer, C., (1978), "Neutral Composition Measurements Between 90- and 220-km Altitude by Rocket-Borne Mass Spectrometer," *Journal of Geophysical Research*, **83**, no. A5, pp 2169-2176.

Triolo, J., Kruger, R., McIntosh, R., Maag, C., and Porzio, P.A., (1984), "Results from a 'Small Box' Real-Time Molecular Contamination Monitor on STS-3," *Journal of Spacecraft and Rockets*, **24**, no. 4, pp 400-404.

Trumble, T.M., (1992), "Experiment M0003-4: Advanced Solar Cell and Coverglass Analysis, an Overview," *Proceedings of the First LDEF Post-retrieval Symposium*, pp 1255-1256. NASA CP-3142(part 3).

van de Pol, F.C.M., (1990), "Thin-Film ZnO – Properties and Applications," *Ceramic Bulletin*, **69**, no. 12, pp 1959-1965.

van Eesbeek, M., (1996), "Atomic Oxygen Fluence Detector for BREMSAT Scientific and Technical Result Reporting," *ESTEC Working Paper 1921*, Noordwijk, The Netherlands, November 1996.

Vendura, G., (1997), TRW Inc., Presentation to the DERA STRV-1c&d Kick-off meeting, DERA Farnborough, March 1997.

Vered, R., Matlis, S., Nahor, G., Lempert, G.D., Grossman, E., Marom, G., and Lifshitz, Y., (1994), "Degradation of Polymers by Hyperthermal Atomic Oxygen," *Surface and Interface Analysis*, **22**, no.1-12, pp 532-537.

Visentine, J.T., Leger, L.J., Kuminecz, J.F., and Spiker, I.K., (1985), "STS-8 Atomic Oxygen Effects Experiment," *AIAA Paper*, AIAA-85-0415.

Visentine, J.T. and Leger, L.J., (1986), "Material Interactions With The Low Earth Orbital Environment: Accurate Reaction Rate Measurements," *in Proceedings of the NASA Workshop on Atomic Oxygen Effects*, Pasadena, CA, USA, pp 11-20, 10th-11th Nov. 1986. JPL-87-14.

von Zahn, U., (1967), "Mass Spectrometric Measurements of Atomic Oxygen in the Upper Atmosphere: A Critical Review," *Journal of Geophysical Research*, **72**, no. 23, pp 5933-5937.

Warren, B.E., (1969), "X-Ray Diffraction," pub. Addison-Wesley, London, UK, 1969, 381 pages.

Weihs, B. and van Eesbeek, M., (1994), "Secondary VUV Erosion Effects on Polymers in the ATOX Atomic Oxygen Exposure Facility," *in Proceedings of the 6th International Symposium on Materials in a Space Environment*, ESTEC, Noordwijk, The Netherlands, pp 277-283, 19th-23rd Sep. 1994. ESA SP-368.

Wells, N., (1999), "STRV-1c&d Mission Definition Specification," DERA Space Department, DERA Farnborough. Project reference: MIS/MGT/SPEC/0091 issue 2.2.

Westley, D.M., (1999), "A Critical Review of Atomic Oxygen Experiment 2 (AOE-2) in Terms of the Zinc Oxide Sensor," Final Year Undergraduate Report (unpublished), Department of Aeronautics and Astronautics, University of Southampton, Southampton, UK.

White, N., (1998), "Thick Film Sensors," Seminar presented to the Electronic Systems Design Group, Department of Electronics and Computer Science, University of Southampton, 25th June 1998.

Wood, N.J., Roberts, G.T., Gabriel, S.B., and Tatnall, A.R.L., (1994), "Development of a Plasma Acceleration Source for a Ground-Based Simulation of Atomic Oxygen," *in Proceedings of the 6th International Symposium on Materials in a Space Environment*, ESTEC, Noordwijk, The Netherlands, pp 265-269, 19th-23rd Sep. 1994. ESA SP-368.

Woollam, J.A., Synowicki, R.A., Hale, J.S., Ianno, N.J., Spady, B.L., Moore, A.W., and Hambourger, P., (1994), "Degradation of Thin Films: Comparison Between Low Earth Orbit Experiments and Laboratory Simulations of the Space Environment," *Thin Solid Films*, **241**, pp 218-221.

Yee, J. H. and Abreu, V. J., (1982), "Optical Contamination on the Atmosphere Explorer-E Satellite," *Proceedings of the Society of Photo-Optical Instrumentation Engineers Technical Symposium*, **338**, pp 120-128.

Yee, J.H. and Abreu, V.J., (1987), "Mesospheric 5577 Å Green Line and Atmospheric Motions - Atmosphere Explorer Satellite Observations," *Planetary and Space Science*, **35**, no. 11, pp 1389-1395.

Yen, J. C., (1975), "An Investigation of the Electrical Properties of Zinc Oxide Influenced by Oxygen Adsorption," *Journal of Vacuum Science and Technology*, **12**, no. 1, pp 47-51.

Young, R.A., (1961), "Measurement of the Atomic Concentration in Planetary Atmospheres", *Proposal for research*, No. 61-202, Stanford Research Institute, Menlo Park, California, USA.

Zangwill, A., (1988), "Physics at Surfaces," pub. Cambridge University Press, Cambridge, UK, 1988, 454 pages.

Zimcik, D.G., Tennyson, R.C., Kolk, L.J., and Maag, C.R., (1985), "The Effect of Low Earth Orbit Space Environment on Polymeric Spacecraft Materials," *in Proceedings of the 3rd European Symposium on Spacecraft Materials in Space Environment*, Noordwijk, The Netherlands, pp 81-89, 1st-4th Oct. 1985. ESA SP-232

Zimcik, D. G. and Maag, C. R., (1988), "Results of Apparent Oxygen Reactions with Spacecraft Materials During Shuttle Flight STS-41G," *Journal of Spacecraft and Rockets*, **25**, no. 2, pp 162-168.

APPENDIX A1

This appendix contains the data acquisition programme that was used to log the data during the experiments conducted in the ATOX test facility at ESTEC. The programme is written in BASIC and is designed to operate on the Macintosh-based computer acquisition system. The programme controls a switch unit, which is a relay-based multiplexer, two voltmeters and a frequency counter. Readings from twelve semiconductor films (6 sensors) and a single C-QCM are logged by the system. In addition, the temperatures of the three sensor substrates and the set-point temperature from the heater controller are also recorded. Only the sensor outputs and the temperature readings are sent through the switch unit, the C-QCM output frequency is fed directly into the frequency counter.

```
REM   ACQUISITION PROGRAM FOR LOGGING DATA FROM 6 MOS SENSORS AND 1
REM   C-QCM

REM *************** OPEN GPIB CONNECTION ***************
LIBRARY "QuickBASIC488.lib"
ibsta%=0 : iberr%=0 : ibcnt&=0
CALL ibinit(ibsta%,iberr%,ibcnt&)

REM *************** OPEN CONNECTION WITH COUNTER 1  ***************
DVM1% = 0
DVNAME1$ = "counter"
CALL IBFIND (DVNAME1$,DVM1%)
CALL IBCLR (DVM1%)
CALL ibwrt(DVM1%,"*RST")
CALL ibwrt(DVM1%,"*CLS")
CALL ibwrt(DVM1%,"*SRE 0")
CALL ibwrt(DVM1%,"*ESE 0")

REM *************** OPEN CONNECTION WITH SWITCH UNIT   ***************
DVM3% = 0
DVNAME3$ = "switch"
CALL IBFIND (DVNAME3$,DVM3%)
CALL IBCLR (DVM3%)
'CALL ibwrt (DVM3%,"CRESET 1,3")
```

```
REM ********** OPEN CONNECTION WITH VOLTMETER 1  **********
DVM5% = 0
DVNAME5$ = "VOLTMETER1"
CALL IBFIND (DVNAME5$,DVM5%)
CALL IBCLR (DVM5%)
CALL ibwrt(DVM5%,"*RST")
CALL ibwrt(DVM5%,"*CLS")

REM ********** OPEN CONNECTION WITH VOLTMETER 2  **********
DVM4% = 0
DVNAME4$ = "VOLTMETER2"
CALL IBFIND (DVNAME4$,DVM4%)
CALL IBCLR (DVM4%)
CALL ibwrt(DVM4%,"*RST")
CALL ibwrt(DVM4%,"*CLS")

REM ********** INITIALIZE AND DIMENSION VARIABLES **********
DIM a(16)
DIM b(16)
countday=0:  REM counter for day
Dtest=0:     REM difference of time at t=0 and time at t
FOR I=1 TO 3:a#(I)=0:NEXT I
rdf$=SPACE$(17):rdv$=SPACE$(10):rtq$=SPACE$(15)

REM ********** WINDOW DEFINITION **********
WINDOW 2,"status",(10,430)-(500,470),2
WINDOW 1,"Result",(2,39)-(610,420),1

REM ********** KEYBOARD INPUT **********
INPUT "How long is the test (in hours) ?",D
INPUT "What is the interval between measurements (in seconds) ?",dt

PRINT  "Save data as:"
file1$=FILES$(0)
IF file1$="" THEN END
filebase$=file1$
```

```
PRINT  "You may enter extra information, not too much!!!"
INPUT comment$

CLS
WINDOW 2
testdate$=DATE$:testtime$=TIME$
CALL TEXTSIZE(9)

PRINT :PRINT "Acquisition started on the ";testdate$;" at ";testtime$
PRINT "Saved in file: "file1$
PRINT  "File created on the ";testdate$;" at ";testtime$,

WINDOW 1
PRINT "Data saved in file " file1$
PRINT  "data saved in a new file every day (same name + day incrementation)."
PRINT "Duration of test:" D " hours."
PRINT "Measurement every " dt " seconds"
CALL TEXTSIZE(9)

REM ***************** STOP MENU *****************
BREAK ON:ON BREAK GOSUB keyboardstop
MENU 1,0,1,"Exit program"
MENU 1,1,1,"Quit"
MENU ON:ON MENU GOSUB menustop

REM ************ OPEN AND CLOSE FILE ROUTINES ************
OPEN file1$ FOR OUTPUT AS #1
PRINT #1, testdate$,testtime$
PRINT #1,comment$
PRINT #1, "n¡,Time,Time (min), T1, R11, R12, R13, R14, QCM, T2, R21, R22, R23, R24,
QCM,  T3, R31, R32, R33, R34, QCM, Tset"
CLOSE#1

REM ***************** MAIN PROGRAMME *****************
GOSUB measurement
GOSUB printresult
CLOCK!=start!:   REM init of the time, used as absolute reference (t0)
```

```
WHILE Dtest<D*3600
   GOSUB acquisition
WEND
PRINT "~~~~~~~~~~~~~~~~~~~~~~~~~~~~~~~~~~~~~~~~~~~~~~~~~~~~~~~~~~~~~~~~~~~"
PRINT "TEST FINISHED"
LIBRARY CLOSE
BREAK OFF:MENU OFF:MENU RESET
END

REM ********************** ACQUIRE DATA **********************
acquisition:
WHILE TIMER-start!<dt
   IF TIMER-start!<0 THEN
      start!=start!-86400&
      countday=countday+1
   END IF
WEND
GOSUB measurement
Dtest=start!+countday*86400!-CLOCK!
GOSUB printresult
RETURN

REM ******************* MAKE MEASUREMENTS *******************
measurement:
FOR I=1 TO 16:a(I)=0:b(I)=0:NEXT I
FOR I=1 TO 3:a#(I)=0:NEXT I
start!=TIMER:  REM init of the time, used to check dt
T$=TIME$
Nm=Nm+1

'                T1
CALL ibwrt (DVM3%,"CRESET 1")
CALL ibwrt (DVM3%,"CRESET 4")
CALL ibwrt (DVM3%,"CRESET 3")
CALL ibwrt(DVM3%,"CLOSE 410")
CALL ibwrt (DVM5%,"MEAS:VOLT:DC?")
CALL ibrd (DVM5%,rtq$)
```

```
CALL ibwrt(DVM5%,"*CLS")
a(1)=VAL(rtq$)

'               R11
CALL ibwrt (DVM3%,"CRESET 1")
CALL ibwrt (DVM3%,"CRESET 4")
CALL ibwrt (DVM3%,"CRESET 3")
CALL ibwrt(DVM3%,"CLOSE 101")
CALL ibwrt (DVM4%,"MEAS:RES?")
CALL ibrd (DVM4%,rtq$)
CALL ibwrt(DVM4%,"*CLS")
a(2)=VAL(rtq$)

'               R12
CALL ibwrt (DVM3%,"CRESET 1")
CALL ibwrt (DVM3%,"CRESET 4")
CALL ibwrt (DVM3%,"CRESET 3")
CALL ibwrt(DVM3%,"CLOSE 102")
CALL ibwrt (DVM4%,"MEAS:RES?")
CALL ibrd (DVM4%,rtq$)
CALL ibwrt(DVM4%,"*CLS")
a(3)=VAL(rtq$)

'               R13
CALL ibwrt (DVM3%,"CRESET 1")
CALL ibwrt (DVM3%,"CRESET 4")
CALL ibwrt (DVM3%,"CRESET 3")
CALL ibwrt(DVM3%,"CLOSE 103")
CALL ibwrt (DVM4%,"MEAS:RES?")
CALL ibrd (DVM4%,rtq$)
CALL ibwrt(DVM4%,"*CLS")
a(4)=VAL(rtq$)

'               R14
CALL ibwrt (DVM3%,"CRESET 1")
CALL ibwrt (DVM3%,"CRESET 4")
CALL ibwrt (DVM3%,"CRESET 3")
```

```
CALL ibwrt(DVM3%,"CLOSE 104")
CALL ibwrt (DVM4%,"MEAS:RES?")
CALL ibrd (DVM4%,rtq$)
CALL ibwrt(DVM4%,"*CLS")
a(5)=VAL(rtq$)

'                QCM 1 FREQUENCY
CALL ibwrt (DVM1%,":MEAS:MAX? (@1)")
CALL ibrd (DVM1%,rdv$)
CALL ibwrt (DVM1%,"*RST")
b=VAL(rdv$)
  IF b<>0 THEN
    CALL ibwrt (DVM1%,"CONF:FREQ 10MHZ, 1HZ, (@1)")
    CALL ibwrt(DVM1%,"INIT")
    CALL ibwrt(DVM1%,"FETCH:FREQUENCY?")
    CALL ibrd (DVM1%,rdf$)
    a#(1)=VAL(rdf$)
  ELSE
    a#(1)=0
  END IF

'                T2
CALL ibwrt (DVM3%,"CRESET 1")
CALL ibwrt (DVM3%,"CRESET 4")
CALL ibwrt (DVM3%,"CRESET 3")
CALL ibwrt(DVM3%,"CLOSE 411")
CALL ibwrt (DVM5%,"MEAS:VOLT:DC?")
CALL ibrd (DVM5%,rtq$)
CALL ibwrt(DVM5%,"*CLS")
a(6)=VAL(rtq$)

'                R21
CALL ibwrt (DVM3%,"CRESET 1")
CALL ibwrt (DVM3%,"CRESET 4")
CALL ibwrt (DVM3%,"CRESET 3")
CALL ibwrt(DVM3%,"CLOSE 106")
CALL ibwrt (DVM4%,"MEAS:RES?")
```

```
CALL ibrd (DVM4%,rtq$)
CALL ibwrt(DVM4%,"*CLS")
a(7)=VAL(rtq$)

'               R22
CALL ibwrt (DVM3%,"CRESET 1")
CALL ibwrt (DVM3%,"CRESET 4")
CALL ibwrt (DVM3%,"CRESET 3")
CALL ibwrt(DVM3%,"CLOSE 107")
CALL ibwrt (DVM4%,"MEAS:RES?")
CALL ibrd (DVM4%,rtq$)
CALL ibwrt(DVM4%,"*CLS")
a(8)=VAL(rtq$)

'               R23
CALL ibwrt (DVM3%,"CRESET 1")
CALL ibwrt (DVM3%,"CRESET 4")
CALL ibwrt (DVM3%,"CRESET 3")
CALL ibwrt(DVM3%,"CLOSE 108")
CALL ibwrt (DVM4%,"MEAS:RES?")
CALL ibrd (DVM4%,rtq$)
CALL ibwrt(DVM4%,"*CLS")
a(9)=VAL(rtq$)

'               R24
CALL ibwrt (DVM3%,"CRESET 1")
CALL ibwrt (DVM3%,"CRESET 4")
CALL ibwrt (DVM3%,"CRESET 3")
CALL ibwrt(DVM3%,"CLOSE 109")
CALL ibwrt (DVM4%,"MEAS:RES?")
CALL ibrd (DVM4%,rtq$)
CALL ibwrt(DVM4%,"*CLS")
a(10)=VAL(rtq$)

'               QCM 2 FREQUENCY
CALL ibwrt (DVM1%,":MEAS:MAX? (@1)")
CALL ibrd (DVM1%,rdv$)
```

```
CALL ibwrt (DVM1%,"*RST")
b=VAL(rdv$)
  IF b<>0 THEN
    CALL ibwrt (DVM1%,"CONF:FREQ 10MHZ, 1HZ, (@1)")
    CALL ibwrt(DVM1%,"INIT")
    CALL ibwrt(DVM1%,"FETCH:FREQUENCY?")
    CALL ibrd (DVM1%,rdf$)
    a#(2)=VAL(rdf$)
  ELSE
    a#(2)=0
  END IF

'               T3
CALL ibwrt (DVM3%,"CRESET 1")
CALL ibwrt (DVM3%,"CRESET 4")
CALL ibwrt (DVM3%,"CRESET 3")
CALL ibwrt(DVM3%,"CLOSE 412")
CALL ibwrt (DVM5%,"MEAS:VOLT:DC?")
CALL ibrd (DVM5%,rtq$)
CALL ibwrt(DVM5%,"*CLS")
a(11)=VAL(rtq$)

'               R31
CALL ibwrt (DVM3%,"CRESET 1")
CALL ibwrt (DVM3%,"CRESET 4")
CALL ibwrt (DVM3%,"CRESET 3")
CALL ibwrt(DVM3%,"CLOSE 301")
CALL ibwrt (DVM4%,"MEAS:RES?")
CALL ibrd (DVM4%,rtq$)
CALL ibwrt(DVM4%,"*CLS")
a(12)=VAL(rtq$)

'               R32
CALL ibwrt (DVM3%,"CRESET 1")
CALL ibwrt (DVM3%,"CRESET 4")
CALL ibwrt (DVM3%,"CRESET 3")
CALL ibwrt(DVM3%,"CLOSE 302")
```

```
CALL ibwrt (DVM4%,"MEAS:RES?")
CALL ibrd (DVM4%,rtq$)
CALL ibwrt(DVM4%,"*CLS")
a(13)=VAL(rtq$)

'                R33
CALL ibwrt (DVM3%,"CRESET 1")
CALL ibwrt (DVM3%,"CRESET 4")
CALL ibwrt (DVM3%,"CRESET 3")
CALL ibwrt(DVM3%,"CLOSE 304")
CALL ibwrt (DVM4%,"MEAS:RES?")
CALL ibrd (DVM4%,rtq$)
CALL ibwrt(DVM4%,"*CLS")
a(14)=VAL(rtq$)

'                R34
CALL ibwrt (DVM3%,"CRESET 1")
CALL ibwrt (DVM3%,"CRESET 4")
CALL ibwrt (DVM3%,"CRESET 3")
CALL ibwrt(DVM3%,"CLOSE 305")
CALL ibwrt (DVM4%,"MEAS:RES?")
CALL ibrd (DVM4%,rtq$)
CALL ibwrt(DVM4%,"*CLS")
a(15)=VAL(rtq$)


'                QCM 3 FREQUENCY
CALL ibwrt (DVM1%,":MEAS:MAX? (@1)")
CALL ibrd (DVM1%,rdv$)
CALL ibwrt (DVM1%,"*RST")
b=VAL(rdv$)
  IF b<>0 THEN
     CALL ibwrt (DVM1%,"CONF:FREQ 10MHZ, 1HZ, (@1)")
     CALL ibwrt(DVM1%,"INIT")
     CALL ibwrt(DVM1%,"FETCH:FREQUENCY?")
     CALL ibrd (DVM1%,rdf$)
     a#(3)=VAL(rdf$)
```

```
  ELSE
    a#(3)=0
  END IF

'              SET POINT TEMPERATURE
CALL ibwrt (DVM3%,"CRESET 1")
CALL ibwrt (DVM3%,"CRESET 4")
CALL ibwrt (DVM3%,"CRESET 3")
CALL ibwrt(DVM3%,"CLOSE 413")
CALL ibwrt (DVM5%,"MEAS:VOLT:DC?")
CALL ibrd (DVM5%,rtq$)
CALL ibwrt(DVM5%,"*CLS")
a(16)=VAL(rtq$)

RETURN

REM ********************* PRINT RESULTS TO: **********************
printresult:

REM ********************** SCREEN **********************
'                        PRINT READING NUMBER, CLOCK TIME, TIME (MINS)
PRINT TIME$ "  n¡" USING "#####";Nm;
PRINT USING "#####.##";Dtest/60;

'                        PRINT T1, R11, R12, R13, R14, QCM
PRINT USING "###.####";a(1);
PRINT USING "########.#";a(2);
PRINT USING "########.#";a(3);
PRINT USING "########.#";a(4);
PRINT USING "########.#";a(5);
PRINT a#(1)

'                        PRINT T2, R21, R22, R23, R24, QCM
PRINT USING "##.####";a(6);
PRINT USING "########.#";a(7);
PRINT USING "########.#";a(8);
PRINT USING "########.#";a(9);
```

```
PRINT USING "########.#";a(10);
PRINT a#(2)

'                          PRINT T3, R31, R32, R33, R34, QCM
PRINT USING "##.####";a(11);
PRINT USING "########.#";a(12);
PRINT USING "########.#";a(13);
PRINT USING "########.#";a(14);
PRINT USING "########.#";a(15);
PRINT a#(3)

'                          PRINT SET POINT TEMPERATURE
PRINT USING "##.####";a(16)

REM ********************** HARD DISK **********************
OPEN file1$ FOR APPEND AS #1

'                          PRINT READING NUMBER, CLOCK TIME, TIME (MINS)
PRINT#1, Nm;",";T$;",";Dtest/60;

'                          PRINT T1, R11, R12, R13, R14, QCM
FOR I=1 TO 5
   PRINT#1, ",";a(I);
NEXT I
PRINT#1, ",";a#(1);

'                          PRINT T2, R21, R22, R23, R24, QCM
FOR J=6 TO 10
   PRINT#1, ",";a(J);
NEXT J
PRINT#1,",";a#(2);

'                          PRINT T3, R31, R32, R33, R34, QCM
FOR K=11 TO 15
   PRINT#1, ",";a(K);
NEXT K
PRINT#1,",";a#(3);
```

```
'                    PRINT SET POINT TEMPERATURE
PRINT#1,","a(16)

CLOSE#1
RETURN

REM ************ BREAK FROM KEYBOARD ************
keyboardstop:
WINDOW 5,"STOP acq", (150,130)-(330,200), 2
PRINT  "Do you really want to quit?"
BUTTON 3,1, "Yes", (20,20)-(160,40), 1
BUTTON 4,1, "Sorry, my mistake!", (20,45)-(160,65),1

WHILE DIALOG(0)<>1:WEND

IF DIALOG(1)=3 THEN
   LIBRARY CLOSE
   BREAK OFF:MENU OFF:MENU RESET
   END
END IF

WINDOW 1

RETURN

REM ************ BREAK FROM MENU ************
menustop:
IF MENU(1)=1 THEN GOSUB keyboardstop
RETURN
```

APPENDIX A2

The purpose of this appendix is to describe the investigations that have been performed to isolate the best data processing route for analysing the data recorded during the AO exposure experiments. A trial and error approach was used to derive the results reported herein.

A2.1 INTRODUCTION

A2.1.1 Background

Reference to the ballistic model presented in Chapter 5 - Equation (5.32) - shows that, at the start of AO exposure, the time rate of change of sensor conductance is proportional to the incident AO flux. The data recorded during AO exposures are actually the resistance values of the sensor films and the time at which the resistance values were recorded. Therefore, it is necessary to convert the resistance values into conductance values and then to numerically differentiate them with respect to time. It is expected that a plot of the differentiated conductance data will display a minimum (negative peak) at the time that the AO flow was initiated. The magnitude of this peak is thus used as the **response** of the sensor to the impinging AO flux - it is these magnitudes that are used in the generation of calibration curves for the sensor films *etc.*

The first stage of the data processing is to convert the recorded resistance data into conductance data. This is most easily accomplished by simply taking the reciprocal of each data value. Then, the data requires numerical differentiation; this is the subject of the next section.

A2.1.2 Numerical differentiation

It is possible to use Taylor's series to develop some expressions to enable numerical differentiation of a given data set. In this investigation attention has only been applied to first and second order approximate difference schemes, since it was deemed that higher orders would be of an inappropriately high accuracy. Note, the terms first and second order, which describe the 'accuracy' of the approximations, should not be confused with the first and second derivatives $\frac{dy}{dx}$ and $\frac{d^2y}{dx^2}$ respectively, which describe the number of differentiations performed on a particular set of data.

Taylor's series states that:

$$f(x+\Delta x) = f(x) + \Delta x\frac{df}{dx} + \frac{\Delta x^2}{2!}\frac{d^2f}{dx^2} + \frac{\Delta x^3}{3!}\frac{d^3f}{dx^3} + \ldots + \frac{\Delta x^n}{n!}\frac{d^nf}{dx^n} + \ldots \quad \text{(A2-1)}$$

and

$$f(x-\Delta x) = f(x) - \Delta x\frac{df}{dx} + \frac{\Delta x^2}{2!}\frac{d^2f}{dx^2} - \frac{\Delta x^3}{3!}\frac{d^3f}{dx^3} + \ldots + \frac{\Delta x^n}{n!}\frac{d^nf}{dx^n} + \ldots \quad \text{(A2-2)}$$

Ignoring $O(x^2)$ and above (A2-1) and (A2-2) become:

$$f(x+\Delta x) = f(x) + \Delta x\frac{df}{dx} \quad \text{(A2-3)}$$

and

$$f(x-\Delta x) = f(x) - \Delta x\frac{df}{dx} \quad \text{(A2-4)}$$

Now, rearranging (A2-3) for $\frac{df}{dx}$ yields the **first order forward difference** approximation:

$$\frac{df}{dx} = \frac{f(x+\Delta x) - f(x)}{\Delta x} \quad \text{(A2-5)}$$

which determines the differential at x using the values f(x) and f(x+Δx). Whereas, rearranging (A2-4) for $\frac{df}{dx}$ yields the **first order backward difference** approximation:

$$\frac{df}{dx} = \frac{f(x) - f(x-\Delta x)}{\Delta x} \quad \text{(A2-6)}$$

which determines the differential at (x+Δx) using the values f(x) and f(x-Δx).

Using Taylor's theorem it is also possible to determine a more accurate second order approximation for the differential, assuming that the data values are recorded at equal intervals of Δx. Subtracting (A2-2) from (A2-1) results in:

$$f(x+\Delta x) - f(x-\Delta x) = \Delta x\frac{df}{dx} + \Delta x\frac{df}{dx} \quad \text{(A2-7)}$$

and then

$$\frac{df}{dx} = \frac{f(x+\Delta x) - f(x-\Delta x)}{2\Delta x} \tag{A2-8}$$

which determines the differential of the function f at x using the values f(x+Δx) and f(x-Δx). Equation (A2-8) is a **second order central difference approximation**.

Thus, using these three equations - (A2-5), (A2-6) and (A2-8) - it is possible to numerically differentiate a data series.

A2.1.3 Data smoothing algorithms

In addition to the investigation of the effects of the order of the difference approximation, the results of utilizing two different data smoothing algorithms have been researched. Whilst not terribly sophisticated, the methods chosen for investigation - 2-point and 3-point moving averages - are easily coded and fast.

In a data set x, x+Δx, x+2Δx, x+3Δx, ..., x+nΔx, ... with corresponding values of f(x), f(x+Δx), f(x+2Δx), f(x+3Δx), ..., f(x+nΔx), ... the 2-point smoothing is applied using the following scheme:

$$f_n(x) = \frac{f(x) + f(x+\Delta x)}{2} \tag{A2-9}$$

Where $f_n(x)$ is the new y-value in the data series at position (x).

Whereas, the 3-point smoothing is applied using the scheme:

$$f_n(x) = \frac{f(x-\Delta x) + f(x) + f(x+\Delta x)}{3} \tag{A2-10}$$

A2.1.4 Analysis programme

A data analysis program has been written by the author in MS Visual Basic 5.0 to perform all of these algorithms. The program allows a data set, like those generated during the experiments at ESTEC to be loaded, and then the user is at liberty to choose various data processes and to 'run' them through the stored data. The advantages of the program, which includes a full graphical user

interface (GUI), is that data can be analysed far faster than can be achieved in a standard spreadsheet package.

The results of the program have been carefully checked against hand-calculations and spreadsheet results to make sure that it is functioning properly. All of the results presented in this thesis that required differentiation of the raw ESTEC data files have been generated using this program.

A2.1.5 Processing routes investigated

From the above it is clear that there are many different data processing routes that could be chosen and applied to the data sets. Those chosen for study in this investigation are:

1. Backward, forward and central difference differentiation of unsmoothed, inverted data.
2. Backward, forward and central difference differentiation of 2-point smoothed, inverted data.
3. Backward, forward and central difference differentiation of 3-point smoothed, inverted data.

A2.2 COMPARISON OF DATA PROCESSING ROUTES

A2.2.1 Case study

Just like the analysis in Section 9.2, the data processing routes described above will be investigated using the data from experiments TF2, 3, 4 and 6. For clarity of presentation only the results from TG08A2b will be examined in this subsection, although it has been found that the conclusions are applicable to the results from TG08A1b as well.

It has been found that the forward and backward difference algorithms generate the same data values. The reason for this is evident from equations (A2-5) and (A2-6) - the two equations use the same data points to calculate the differential, but evaluate it at a different x-wise position - in this case time. For this reason, results will only be presented from forward and central difference equations.

Figure A2-1 shows six graphs derived from TG08A2b during experiment TF3. The effects of the different data processing routes can be seen. The sensor response is the magnitude of the maximum negative differential, see Figure 9.11. In the graphs below the points defining these negative peaks, for the want of a better phrase, have been circled.

Parts (a) and (b) show the results of simply differentiating the raw data, using the first order forward and second order central difference schemes respectively. No smoothing was applied to

the data in either of these two graphs. It is clear that the data resulting from the 1st order scheme is very noisy, in fact, so much so that the peak value defining the sensor response is hard to distinguish from the other minima. Whereas, the sensor response peak in part (b), after the central difference differentiation, is much more easily distinguished from the noise values. Comparison of these two graphs clearly shows that the magnitudes of the response peaks are not equal, that arising from the 1st order scheme is some 57% greater than that from the 2nd order scheme.

Applying a 2-point smoothing algorithm before the difference schemes has the effect of making the first order data less oscillatory and noisy, whilst also making the peak response easier far to distinguish. The same smoothing algorithm, when applied before the second order difference equation, also has the effect of reducing noise. However, it also reduces the visibility of the peak in that there are more data points crowded around the peak value, and the magnitude of the peak is reduced by 30% from the unsmoothed value.

Applying three point smoothing schemes to the data processing reduces the noise values even further in both difference cases. However, peak visibility is also reduced in both cases, again because more data points are 'dragged' by the smoothing process from the baseline (near zero values) to the peak.

It is also evident that applying any smoothing reduces the absolute value of the minima that defines the response of the sensor. For example, one can see in parts (b), (d) and (e) that the minima reduces from -1.6×10^{-6} mhos.min^{-1} with no smoothing, to -1.1×10^{-6} mhos.min^{-1} with 2-point smoothing and then to -9.7×10^{-6} mhos.min^{-1} with 3-point smoothing. This reduction is coupled to the reducing visibility of the minima.

Thus, in the case of the 1st order difference scheme, it appears that peak visibility increases as a result of two point smoothing, but decreases as a result of three point smoothing. In comparison, peak visibility decreases as a result of application of two point smoothing and decreases even more if three point smoothing is applied before the central difference scheme.

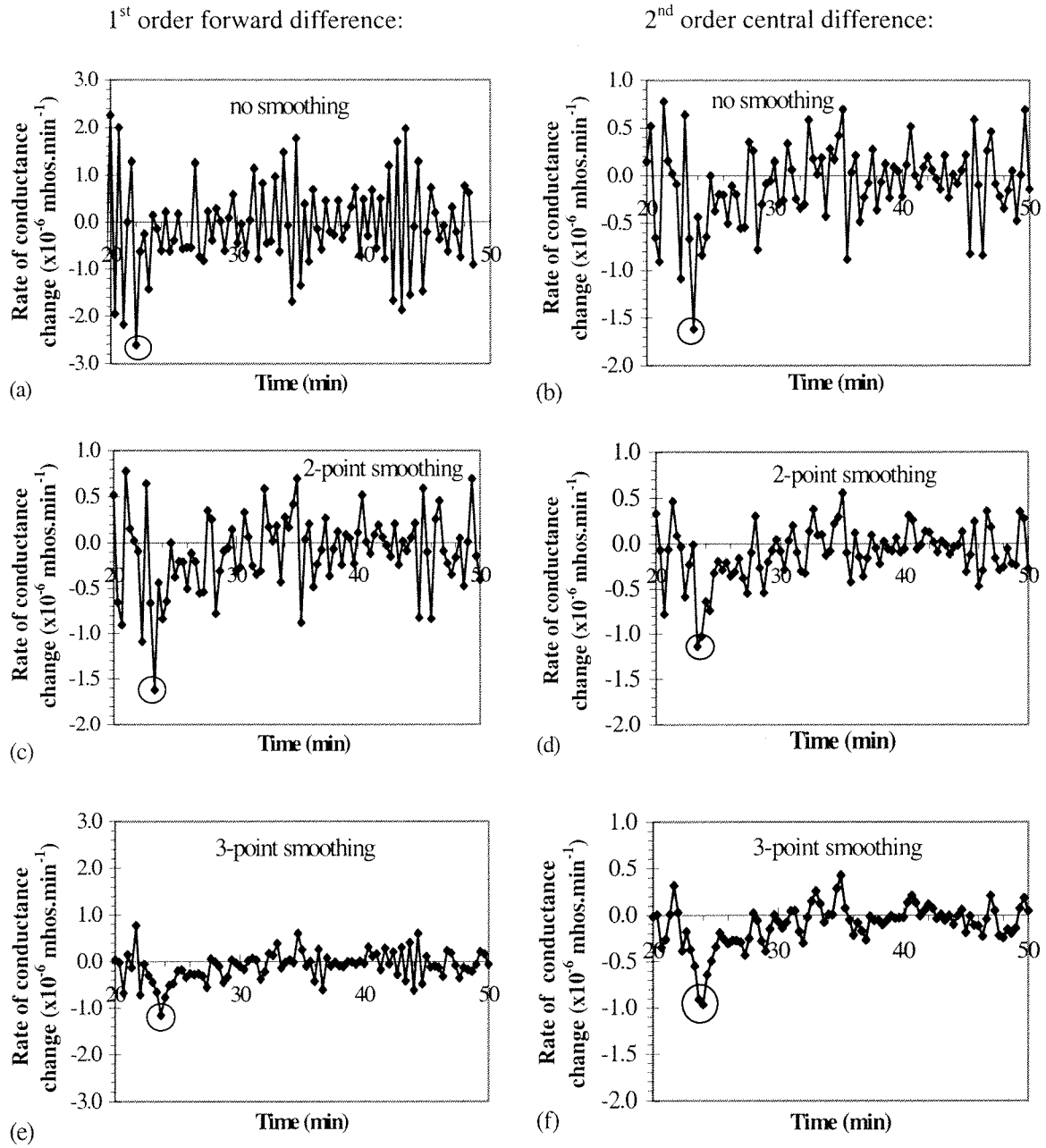

Figure A2-1 - TG08A2b data from TF3 after several processing schemes

A2.2.2 Effect of processing scheme upon results

Table A2-1 (a) and (b) shows the data generated by the different processing schemes for experiments TF2, 3, 4 and 6. Figure A2-2 contains plots of the data contained in the two tables. Part (a) of the figure displays the data from Table A2-1 part (a), for the first order forward difference scheme. The work presented in Chapter 5 showed that the sensor response should be a linear function of AO flux. It is apparent that only one of the three smoothing cases - when applied to the inverted data before the forward difference scheme - generates results that obey the mathematical expectations of the ballistic model. That is, the two point smoothing algorithm. Whilst the response versus flux curves generated by the other processing routes (no smoothing

and 3-point smoothing) are highly non-linear. Since the data resulting from these processing routes is non-linear, the schemes are not appropriate or acceptable for application in this work.

Test	AO flux ($x\ 10^{15}$ atoms.cm^{-2}.s^{-1})	No smoothing ($x10^{-6}$ mhos.min^{-1})	2-pt smoothing ($x10^{-6}$ mhos.min^{-1})	3-pt smoothing ($x10^{-6}$ mhos.min^{-1})
TF2	2.12618	-3.74	-3.18	-2.66
TF6	1.41725	-2.56	-2.15	-1.84
TF3	0.90922	-2.61	-1.62	-1.16
TF4	0.47048	-2.78	-0.95	-1.54

(a) First order forward difference

Test	AO flux ($x\ 10^{15}$ atoms.cm^{-2}.s^{-1})	No smoothing ($x10^{-6}$ mhos.min^{-1})	2-pt smoothing ($x10^{-6}$ mhos.min^{-1})	3-pt smoothing ($x10^{-6}$ mhos.min^{-1})
TF2	2.12618	-3.18	-2.72	-2.52
TF6	1.41725	-2.15	-1.82	-1.71
TF3	0.90922	-1.62	-1.14	-0.97
TF4	0.47048	-0.95	-0.95	-0.79

(b) Second order central difference

Table A2-1 - Results of several different processing schemes

The second part of the figure shows a different pattern. In this case - the central difference scheme - it appears that only the no-smoothing route generates the expected linear data. Applying any smoothing to the data whatsoever removes the linearity in favour of non-linear response curves. Thus, by the previous argument, the only applicable data processing route involving the second order central difference scheme is that using no smoothing.

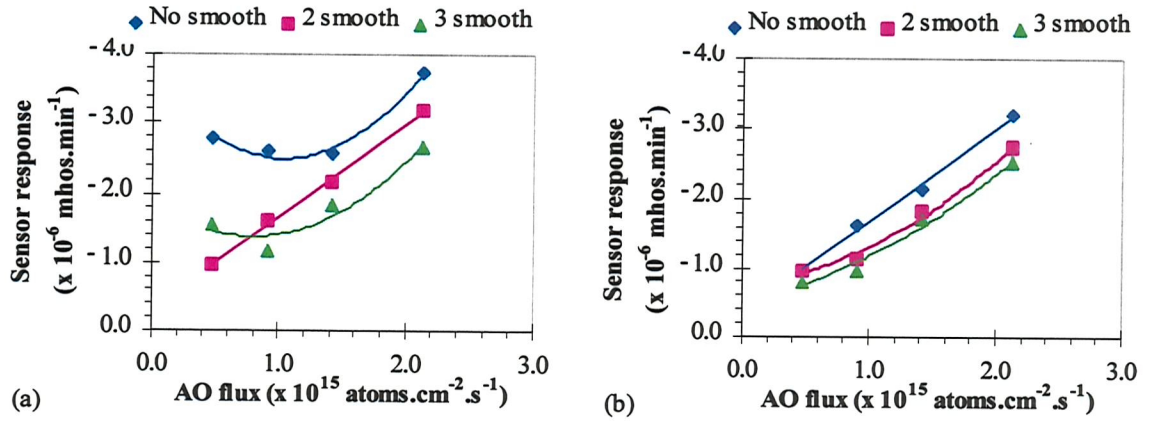

Figure A2-2 - Plots of different processing schemes: (a) forward; (b) central difference

Reference to the previous section indicates that the patterns of acceptability discussed above concur with the patterns of peak visibility and noise reduction. Thus the most acceptable data processing techniques result in the most clearly defined, visible sensor responses. In fact, an examination of Figure A2-1 parts (b) and (c) show that the differentiated data (first order after 2-

point smoothing and second order with no smoothing) are identical. It is possible to show why mathematically.

If a data set consists of the elements:

f(x), f(x+Δx), f(x+2Δx), f(x+3Δx), f(x+4Δx), ..., f(x+nΔx), ...

at positions x, x+Δx, x+2Δx, x+3Δx, x+4Δx, ..., x+nΔx,....

Then using 2 point smoothing algorithm results in:

$$\frac{f(x)+f(x+\Delta x)}{2}, \frac{f(x+\Delta x)+f(x+2\Delta x)}{2}, \frac{f(x+2\Delta x)+f(x+3\Delta x)}{2}, \ldots\ldots$$

at positions x, x+Δx, x+2Δx, x+3Δx, x+4Δx, ...

If this data is then differentiated using the 1st order forward difference equation at position x, the results look like:

$$\frac{df}{dx} = \frac{\frac{f(x+\Delta x)+f(x+2\Delta x)}{2} - \frac{f(x+\Delta x)+f(x)}{2}}{\Delta x} = \frac{f(x+2\Delta x)-f(x)}{2\Delta x}$$

Which is the same expression as that which results from applying the second order difference scheme at (x+Δx).

A2.3 APPENDIX CONCLUSION

It is clear from the previous investigations and discussion that there are two valid data processing routes. The first is to smooth the inverted raw resistance data and then to apply a first order forward (or backward) difference scheme to differentiate the data with respect to time. Alternatively, it is possible to invert the raw resistance data and to apply a second order central difference scheme, without the application of any smoothing.

The results from these two processes are identical, but since the first involves two steps and the second involves only one, it has been decided to adopt the central difference route for the data processing in this thesis. In this way the data processing is easier to code, and faster to run.